



Virginia Commonwealth University  
VCU Scholars Compass

---

Theses and Dissertations

Graduate School

---


2016

## Fabrication of Multifunctional Nanostructured Porous Materials

Ahmed A. Farghaly

*Department of Chemistry, Virginia Commonwealth University, Richmond, Virginia 23284-2006, United States*

Follow this and additional works at: <https://scholarscompass.vcu.edu/etd>

 Part of the [Analytical Chemistry Commons](#), [Inorganic Chemistry Commons](#), [Materials Chemistry Commons](#), and the [Polymer Chemistry Commons](#)

© The Author

---

Downloaded from

<https://scholarscompass.vcu.edu/etd/4189>

This Dissertation is brought to you for free and open access by the Graduate School at VCU Scholars Compass. It has been accepted for inclusion in Theses and Dissertations by an authorized administrator of VCU Scholars Compass. For more information, please contact [libcompass@vcu.edu](mailto:libcompass@vcu.edu).

# **Fabrication of Multifunctional Nanostructured Porous Materials**

A dissertation submitted in partial fulfillment of the requirements for the degree of  
Doctor of Philosophy at Virginia Commonwealth University.

by

Ahmed Abdelsameh Abozeed Farghaly

Master of Science, Assiut University, Egypt, 2008

Bachelor of Science, Assiut University, Egypt, 2001

Director: Dr. Maryanne M. Collinson

Professor of Chemistry

Virginia Commonwealth University

Richmond, Virginia

May, 2016

## Acknowledgements

In completion of this dissertation, there are many people to thank and gratitude; without them the accomplishment of this journey would have never become possible. First, I would like to thank my parents, wife Heba Ali and lovely children Muhammad, Hannah and Emma for their constant encouragement, love, smile and support that keeps me going every day of my life. I am very grateful and appreciative to my advisor Prof. Maryanne M. Collinson for her continuous guidance, support and encouragement throughout my PhD research work. Thanks Prof. Maryanne for giving me the opportunity to be a member in your wonderful research group. Truly, I consider myself very lucky to have had the chance to work with a great, considerable, smart, knowledgeable and supportive scientist like her. Indeed, an endless number of pages is required to express, how much I am thankful and grateful to Prof. Maryanne. Whatever I achieved during my PhD work would not have been possible without her. I would also like to thank my lab mates, friends, brothers, and sisters for their continuous support. I am grateful and thankful to my committee members Prof. Hani M. El-Kaderi, Prof. Indika U. Arachchige, and Prof. Dexian Ye for their continuous support, encouragements, follow up and time. Also, I am very thankful to my collaborators for giving me the opportunity to be a part of their research projects. I would like to specifically thank Prof. Ram B. Gupta, Associate Dean for Research for his continuous support and interest in my work. Many thanks to Dr. Dmitry Pestov for this help, time and support during the instrumental analysis. I am also very thankful to all the teaching Professors I worked with them during my stay at the Chemistry Department, VCU especially Prof. Joseph Topich. Thanks must also go to the Professors of the Chemistry department at Assiut University, without the science and knowledge I got from them, my research would not have been as successful and for giving me the permission to pursue my PhD degree at VCU. I also must thank my Master thesis advisors Prof. Said A. Ibrahim, Prof. Sahar A. El-Gyar, and Prof. Mohamed A. El-Gahami. The experience and knowledge I built in your lab helped me to be a successful, productive and creative scientist since my first day at VCU. Lastly, I would like to acknowledge the VCU Chemistry Department for providing a wonderful and rich scientific environment and for the fund.

## Table of Contents

Acknowledgements.....	ii
List of Figures.....	vii
List of Tables.....	xxii
List of Abbreviations.....	xxiii
Abstract.....	xxviii
Chapter 1: Introduction.....	1
1.1 Introduction.....	2
1.2 Overview of the Noble Metal-Based Porous Materials.....	2
1.3 Fabrication Strategies of Nanostructured Porous Noble Metals.....	4
1.3.1 Template Approach.....	5
1.3.2 Hard Templates.....	6
1.3.3 Soft Templates.....	8
1.3.4 Synthesis of Noble Metal Aerogels by the Sol-Gel Assembly Approach.....	10
1.3.5 Combustion Synthesis of Nanoporous Metal Foams.....	12
1.3.6 Dealloying Approach.....	15
1.4 Applications of Porous Noble Metals.....	19
1.4.1 Sensing Applications of NPNMs.....	19
1.4.2 Catalytic Applications of NPNMs.....	22
1.5 Nanostructured Materials by Electrodeposition.....	24
1.5.1 Nucleation and Growth.....	25

1.5.2 Electroassisted Deposition of Sol-Gel Derived Materials.....	28
1.5.3 Cathodic Electrodeposition of Conducting Polymers.....	37
1.6 Why are New Fabrication Strategies for Nanostructured Porous Materials Required?.....	40
1.7 Thesis Statement.....	41
1.8 References.....	43
Chapter 2: Characterization Techniques.....	55
2.1 Introduction.....	56
2.2 Electrochemical Techniques .....	56
2.2.1 Cyclic Voltammetry.....	59
2.2.2 Chronoamperometry.....	62
2.3 Scanning Electron Microscopy (SEM).....	64
2.4 Energy-Dispersive X-ray Spectroscopy (EDS).....	67
2.5 X-ray Diffraction (XRD).....	69
2.6 X-ray Photoelectron Spectroscopy (XPS).....	72
2.7 Contact Surface Profilometry Analysis.....	75
2.8 References.....	77
Chapter 3: Fabrication of Nanostructured Porous Gold.....	78
3.1. Introduction.....	79
3.2. Experimental Section.....	81
3.2.1 Reagents and Materials.....	81
3.2.2 Co-Electrodeposition of Gold/Sol-Gel (Au-SiO <sub>2</sub> ) Nanocomposite Thin Films.....	81
3.2.3 Fabrication of Coral-Like Nanostructured Porous Gold (NSPG) Thin Films.....	83
3.2.4 Characterization. ....	83
3.3. Results and Discussion .....	84

3.3.1 Sol-Gel (Au-SiO <sub>2</sub> ) Nanocomposite Films.....	84
3.3.2 Nanostructured Porous Gold (NSPG) Films.....	94
3.3.3 Nanostructured Porous Gold (NSPG) Films: Morphology Control.....	102
3.4. Conclusion .....	113
3.5. References .....	114
Chapter 4: Fabrication of Strata-Like Mesoporous Polypyrrole-Silica Nanostructures.....	118
4.1. Introduction .....	119
4.2. Experimental Section .....	121
4.2.1. Reagents and Materials .....	121
4.2.2. Co-electrodeposition of Polypyrrole-Silica-Silver (Ppy-SiO <sub>2</sub> -Ag@Au) and Polypyrrole-Silica (Ppy-SiO <sub>2</sub> @Ag) Hybrid Nanocomposite Films on Gold and Silver Substrates, Respectively.....	122
4.2.3. Fabrication of Free-Standing and Transferable Polypyrrole Thin Films .....	123
4.2.4. Characterization .....	127
4.3. Results and Discussion.....	127
4.3.1. Synthesis of Conducting Polymer-Silica (Ppy-SiO <sub>2</sub> -Ag@Au & Ppy-SiO <sub>2</sub> @Ag) Nanocomposite Thin Films.....	127
4.3.2. Surface Morphology.....	131
4.3.3. Free Standing and Transferable Composite Films by LDCD.....	136
4.3.4. Chemical Composition.....	141
4.3.5. Electrochemical Measurements.....	149
4.3.6. Strata-Like Mesoporous Structure.....	152
4.3.7. Proposed Reaction Mechanism.....	158
4.4. Conclusions.....	162
4.5. References.....	163
Chapter 5: Bicontinuous Nanoporous Platinum.....	166

5.1 Introduction.....	167
5.2 Experimental Section.....	171
5.2.1 Reagents and Materials.....	171
5.2.2 Preparation of the Conductive Substrate.....	171
5.2.3 Fabrication of Three-Dimensional Bicontinuous Nanoporous Platinum Thin Films.....	172
5.2.4 Characterization of 3D-BC-NP-Pt Electrodes.....	175
5.2.5 Electrochemical Measurements.....	176
5.3 Results and Discussion.....	178
5.3.1 Fabrication of Three-Dimensional Bicontinuous Nanoporous Platinum Thin Films.....	178
5.3.2 Morphology and Pt : Ag Mole Ratio.....	181
5.3.3 Film Thickness.....	185
5.3.4 Template-Less Fabrication of 3D Bicontinuous Porous Platinum Nanorods.....	188
5.3.5 Electrochemical Measurements.....	192
5.4 Conclusion.....	207
5.5 References.....	209
Chapter 6: Conclusions and Future Work.....	213
6.1 Conclusion.....	214
6.2 Future Work.....	217
6.2.1 Electroassisted Fabrication of Metal/Sol-Gel Nanocomposites.....	218
6.2.2 Electroassisted Fabrication of Polymer-Metal/Metal Oxide Nanocomposites.....	220
6.2.3 Bicontinuous Porous Platinum.....	220
6.3 References .....	223
Vita .....	224

## List of Figures

### Chapter 1

- Figure 1.1.** Fabrication of ordered nanostructured porous metals using the hard template approach. Adapted with permission from reference 34. Copyright 2008 John Wiley and Sons, Inc. .... 7
- Figure 1.2.** Fabrication of ordered nanostructured porous metals using the soft template approach. Adapted with permission from reference 34. Copyright 2008 John Wiley and Sons, Inc. .... 9
- Figure 1.3.** Fabrication of noble metal aerogels by the the sol-gel assembly approach. .... 11
- Figure 1.4.** TEM images of multimetallic Au-Pd, Pt-Pd and Ag-Pd aerogels. Adapted with permission from reference 67. Copyright 2014 American Chemical Society..... 12
- Figure 1.5.** (a) Bistetrazolamine (BTA) ligand and (b) BTA metal complex (M: Fe<sup>3+</sup> or Co<sup>3+</sup>) 14
- Figure 1.6.** Co nanofoams prepared by the combustion of cobalt bistetrazolamine complex with porosity ranging from nm to mm. Adapted with permission from reference 5. Copyright 2010 John Wiley and Sons, Inc..... 14
- Figure 1.7.** SEM micrographs of 3D bicontinuous nanoporous gold on glass at different magnifications. SEMs collected by Ahmed A. Farghaly. Fabrication method was developed by Ahmed A. Farghaly and Hajira Choudhary. Sample prepared by Christopher J. Freeman. All the work done under supervision of Prof. Maryanne M. Collinson. .... 16



- Figure 1.8.** Schematic illustration of the fabrication of NPG-based immunosensor for hepatitis B. Reprinted with permission from reference 93. Copyright 2010 Elsevier. .... 21
- Figure 1.9.** Schematic illustration of the different modes of thin film growth (a) 3D islands (Volmer - Weber mode), (b) 2D layer-by-layer (Frank-van der Merve mode), and (c) 2D layer + 3D islands (Stranski-Krastanov mode). Modified from reference 116..... 27
- Figure 1.10.** Schematic diagrams of possible cyclic siloxane structures in silica gels. Reprinted with permission from reference 38. Copyright 2013 American Chemical Society. .... 33
- Chapter 2**
- Figure 2.1.** Three-electrode electrochemical cell..... 57
- Figure 2.2.** Potential waveform for cyclic voltammetry (Adopted from ref. 1) ..... 60
- Figure 2.3.** Typical cyclic voltammogram of a reversible redox couple, 1 mM  $\text{FcCH}_2\text{OH}$ / 0.1 M KCl on NPG electrode at 10 mV/s..... 60
- Figure 2.4.** Typical chronoamperometric potential waveform (a), the corresponding concentration gradient profile as the reaction time proceeds (b) and the resulting current-time response (c). (Adopted from ref. 1). .... 63
- Figure 2.5.** Illustration of the different signals generated by the electron beam-sample interactions in the scanning electron microscope.(Adopted from ref. 7). .... 65
- Figure 2.6.** Schematic illustration of the scanning electron microscope. (Adopted from ref. 6). 67
- Figure 2.7.** Schematic representation of the X-ray production through the ejection of an inner-shell electron. .... 69

- Figure 2.8.** Graphical representation of Bragg's law for the X-ray diffraction. (Adopted from ref. 11). ..... 71
- Figure 2.9.** Schematic representation of the X-ray diffractometer. (Adopted from ref. 11). ..... 72
- Figure 2.10.** Graphical representation of the main components of the XPS system. (Adopted from ref. 13)..... 74
- Figure 2.11.** Photograph of the KLA-Tencor Alpha-Step IQ surface profiler.....76
- Chapter 3**
- Figure 3.1.** Schematic illustration (not drawn to scale) of the fabrication of Au-SiO<sub>2</sub> nanocomposite films and coral-like nanostructured porous gold (NSPG) through the electroassisted deposition of silica from a partially hydrolyzed silica sol and the concurrent reduction of gold ions. Reprinted with permission from reference 1. Copyright 2014 American Chemical Society. .... 85
- Figure 3.2.** SEM images of the as-prepared Au-SiO<sub>2</sub> nanocomposite films (a, b, and c) electrodeposited at -0.8 volts for 15 min from a solution containing KAuCl<sub>4</sub> (5.29 mM) and TMOS (0.14 mM) and the coral-like NSPG (d, e and f) after etching in HF. The inset in (d) is a low magnification of SEM image of a crack-free NSPG film. Reprinted with permission from reference 1. Copyright 2014 American Chemical Society. .... 87
- Figure 3.3.** SEM images of a planar gold film electrodeposited at -0.8 volts for 15 min in 5.29 mM KAuCl<sub>4</sub>. Scale bars are 5 mm and 500 nm for (a) and (b), respectively. Reprinted with permission from reference 1. Copyright 2014 American Chemical Society..... 88

**Figure 3.4.** Surface profiles of an as-prepared Au-SiO<sub>2</sub> nanocomposite film and coral-like NSPG obtained after etching in HF. Electrodeposition potential = -0.6 volts for 15 min. [KAuCl<sub>4</sub>] = 5.29 mM; [TMOS] = 0.14 M. The films were scratched to create sharp edges. The blue circles display the decrease in the surface roughness after etching in HF. Reprinted with permission from reference 1. Copyright 2014 American Chemical Society. .... 89

**Figure 3.5.** The average height of the oscillations (surface roughness indicator) recorded from the surface profiles acquired on Au-SiO<sub>2</sub> nanocomposite films electrodeposited at different potentials for 15 min. Inset is a surface profile of an as-prepared Au-SiO<sub>2</sub> nanocomposite film at -0.8 volts for 15 min and after etching (NSPG). [KAuCl<sub>4</sub>] = 5.29 mM; [TMOS] = 0.14 M. Reprinted with permission from reference 1. Copyright 2014 American Chemical Society. .... 90

**Figure 3.6.** Composition of the as-prepared Au-SiO<sub>2</sub> nanocomposite films (solid lines) and coral-like NSPG (dashed line, open points) at (a) different deposition potentials (-0.6, -0.8, -1.0 and -1.2 volts) for 15 min and (b) different deposition times (05, 10, 15, 20, 25 and 30 min) at -0.8 volts. [KAuCl<sub>4</sub>] = 5.29 mM; [TMOS] = 0.14 M. A small amount (<1 wt%) of potassium originating from the supporting electrolyte was observed in some of the Au-SiO<sub>2</sub> nanocomposite films. Reprinted with permission from reference 1. Copyright 2014 American Chemical Society. .... 91

**Figure 3.7.** SEM image of a scratched NSPG prepared from an Au-SiO<sub>2</sub> nanocomposite film electrodeposited at -0.8 volts for 15 min from a solution containing 5.29 mM KAuCl<sub>4</sub> and 0.54 M TMOS. The image reflects the continuous formation of the gold corals at the conductive substrate

surface (dark area). Reprinted with permission from reference 1. Copyright 2014 American Chemical Society. .... 95

**Figure 3.8.** EDX spectra of (a) electrodeposited (ED) planar gold film (b) coral-like NSPG and (c) Au-SiO<sub>2</sub> nanocomposite film electrodeposited at -0.8 volts for 15 min in 5.29 mM KAuCl<sub>4</sub> and 0.14 M TMOS (b, c only). Reprinted with permission from reference 1. Copyright 2014 American Chemical Society. .... 97

**Figure 3.9.** XPS spectra of (a) the Au 4f core-level and (b) Si 2p core-level from the Au-SiO<sub>2</sub> nanocomposite films electrodeposited at -0.8 volts for 15 min and coral-like NSPG obtained after the 2-step etching in HF. [KAuCl<sub>4</sub>] = 5.29 mM; [TMOS] = 0.14 mM. Reprinted with permission from reference 1. Copyright 2014 American Chemical Society..... 98

**Figure 3.10.** Powdered XRD patterns of as-prepared Au-SiO<sub>2</sub> and the coral-like NSPG obtained via electrodeposition at -0.8 volts for 15 min from a solution containing 5.29 mM KAuCl<sub>4</sub> and 0.14 mM TMOS. Reprinted with permission from reference 1. Copyright 2014 American Chemical Society. .... 100

**Figure 3.11.** Cyclic voltammograms of NSPG electrodes (solid lines) in 0.5 M H<sub>2</sub>SO<sub>4</sub> at a scan rate of 10 mV/s. The NSPG electrodes were obtained by etching Au-SiO<sub>2</sub> nanocomposite films electrodeposited at (a) different deposition potentials and (b) different deposition times. The dashed line in (a) was obtained at a planar gold electrode electrodeposited at -0.8 volts for 15 min. Reprinted with permission from reference 1. Copyright 2014 American Chemical Society..... 101

- Figure 3.12.** SEM images of coral-like NSPG prepared from Au-SiO<sub>2</sub> nanocomposite films electrodeposited at -0.6, -1.0 and -1.2 volts for 15 min. [KAuCl<sub>4</sub>] = 5.29 mM; [TMOS] = 0.14 M. The white and yellow circles indicate relatively low density gold agglomerates and higher density gold agglomerates, respectively. Reprinted with permission from reference 1. Copyright 2014 American Chemical Society. .... 103
- Figure 3.13.** SEM images of coral-like NSPG prepared from Au-SiO<sub>2</sub> nanocomposite films electrodeposited at -0.8 volts for different deposition times. [KAuCl<sub>4</sub>] = 5.29 mM; [TMOS] = 0.14 mM. The white and yellow circles indicate relatively low density gold agglomerates and higher density gold agglomerates, respectively. Reprinted with permission from reference 1. Copyright 2014 American Chemical Society. .... 104
- Figure 3.14.** Thickness and the roughness factors (RF) of NSPG prepared from Au-SiO<sub>2</sub> nanocomposite films electrodeposited (a) for 15 min at different deposition potentials and (b) at -0.8 volts for different deposition times. [KAuCl<sub>4</sub>] = 5.29 mM; [TMOS] = 0.14 mM. Reprinted with permission from reference 1. Copyright 2014 American Chemical Society. .... 106
- Figure 3.15.** Variation in normalized surface area of NSPG electrodes with potential (a) and time (b). Reprinted with permission from reference 1. Copyright 2014 American Chemical Society. .... 107
- Figure 3.16.** SEM images of coral-like NSPG prepared from Au-SiO<sub>2</sub> nanocomposite films electrodeposited at -0.8 volts for 15 min from solutions containing 0.14 mM TMOS and different concentrations of gold ions. The white and yellow circles indicate relatively low density gold

agglomerates and higher density gold agglomerates, respectively. Reprinted with permission from reference 1. Copyright 2014 American Chemical Society. .... 108

**Figure 3.17.** SEM images of coral-like NSPG prepared from Au-SiO<sub>2</sub> nanocomposite films electrodeposited at -0.8 volts for 15 min from solutions containing 5.29 mM KAuCl<sub>4</sub> and different concentrations of TMOS. The white and yellow circles indicate relatively low density gold agglomerates and higher density gold agglomerates, respectively. Reprinted with permission from reference 1. Copyright 2014 American Chemical Society. .... 109

**Figure 3.18.** Thickness and the roughness factors (RF) of NSPG prepared from Au-SiO<sub>2</sub> nanocomposite films electrodeposited at -0.8 volts for 15 min as a function of (a) gold ions concentration (2.65, 5.29, 10.6, 15.9, and 21.2 mM), and (b) sol-gel monomer concentration (0.07, 0.14, 0.27, and 0.54 mM). Reprinted with permission from reference 1. Copyright 2014 American Chemical Society. .... 110

**Figure 3.19.** Reproducibility of the method at different deposition parameters. The error bars signify  $\pm 1\sigma$ . N = 3. Reprinted with permission from reference 1. Copyright 2014 American Chemical Society. .... 112

#### Chapter 4

**Figure 4.1.** Fabrication of free-standing and transferable polypyrrole-based thin films by the localized drop-cast dealloying (LDCD) technique (a-e). Loading the free-standing film on ITO electrode and weighting paper (f). .... 125

- Figure 4.2.** Schematic Illustration (Not Drawn to Scale) of the Fabrication of Ppy-SiO<sub>2</sub> Mesoporous Nanostructured Composite Films through the Cathodic Co-Deposition of Ppy and SiO<sub>2</sub> from Pyrrole-Silica Sol and the Application of the LCDC Etching Strategy to Produce Ppy-SiO<sub>2</sub> and Ppy Free-Standing Films. .... 128
- Figure 4.3.** Photographs at different intervals during the co-electrodeposition of the nanocomposite film. The electrogenerated nitrosonium NO<sup>+</sup> ions started to diffuse beyond the electrode surface at t = 60 sec and complete diffusion was achieved at t = 600 sec. The pyrrole monomers in the bulk oxidized at t = 800 sec. The progress of reaction indicates that Ppy deposited within and around the silica mesopores. .... 131
- Figure 4.4.** SEM images of the as-prepared Ppy-SiO<sub>2</sub>-Ag@Au (a-c, sample A) and Ppy-SiO<sub>2</sub>@Ag (d-f, sample B) nanocomposite films electrodeposited at -1.0 volts for 30 min. .... 132
- Figure 4.5.** SEM images of Ppy-SiO<sub>2</sub>-Ag@Au nanocomposite films prepared at different deposition times at -1.0 volts. At early stages of the reaction (t ≤ 60 sec) spherical nanoparticles formed. At t ≥ 2 min the 3D open framework forms and the film continues to grow thicker with time. .... 134
- Figure 4.6.** SEM images of Ppy-SiO<sub>2</sub>-Ag@Au nanocomposite films prepared at: -0.6 volts (a & b) and -0.8 volts (c & d) for 30 min. .... 135
- Figure 4.7.** SEM images reflect the effect of different concentration parameters on the morphology of Ppy-SiO<sub>2</sub>-Ag@Au nanocomposite films electrodeposited at -1.0 volts for 30 min. .... 136

- Figure 4.8.** SEM micrographs of the Ppy-Ag free-standing film obtained by treating sample A with HF (a-c) and Ppy free-standing film obtained by treating sample A with HF and HNO<sub>3</sub>, successively (d-f). ..... 137
- Figure 4.9.** SEM images of Ppy@Ag thin film obtained by treating sample B with HF (a-c). Ppy free-standing free obtained by treating sample B with HF and HNO<sub>3</sub>, successively (d-f). Ppy-SiO<sub>2</sub> free-standing film obtained by treating sample B with HNO<sub>3</sub> (g-i). Ppy free-standing film obtained by treating sample B with HNO<sub>3</sub> and HF, successively (j-l). The non-destruction of the film reflects its homogeneity. .... 138
- Figure 4.10.** Surface profiles of the as-prepared Ppy-SiO<sub>2</sub>-Ag@Au nanocomposite film (sample A), Ppy-Ag free-standing nanocomposite film (sample A + HF) and Ppy free-standing film (sample A + HF + HNO<sub>3</sub>). The homogeneity of the deposited nanocomposite film is evident. 139
- Figure 4.11. Nitrogen adsorption/desorption isotherms of the as-prepared Ppy-SiO<sub>2</sub>-Ag@Au (sample A) and the Ppy-SiO<sub>2</sub> (obtained by applying the LDCD etching strategy to sample A) nanocomposite films and the corresponding BJH-modeled pore size distribution..... 140
- Figure 4.12.** X-ray diffraction patterns of the as-prepared Ppy-SiO<sub>2</sub>-Ag@Au nanocomposite film (sample A) and the free-standing Ppy-SiO<sub>2</sub> and Ppy films obtained by applying the LDCD etching strategy. .... 142
- Figure 4.13.** EDX spectra of the as-prepared Ppy-SiO<sub>2</sub>-Ag@Au (sample A), Ppy-SiO<sub>2</sub> (sample B, after Ag substrate removal) free-standing film and Ppy free-standing film obtained by treating



sample A with HNO<sub>3</sub> and HF, successively. The success of the co-electrodeposition process and the LDCD etching strategy is evident. .... 143

**Figure 4.14.** EDX elemental mapping images of the as-prepared Ppy-SiO<sub>2</sub>-Ag@Au (sample A). The bottom right SEM image shows the area over which the EDX elemental maps were collected. The inset in the bottom right SEM image is an overlay of all the collected elemental maps. .... 144

**Figure 4.15.** EDX elemental mapping images of the as-prepared Ppy-SiO<sub>2</sub>@Ag (sample B). The inset SEM image in the bottom right displays the area over which the maps collected. .... 145

**Figure 4.16.** EDX elemental mapping images of the free-standing Ppy-Ag hybrid film obtained by treating sample A with HF. The inset SEM image in the bottom right displays the area over which the maps collected. .... 146

**Figure 4.17.** EDX elemental mapping images of the free-standing Ppy film obtained by treating sample A with HNO<sub>3</sub> and HF, successively. The SEM image in the bottom displays the area over which the maps collected. .... 147

**Figure 4.18.** EDX elemental mapping images of the free-standing Ppy-SiO<sub>2</sub> film obtained by treating sample B with HNO<sub>3</sub>. The SEM image in the bottom right displays the area over which the maps collected. The bottom left image is an overlay of all the elemental maps. Note: the color of the Si map in this figure is different from that in the other figures due to the fact that the elemental maps for this sample were collected on a different SEM-EDS instrument. .... 148

**Figure 4.19.** Single point-scan EDX spectrum of Ppy-SiO<sub>2</sub> free-standing film obtained by treating sample B (Ppy-SiO<sub>2</sub>@Ag) with HNO<sub>3</sub>. .... 149

- Figure 4.20.** Cyclic voltammograms of the Ppy-SiO<sub>2</sub> free-standing film loaded on gold substrate and bare gold electrode in 1.0 M Na<sub>2</sub>SO<sub>4</sub> at a scan rate of 1000 mV/s (a). CVs of Ppy-SiO<sub>2</sub> free-standing film loaded on gold substrate in 1.0 M Na<sub>2</sub>SO<sub>4</sub> at different scan rates (b). ..... 150
- Figure 4.21.** Cyclic voltammograms of the Ppy-SiO<sub>2</sub> free-standing film loaded on ITO substrate (red solid line, a), anodically deposited Ppy on ITO substrate (red solid line, b) and bare ITO electrode (black solid line in a, b) in 10 mM K<sub>3</sub>Fe(CN)<sub>6</sub>] in 0.2 M KCl (pH ~ 7) at a scan rate of 20 mV/s<sup>-1</sup>..... 151
- Figure 4.22.** Cross-sectional SEM micrograph of the as-prepared Ppy-SiO<sub>2</sub>-Ag@Au nanocomposite film (sample A) at -1.0 volts for 30 min. The nanocomposite film has a strata-like structure with the middle stratum being more porous than the inner and outer strata..... 152
- Figure 4.23.** Cross-sectional EDX line scan profile and cross-sectional EDX line scan elemental mapping of the as-prepared Ppy-SiO<sub>2</sub>-Ag@Au nanocomposite film (sample A). The different Ppy and silica electrodeposition kinetics are evident..... 154
- Figure 4.24.** Kinetics of Ppy and silica electrodeposition during the formation of Ppy-SiO<sub>2</sub>-Ag@Au nanocomposite film (sample A) as presented by (a and b) the cross-sectional selected area EDX data and (c) EDX spectral data (Wt%) collected at different deposition times..... 156
- Figure 4.25.** Kinetics of Ppy and silver electrodeposition during the formation of Ppy-SiO<sub>2</sub>-Ag@Au nanocomposite film (sample A) as presented by EDX spectral data (Wt%) collected at different deposition times. .... 158

**Figure 4.26.** SEM images of Ppy-SiO<sub>2</sub>-Ag@Au nanowires prepared from the original electroplating solution but in absence of ethanol at -1.0 volts 30 min. The solvent effect on the nanocomposite film morphology is clearly evident..... 161

## Chapter 5

**Figure 5.1.** Schematic Illustration (Not Drawn to Scale) of the Fabrication of Three-Dimensional Bicontinuous Nanoporous Platinum (3D-BC-NP-Pt) Structures through Chemical Dealloying of the Co-Electrodeposited Pt-Ag Binary Alloy Thin Films..... 178

**Figure 5.2.** SEM micrographs of the post-dealloying porous platinum particulate-like structure (a-d, sample A), crack-free 3D-BC-NP-Pt structure with hierarchical porosity (e-h, sample B), and hierarchical 3D-BC-NP-Pt structure with nano-cracks (i-h, sample C). Electroplating solutions of 9.27:2.56, 9.27:3.17, and 9.27:6.72 Pt:Ag mole ratios were used to produce the pre-dealloying films corresponding to samples A, B and C, respectively. .... 181

**Figure 5.3.** SEM images of the electrodeposited Pt-Ag thin film (pre-dealloying sample C) from a plating solution containing 9.27:6.72 Pt:Ag mole ratio at -1.0 V for 10 min. .... 182

**Figure 5.4.** Cross-sectional SEM images of the post-dealloying porous platinum thin films; sample A (a) and sample B (b). The images evident the preservation of the porous microstructural features throughout the film thickness and demonstrate the increase of the films thickness with the increase of silver content in the electroplating solution..... 184

- Figure 5.5.** Cross-sectional SEM images of the hierarchical 3D-BC-NP-Pt structure with nano-cracks (sample C). The images evident the preservation of the bicontinuous porous microstructural features throughout the film thickness..... 186
- Figure 5.6.** EDX spectra of the electrodeposited Pt-Ag thin film from a solution containing Pt:Ag mole ratio of 9.27:6.72 at -1.0 V for 10 min and the 3D-BC-NP-Pt thin film (sample C) obtained by the selective removal of Ag in HNO<sub>3</sub>. The success of the co-electrodeposition of silver-rich platinum alloy thin film and the high efficiency of the dealloying process is evident. .... 187
- Figure 5.7.** (a-g) SEM images of the electrodeposited Pt-Ag thin film from the same plating solution used for sample A after modifying it through depositing Pt-Ag for 2 min at -1.0 V then replacing the conductive substrate and continue the deposition for 10 min at -1.0 V. (e-h) SEM images of the resulting 3D-BC-NP-Pt structure (sample D) after the dealloying process. .... 189
- Figure 5.8.** Cross-sectional SEM micrographs of the 3D-BC-NP-Pt structure (sample D). The images demonstrate that the post-dealloyed film is composed of 3D-BC-NP-Pt nanorods with circular apex and ice-cream-cone-like structure. .... 191
- Figure 5.9.** Cyclic voltammetric (CV) curves of the as-prepared 3D-BC-NP-Pt electrode (sample C) and planar platinum electrode in 0.5 M H<sub>2</sub>SO<sub>4</sub> at a scan rate of 50 mV/s (a). The roughness factor (surface area enhancement) of four different 3D-BC-NP-Pt electrodes prepared at different days was found to be  $19.81 \pm 2.31$ , N = 4, (b)..... 193
- Figure 5.10.** Cyclic voltammetric (CV) curves of 3D-BC-NP-Pt (sample C) and planar platinum electrodes obtained at 100 mV/s in 0.1 M KCl. The inset displays the relation of the non-Faradaic

charging current at 0.25 V vs the scan rate. The slope the current vs scan rate curve for the is much higher than that for the planar platinum electrode which demonstrates the high surface area of the electrode, ~ 28 times higher than that of the planar electrode. .... 195

**Figure 5.11.** Cyclic voltammetric (CV) curves of 10 mM  $[\text{Fe}(\text{CN})_6]^{3-}$  in 0.1 M KCl acquired at 3D-BC-NP-Pt electrode (sample C) at different scan rates. The inset is a plot of the peak Faradaic current as a function of the square root of scan rate. The tested electrodes displayed the same slope for the current vs the square root of scan rate curve which reveals a typical sensing behavior for the 3D-BC-NP-Pt electrode. .... 197

**Figure 5.12.** Cyclic voltammetric (CV) curves of 10 mM  $[\text{Fe}(\text{CN})_6]^{3-}$  in 0.1 M KCl acquired at planar Pt electrode at different scan rates. .... 198

**Figure 5.13.** Cyclic voltammetric (CV) curves obtained at planar platinum electrode in 10 mM  $[\text{Fe}(\text{CN})_6]^{3-}$  in 0.1 M phosphate buffer (pH 7.4, 0.1 M KCl) before (black curve) and after (red curve) addition of bovine fibrinogen (1 mg/mL). Scan rate: 100 mV/s. The electrode was incubated for 1 min before collecting the CV. The effect of the fouling agent is pronounced where the electrode failed to produce any significant electrochemical response. .... 201

**Figure 5.14.** Cyclic voltammetric (CV) curves acquired at 3D-BC-NP-Pt electrode (sample C) in 10 mM  $[\text{Fe}(\text{CN})_6]^{3-}$  in 0.1 M phosphate buffer (pH 7.4, 0.1 M KCl) before (0.0 min) and after addition of bovine fibrinogen (1 mg/mL). Scan rate: 100 mV/s. The electrode was incubated for 1 min before collecting the CVs over a 60 min period. CVs of well-defined peaks obtained which

reflecting the excellent performance of the porous platinum electrode in biofouling environments.

..... 202

**Figure 5.15.** Peak current data acquired at 3D-BC-NP-Pt (sample C, back line) and planar platinum (red line) electrodes from a 10 mM  $[\text{Fe}(\text{CN})_6]^{3-}$  in 0.1 M phosphate buffer (pH 7.4, 0.1 M KCl) aqueous solution before ( $t = 0$ ) and after the addition of fibrinogen (1mg/mL) to the solution. Data recorded over a 60 min period at a scan rate of 100 mV/s. The error bars represent the standard deviations of the peak current data acquired simultaneously from 3 porous platinum electrodes. Planar platinum electrode peak current signal vanished in the biofouling environment while that of the porous platinum almost did not change. .... 203

**Figure 5.16.** Comparison of the cyclic voltammetric (CV) curves for methanol electro-oxidation obtained at 3D-BC-NP-Pt electrode (sample C, black curve) and planar platinum electrode (red curve) from alkaline solution containing 0.5 M  $\text{CH}_3\text{OH}$  in 1.0 M KOH. Scan rate: 50 mVs. The high catalytic activity of 3D-BC-NP-Pt electrode toward methanol electro-oxidation is obvious and the rate of methanol electro-oxidation at BC-NP-Pt electrode is 30 times higher than that on planar platinum electrode..... 205

## Chapter 6

**Figure 6.1.** Graphical representation of a perpendicular silica structure.....202

## List of Tables

### Chapter 4

**Table 4.1.** Polypyrrole and polypyrrole hybrid nanocomposite thin films.....126

### Chapter 5

**Table 5.1.** Experimental details for preparing the nanoporous platinum structures.....174

**Table 5.2.** As-obtained ICP data for the nanoporous platinum electroplating solutions.....176

**Table 5.3.** Electrochemical characteristics of nanoporous platinum in 10 mM  $[\text{Fe}(\text{CN})_6]^{3-}$ .....199

**Table 5.4.** Electrochemical characteristics of planar platinum in 10 mM  $[\text{Fe}(\text{CN})_6]^{3-}$ .....199

## List of Abbreviations

NPNMs:	Nanostructured porous noble metals
NPNM:	Nanostructured porous noble metal
NPG:	Nanostructured porous gold
Au:	Gold
Pd:	Palladium
Pt:	Platinum
Ni:	Nickel
Co:	Cobalt
Ag:	Silver
Zn:	Zinc
CO:	Carbon monoxide
CO <sub>2</sub> :	Carbon dioxide
2D:	Two dimension
3D:	Three dimension
LLCs:	Lyotropic liquid crystals
C(NO <sub>2</sub> ) <sub>4</sub> :	Tetranitromethane
NMF:	Nanoporous metal foam
SHS:	Self-propagating high temperature synthesis
BTA:	Bistetrazolamine
HBs	Hepatitis B



Ag	Antigen
Ab:	Antibody
HRP:	Horseradish-peroxidase
HBsAb:	Hepatitis B antibody
HBsAg:	Hepatitis B antigen
NPs:	Nanoparticles
OPD:	o-Phenylenediamine
H <sub>2</sub> O <sub>2</sub> :	Hydrogen peroxide
DAP:	2,3-Diaminophenazine
DAFCs	Direct alcohol fuel cells
ORR:	Oxygen reduction reaction
EOR:	Ethanol oxidation reaction
MOR:	Methanol oxidation reaction
PEMFC:	Polymer electrolyte membrane fuel cell
$\eta$ :	Electrodeposition reaction overpotential value
TMOS:	Tetramethoxysilane
MPTMS:	(3-Mercaptopropyl)trimethoxysilane
WE:	Working electrode
RE:	Reference electrode
CE:	Counter electrode
SCE:	Saturated calomel electrode
CV:	Cyclic voltammetry
$E_{\text{initial}}$ :	Initial potential
$E_{\text{final}}$ :	Final potential

$i_{pc}$ :	Cathodic peak current
$i_{pa}$ :	Anodic peak current
$\Delta E_p$ :	Potential peak separation in CV
$n$ :	Number of the electrons
$E^{\circ}$ :	Formal potential
$E_{pa}$ :	Anodic peak potential
$E_{pc}$ :	Cathodic peak potential
$i_p$ :	Peak current
$A$ :	Electrode area
$C$ :	Molar concentration
$D$ :	Diffusion coefficient
$v$ :	Scan rate
$E_1$ :	Potential corresponds to none a Faradaic process
$E_2$ :	Potential corresponds to a Faradaic process
$i$ :	Current
$F$ :	Faraday's constant
$t$ :	Reaction time
$C_0$ :	Molar concentration
SEM:	Scanning electron microscopy
$d$ :	Resolution limit of a microscope
$\lambda$ :	Wavelength
NA:	Numerical aperture
$n$ :	Refraction index
$\alpha$ :	Half aperture angle

TEM:	Transmission electron microscope
BSEs:	Backscattered electrons
W:	Tungsten
LaB <sub>6</sub> :	Lanthanum hexaboride
EDS:	Energy-dispersive X-ray spectroscopy
Si:	Silicon
Li:	Lithium
XRD:	X-ray diffraction
Cu:	Copper
Å:	Angstrom
d:	Spacing between atom layers
$\theta$ :	Radiation angle
$2\theta$ :	Detector angle
ICDD:	International Center for Diffraction Data
JCPDS:	Joint Committee on Powder Diffraction Standards
XPS:	X-ray photoelectron spectroscopy
Ar:	Argon
C:	Carbon
ESCA:	Electron spectroscopy for chemical analysis
CHA:	Concentric hemispherical electron energy analyser

$E_{\text{kinetic}}$ :	Kinetic energy
$E_{\text{binding}}$ :	Binding energy
$E_{\text{photon}}$ :	Photon energy
$\Phi$ :	Work function
Al:	Aluminum
Mg:	Magnesium
eV:	Electron volts
NSPG:	Nanostructured porous gold
$\text{SiO}_2$ :	Silica
$\text{KAuCl}_4$ :	Potassium tetrachloroaurate (III)
$\text{K}_3[\text{Fe}(\text{CN})_6]$ :	Potassium ferricyanide
3D-BC-NP-Pt:	Three-dimensional bicontinuous nanoporous platinum
$\text{K}_2\text{PtCl}_4$ :	Potassium tetrachloroplatinate (II)
$\text{KH}_2\text{PO}_4$ :	Potassium phosphate monobasic
$\text{K}_2\text{HPO}_4$ :	Potassium phosphate dibasic

## Abstract

### **Fabrication of Multifunctional Nanostructured Porous Materials**

By Ahmed A. Farghaly, Ph.D.

A dissertation submitted in partial fulfillment of the requirements for the degree of  
Doctor of Philosophy at Virginia Commonwealth University.

Virginia Commonwealth University, 2016

Director: Dr. Maryanne M. Collinson  
Professor of Chemistry

Nanostructured porous materials generally, and nanoporous noble metals specifically, have received considerable attention due to their superior chemical and physical properties over nanoparticles and bulk counterparts. This dissertation work aims to develop well-established strategies for the preparation of multifunctional nanostructured porous materials based on the combination of inorganic-chemistry, organic-chemistry and electrochemistry. The preparation strategies involved one or more of the following processes: sol-gel synthesis, co-electrodeposition,

metal ions reduction, electropolymerization and dealloying or chemical etching. The study did not stop at the preparation limits but extended to investigate the reaction mechanism behind the formation of these multifunctional nanoporous structures in order to determine the different factors controlling the nanoporous structures formation. First, gold-silica nanocomposites were prepared and used as a building blocks for the fabrication of high surface area gold coral electrodes. Well-controlled surface area enhancement, film thickness and morphology were achieved. An enhancement in the electrode's surface area up to 57 times relative to the geometric area was achieved. A critical sol-gel monomer concentration was also noted at which the deposited silica around the gold coral was able to stabilize the gold corals and below which the deposited coral structures are not stable. Second, free-standing and transferable strata-like 3D porous polypyrrole nanostructures were obtained from chemical etching of the electrodeposited polypyrrole-silica nanocomposite films. A new reaction mechanism was developed and a new structural directing factor has been discovered for the first time. Finally, silver-rich platinum alloys were prepared and dealloyed in acidic medium to produce 3D bicontinuous nanoporous platinum nanorods and films with a nanoporous gold-like structure. The 3D-BC-NP-Pt displayed high surface area, typical electrochemical sensing properties in an aqueous medium, and exceptional electrochemical sensing capability in a complex biofouling environment containing fibrinogen. The 3D-BC-NP-Pt displayed high catalytic activity toward the methanol electro-oxidation that is 30 times higher than of planar platinum and high volumetric capacitance of 400 F/cm<sup>3</sup>. These findings will pave the

way toward the development of high performance and reliable electrodes for catalysis, sensing, high power outputs fuel cells, battery-like supercapacitors and miniaturized device applications.

## Chapter 1: Introduction



## 1.1 Introduction

This dissertation work aims to develop well-established strategies for the preparation of multifunctional nanostructured porous materials based on the combination of inorganic-chemistry, organic-chemistry and electrochemistry. The preparation strategies involved one or more of the following processes: sol-gel synthesis, co-electrodeposition, metal ions reduction, electropolymerization and dealloying or chemical etching. The study did not stop at the preparation limits but extended to investigate the reaction mechanism behind the formation of these multifunctional nanoporous structures in order to determine the different factors controlling the nanoporous structures formation. New parameters that control the formation mechanism of these nanoporous materials were discovered and discussed in details for the first time. Electroanalytical chemistry and electrocatalysis came in the heart of this work to study the potential applications of the prepared nanoporous materials. This chapter begins with an overview of the noble metal-based porous materials, their properties, fabrication methods and applications. The electroassisted chemical synthesis of metal, sol-gel and polymer structures will be addressed in the second part of this chapter.

## 1.2 Overview of the Noble Metal-Based Porous Materials

Nanomaterials generally, and nanostructured porous metals specifically, have fascinated scientists due to their exotic and promising properties and applications in sensing, catalysis and energy devices.<sup>1,2</sup> The term nanoporous is widely used to refer to porous materials with pore size within the nanometer regime. The IUPAC classified porous materials into three main categories

microporous, mesoporous and macroporous with pore size in the orders of 0.2–2 nm, 2–50 nm and 50–1000 nm, respectively.<sup>3</sup> Nanostructured porous noble metals (NPNMs) have received a considerable attention due to their superior chemical and physical properties over nanoparticles and bulk counterparts. Nanoporous metals possess an interesting combination of properties owing to their metallic nature and the nanoscale features or the so-called “finite-size effect”.<sup>4, 5</sup> These intriguing properties are of particular interest from the fundamental research and technological applications points of view. Among the different types of porous materials, NPNMs (e.g. Au, Pd and Pt) have fascinated scientists due to their nobility, biocompatibility (e.g. Pt and Au), tunable pore structure, high surface-to-volume ratio, unique optical properties (e.g. Au), excellent electrical and thermal conductivities, good mechanical stability, low density, high catalytic activity (e.g. Pd and Pt), ease of functionalization and large surface area, which has placed them in the forefront as potential candidates for a wide range of technological applications including sensing, catalysis, drug delivery, and energy storage.<sup>1, 2, 6-8</sup> For example, bulk gold is chemically inert, while nanostructured porous gold (NPG) displays an extraordinary catalytic activity for a variety of heterogeneous catalytic and electrocatalytic reactions due to its high surface area, facile recovery, large number of active sites and the enhanced mass transport through the porous structure.<sup>2, 9</sup> NPG has been found to act as an excellent catalyst for selective oxidation of alcohols (e.g. methanol),<sup>10</sup> low-temperature CO oxidation,<sup>11, 12</sup> glucose oxidation,<sup>13, 14</sup> oxidation of formic acid,<sup>15, 16</sup> and many other reactions.<sup>17, 18</sup> Nanoporous palladium and platinum are excellent catalysts in alcohol-based fuel cells.<sup>19-22</sup> Nanostructured porous noble metal (NPNM) electrodes are characterized by much

higher electrochemically active surface area, slower mass transport and higher electron transfer rate through the porous metallic network with respect to traditional flat metal electrodes and metal-nanoparticles-based electrodes.<sup>23</sup> As a result, the introduction of these electrodes into the field of analytical chemistry is advantageous in terms of improving the sensitivity and lowering the detection limits of sensing devices, which would hold promise for device miniaturization.<sup>23-25</sup> Another merit offered by NPNM electrodes is their biocompatibility (e.g. Pt and Au) and rich surface chemistry (e.g. Au), which leads to ease of surface functionalization and biological molecules (e.g. enzymes, antibodies or proteins) immobilization. These characteristics could make nanostructured porous metal electrodes ideal substrates for biosensing applications.<sup>26-28</sup> For example, NPG electrodes have been successfully used in the detection of DNA,<sup>29, 30</sup> dopamine,<sup>31</sup> L-cysteine,<sup>32</sup> hydrazine, and nitrite.<sup>33</sup>

### **1.3 Fabrication Strategies of Nanostructured Porous Noble Metals**

Porous materials like soil, sponges, biological tissues and zeolites are present in nature but nanoporous metals mainly come from synthetic routes. The fabrication of nanoporous metals is challenging due to surface energy constraints.<sup>1</sup> However, significant efforts have been devoted toward the fabrication of nanoporous metals motivated by their potential applications in catalysis, energy and sensing sectors. A number of approaches have been developed to fabricate 2D (e.g. thin films) and 3D (e.g. metal foams, metal aerogels and three dimensional bicontinuous porous metal structures) porous metals such as lyotropic liquid crystals soft template technique,<sup>34</sup> hard templating of mesoporous silica, porous alumina or carbon,<sup>23, 34</sup> dynamic templating by the use of

the hydrogen bubbles,<sup>35</sup> sputtering,<sup>36, 37</sup> combustion synthesis,<sup>5</sup> sol-gel assembly of prefabricated metals nanoparticles,<sup>38, 39</sup> electrochemical sol-gel methodology,<sup>40, 41</sup> dealloying techniques,<sup>42, 43</sup> and electrochemical deposition.<sup>44, 45</sup>

Based on the applied synthesis strategy two types of nanoporous noble metal structures can be produced, ordered and non-ordered structures. The combination of more than one preparation strategy can produce nanoporous noble metal structures with hierarchical pore organization. Hierarchical porous structures may contain ordered or non-ordered pores or a combination of both. They are often made up of an ordered large pore structure with the ligaments connecting the large pores consisting of ordered/non-ordered pores. In the following sections, I will discuss the application of the templating techniques to prepare ordered porous noble metal structures, sol-gel assembly and combustion methods to prepare non-ordered porous noble metal structures and the dealloying approach to fabricate 3D bicontinuous noble metal nanoporous structures.

### **1.3.1 Template Approach**

Templating techniques are well-known as straightforward and effective strategies to fabricate porous metals with ordered structure since the 1990s.<sup>34, 46</sup> The popularity of templating techniques arise from their simplicity and ability to fine-tune the pores size and shape. Hierarchical porosity is feasible through the application of templates of various sizes/types.<sup>25</sup> The pore size of the produced porous metal can range from micrometer to macrometer scale based on size of the pores in the mother template. Generally, there are two main kinds of templates that can be used as scarifying molds for noble metals nanocasting; hard and soft templates.<sup>34</sup>

### 1.3.2 Hard Templates

In comparison with other preparation techniques, the hard templating strategy is considered the most widely used methodology for preparing ordered porous nanostructures.<sup>47</sup> The history of applying the hard template technique in preparing ordered porous structures is new and dates back to late 1990s when a variety of porous carbon materials were prepared using a sacrificial porous mold.<sup>46, 48-50</sup> Although there are many types of templates that can be used to produce long-range ordered porous metal structures such as assembled colloidal crystals (e.g. array of silica or polystyrene spheres), anodic aluminum oxide (AAO), and others.<sup>34, 51, 52</sup>

Typically, the fabrication of ordered porous metal nanostructures using the hard template technique involves three main steps as shown in **Figure 1.1**:<sup>34</sup> a) preparing or choosing a template with a desirable ordered pore structure and size, and uniformly filling the ordered template pores/void spaces with the target precursors solution (e.g. impregnation of the template in metal ions solution), b) casting the target precursors (e.g. dissolved metal ions) by converting it into a solid phase through chemical or electrochemical reduction/deposition process to produce template-target material composite, and c) generation of the ordered metal porous structure via the template removal. The resulting porous structure is a negative metal replica or inverse structure of the original template. There are two main criteria that should be considered in choosing a template: a) stability of the template during the impregnation and metal deposition processes, and b) how easy it can be removed without disturbing/damaging the deposited metal replica.

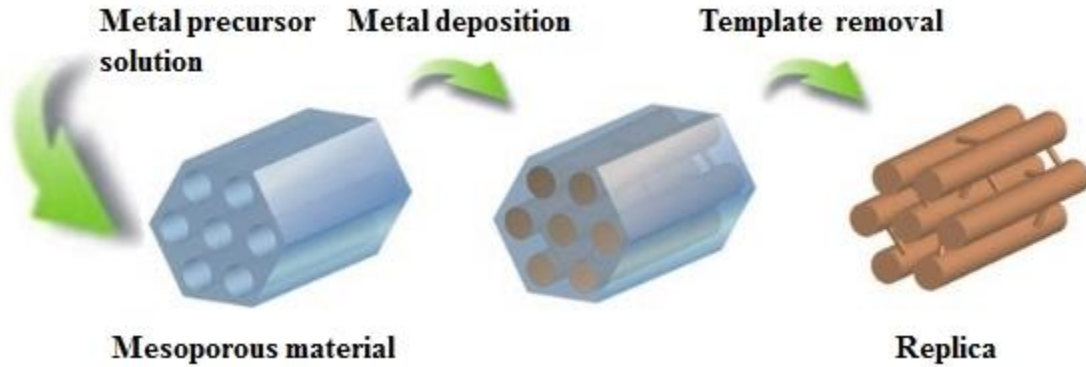


**Figure 1.1.** Fabrication of ordered nanostructured porous metals using the hard template approach. Adapted with permission from reference 34. Copyright 2008 John Wiley and Sons, Inc.

Variety of noble metal nanostructures including nanotubes, nanowires, nanoparticles, nanoworms, 2D and 3D ordered porous structures have been prepared by the application of the hard templating technique.<sup>34, 47</sup> For example, in 2002 Bartlett et al. electrodeposited gold and platinum within the voids of colloidal crystals made up of polystyrene latex spheres. Upon treatment of the composite metal-polystyrene films with toluene, the polystyrene latex spheres composing the colloidal crystal hard template dissolved to produce high surface area noble metal structures with highly ordered macroporous three-dimensional frameworks.<sup>53</sup> Collinson and co-workers employed the electrochemical reduction of gold ions within void spaces of colloidal crystal latex templates to fabricated porous gold films with 3D network structures.<sup>25, 51</sup> Long ordered porous gold structures with uniform pores size distribution were obtained by applying latex spheres of one size while applying latex spheres of two different sizes resulted in the

formation of hierarchical porous gold structures.<sup>25, 51</sup> Silica colloidal crystals have been employed by Colvin and co-workers to fabricate porous gold films with pore sizes in the micrometer scale.<sup>54</sup>

### 1.3.3 Soft Templates

The soft templating technique is also known as the direct-templating technique and it depends on the utilization of lyotropic liquid crystalline (LLC) phases to develop nanoporous noble metal structures.<sup>34, 47</sup> The lyotropic liquid crystals (LLCs) are consisting of two components, an amphiphile (**A**) and solvent (**B**, e.g. water). The component **A** is an amphiphilic molecule composed of an ionic or non-ionic hydrophilic head-group that links covalently to a hydrophobic tail (e.g. surfactants and amphiphilic block copolymers). When **A** dissolves in **B** a long-ranged order periodic structure is obtained with meso- to nanometer scale ranged lattice parameters. The microstructure of the evolved LLC mesophase is concentration, solvent, temperature and molecular structure dependent. For example, by controlling the composition ratio (**A** : **B**) of the LLC solution a variety of LLC structural mesophases can be obtained including spherical micellar, inverse micellar, cubic, hexagonal and lamellar.<sup>34, 47</sup> The 1992 breakthrough by Mobil Oil researchers<sup>55, 56</sup> who succeeded in preparing a variety of mesoporous based silica materials (MCM) opened the gates for the preparation of many new structural porous materials.

The soft template approach includes: mixing the LLCs with the desired noble metal ions (**M**) to prepare a stable long-range ordered mesophases, formation of LLCs replica/cast by chemical or electrochemical reduction of the confined metal ions in the LLC mesophases, and finally the LLCs template removal to produce a mesoporous noble metal structure as depicted in

**Figure 1.2.**<sup>34</sup> Preparation of noble metal nanoparticles or nanowires is also possible via controlling the composition ratio **A : B : M** in the deposition bath.

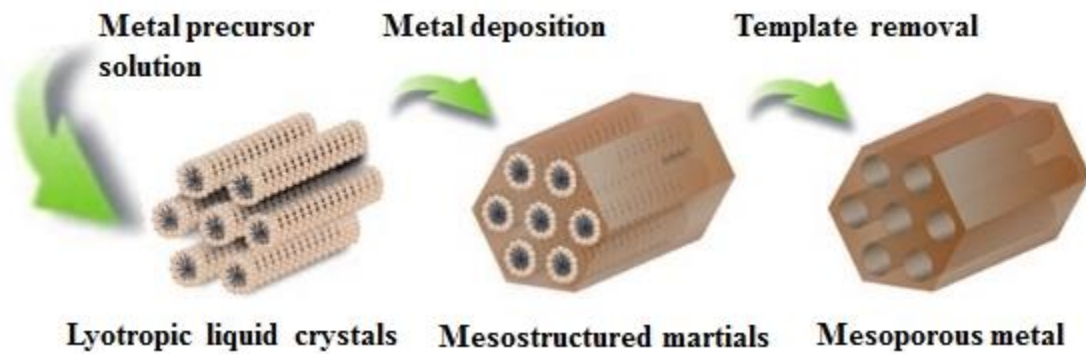


**Figure 1.2.** Fabrication of ordered nanostructured porous metals using the soft template approach. Adapted with permission from reference 34. Copyright 2008 John Wiley and Sons, Inc.

The first fabrication of mesostructured porous noble metal via the soft templating approach was reported by Attard and co-workers in 1997.<sup>57, 58</sup> Mesoporous platinum thin films were prepared from aqueous-based highly concentrated nonionic surfactants LLCs plating solution via electrochemical reduction of the platinum ions confined in the LLCs mesophases.<sup>57</sup> Attard's pioneering work provided a new route for the preparation of many mesoporous metals such as Pt, Co, Ni and Pt-alloys.<sup>57-63</sup> Ryoo and co-workers reported the use of mesopores silica templates (e.g. MCM-48) and hydrogen reduction at elevated temperatures to fabricate mesoporous platinum structures.<sup>64</sup> Platinum nanowires were obtained when SBA-15 and/or MCM-41 mesoporous silica templates were applied.



### 1.3.4 Synthesis of Noble Metal Aerogels by the Sol-Gel Assembly Approach

Noble metal aerogels represent new and unique class of porous materials.<sup>65</sup> They are characterized by their ultralow densities, very high surface area and presence of non-ordered hierarchically porous three-dimensional open network structure consisting of extended and interconnect metal nanoparticles.<sup>65</sup> The history of aerogel synthesis dates back to 1931 when Samuel Kistler succeeded in the preparation of silica aerogel, which is considered the first synthesized aerogel.<sup>66</sup> Since then, extensive research in the aerogel synthesis resulted in the development of many new classes of the aerogel including organic, inorganic, organic-inorganic hybrid and carbon aerogels.<sup>65</sup> Although the success in the preparation of many inorganic aerogels (e.g. metal oxides, metal sulfides and metal-metal oxides nanocomposite) and few metallic aerogels (e.g. Fe, Cu and Co) from carbothermally reducible metal oxides, the synthesis of noble metal aerogels has become feasible only very recent through the development of the well-known sol-gel bottom up synthesis strategy.<sup>65</sup>

**Figure 1.3** shows the noble metal aerogels synthesis protocol based on sol-gel assembly of the noble metal nanoparticles. The synthesis strategy consists of three steps: (a) chemical reduction of the metal ions to form metal nanoparticles; (b) assembly/gelation of the nanoparticles to form a metal hydrogel. Hydrogel formation is the most critical step during the noble metal aerogels synthesis because the microstructure of the final aerogel is a reflection of the hydrogel microstructure; and (c) supercritical or freeze drying of the metal hydrogel to produce the metal aerogel.<sup>65</sup> Steps (a) and (b) can be separated or combined in a one step process called spontaneous

gelation.<sup>65</sup> Chemical reduction of the noble metal ions aqueous solution is induced by the addition of  $\text{NaBH}_4$  in the presence of trisodium citrate or glutathione as stabilizing agent to produce a stable

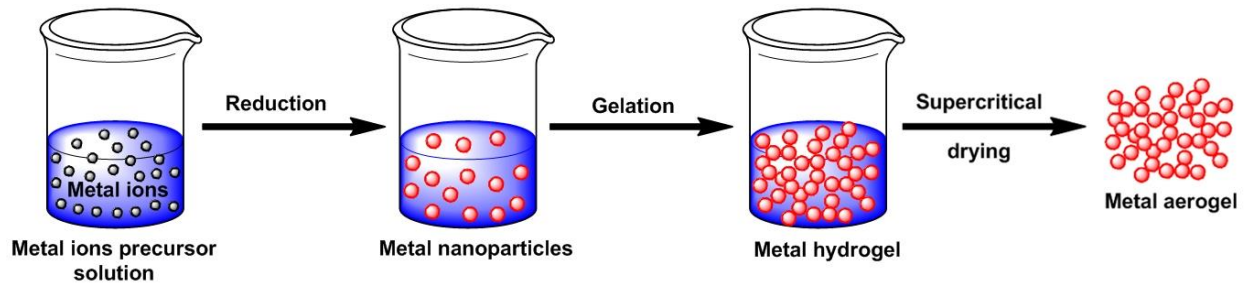


**Figure 1.3.** Fabrication of noble metal aerogels by the the sol-gel assembly approach.

colloidal sol.<sup>67-70</sup> The hydrogel gel is obtained by concentrating the colloidal sol (citrate- or thiolate-coated nanoparticles) by a factor of 10-50 using centrifugal filtration (e.g. Sartorius Vivaspin centrifuge filters MWCO 30,000) or rotary evaporation techniques. Then, the concentrated colloidal solution is converted into hydrogel gel by allowing it to set for several hours or by addition of a destabilizing agent such as tetranitromethane ( $\text{C}(\text{NO}_2)_4$ ).<sup>70</sup> To avoid the shrinkage and collapse of the hydrogel network structure during the regular drying, a  $\text{CO}_2$  supercritical drying was utilized to convert the hydrogel into aerogel. A wide range of mono and binary noble metal aerogels were produced by this methods including the mono aerogels of Ag, Au, Pt, and Pd plus their binary mixtures aerogel as depicted in **Figure 1.4**.<sup>68</sup>

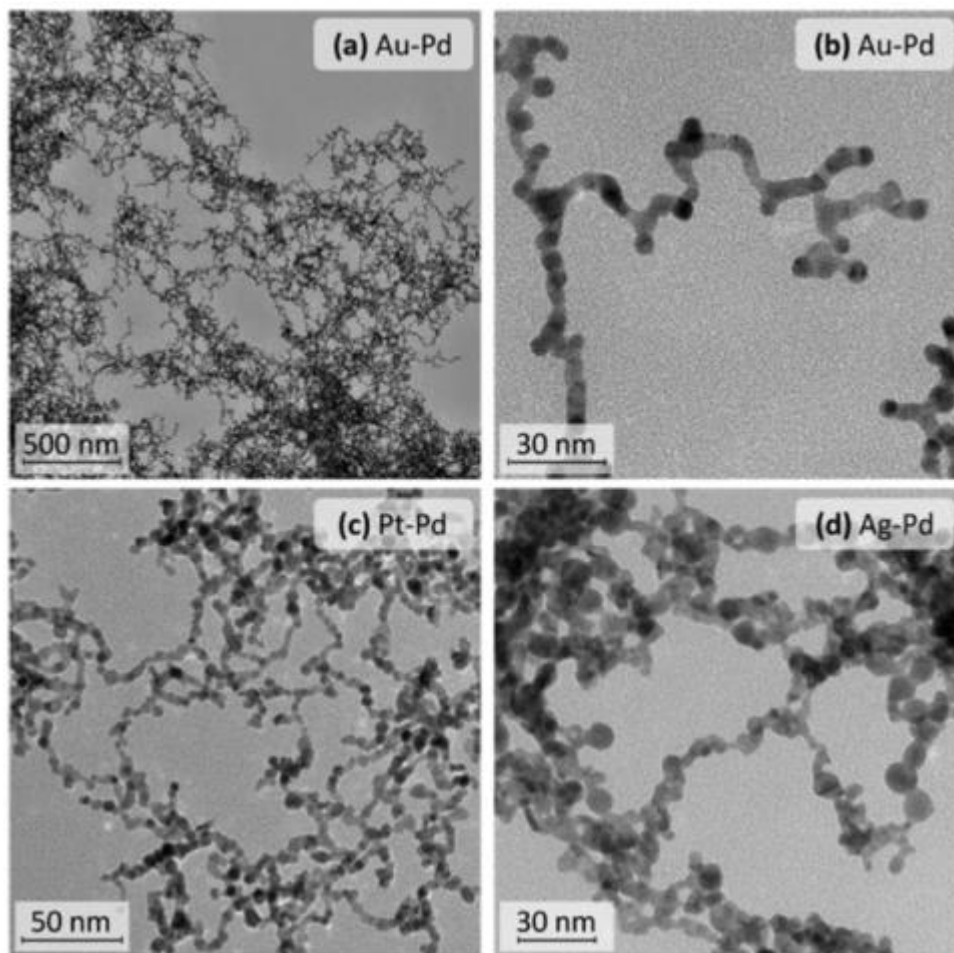


**Figure 1.4.** TEM images of multimetallic Au-Pd, Pt-Pd and Ag-Pd aerogels. Adapted with permission from reference 67. Copyright 2014 American Chemical Society.

### 1.3.5 Combustion Synthesis of Nanoporous Metal Foams

A highly porous metal nanostructure with a low relative density ( $d_{st}/d_{bulk}$ ) and porosity higher than 50% that is composed of metal nanoparticles or nanowires assembled/interconnected in a 3D fashion called nanoporous metal foam (NMF).<sup>5</sup> The high surface area of NMFs originates from the presence of a large population of cluttered pores of all sizes (10-200 nm) including

micropores, mesopores, and macropores. Although there are different methodologies to prepare NMFs such as nanosmelting,<sup>71</sup> templating<sup>35, 72</sup> and sol-gel assembly techniques,<sup>65</sup> here I will exclusively focus on the most recent preparation strategy developed in Los Alamos and denominated as combustion synthesis or self-propagating high temperature synthesis (SHS).<sup>5</sup> The combustion synthesis depends on the decomposition of highly energetic metal precursors (e.g. nitrogen-rich metal complexes) to produce the metal foam, where the high energy generated/obtained from the combustion process drives the metal foam formation reaction to completion.<sup>5</sup> Los Alamos scientists Tappan, Steiner, and Luther observed that unlike most of the nitrogen-rich complexes and salts that display vigorous and fast combustion process or even detonate to produce powders, the bistetrazolamine (BTA) metal complexes are characterized by a controllable, self-sustained and relatively slow combustion behavior to produce nanofoams.<sup>5</sup> During the combustion of the BTA metal complexes (**Figure 1.5**), the electron-rich nitrogen centers reduce the divalent or trivalent metal ion ( $M^{2+}$  or  $M^{3+}$ ) into a metal atom ( $M^0$ ) and nitrogen gas is evolved. The produced nitrogen gas drives the agglomeration of the metal atoms with each other to produce metal nanoparticles, which further agglomerate to produce a 3-dimensional porous network or the so called nanofoams. A typical example of metal nanofoams synthesized by the combustion method is shown in **Figure 1.6**.<sup>5</sup>

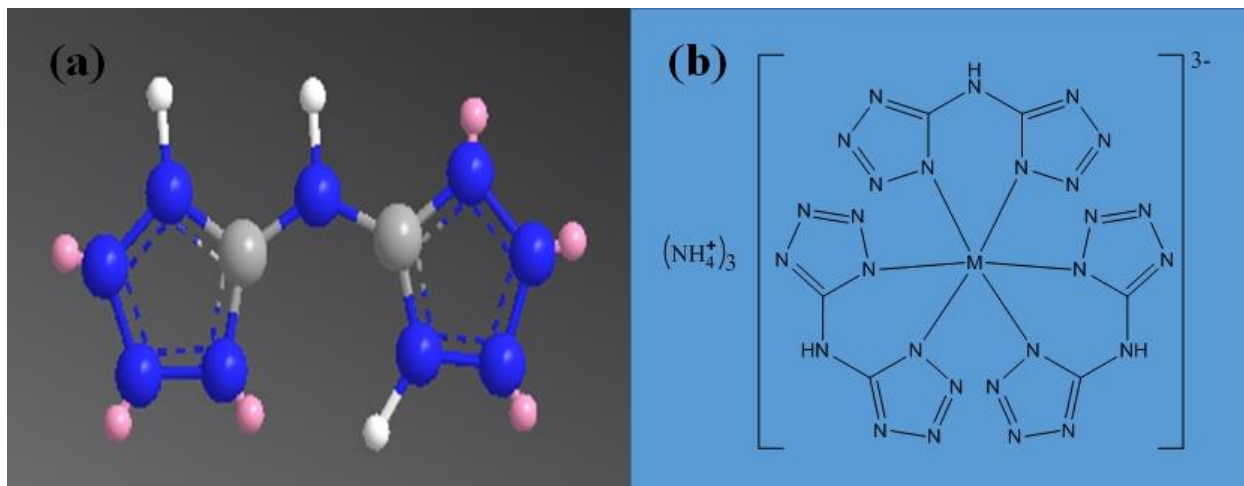


**Figure 1.5.** (a) Bistetrazolamine (BTA) ligand and (b) BTA metal complex (M: Fe<sup>3+</sup> or Co<sup>3+</sup>)



**Figure 1.6.** Co nanofoams prepared by the combustion of cobalt bistetrazolamine complex with porosity ranging from nm to mm. Adapted with permission from reference 5. Copyright 2010 John Wiley and Sons, Inc.

### 1.3.6 Dealloying Approach

The dealloying approach holds promise as a tool to prepare three dimensional bicontinuous porous noble metals nanostructured frameworks. The presence of continuous, non-intersecting and oriented plane/surface (e.g. vertical, horizontal, etc.) within a volume furnishes continuously interpenetrated sub-volumes. This partition fashion called bicontinuous partitioning. A 3D structure composed of a bicontinuously partitioned sub-volumes each of them is filled with a distinguished and connected phase of matter (e.g. solid, gas, or liquid) called a 3D bicontinuous structure.<sup>73</sup> For example, sponge composed of connected solid phase and connected gas phase across the sample. Another common example is the field of electrochemical sensing is nanoporous gold (NPG). The unique structure of NPG is made up of bicontinuous noble metal nanopores and ligaments as can be seen in **Figure 1.7**.<sup>73</sup>

Dealloying, also known as depletion gilding or selective dissolution, is a corrosion process, in which the least noble component is selectively removed from an alloy in a corrosive medium (e.g. silver in silver-rich gold alloy). The dealloying process will occur only when the alloy components (binary, ternary or multicomponent) have an adequate oxidation potential difference. The challenge in the formation of 3D bicontinuous porous noble metal structures via the dealloying technique is attributed to the fact that dealloying of a given system (e.g. Au–Ag) is only possible within a narrow compositional range. Outside this range and at high percentage of the more noble metal, the complete dissolution of the less noble alloy component is impossible and random pores are obtained.<sup>74,75</sup> While at low concentrations of the more noble metal, formation of microscopic

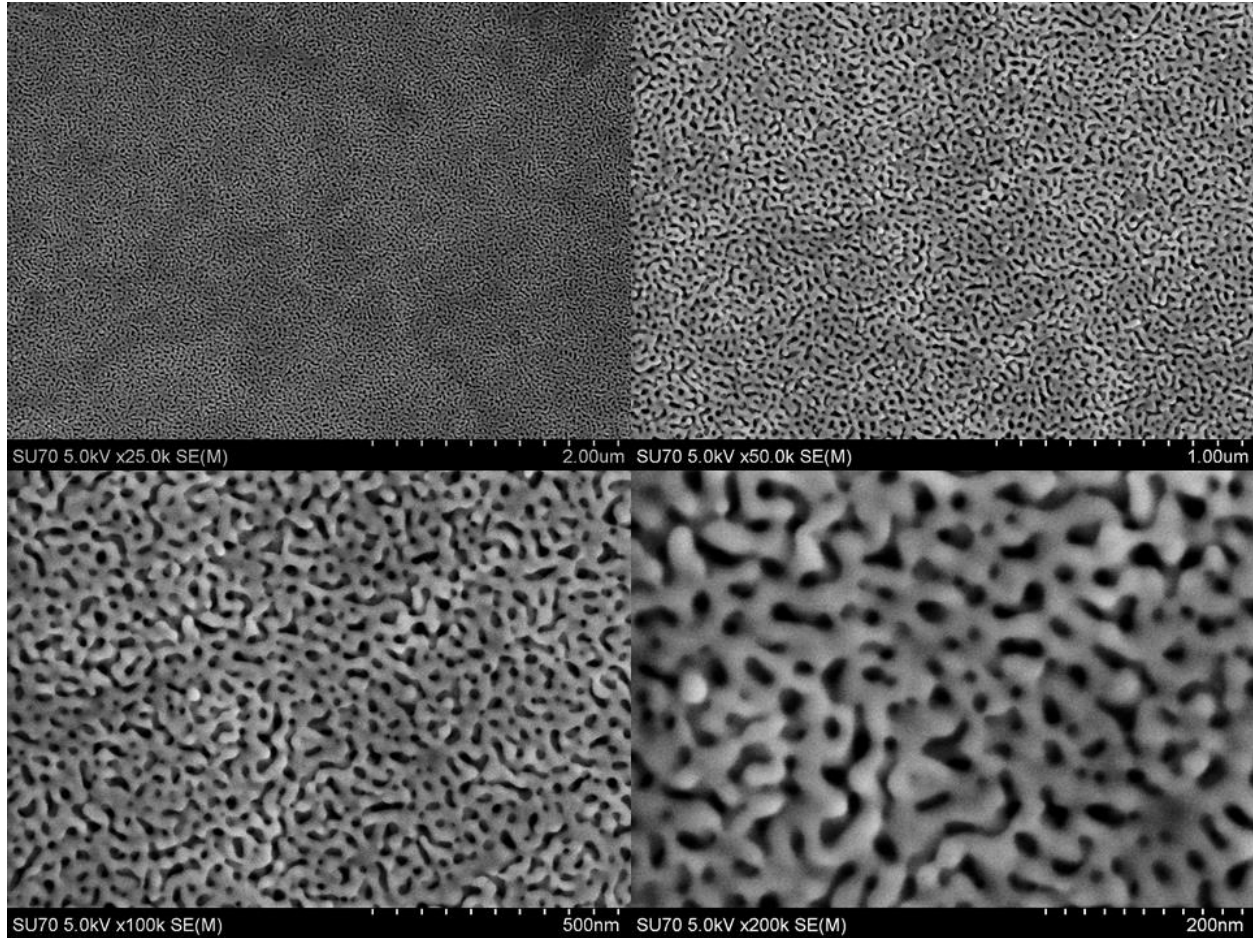


**Figure 1.7.** SEM micrographs of 3D bicontinuous nanoporous gold on glass at different magnifications. SEMs collected by Ahmed A. Farghaly. Fabrication method was developed by Ahmed A. Farghaly and Hajira Choudhary. Sample prepared by Christopher J. Freeman. All the work done under supervision of Prof. Maryanne M. Collinson.

cracks or complete destruction of the resulting porous framework is possible. It is worthwhile to point out that, this narrow compositional range is mainly governed by the diffusion rates of the alloy constituents. After the preferential dissolution of the more active metal (e.g. Ag in Au–Ag), either chemically or electrochemically, the atoms of the less active metal (e.g. Au) undergo a series

of structural rearrangements to form a porous network.<sup>76</sup> By controlling the composition of the starting alloy and the dealloying reaction parameters, nanoparticles, nanowires or porous structures of a well-defined pores and ligaments size can be obtained.<sup>23, 76-78</sup> In this section, the focus will be on the dealloying fabrication of 3D bicontinuous nanoporous gold (NPG), the most common porous nanostructured noble metal.

### 1.3.6.1 Preparation of Gold Alloys

The most common binary alloy that has been used to fabricate NPG is Au–Ag system.<sup>23, 47, 77, 78</sup> Examples of other alloys that have been used to fabricate NPG are Au–Ni<sup>79</sup> and Au–Zn.<sup>80</sup> There are a number of techniques that have been developed to prepare the Au–Ag binary alloy. For example, the alloy can be obtained via electrodeposition of Au and Ag from a cyanide-<sup>81, 82</sup> or thiosulfate-based<sup>83</sup> plating solutions through the application of a sufficient negative potential. The applied cathodic potential at the working electrode reduces the gold and silver ions at the electrode/electrolyte interface and hence metallic Au and Ag are co-electrodeposited on the working electrode surface. The composition ratio Au : Ag in the resulting alloy can be fine-tuned by controlling the composition of the plating solution and/or magnitude of the applied negative potential. Binary alloys of various compositions, shapes and sizes can be obtained by melting highly pure Au and Ag metal targets at very high temperatures followed by dicing or rolling.<sup>84-86</sup> The same metal targets can be used to produce Au–Ag alloys of various compositions and thicknesses by the application of sputter coating, thermal or electron beam evaporation



techniques.<sup>87, 88</sup> Binary Au : Ag (~1 : 1) alloy, e.g., 12 Karat white gold leaf, is commercially available at the art stores from Monarch company and others.<sup>23, 89</sup>

### 1.3.6.2 Mechanism of Porosity Evolution

In 2001, Erlebacher and co-workers succeeded in developing a kinetic model to explain the mechanism of pore formation during the dealloying fabrication of NPG from Au–Ag system.<sup>76,</sup>

<sup>90</sup> When a homogenous single phase Au–Ag alloy is immersed in a corrosive medium (e.g. HNO<sub>3</sub>), the Ag atoms at the most top surface layer dissolve and the Au atoms diffuse very fast and aggregate at the solid/electrolyte interface to form two-dimensional gold clusters and islands. The net result will be the formation of a pore and the next underlying Au–Ag layer will be exposed to the corrosive medium. As a result, the dealloying process continues, more silver atoms dissolve and more gold atoms rearrange to form the 3D bicontinuous nanoporous network.<sup>76, 90</sup>

Many scientists utilized the dealloying approach to prepare nanoporous gold structures. For example, Erlebacher's research group and Collinson and co-workers prepared NPG free-standing films by chemical etching of silver in 12 Karat white gold leaf using HNO<sub>3</sub>.<sup>89, 91</sup> The resulting films are crack-free and can be transferred to any suitable substrate (e.g. GCE, gold or glass slides) based on the desired application. Ji et al.<sup>82</sup> and Wang and co-workers<sup>92, 93</sup> electrodeposited Au–Ag binary alloy to produce different NPG structures. Ji et al. simultaneously electrodeposited Au and Ag in porous anodic alumina substrates (AAO) from cyanide-based plating solutions, followed by selective removal of the AAO template and Ag to produce porous gold nanowires.<sup>82</sup> Wang and co-workers used the sequential electrodeposition in AAO to form

Au–Ag alloys of different compositions. Upon silver etching porous gold nanowires of various morphologies obtained.<sup>92</sup> Wang's research group also electrodeposited Au–Ag in the voids of closely packed polystyrene spheres within a polycarbonate membrane. Selective dissolution of Ag and the double template resulted in the formation of hierarchical porous gold microwires.<sup>93</sup> Almost, at the same time but separately, Collinson and co-workers prepared hierarchical nanoporous gold electrodes via dissolution of silver in the electrodeposited Au–Ag alloy within the interstitial spaces of polystyrene spheres-based colloidal crystal.<sup>94</sup>

## **1.4 Applications of Porous Noble Metals**

The intrinsic properties of NPNMs such as their large surface area, high surface area-to-volume ratio, excellent electrical conductivity, ease of modification, high stability, high durability, tunable porosity, resistance to fouling agents, biocompatibility and superior catalytic activity made them ideal platforms for sensing and catalytic applications.<sup>1, 5, 47, 65</sup>

### **1.4.1 Sensing Applications of NPNMs**

In the field of sensing, NPNMs-based electrochemical sensors and biosensors displayed high sensitivity, lower detection limits and excellent performance even in complex environments such as milk, blood and other biological fluids with respect to their planar counterparts.<sup>1, 23, 24, 78</sup> Furthermore, NPNMs-based sensors are advantageous in studying and detecting electroactive species with sluggish electron transfer kinetics.<sup>13, 28, 95, 96</sup> It is quite important to emphasize that in order to gain these merits, considerable attention must be paid to the sensor design. For example, control over the pore diameter needs to be achieved to avoid the mass transport problems, ensure

access of the electroactive species being detected into the inner surface of the electrode and to prevent the blockage of the electrode surface when it used in complex fouling environments. A large number of NPNMs-based sensors have been developed. For example, Hieda et al. demonstrated a 40-fold increase in the sensitivity of quartz crystal microbalance-based gas sensors when planar gold electrodes were replaced by NPG electrodes.<sup>97</sup> Collinson and co-workers demonstrated that 3D bicontinuous NPG electrodes made by chemical etching of Ag in nitric acid are excellent sensors in complex biological environments that contain biofouling agents such as bovine serum albumin and fibrinogen.<sup>91</sup> The study showed that bicontinuous NPG electrodes displayed well-defined cyclic voltammetric peaks when immersed in blood containing potassium ferricyanide while planar gold electrode suffered from biofouling effects. Seker and co-worker, further expanded Collinson's approach<sup>91</sup> to detect nucleic acids (e.g. DNA) in biofouling environments containing bovine serum albumin (BSA) and fetal bovine serum (FBS).<sup>98</sup> ssDNA probes (26 bp) samples were immobilized on three different types of gold electrodes: planar gold, nanoporous gold obtained by dealloying Au-Ag thin film in nitric acid, and dealloyed nanoporous gold that underwent annealing before use. The response of the modified gold electrodes toward methylene blue (MB), a DNA redox marker, in biofouling environments was monitored by square wave voltammetry (SWV). The planar electrodes biofouled and became irresponsive. Both nanoporous gold and annealed nanoporous gold displayed a well-fined response with the annealed electrode being more sensitive due to the enhanced mass transfer through the larger pores. DNA molecules with concentrations between 200 nM down to 10 nM were successfully detected.<sup>98</sup>

Ding et al. used NPG electrodes, gold nanoparticles and differential pulse voltammetry to develop a sandwich-like electrochemical immunosensor for the detection of hepatitis B (HBs) with a detection limit of 2.3 pg/mL.<sup>99</sup> Generally, an immunosensor is an analytical sensor used to detect the antigen (Ag) - antibody (Ab) interactions during the Ag-Ab complex formation. **Figure 1.8** depicts the sandwich-like hepatitis B immunosensor. First, a white gold leaf (Au-Ag alloy, 1:1 wt %) was immersed in 1: 1 nitric acid solution to selectively remove Ag to produce NPG, which is

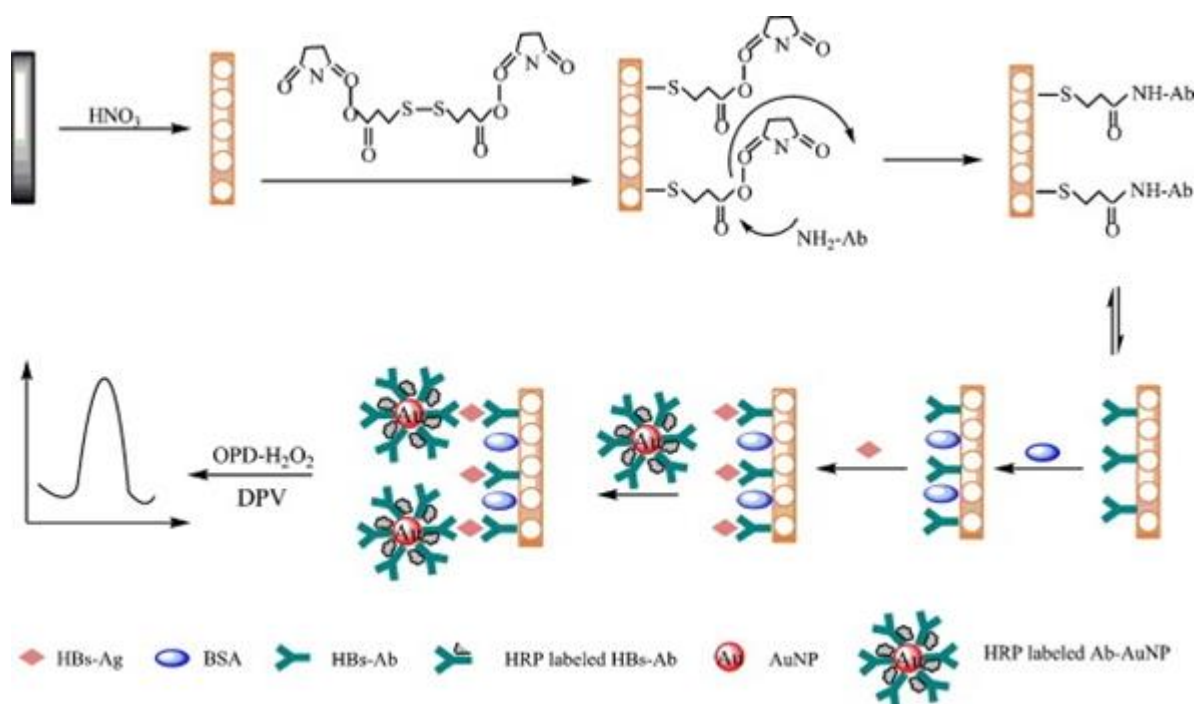


**Figure 1.8.** Schematic illustration of the fabrication of NPG-based immunosensor for hepatitis B. Reprinted with permission from reference 93. Copyright 2010 Elsevier.

then subsequently loaded on GCEs. Horseradish-peroxidase (HRP) labeled hepatitis B antibody (HBsAb) gold nanoparticles bioconjugate (HRP-HBsAb–Au NPs) was obtained by mixing the gold nanoparticles with HBsAb at pH ~ 9. The authors utilized the gold-thiol chemistry to covalently immobilize the hepatitis B antibodies (HBsAb) on the NPG surface. Then, the modified NPG electrode was immersed in HBsAg solution and HRP-HBsAb–Au NPs was dripped onto it to form the sandwich Ag-Ab complex. In order to determine the concentration of HBsAg, the final modified NPG electrode was immersed in o-phenylenediamine (OPD) and H<sub>2</sub>O<sub>2</sub> solution where the HRP on the NPG electrode surface catalyzed the interaction between OPD and H<sub>2</sub>O<sub>2</sub> to produce an electrochemically active species, 2,3-diaminophenazine (DAP), which was measured by means of differential pulse voltammetry.

Many other types of NPNMs-based sensors have been developed such as DNA sensors,<sup>100,</sup><sup>101</sup> enzyme-based biosensors,<sup>102, 103</sup> Raman sensors<sup>104, 105</sup> and small molecule sensors.<sup>31, 33</sup>

#### **1.4.2 Catalytic Applications of NPNMs**

In this section only the electrocatalytic applications of NPNMs will be discussed. In general, NPNMs-based catalysts displayed improved electrocatalytic activity, high stability and recyclability compared with their non-porous or nanoparticles-based counterparts.<sup>47, 65</sup> Fuel cells are highly efficient devices that can directly convert the chemical energy of a fuel (e.g. hydrogen or methanol) into electric current through an electrochemical reaction and they represent the most important clean energy application of NPNMs-based electrocatalysts. Currently, fuel cells are receiving tremendous interest due to the fact that they are clean sources of energy. To date, the

most efficient catalysts in fuel cells generally and direct alcohol fuel cells (DAFCs) specifically are Pt- and Pd-based materials. Interestingly, in fuel cells a Pt-based catalyst can serve as anode to catalyze the oxidation of small molecules (e.g. hydrogen, methanol, ethanol, etc.) or cathode to catalyze the oxygen reduction reaction (ORR).<sup>19, 21, 22, 106</sup> For example, Liu et al. studied the electrocatalytic activity of Pd aerogels and commercial Pd/C(10 wt%) toward the ethanol oxidation reaction (EOR) by means of cyclic voltammetry and chronoamperometry.<sup>107</sup> They found that Pd aerogels displayed faster EOR kinetics, higher stability, and much higher current densities (A/mg) in the forward CV scan than the commercial Pd/C catalyst.

Erlebacher and co-workers<sup>108</sup> and Xiao et al.<sup>109</sup> demonstrated the electroless deposition of a thin layer of platinum and platinum nanoparticles on NPG films, respectively. Erlebacher's group prepared a NPG template by dealloying a white gold leaf (12-carat, Monarch) in concentrated nitric acid. The NPG template floated on a 2 mM  $\text{Na}_2\text{Pt}(\text{OH})_6$  solution at pH ~10 and a vapor of hydrazine was allowed to flow at NPG-platinum ions solution interface. By doing this, they succeeded in depositing a highly uniform thin layer (1-5 nm) of platinum within the NPG pores. A power density of 4.5 kW/g comparable to that of conventional fuel cells was obtained when the Pt-coated-NPG used in fuel cell applications. Xiao et al. followed the same chemical dealloying strategy to create NPG. The NPG was allowed to set in contact with a solution containing 0.31 mM  $\text{H}_2\text{PtCl}_6$  as a Pt precursor and 0.13 mM HCOOH as a reducing agent. The net result was decoration of the NPG with Pt nanoparticles. Compared with pristine NPG, which displayed no

catalytic activity toward the methanol oxidation reaction (MOR), the Pt (NPs)-coated-NPG heterogeneous catalyst demonstrated excellent catalytic activity and high tolerance in the MOR.<sup>109</sup>

The application of NPNMs-based catalysts as cathode materials in the polymer electrolyte membrane fuel cell (PEMFC) to catalyze the ORR is of growing interest.<sup>47, 65</sup> Many NPNMs-based catalysts displayed higher catalytic activity toward the ORR than the state-of-the-art Pt/C (3 nm Pt NPs support in C). For example, Liu et al. studied the electrocatalytic activity of Pt-Pd aerogels toward the ORR.<sup>110</sup> They found that Pt-Pd aerogels are superior catalysts toward the ORR compared with the commercial Pt/C (20 wt%) catalyst. Among the different studied Pt-Pd aerogel compositions, Pt<sub>80</sub>-Pd<sub>20</sub> aerogel displayed the highest catalytic activity toward the ORR, 5 times greater than that of the Pt/C (20 wt%) and exceeds the United States DOE 2017 target<sup>111</sup> for the ORR fuel cell catalysts (0.44 A/ mg Pt). In addition, there are many reports of the use of nanoporous platinum based materials especially Pt-Ni as active catalysts in ORR reactions.<sup>112, 113</sup>

## 1.5 Nanostructured Materials by Electrodeposition

Recently, electrodeposition has received considerable attention as a versatile technique to fabricate nanostructured materials. Electrodeposition is a low temperature (in most cases), simple, cost- and time-effective technique that doesn't involve intensive instrumentation for the preparation of metals, bi or multicomponent metal alloys of different configurations and compositions. Electrodeposition enables the formation of nanostructures in complex environments and shapes that are not accessible by conventional nanomaterials preparation methods. A basic requirement for any electrodeposition reaction to occur is the presence of a conductive substrate.

Noble metal nanoparticles, wires, tubes, and even complex structures (e.g. hierarchical, coral-like, layered, foams etc.) of different sizes and morphologies can be prepared either as thin films or as free-standing entities by the electrochemical reduction of the corresponding metal ions or complexes.<sup>114, 115</sup> High degree of control over the thickness and morphology of the electrodeposited films can be achieved by manipulating/controlling the electrodeposition reaction parameters, such as the magnitude of the applied deposition potential, composition of the electroplating solution, reaction time and temperature.<sup>114, 115</sup> In the field of the nanoscale materials synthesis, electrodeposition techniques possess an important advantage that is not offered by most of the conventional nanomaterials preparation strategies, which is the outstanding degree of reproducibility.<sup>114, 116-119</sup>

### **1.5.1 Nucleation and Growth**

The nanoscale features and microstructure of an electrodeposited material is dependent of the nucleation and growth modes.<sup>114, 115</sup> Electrodeposition of nanocrystalline materials, materials composed of nanocrystals, is possible by controlling the electrodeposition reaction parameters especially in low exchange current density systems where rate of the electron transfer between the electroactive species and the electrode is slow. The first stage during the electrodeposition process involves the formation of nucleation sites on the conductive substrate surface. The number of nuclei (first crystals) formed at the beginning of the electrodeposition reaction is a function of the applied potential and concentration of the deposited material precursors and they are correlated with a Nernst-type relationship.<sup>120</sup> The nucleation process is governed by the following relation:<sup>121</sup>



$$N = N_o [1 - e^{-Rt}] \quad (1.1)$$

where N represents the density of the surface nuclei formed,  $N_o$  is a constant related to the saturation value, t is the deposition time, and R is the nucleation rate and it given by the following equation:<sup>122</sup>

$$R = A e^{-B/\eta^2} \quad (1.2)$$

where  $\eta$  is the electrodeposition reaction overpotential value and A and B are overpotential-independent constants. It is important to point out that the nucleation process starts only on the active nucleation sties, which their number is potential and concentration dependent as pointed out earlier and not on the entire electrode surface. Homogeneous distribution of the nucleation centers is possible at large R values. Based on the nature of the interaction between the atoms or molecules of the electrodeposited material and the conductive substrate surface, three different types of growth modes can be distinguished as shown in **Figure 1.9**.<sup>123</sup> In other words, the magnitude of the binding energy between atoms or molecules of the electrodeposited material and substrate lattice is governing the growth mechanism. **Figure 1.9 (a)** displays the direct formation/nucleation of three dimensional clusters on surface of a conductive substrate that grows into 3D islands according to the Volmer-Weber island growth mode. An electrodeposited film will grow according to the island growth model when lattice misfit is absent and the binding energy between the deposited atoms or adatoms and each other is higher than that between the deposited atoms and the substrate surface.<sup>114</sup> The opposite situation is also possible when the deposited metal atoms

bind stronger to the substrate than to each other leading to the formation of two-dimensional structures, where a complete monolayer of the deposited metal atoms must be formed first before the next layer begins to grow as depicted in **Figure 1.9 (b)**.<sup>114</sup> This layer-by-layer growth mode called Frank–van der Merve growth mode and is characterized by a lattice misfit between the metal adatoms and substrate lattice. An intermediate layer-plus-island growth mode also exist and called Stranski-Krastanov growth mode. This growth mechanism starts with the formation of a high free energy two-dimensional layer followed by the growth of three-dimensional islands on its surface as shown in **Figure 1.9 (c)**. The switch between the layers and islands growth modes could be attributed to the change in energetics, which mainly arises from the orientation and/or symmetry of the adatoms in the in intermediate layer.<sup>114</sup> This energy change hinders the growth of the intermediate layer into a bulk crystal and favors the islands formation.<sup>114, 123</sup>

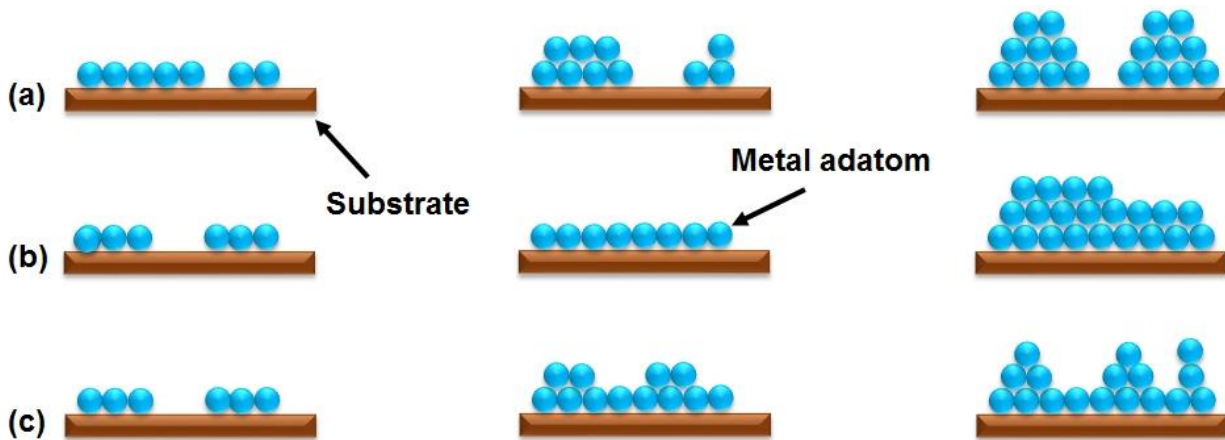


**Figure 1.9.** Schematic illustration of the different modes of thin film growth (a) 3D islands (Volmer - Weber mode), (b) 2D layer-by-layer (Frank-van der Merve mode), and (c) 2D layer + 3D islands (Stranski-Krastanov mode). Modified from reference 116.

Stranski-Krastanov (layer-plus-island) and Volmer-Weber (island) modes are the most common growth modes during the electrodeposition of metals from aqueous solutions. For example, Pötzschke et al. demonstrated that the electrodeposition of silver from 0.01 M  $\text{AgClO}_4$  aqueous solution on highly oriented pyrolytic graphite followed the Volmer–Weber island growth mode due to the weak interaction between the substrate and the deposit.<sup>124</sup> Brande et al. reported that electrodeposition of copper on polycrystalline silver substrate followed the Volmer–Weber island growth mode while a layer-by-layer Frank–van der Merve growth mode was demonstrated during the copper deposition by magnetron-enhanced sputtering.<sup>125, 126</sup> The layer-plus-island Stranski-Krastanov growth mode was demonstrated during the electrodeposition of Pd on a well-defined 111 Pt surface.<sup>127, 128</sup>

By combining the electrodeposition and dealloying or templating techniques, NPNMs of different morphologies can be prepared.<sup>23, 78, 89</sup> Fabrication of nanoporous gold by dealloying an electrodeposited Au-Ag alloy has been demonstrated by many research groups.<sup>23, 78, 89</sup> Electrodeposition of noble metals within template voids followed by the template removal resulted in the formation of many noble metal porous structures (e.g. NPG from gold electrodeposited on polystyrene latex<sup>25, 51</sup> and Pd electrodeposited within vertically aligned silica<sup>129</sup>).

### **1.5.2 Electroassisted Deposition of Sol-Gel Derived Materials**

In order to get a good understanding of the electroassisted deposition of sol–gel derived materials, this section begins by a concise overview of the sol-gel process history and chemistry and ended by discussing the electrodeposition of silica-based thin films.

## 1.5.2.1 Sol-Gel Process

### 1.5.2.1.1 Historical Background

The history of the sol-gel process is relatively old and rich with many events and discoveries. Only the remarkable achievements in the field will be addressed in this concise historical survey about the sol-gel process. The discovery of the sol-gel process dates back to the mid-1800s.<sup>130</sup> In 1846 Ebelmen reported the first preparation of a glass-like transparent material “SiO<sub>2</sub>” based on the slow hydrolysis of silicic acid ester (tetraethyl orthosilicate; TEOS) under acid-catalyzed conditions.<sup>130</sup> About twenty years later (1864), Thomas Graham a Scottish chemist introduced for the first time the terms sol and gel through his work on silicic acid and silica sols.<sup>131</sup> These discoveries did not receive considerable attention from the technological community at that time due to the exceptionally long time of the process (e.g. the drying step was ~ a year). However, the curiosity of the scientific community for preparing new materials did not stop. Almost fifty years later, two active groups of German scientists in the University of Göttingen (Patrick)<sup>132</sup> and Schott Glaswerke company (Geffcken & Berger)<sup>133</sup> modified Ebelmen’s method and succeeded to reduce the reaction time significantly. In 1919 (Patrick)<sup>132</sup> and 1939 (Geffcken & Berger)<sup>133</sup>, the first two-patent in the field of the sol-gel chemistry regarding the preparation of silica gel and sol-gel derived oxide coatings, respectively, were accepted. The commercialization of sol-gel products started in 1953 and the large scale production occurred in 1959 (automotive TiO<sub>2</sub>-SiO<sub>2</sub>-TiO<sub>2</sub> rear-view mirrors).<sup>134</sup>

Although the 70s of the 20th century were a witnesses on a revolution in the fabrication of the sol-gel materials or the so-called “sol-gel materials era”,<sup>134</sup> the start of the sol-gel materials revolution can be traced to the 1950s and 1960s where Roy et al.<sup>135</sup> and Schroeder<sup>136</sup> prepared a large number of colloidal oxides and thin films based on the sol-gel process. The most two common forms of colloidal silica particles known these days, Ludox and Stöber spheres were developed at that time by Iler (1955)<sup>137</sup> and Stöber et al. (1968).<sup>138</sup> In the late 60s and early 70s Levene et al. and Dislich et al. reported the synthesis of a large number of multicomponent oxides utilizing the sol-gel process; their reports are considered the real start for the sol-gel materials era.<sup>134</sup> So from 1971 till now there is a growing interest in sol-gel materials due to their potential applications in the fields of long-lasting fragrances, sensing, separation, catalysis, smart glass, drug delivery, inks and protective coatings (e.g. anticorrosion, antimicrobial, easy-to-clean, and antiscratch coatings).<sup>38</sup>

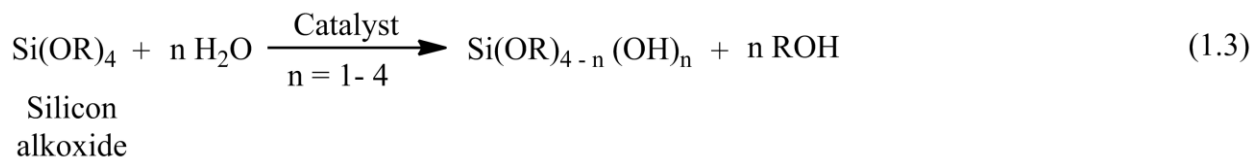
#### **1.5.2.1.2 Chemistry of the Sol-Gel Process**

Sol is a fluid colloidal system formed by the dispersion of colloidal/nanoparticles (1-100 nm) in a liquid, e.g. blood and cell fluids.<sup>139</sup> Gel is a non-fluid heterogeneous system of liquid molecules dispersed in a solid medium with a semi-rigid jelly-like interconnected 3-D network and pores in the sub-micrometer range, e.g. silica gel.<sup>139</sup> Sol-gel process is a powerful, scalable, reproducible and simple strategy that has been used to produce large number of inorganic oxides, hydroxides and composites in a variety of forms (powders, fibers, films, etc.) and compositions at low temperatures. Sol-gel derived materials are of particular technological importance and have a

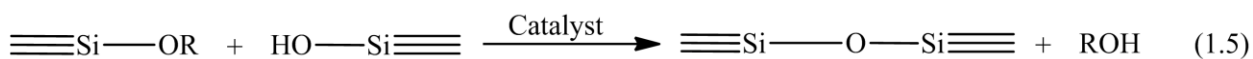
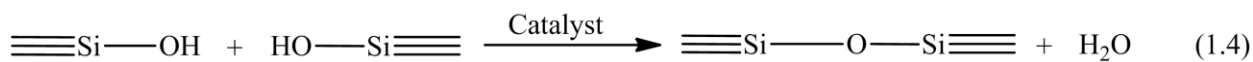
wide range of potential applications in catalysis, sensing, separation, biotechnology, optical and protective coatings, energy conservation, environmental remediation, etc.<sup>38</sup>

In general, sol-gel materials can be prepared from the hydrolysis and polycondensation of a liquid precursor/s (e.g. silicon alkoxide) or from a colloidal particle solution as shown in the following equations.<sup>140</sup>

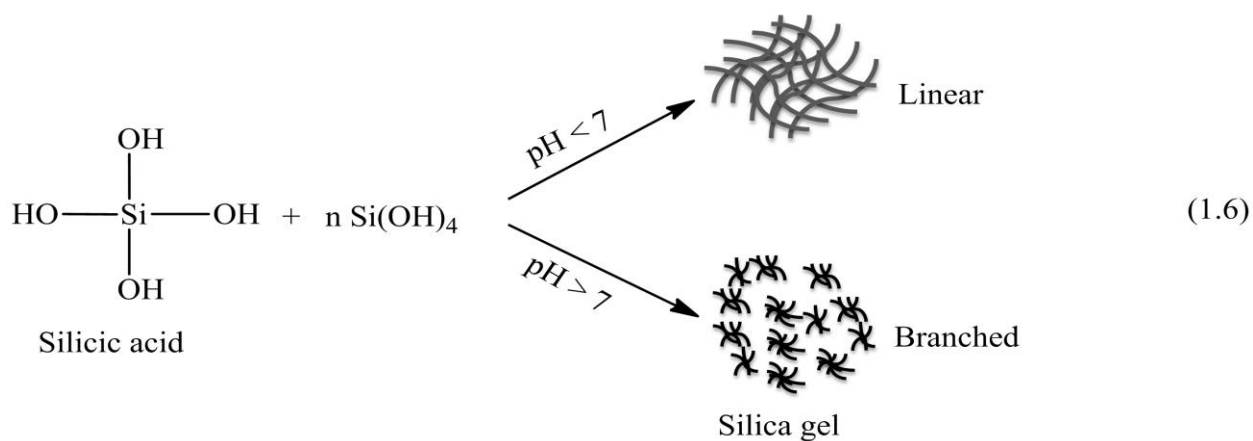
(a) Hydrolysis



(b) Condensation (through the elimination of water or alcohol)



Further condensation



What actually determines the structure of the gel is the relative kinetics of hydrolysis and condensation/polycondensation processes (rate constants ratio,  $k_h/k_c$ ).<sup>139</sup> In general, the hydrolysis and condensation are slow processes occurring simultaneously and kinetics of the reactions is a pH dependent. So, catalyst (acid  $H_3O^+$  or base  $OH^-$ ) addition is essential to enhance the slow rates of the hydrolysis and the polycondensation reactions and control the structure of the resulting gel.<sup>38, 139</sup> Under acid-catalyzed conditions, the silica monomers will polymerize mostly in linear-like structures/gels with a small degree of cross-linkage due to the enhancement in the rate of the hydrolysis reaction over that of the condensation reaction.<sup>38, 139</sup> Highly cross-linked branched gels are produced when the rate of the condensation is higher than that of the hydrolysis, which is the case in base-catalyzed reactions.<sup>38, 139</sup> Although pH is a major player in controlling the relative rates of the hydrolysis and polycondensation and so the final structure of the gel, there are other parameters that can affect the kinetics of the process such as the reaction temperature, precursor/s concentration and type, and solvent nature.<sup>38, 139, 141</sup>

Generally, in silica gel there are two possible cyclic siloxane structures that can be adopted by the SiO units as shown in **Figure 1.10**. The 4-rings structure is predominant in silica gels derived from pure silicon alkoxide precursors (e.g. tetramethoxysilane TMOS) while alkyl alkoxides precursors (e.g. methyltrimethoxysilane, MeTMOS) favor the formation of a 6-rings structures.<sup>38</sup> Xerogels or aerogels could be obtained based on the drying protocol of the wet gel (e.g. alcogel). The former is usually obtained by thermal treatment at ambient pressure while supercritical drying is used to produce aerogels.

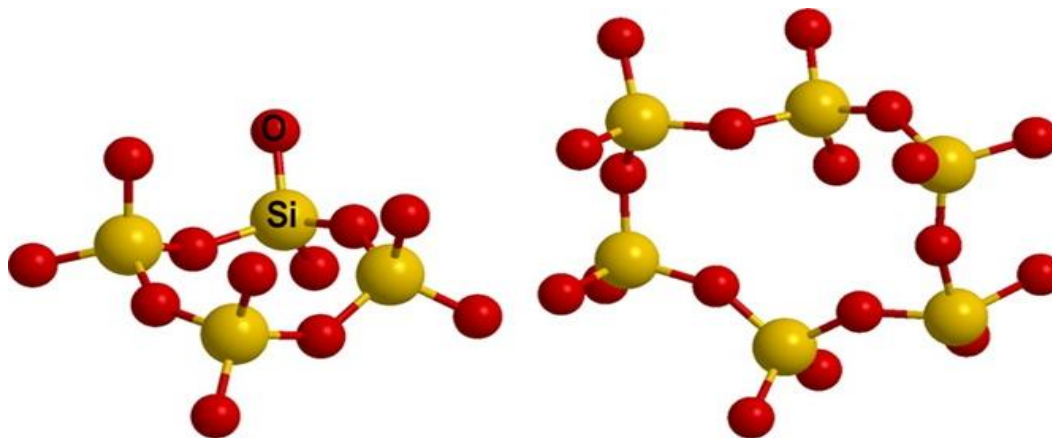


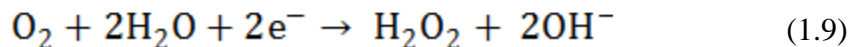
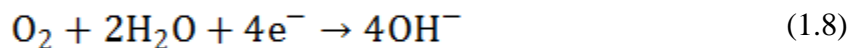
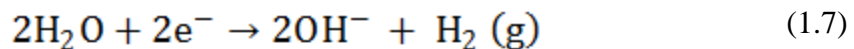
**Figure 1.10.** Schematic diagrams of possible cyclic siloxane structures in silica gels. Reprinted with permission from reference 38. Copyright 2013 American Chemical Society.

Traditionally, silica-based thin films are prepared from a silica sol (silicon alkoxide precursor + ethanol + water + acid or base catalyst) by spin-coating, dip-coating or spraying.<sup>142</sup> Typically these techniques involve the coating of a suitable substrate with silica sol followed by aging and drying at moderate temperatures where gelation and solvent evaporation events occur simultaneously and a three-dimensional network is formed.<sup>142, 143</sup> As a consequence of the simultaneous deposition and drying, the resulting films tend to be compact and not very porous.<sup>142, 143</sup> Another disadvantage of the traditional techniques is that thick films are difficult to be obtained and usually crack during the drying process due to the large lateral stress.<sup>143, 144</sup> An alternative route for the fabrication of silica-based thin films that overcomes these drawbacks and holds many promising advantages over the traditional ones is the sol-gel electrodeposition approach.<sup>40, 140</sup>



### 1.5.2.2 Electrodeposition of Sol–Gel Derived Silica Films

Electrochemical deposition, also known as electrolytic deposition, is an attractive and versatile approach to prepare metal and/or metal oxides films and nanostructures on substrates of varying geometry and size, both patterned and unpatterned as pointed out earlier.<sup>145, 146</sup> Advantages include low cost, simplicity, and ability to tailor the properties of the material such as its composition, thickness, and porosity through variations in process parameters such as time, potential, and concentration. Metal electrodeposition can take place at the electrode/solution interface by a number of different routes including the direct reduction of a metal ion/metal ion complex as mentioned earlier and/or via electrogeneration of base leading to deposition.<sup>146</sup> For sol-gel electrodeposition, deposition takes place by the electrogeneration of the polycondensation base catalyst ( $\text{OH}^-$ ) at the electrode/electrolyte interface<sup>141, 147</sup> from the reduction of oxygen and/or solvent ( $\text{H}_2\text{O}$  in EtOH/ $\text{H}_2\text{O}$  system) upon the application of sufficiently negative potentials to the electrode surface.<sup>148</sup>



The electrogenerated  $\text{OH}^-$  catalyzes the polycondensation of the metal precursors (e.g. metal ions), which results in the formation of colloidal particles that aggregate to produce a solid metal oxide film at the electrode/electrolyte interface.<sup>40, 141, 148-152</sup> The characteristics of the

electrodeposited metal oxide depend on a number of variables including the magnitude of applied cathodic potential, concentration of the metal precursor, composition of the electroplating solution and the nature and cleanliness of the conductive substrate at which the electrochemical reduction reaction takes place. For example, the precipitation of nickel hydroxide on the electrode surface via the electrogeneration of  $\text{OH}^-$  in a nickel nitrate solution.<sup>146</sup>

Metal oxide films can also be formed from sol-gel monomers via *in situ* electrogeneration of  $\text{OH}^-$ . In this case, the production of  $\text{OH}^-$  at the electrode surface catalyzes the polycondensation of the pre-hydrolyzed monomeric precursors near the electrode surface leading to the deposition of a relatively porous film.<sup>40, 141, 148-152</sup> The history of the sol-gel (e.g. silica) electrodeposition is relatively new and date backs to 1999 when Mandler and co-workers demonstrated for the first time the cathodic electrodeposition of “methylated sol-gel films”. Silica thin films were electrodeposited from a pre-hydrolyzed silica monomer (e.g. methyltrimethoxysilane, MeTMOS) on indium-tin-oxide (ITO) and gold substrates. Application of a sufficiently negative potential resulted in the electrogeneration of  $\text{OH}^-$  at the electrode/electrolyte interface which catalyzed the condensation of the pre-hydrolyzed MeTMOS and finally deposition of the sol-gel derived silica film at the electrode surface. Control over the thickness of the precipitated silica films was achieved by controlling the magnitude of the applied negative potential. Four years later, the cathodic electrodeposition of silica-based films from new precursors and on new substrates was demonstrated by Collinson’s and Walcarius’s research groups, separately. Collinson and co-workers, electrodeposited silica films on glassy carbon electrodes from a pre-hydrolyzed

tetramethoxysilane (TMOS) by applying a large enough negative potential.<sup>148</sup> Films with thickness in the range of 75 nm to 15  $\mu\text{m}$  were obtained by varying the magnitude of the applied cathodic potential. They went one step further and proved that it is feasible to trap chemical reagents (e.g. ferrocene methanol) within the framework of the growing silica films by mixing the chemical reagent with the pre-hydrolyzed TMOS sol before the electrodeposition event starts.<sup>148</sup> Walcarius and co-workers electrodeposited silica-based films on gold electrodes from a pre-hydrolyzed (3-mercaptopropyl)trimethoxysilane (MPTMS).<sup>153</sup> Later, they showed that the use of “glue” is crucial to form a well adhered silica film on gold electrodes.<sup>151, 154</sup> They used a very thin film of MPTMS as a glue to strongly and covalently attach the growing silica film to the surface of gold electrodes.<sup>151, 154</sup> The 2003 potential contributions of Collinson and Walcarius paved the road for the wide spreading of the electroassisted sol-gel route initially developed by Mandler and co-workers.

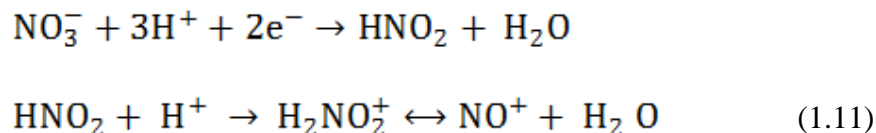
The electroassisted sol-gel route, in particular, has opened up new avenues for the formation of porous silica structures on a variety of different substrates that couldn't otherwise be made using conventional spin coating or dip coating techniques including patterned surfaces and printed circuits.<sup>155-157</sup> Furthermore, when combined with electrochemical reduction of easily reducible metal salts, the electroassisted sol-gel route provides a unique and powerful approach to fabricate metal-metal oxide nanocomposites.<sup>41</sup> Such nanocomposites are interesting and valuable materials because their physical and chemical properties are different than those of the pure components, often enhancing the capabilities of the material allowing new potential applications

to be pursued.<sup>158</sup> The pioneering work of Avinr and Mandler in the electrodeposition of sol-gel derived silica thin films, copper-silica and gold nanoparticles-silica nanocomposites<sup>40, 41,159</sup> inspired us to develop methodologies for the co-electrodeposition of new silica-based nanocomposites and then explore their utilization as building blocks to fabricate high surface area porous metal electrodes. Other examples of reported work include the formation of Cu-TiO<sub>2</sub>,<sup>160</sup> Ni-SiO<sub>2</sub>,<sup>161</sup> Zn-SiO<sub>2</sub><sup>162</sup> composite films and most recently TiO<sub>2</sub>-SiO<sub>2</sub><sup>163</sup> and polymer-SiO<sub>2</sub> composite films<sup>164</sup>.

### 1.5.3 Cathodic Electrodeposition of Conducting Polymers

Conducting polymers have fascinated scientists due to their important properties and potential technological applications in energy storage, electrocatalysis, and chemical sensing, as well as in the fabrication of flexible electronics, supercapacitors, batteries, etc.<sup>165-169</sup> However, reduced mechanical properties, stability and processability of the conductive polymer materials have often limited such applications. Conducting polymers can be prepared chemically via addition of an oxidizing (e.g. FeCl<sub>3</sub>) or electrochemically via direct oxidation of monomers through the application of anodic potential or electrogeneration of an oxidizing agent.<sup>167, 168, 170, 171</sup> The advantage that an electrochemical method provides is the ability to control and fine-tune the film thickness and nanoscale morphology of the composite material by simply varying the applied potential. In 2009 Choi and co-workers<sup>171</sup> demonstrated the ability to form a conducting polymer, e.g., polypyrrole cathodically by coupling the electrogeneration of the nitrosonium ion (NO<sup>+</sup>), as an oxidizing agent with the oxidative polymerization of the pyrrole monomers. NO<sup>+</sup> ions were

generated through the electrochemical reduction of  $\text{NO}_3^-$  ions in a strongly acidic aqueous environment as shown in the following equations.



A particulate-like polypyrrole thin film was then cathodically deposited on a copper substrate by the reaction of the electrogenerated oxidizing agent  $\text{NO}^+$  ions and pyrrole monomers at the electrode surface.<sup>171</sup> Since then, few reports about conducting polymer formation via cathodic deposition have been published. For example, Koh et al., reported that cathodic electrodeposition of three-dimensional mesoporous polypyrrole structures on copper electrodes via the *in situ* electrogeneration of an oxidizing agent, the  $\text{NO}^+$  ions.<sup>172</sup> The morphology of the deposited films was found to be a function of the magnitude of the applied negative potential where at low current densities (e.g. -0.5 and -0.6 volts) films composed of spherical particles were obtained while nanorods-like structured films were obtained at high current densities (e.g. -0.7 volts). The formation of such structures was revealed to the dependence of the polypyrrole polymerization kinetics on the concentration of the *in situ* electrogenerated  $\text{NO}^+$  ions. No details, however, were given about how the concentration of the  $\text{NO}^+$  ions affects the morphology of a deposited polypyrrole film. Nam et al., demonstrated the synthesis of polypyrrole nanowires-based thin films by cathodic electropolymerization.<sup>173</sup> Application of cathodic pulses to the oxidizable substrate surface (e.g. Cu and Ni) resulted in the formation of  $\text{NO}^+$  ions, which act as oxidizing agent to oxidize the pyrrole monomers and a polypyrrole thin film is eventually deposited. The

effect of the aqueous-based electrodeposition solution composition (e.g.  $\text{NaNO}_3$  and pyrrole) on the morphology of the deposited polypyrrole films was studied. He proposed that the morphology of the resulting polypyrrole film was dependent of the reactivity of the pyrrole radical cation, which results from the interaction between the  $\text{NO}^+$  ions and the pyrrole monomers.<sup>173</sup> I do believe that it is more convenient to correlate the morphology changes in the deposited polypyrrole structures to the population of the produced pyrrole radical cations at the electrode surface rather than the reactivity. As the  $\text{NaNO}_3$  concentration increased, the morphology of the deposited films changed from wire-like to particulate-like due to the production of large number of the  $\text{NO}^+$  ions that interact with the pyrrole monomers to produce a large population of the pyrrole radical cations. The radical cations interact quickly with each other to deposit films composed of spherical particles. Nam revealed the formation of these particulate-like films to the formation of highly reactive radical cations.<sup>173</sup> A similar effect was observed with the decrease of the pyrrole monomer concentration and attributed again to the reactivity of the produced radical cations. Hnida et al, combined the conducting polymers cathodic deposition approach with the templating technique to produce polypyrrole-Ag nanowires.<sup>174</sup> Nanowires with 80 nm diameter of polypyrrole decorated with silver particles were obtained by the cathodic co-electrodeposition of silver and pyrrole within the pores of anodic aluminum oxide (AAO) template followed by the template removal. In recent work by Mandler and co-workers, polymer-silica nanocomposite films were prepared via application of alternating potentials.<sup>164</sup> Polypyrrole was deposited upon application of an anodic potential pulse while silica was deposited during the cathodic pulse. A composite film was thus

produced, with the morphology and extent of homogeneity of the deposits dependent on the applied potentials, the order of their application, deposition time and electrode material.<sup>164</sup>

## **1.6 Why are New Fabrication Strategies for Nanostructured Porous Materials Required?**

Although the aforementioned fabrication techniques possess merits and have been proven to be suitable routes to prepare a variety of NPNMs, the implementation of these methods to prepare nanoporous precious metals still represents a challenge in many circumstances. The liquid crystal templating technique is inapplicable to produce porous gold due to auto-reduction of the gold ions to gold nanoparticles.<sup>34, 175, 176</sup> Hard templating is a time consuming multistep process in that it requires the preparation of a sacrificial template, metal deposition within the pores of the sacrificial template, and generation of the porous metal structure after the removal of the original template.<sup>177</sup> In general, templating approaches are difficult to implement for the large-scale production due to the necessity to adopt many factors in the templating process (e.g. concentration, temperature, pH, etc.), the limitation to produce one-dimensional porous structures at most (e.g. array of tubes), and the absence of dynamic control over the length scale are disadvantageous.<sup>42</sup> Although the apparent simplicity of the dealloying technique, in which the porous metal structure is obtained by the selective removal of the least noble component from an alloy in a corrosive medium (e.g. silver in silver-rich gold alloy), it has some shortcomings such as the use of elevated temperatures in the preparation of desirable alloys, the sophisticated manipulation required to handle the ultra-thin commercially available gold leaf (~ 100 nm in thickness), and the thermal

treatment required after the dealloying process to control the pore size for specific applications.<sup>43,</sup>  
<sup>178</sup> Other preparation techniques usually include the use of high temperatures, expensive equipment, or high vacuum.<sup>177, 179</sup> However, most of these drawbacks could be overcome by using electrodeposition methods to prepare the alloys. Therefore, there is a need to explore novel and robust strategies for the fabrication of nanostructured porous noble metals and/ or development of the existing ones. Based on the previous discussion and literature reviews, the electrochemical-based fabrication methods are potential candidates for nanostructured porous materials fabrication due to the simplicity, and possibility to create new materials, particularly, composites that have not been made before which may overcome issues related to reproducibility, scalability, etc. For example, the electrochemical sol-gel approach holds the promise for a facile synthesis of silica-based nanocomposite films that can be used as building blocks in the synthesis of high surface area nanostructured porous precious metal and polymer electrodes. Dealloying of the electrodeposited metal alloys represents the only promising route so far for the preparation of 3D bicontinuous nanoporous precious metal structures.

## **1.7 Thesis Statement**

The goals of this dissertation work are to design and develop novel, reliable and reproducible synthetic protocols to fabricate new nanoporous metal/sol-gel, metal/polymer sol-gel, and binary metal nanocomposites using the electroassisted sol-gel deposition and/ or electrodeposition approaches, study the different factors that affect material formation in order to understand the reaction mechanism and achieve control over composition, thickness, morphology



and surface area, and explore the possibility of using these nanocomposites as building blocks for the fabrication of high surface area noble metal electrodes for electrochemical applications including biosensing in complex matrices and potential catalytic application in fuel cells. The three nanocomposite materials designed and fabricated in this work are:

1. Gold-Silica Nanocomposites for the fabrication of nanostructured coral gold (Ch. 3)
2. Polymer-Silica-Silver Nanocomposites for the fabrication of free-standing pure and hybrid polymer thin films (Ch. 4)
3. Platinum-Silver Binary Alloy Films for the fabrication of 3D bicontinuous nanoporous platinum (Ch. 5).

## 1.8 References

1. Zhang, J. T.; Li, C. M., Nanoporous Metals: Fabrication Strategies and Advanced Electrochemical Applications in Catalysis, Sensing and Energy Systems. *Chemical Society Reviews* **2012**, 41, (21), 7016-7031.
2. Guo, D. J.; Ding, Y., Porous Nanostructured Metals for Electrocatalysis. *Electroanalysis* **2012**, 24, (11), 2035-2043.
3. Rouquerol, J.; Avnir, D.; Fairbridge, C. W.; Everett, D. H.; Haynes, J. H.; Pernicone, N.; Ramsay, J. D. F.; Sing, K. S. W.; Unger, K. K., Recommendations for the Characterization of Porous Solids. *Pure and Applied Chemistry* **1994**, 66, (8), 1739-1758.
4. Erlebacher, J.; Seshadri, R., Hard Materials with Tunable Porosity. *MRS Bulletin* **2009**, 34, (08), 561-568.
5. Tappan, B. C.; Steiner, S. A.; Luther, E. P., Nanoporous Metal Foams. *Angewandte Chemie International Edition* **2010**, 49, (27), 4544-4565.
6. Wittstock, A.; Wichmann, A.; Biener, J.; Baumer, M., Nanoporous gold: a New Gold Catalyst with Tunable Properties. *Faraday Discussions* **2011**, 152, 87-98.
7. Menzel, N.; Ortel, E.; Kraehnert, R.; Strasser, P., Electrocatalysis Using Porous Nanostructured Materials. *Chemphyschem* **2012**, 13, (6), 1385-1394.
8. Fujita, T.; Guan, P. F.; McKenna, K.; Lang, X. Y.; Hirata, A.; Zhang, L.; Tokunaga, T.; Arai, S.; Yamamoto, Y.; Tanaka, N.; Ishikawa, Y.; Asao, N.; Yamamoto, Y.; Erlebacher, J.; Chen, M. W., Atomic Origins of the High Catalytic Activity of Nanoporous Gold. *Nature Materials* **2012**, 11, (9), 775-780.
9. Bond, G. C.; Thompson, D. T., Catalysis by Gold. *Catalysis Reviews* **1999**, 41, (3-4), 319-388.
10. Wittstock, A.; Zielasek, V.; Biener, J.; Friend, C. M.; Bäumer, M., Nanoporous Gold Catalysts for Selective Gas-Phase Oxidative Coupling of Methanol at Low Temperature. *Science* **2010**, 327, (5963), 319-322.
11. Seo, H. O.; Jeong, S. H.; Lee, H. J.; Jee, H. G.; Boo, J. H.; Lim, D. C.; Kim, Y. D., CO Oxidation on Rough Au Thin Films Grown on Si Wafer. *Applied Catalysis A: General* **2008**, 347, (1), 112-116.
12. Campbell, C. T., The Active Site in Nanoparticle Gold Catalysis. *Science* **2004**, 306, (5694), 234-235.
13. Yin, H. M.; Zhou, C. Q.; Xu, C. X.; Liu, P. P.; Xu, X. H.; Ding, Y., Aerobic Oxidation of D-glucose on Support-Free Nanoporous Gold. *Journal of Physical Chemistry C* **2008**, 112, (26), 9673-9678.
14. Jeong, H.; Kim, J., Electrochemical Oxidation of Glucose at Nanoporous Black Gold Surfaces in the Presence of High Concentration of Chloride Ions and Application to Amperometric Detection. *Electrochimica Acta* **2012**, 80, 383-389.

15. Liu, J.; Cao, L.; Huang, W.; Li, Z. L., Preparation of AuPt Alloy Foam Films and Their Superior Electrocatalytic Activity for the Oxidation of Formic Acid. *Acs Applied Materials & Interfaces* **2011**, 3, (9), 3552-3558.
16. Lee, D.; Jang, H. Y.; Hong, S.; Park, S., Synthesis of Hollow and Nanoporous Gold/Platinum Alloy Nanoparticles and Their Electrocatalytic Activity for Formic Acid Oxidation. *Journal of Colloid and Interface Science* **2012**, 388, 74-79.
17. Fu, Q.; Saltsburg, H.; Flytzani-Stephanopoulos, M., Active Nonmetallic Au and Pt Species on Ceria-Based Water-Gas Shift Catalysts. *Science* **2003**, 301, (5635), 935-938.
18. Barakat, T.; Rooke, J. C.; Genty, E.; Cousin, R.; Siffert, S.; Su, B. L., Gold Catalysts in Environmental Remediation and Water-Gas Shift Technologies. *Energy & Environmental Science* **2013**, 6, (2), 371-391.
19. Antolini, E., Platinum-Based Ternary Catalysts for Low Temperature Fuel Cells: Part II. Electrochemical Properties. *Applied Catalysis B: Environmental* **2007**, 74, (3-4), 337-350.
20. Basri, S.; Kamarudin, S. K.; Daud, W. R. W.; Yaakub, Z., Nanocatalyst for Direct Methanol Fuel Cell (DMFC). *International Journal of Hydrogen Energy* **2010**, 35, (15), 7957-7970.
21. Bianchini, C.; Shen, P. K., Palladium-Based Electrocatalysts for Alcohol Oxidation in Half Cells and in Direct Alcohol Fuel Cells. *Chemical Reviews* **2009**, 109, (9), 4183-4206.
22. Antolini, E., Palladium in Fuel Cell Catalysis. *Energy & Environmental Science* **2009**, 2, (9), 915-931.
23. Collinson, M. M., Nanoporous Gold Electrodes and Their Applications in Analytical Chemistry. *ISRN Analytical Chemistry* **2013**, 2013, 21.
24. Zheng, L. T.; Wei, Y. L.; Gong, H. Q.; Qian, L., Application Progress of Nanoporous Gold in Analytical Chemistry. *Chinese Journal of Analytical Chemistry* **2013**, 41, (1), 137-144.
25. Zhao, B.; Collinson, M. M., Hierarchical Porous Gold Electrodes: Preparation, Characterization, and Electrochemical Behavior. *Journal of Electroanalytical Chemistry* **2012**, 684, 53-59.
26. Li, T.; Jia, F.; Fan, Y.; Ding, Z.; Yang, J., Fabrication of Nanoporous Thin-Film Working Electrodes and Their Biosensing Applications. *Biosensors and Bioelectronics* **2013**, 42, (0), 5-11.
27. Chen, L. Y.; Fujita, T.; Chen, M. W., Biofunctionalized Nanoporous Gold for Electrochemical Biosensors. *Electrochimica Acta* **2012**, 67, 1-5.
28. Chen, L. Y.; Lang, X. Y.; Fujita, T.; Chen, M. W., Nanoporous Gold for Enzyme-Free Electrochemical Glucose Sensors. *Scripta Materialia* **2011**, 65, (1), 17-20.
29. Yan, M.; Zhang, M.; Ge, S. G.; Yu, J. H.; Li, M.; Huang, J. D.; Liu, S., Ultrasensitive Electrochemiluminescence Detection of DNA Based on Nanoporous Gold Electrode and PdCu@Carbon Nanocrystal Composites as Labels. *Analyst* **2012**, 137, (14), 3314-3320.
30. Hu, K. C.; Lan, D. X.; Li, X. M.; Zhang, S. S., Electrochemical DNA Biosensor Based on Nanoporous Gold Electrode and Multifunctional Encoded DNA-Au Bio Bar Codes. *Analytical Chemistry* **2008**, 80, (23), 9124-9130.

31. Qiu, H. J.; Zhou, G. P.; Ji, G. L.; Zhang, Y.; Huang, X. R.; Ding, Y., A novel Nanoporous Gold Modified Electrode for the Selective Determination of Dopamine in the Presence of Ascorbic Acid. *Colloids and Surfaces B-Biointerfaces* **2009**, 69, (1), 105-108.
32. Liu, Z. N.; Zhang, H. C.; Hou, S. F.; Ma, H. Y., Highly Sensitive and Selective Electrochemical Detection of L-Cysteine Using Nanoporous Gold. *Microchimica Acta* **2012**, 177, (3-4), 427-433.
33. Ge, X. B.; Wang, L. Q.; Liu, Z. N.; Ding, Y., Nanoporous Gold Leaf for Amperometric Determination of Nitrite. *Electroanalysis* **2011**, 23, (2), 381-386.
34. Yamauchi, Y.; Kuroda, K., Rational Design of Mesoporous Metals and Related Nanomaterials by a Soft-Template Approach. *Chemistry-an Asian Journal* **2008**, 3, (4), 664-676.
35. Li, Y.; Song, Y. Y.; Yang, C.; Xia, X. H., Hydrogen Bubble Dynamic Template Synthesis of Porous Gold for Nonenzymatic Electrochemical Detection of Glucose. *Electrochemistry Communications* **2007**, 9, (5), 981-988.
36. Andersen, H. H.; Johansen, A.; Touboltsev, V. S., The Angular Distribution of Gold Self-Sputtered Under Thermal-Spike Conditions. *Nuclear Instruments & Methods in Physics Research Section B-Beam Interactions with Materials and Atoms* **2000**, 164, 727-732.
37. Andersen, H. H.; Bay, H. L., Heavy-Ion Sputtering Yields of Gold: Further Evidence of Nonlinear Effects. *Journal of Applied Physics* **1975**, 46, (6), 2416-2422.
38. Ciriminna, R.; Fidalgo, A.; Pandarus, V.; Beland, F.; Ilharco, L. M.; Pagliaro, M., The Sol-Gel Route to Advanced Silica-Based Materials and Recent Applications. *Chemical Reviews* **2013**, 113, (8), 6592-6620.
39. Artzi-Gerlitz, R.; Benkstein, K. D.; Lahr, D. L.; Hertz, J. L.; Montgomery, C. B.; Bonevich, J. E.; Semancik, S.; Tarlov, M. J., Fabrication and Gas Sensing Performance of Parallel Assemblies of Metal Oxide Nanotubes Supported by Porous Aluminum Oxide Membranes. *Sensors and Actuators B-Chemical* **2009**, 136, (1), 257-264.
40. Shacham, R.; Avnir, D.; Mandler, D., Electrodeposition of Methylated Sol-Gel Films on Conducting Surfaces. *Advanced Materials* **1999**, 11, (5), 384-388.
41. Toledano, R.; Shacham, R.; Avnir, D.; Mandler, D., Electrochemical Co-Deposition of Sol-Gel/Metal Thin Nanocomposite Films. *Chemistry of Materials* **2008**, 20, (13), 4276-4283.
42. Zhang, Z. H.; Wang, Y.; Qi, Z.; Somsen, C.; Wang, X. G.; Zhao, C. C., Fabrication and Characterization of Nanoporous Gold Composites Through Chemical Dealloying of Two Phase Al-Au Alloys. *Journal of Materials Chemistry* **2009**, 19, (33), 6042-6050.
43. Gupta, G.; Thorp, J. C.; Mara, N. A.; Dattelbaum, A. M.; Misra, A.; Picraux, S. T., Morphology and Porosity of Nanoporous Au Thin Films Formed by Dealloying of  $Au_xSi_{1-x}$ . *Journal of Applied Physics* **2012**, 112, (9).
44. Shin, C.; Shin, W.; Hong, H. G., Electrochemical Fabrication and Electrocatalytic Characteristics Studies of Gold Nanopillar Array Electrode (AuNPE) for Development of a Novel Electrochemical Sensor. *Electrochimica Acta* **2007**, 53, (2), 720-728.

45. Bonroy, K.; Friedt, J. M.; Frederix, F.; Laureyn, W.; Langerock, S.; Campitelli, A.; Sara, M.; Borghs, G.; Goddeeris, B.; Declerck, P., Realization and Characterization of Porous Gold for Increased Protein Coverage on Acoustic Sensors. *Analytical Chemistry* **2004**, 76, (15), 4299-4306.
46. Ying, J. Y.; Mehnert, C. P.; Wong, M. S., Synthesis and Applications of Supramolecular-Templated Mesoporous Materials. *Angewandte Chemie-International Edition* **1999**, 38, (1-2), 56-77.
47. Zhu, C.; Du, D.; Eychmueller, A.; Lin, Y., Engineering Ordered and Nonordered Porous Noble Metal Nanostructures: Synthesis, Assembly, and Their Applications in Electrochemistry. *Chemical Reviews* **2015**, 115, (16), 8896-8943.
48. Zakhidov, A. A.; Baughman, R. H.; Iqbal, Z.; Cui, C. X.; Khayrullin, I.; Dantas, S. O.; Marti, I.; Ralchenko, V. G., Carbon Structures with Three-Dimensional Periodicity at Optical Wavelengths. *Science* **1998**, 282, (5390), 897-901.
49. Lee, J.; Yoon, S.; Hyeon, T.; Oh, S. M.; Kim, K. B., Synthesis of a New Mesoporous Carbon and its Application to Electrochemical Double-Layer Capacitors. *Chemical Communications* **1999**, (21), 2177-2178.
50. Ryoo, R.; Joo, S. H.; Jun, S., Synthesis of Highly Ordered Carbon Molecular Sieves via Template-Mediated Structural Transformation. *Journal of Physical Chemistry B* **1999**, 103, (37), 7743-7746.
51. Zhao, B.; Collinson, M. M., Well-Defined Hierarchical Templates for Multimodal Porous Material Fabrication. *Chemistry of Materials* **2010**, 22, (14), 4312-4319.
52. Heim, M.; Reculosa, S.; Ravaine, S.; Kuhn, A., Engineering of Complex Macroporous Materials Through Controlled Electrodeposition in Colloidal Superstructures. *Advanced Functional Materials* **2012**, 22, (3), 538-545.
53. Bartlett, P. N.; Baumberg, J. J.; Birkin, P. R.; Ghanem, M. A.; Netti, M. C., Highly Ordered Macroporous Gold and Platinum Films Formed by Electrochemical Deposition through Templates Assembled from Submicron Diameter Monodisperse Polystyrene Spheres. *Chemistry of Materials* **2002**, 14, (5), 2199-2208.
54. Jiang, P.; Cizeron, J.; Bertone, J. F.; Colvin, V. L., Preparation of Macroporous Metal Films from Colloidal Crystals. *Journal of the American Chemical Society* **1999**, 121, (34), 7957-7958.
55. Beck, J. S.; Vartuli, J. C.; Roth, W. J.; Leonowicz, M. E.; Kresge, C. T.; Schmitt, K. D.; Chu, C. T. W.; Olson, D. H.; Sheppard, E. W.; McCullen, S. B.; Higgins, J. B.; Schlenker, J. L., A New Family of Mesoporous Molecular-Sieves Prepared with Liquid-Crystal Templates. *Journal of the American Chemical Society* **1992**, 114, (27), 10834-10843.
56. Kresge, C. T.; Leonowicz, M. E.; Roth, W. J.; Vartuli, J. C.; Beck, J. S., Ordered Mesoporous Molecular-Sieves Synthesized by a Liquid-Crystal Template Mechanism. *Nature* **1992**, 359, (6397), 710-712.
57. Attard, G. S.; Bartlett, P. N.; Coleman, N. R. B.; Elliott, J. M.; Owen, J. R.; Wang, J. H., Mesoporous Platinum Films from Lyotropic Liquid Crystalline Phases. *Science* **1997**, 278, (5339), 838-840.

58. Attard, G. S.; Goltner, C. G.; Corker, J. M.; Henke, S.; Templer, R. H., Liquid-Crystal Templates for Nanostructured Metals. *Angewandte Chemie-International Edition in English* **1997**, 36, (12), 1315-1317.
59. Attard, G. S.; Leclerc, S. A. A.; Maniguet, S.; Russell, A. E.; Nandhakumar, I.; Bartlett, P. N., Mesoporous Pt/Ru Alloy from the Hexagonal Lyotropic Liquid Crystalline Phase of a Nonionic Surfactant. *Chemistry of Materials* **2001**, 13, (5), 1444-+.
60. Yamauchi, Y.; Tonegawa, A.; Komatsu, M.; Wang, H.; Wang, L.; Nemoto, Y.; Suzuki, N.; Kuroda, K., Electrochemical Synthesis of Mesoporous Pt-Au Binary Alloys with Tunable Compositions for Enhancement of Electrochemical Performance. *Journal of the American Chemical Society* **2012**, 134, (11), 5100-5109.
61. Zhou, W.-J.; Zhang, J.; Xue, T.; Zhao, D.-D.; Li, H.-l., Electrodeposition of Ordered Mesoporous Cobalt Hydroxide Film from Lyotropic Liquid Crystal Media for Electrochemical Capacitors. *Journal of Materials Chemistry* **2008**, 18, (8), 905-910.
62. Nelson, P. A.; Elliott, J. M.; Attard, G. S.; Owen, J. R., Mesoporous Nickel/Nickel Oxide - a Nanoarchitected Electrode. *Chemistry of Materials* **2002**, 14, (2), 524-529.
63. Luo, H.; Sun, L.; Lu, Y.; Yan, Electrodeposition of Mesoporous Semimetal and Magnetic Metal Films from Lyotropic Liquid Crystalline Phases. *Langmuir* **2004**, 20, (23), 10218-10222.
64. Shin, H. J.; Ko, C. H.; Ryoo, R., Synthesis of Platinum Networks with Nanoscopic Periodicity using Mesoporous Silica as Template. *Journal of Materials Chemistry* **2001**, 11, (2), 260-261.
65. Liu, W.; Herrmann, A.-K.; Bigall, N. C.; Rodriguez, P.; Wen, D.; Oezaslan, M.; Schmidt, T. J.; Gaponik, N.; Eychmueller, A., Noble Metal Aerogels-Synthesis, Characterization, and Application as Electrocatalysts. *Accounts of Chemical Research* **2015**, 48, (2), 154-162.
66. Kistler, S. S., Coherent Expanded Aerogels and Jellies. *Nature* **1931**, 127, 741-741.
67. Bigall, N. C.; Herrmann, A.-K.; Vogel, M.; Rose, M.; Simon, P.; Carrillo-Cabrera, W.; Dorfs, D.; Kaskel, S.; Gaponik, N.; Eychmueller, A., Hydrogels and Aerogels from Noble Metal Nanoparticles. *Angewandte Chemie-International Edition* **2009**, 48, (51), 9731-9734.
68. Herrmann, A.-K.; Formanek, P.; Borchardt, L.; Klose, M.; Giebeler, L.; Eckert, J.; Kaskel, S.; Gaponik, N.; Eychmueller, A., Multimetallic Aerogels by Template-Free Self-Assembly of Au, Ag, Pt, and Pd Nanoparticles. *Chemistry of Materials* **2014**, 26, (2), 1074-1083.
69. Ranmohotti, K. G. S.; Gao, X.; Arachchige, I. U., Salt-Mediated Self-Assembly of Metal Nanoshells into Monolithic Aerogel Frameworks. *Chemistry of Materials* **2013**, 25, (17), 3528-3534.
70. Gao, X.; Esteves, R. J.; Thi Thu Hien, L.; Jaini, R.; Arachchige, I. U., Oxidation-Induced Self-Assembly of Ag Nanoshells into Transparent and Opaque Ag Hydrogels and Aerogels. *Journal of the American Chemical Society* **2014**, 136, (22), 7993-8002.
71. Leventis, N.; Chandrasekaran, N.; Sadekar, A. G.; Sotiriou-Leventis, C.; Lu, H., One-Pot Synthesis of Interpenetrating Inorganic/Organic Networks of CuO/Resorcinol-Formaldehyde Aerogels: Nanostructured Energetic Materials. *Journal of the American Chemical Society* **2009**, 131, (13), 4576-4577.

72. Nyce, G. W.; Hayes, J. R.; Hamza, A. V.; Satcher, J. H., Synthesis and Characterization of Hierarchical Porous Gold Materials. *Chemistry of Materials* **2007**, 19, (3), 344-346.
73. Scriven, L. E., Equilibrium Bicontinuous Structure. *Nature* **1976**, 263, (5573), 123-125.
74. Lu, X.; Balk, T. J.; Spolenak, R.; Arzt, E., Dealloying of Au-Ag Thin Films with a Composition Gradient: Influence on Morphology of Nanoporous Au. *Thin Solid Films* **2007**, 515, (18), 7122-7126.
75. Lu, X.; Bischoff, E.; Spolenak, R.; Balk, T. J., Investigation of Dealloying in Au-Ag Thin Films by Quantitative Electron Probe Microanalysis. *Scripta Materialia* **2007**, 56, (7), 557-560.
76. Erlebacher, J.; Aziz, M. J.; Karma, A.; Dimitrov, N.; Sieradzki, K., Evolution of Nanoporosity in Dealloying. *Nature* **2001**, 410, (6827), 450-453.
77. Xiao, X.; Si, P.; Magner, E., An Overview of Dealloyed Nanoporous Gold in Bioelectrochemistry. *Bioelectrochemistry* **2016**, 109, 117-126.
78. Seker, E.; Reed, M. L.; Begley, M. R., Nanoporous Gold: Fabrication, Characterization, and Applications. *Materials* **2009**, 2, (4), 2188-2215.
79. Rouya, E.; Reed, M. L.; Kelly, R. G.; Bart-Smith, H.; Begley, M.; Zangari, G., Synthesis of Nanoporous Gold Structures via Dealloying of Electroplated Au-Ni Alloy Films. *ECS Transactions* **2007**, 6, (11), 41-50.
80. Huang, J. F.; Sun, I. W., Fabrication and Surface Functionalization of Nanoporous Gold by Electrochemical Alloying/Dealloying of Au-Zn in an Ionic Liquid, and the Self-Assembly of L-Cysteine Monolayers. *Advanced Functional Materials* **2005**, 15, (6), 989-994.
81. Bozzini, B.; Pietro De Gaudenzi, G.; Mele, C., A SERS Investigation of the Electrodeposition of Ag-Au Alloys from Free-Cyanide Solutions. *Journal of Electroanalytical Chemistry* **2004**, 563, (1), 133-143.
82. Ji, C. X.; Searson, P. C., Synthesis and Characterization of Nanoporous Gold Nanowires. *Journal of Physical Chemistry B* **2003**, 107, (19), 4494-4499.
83. McCurry, D. A.; Kamundi, M.; Fayette, M.; Wafula, F.; Dimitrov, N., All Electrochemical Fabrication of a Platinized Nanoporous Au Thin-Film Catalyst. *ACS Applied Materials & Interfaces* **2011**, 3, (11), 4459-4468.
84. Barnes, A.; Senior, N. A.; Newman, R. C., Film-Induced Cleavage of Ag-Au Alloys. *Metallurgical and Materials Transactions a-Physical Metallurgy and Materials Science* **2009**, 40A, (1), 58-68.
85. Senior, N. A.; Newman, R. C., Synthesis of Tough Nanoporous Metals by Controlled Electrolytic Dealloying. *Nanotechnology* **2006**, 17, (9), 2311-2316.
86. Dursun, A.; Pugh, D. V.; Corcoran, S. G., A Steady-State Method for Determining the Dealloying Critical Potential. *Electrochemical and Solid State Letters* **2003**, 6, (8), B32-B34.
87. Daggumati, P.; Kurtulus, O.; Chapman, C. A. R.; Dimlioglu, D.; Seker, E., Microfabrication of Nanoporous Gold Patterns for Cell-material Interaction Studies. *Jove-Journal of Visualized Experiments* **2013**, (77).

88. Seker, E.; Gaskins, J. T.; Bart-Smith, H.; Zhu, J.; Reed, M. L.; Zangari, G.; Kelly, R.; Begley, M. R., The Effects of Post-Fabrication Annealing on the Mechanical Properties of Free-Standing Nanoporous Gold Structures. *Acta Materialia* **2007**, 55, (14), 4593-4602.
89. Ding, Y.; Kim, Y. J.; Erlebacher, J., Nanoporous Gold Leaf: "Ancient Technology"/Advanced Material. *Advanced Materials* **2004**, 16, (21), 1897-+.
90. Erlebacher, J., An Atomistic Description of Dealloying - Porosity Evolution, the Critical Potential, and Rate-Limiting Behavior. *Journal of the Electrochemical Society* **2004**, 151, (10), C614-C626.
91. Patel, J.; Radhakrishnan, L.; Zhao, B.; Uppalapati, B.; Daniels, R. C.; Ward, K. R.; Collinson, M. M., Electrochemical Properties of Nanostructured Porous Gold Electrodes in Biofouling Solutions. *Analytical Chemistry* **2013**, 85, (23), 11610-11618.
92. Laocharoensuk, R.; Sattayasamitsathit, S.; Burdick, J.; Kanatharana, P.; Thavarungkul, P.; Wang, J., Shape-Tailored Porous Gold Nanowires: From Nano Barbells to Nano Step-Cones. *ACS Nano* **2007**, 1, (5), 403-408.
93. Sattayasamitsathit, S.; Gu, Y.; Kaufmann, K.; Minter, S.; Polsky, R.; Wang, J., Tunable Hierarchical Macro/Mesoporous Gold Microwires Fabricated by Dual-Templating and Dealloying Processes. *Nanoscale* **2013**, 5, (17), 7849-7854.
94. Damle, M. S. a., *Fabrication and Characterization of High Surface Area Gold Electrodes*. Virginia Commonwealth University, Richmond, Va : Virginia Commonwealth University: 2014.
95. Liu, Z. N.; Huang, L. H.; Zhang, L. L.; Ma, H. Y.; Ding, Y., Electrocatalytic Oxidation of D-Glucose at Nanoporous Au and Au-Ag Alloy Electrodes in Alkaline Aqueous Solutions. *Electrochimica Acta* **2009**, 54, (28), 7286-7293.
96. Song, Y. Y.; Zhang, D.; Gao, W.; Xia, X. H., Nonenzymatic Glucose Detection by using a Three-Dimensionally Ordered, Macroporous Platinum Template. *Chemistry-a European Journal* **2005**, 11, (7), 2177-2182.
97. Hieda, M.; Garcia, R.; Dixon, M.; Daniel, T.; Allara, D.; Chan, M. H. W., Ultrasensitive Quartz Crystal Microbalance with Porous Gold Electrodes. *Applied Physics Letters* **2004**, 84, (4), 628-630.
98. Daggumati, P.; Matharu, Z.; Wang, L.; Seker, E., Biofouling-Resilient Nanoporous Gold Electrodes for DNA Sensing. *Analytical Chemistry* **2015**, 87, (17), 8618-8622.
99. Ding, C.; Li, H.; Hu, K.; Lin, J.-M., Electrochemical Immunoassay of Hepatitis B Surface Antigen by the Amplification of Gold Nanoparticles Based on the Nanoporous Gold Electrode. *Talanta* **2010**, 80, (3), 1385-1391.
100. Hu, K.; Lan, D.; Li, X.; Zhang, S., Electrochemical DNA Biosensor Based on Nanoporous Gold Electrode and Multifunctional Encoded DNA-Au Bio Bar Codes. *Analytical Chemistry* **2008**, 80, (23), 9124-9130.
101. Hu, K.; Liu, P.; Ye, S.; Zhang, S., Ultrasensitive Electrochemical Detection of DNA Based on PbS Nanoparticle Tags and Nanoporous Gold Electrode. *Biosensors & Bioelectronics* **2009**, 24, (10), 3113-3119.



102. Qiu, H.; Xu, C.; Huang, X.; Ding, Y.; Qu, Y.; Gao, P., Adsorption of Laccase on the Surface of Nanoporous Gold and the Direct Electron Transfer between Them. *The Journal of Physical Chemistry C* **2008**, 112, (38), 14781-14785.
103. Wang, X.; Liu, X.; Yan, X.; Zhao, P.; Ding, Y.; Xu, P., Enzyme-Nanoporous Gold Biocomposite: Excellent Biocatalyst with Improved Biocatalytic Performance and Stability. *Plos One* **2011**, 6, (9).
104. Qian, L.; Das, B.; Li, Y.; Yang, Z., Giant Raman Enhancement on Nanoporous Gold Film by Conjugating with Nanoparticles for Single-Molecule Detection. *Journal of Materials Chemistry* **2010**, 20, (33), 6891-6895.
105. Zhang, L.; Lang, X.; Hirata, A.; Chen, M., Wrinkled Nanoporous Gold Films with Ultrahigh Surface-Enhanced Raman Scattering Enhancement. *Acs Nano* **2011**, 5, (6), 4407-4413.
106. Jung, N.; Chung, D. Y.; Ryu, J.; Yoo, S. J.; Sung, Y.-E., Pt-Based Nanoarchitecture and Catalyst Design for Fuel Cell Applications. *Nano Today* **2014**, 9, (4), 433-456.
107. Liu, W.; Herrmann, A.-K.; Geiger, D.; Borchardt, L.; Simon, F.; Kaskel, S.; Gaponik, N.; Eychmueller, A., High-Performance Electrocatalysis on Palladium Aerogels. *Angewandte Chemie-International Edition* **2012**, 51, (23), 5743-5747.
108. Zeis, R.; Mathur, A.; Fritz, G.; Lee, J.; Erlebacher, J., Platinum-Plated Nanoporous Gold: An Efficient, Low Pt Loading Electrocatalyst for PEM Fuel Cells. *Journal of Power Sources* **2007**, 165, (1), 65-72.
109. Xiao, S.; Xiao, F.; Hu, Y.; Yuan, S.; Wang, S.; Qian, L.; Liu, Y., Hierarchical Nanoporous Gold-Platinum with Heterogeneous Interfaces for Methanol Electrooxidation. *Scientific Reports* **2014**, 4.
110. Liu, W.; Rodriguez, P.; Borchardt, L.; Foelske, A.; Yuan, J.; Herrmann, A.-K.; Geiger, D.; Zheng, Z.; Kaskel, S.; Gaponik, N.; Koetz, R.; Schmidt, T. J.; Eychmueller, A., Bimetallic Aerogels: High-Performance Electrocatalysts for the Oxygen Reduction Reaction. *Angewandte Chemie-International Edition* **2013**, 52, (37), 9849-9852.
111. Debe, M. K., Electrocatalyst Approaches and Challenges for Automotive Fuel Cells. *Nature* **2012**, 486, (7401), 43-51.
112. Huang, X.; Zhu, E.; Chen, Y.; Li, Y.; Chiu, C.-Y.; Xu, Y.; Lin, Z.; Duan, X.; Huang, Y., A Facile Strategy to Pt<sub>3</sub>Ni Nanocrystals with Highly Porous Features as an Enhanced Oxygen Reduction Reaction Catalyst. *Advanced Materials* **2013**, 25, (21), 2974-2979.
113. Gan, L.; Heggen, M.; O'Malley, R.; Theobald, B.; Strasser, P., Understanding and Controlling Nanoporosity Formation for Improving the Stability of Bimetallic Fuel Cell Catalysts. *Nano Letters* **2013**, 13, (3), 1131-1138.
114. Bicelli, L. P.; Bozzini, B.; Mele, C.; D'Urzo, L., A Review of Nanostructural Aspects of Metal Electrodeposition. *International Journal of Electrochemical Science* **2008**, 3, (4), 356-408.
115. Mohanty, U. S., Electrodeposition: A Versatile and Inexpensive Tool for the Synthesis of Nanoparticles, Nanorods, Nanowires, and Nanoclusters of Metals. *Journal of Applied Electrochemistry* **2011**, 41, (3), 257-270.

116. Natter, H.; Hempelmann, R., Nanocrystalline Metals Prepared by Electrodeposition. *Zeitschrift Fur Physikalische Chemie-International Journal of Research in Physical Chemistry & Chemical Physics* **2008**, 222, (2-3), 319-354.
117. Penner, R. M., Mesoscopic Metal Particles and Wires by Electrodeposition. *Journal of Physical Chemistry B* **2002**, 106, (13), 3339-3353.
118. Janaky, C.; Kecsenovity, E.; Rajeshwar, K., Electrodeposition of Inorganic Oxide/Nanocarbon Composites: Opportunities and Challenges. *Chemelectrochem* **2016**, 3, (2), 181-192.
119. Lai, M.; Riley, D. J., Templated Electrosynthesis of Nanomaterials and Porous Structures. *Journal of Colloid and Interface Science* **2008**, 323, (2), 203-212.
120. Jenkins, L. H., Galvanostatic Overpotential Transients and Electrocrystallization Processes on Copper Single Crystals in Solutions of Cupric Perchlorate. *Journal of the Electrochemical Society* **1970**, 117, (5), 630-640.
121. Fleischmann, M.; Thirsk, H. R., The Potentiostatic Study of the Growth of Deposits on Electrodes. *Electrochimica Acta* **1959**, 1, (2-3), 146-160.
122. Erdey-Gruz, T.; Volmer, M., Overvoltage of Metals. *Z. physik. Chem.* **1931**, A157, 165-81.
123. Budevski, E.; Staikov, G.; Lorenz, W. J.; Editors, *Electrochemical Phase Formation and Growth: An Introduction to the Initial Stages of Metal Deposition*. VCH: 1996; p 410 pp.
124. Potzschke, R. T.; Gervasi, C. A.; Vinzelberg, S.; Staikov, G.; Lorenz, W. J., Nanoscale Studies of Ag Electrodeposition On HOPG(0001). *Electrochimica Acta* **1995**, 40, (10), 1469-1474.
125. Vandenbrande, P.; Winand, R., First Stages of the Formation of Copper Electrodeposits and Copper Sputtered Deposits on Amorphous-Carbon and Polycrystalline Silver Substrates. *Journal of Applied Electrochemistry* **1993**, 23, (11), 1089-1096.
126. Vanden Brande, P.; Winand, R., Nucleation and Initial Growth of Copper Electrodeposits under Galvanostatic Conditions. *Surface & Coatings Technology* **1992**, 52, (1), 1-7.
127. Park, Y.; Baricuatro, J.; Hossain, M.; Soriaga, M., Highly-Ordered Ultrathin Pd Films on Pt (111): Electrodeposition and Structural Characterization. *ECS Transactions* **2007**, 3, (34), 65-103.
128. Soriaga, M. P.; Baricuatro, J.; Park, Y.-S.; Kim, Y.-G.; Hossain, M. In *Electrodeposition of Ultrathin Films on Well-Defined Noble-Metal Electrodes: Studies by UHV-EC-STM*, Meeting Abstracts, 2009; The Electrochemical Society: 2009; pp 970-970.
129. Li, C.; Jiang, B.; Miyamoto, N.; Kim, J. H.; Malgras, V.; Yamauchi, Y., Surfactant-Directed Synthesis of Mesoporous Pd Films with Perpendicular Mesochannels as Efficient Electrocatalysts. *Journal of the American Chemical Society* **2015**, 137, (36), 11558-11561.
130. Ebelmen, J. J., *Ann. Chim. Phys.* **1846**, 16, 129.
131. Graham, T., XXXV.-On the Properties of Silicic Acid and Other Analogous Colloidal Substances. *Journal of the Chemical Society* **1864**, 17, (0), 318-327.
132. Patrick, W. A. Silica Gel. US1297724, 1919.

133. Geffcken, W.; Berger, E. Changing the Reflective Capacity of Optical Glass. DE736411, 1939.
134. Dislich, H.; Hinz, P., History and Principles of the Sol-Gel Process, and Some New Multicomponent Oxide Coatings. *Journal of Non-Crystalline Solids* **1982**, 48, (1), 11-16.
135. Roy, R., Aids in Hydrothermal Experimentation: II, Methods of Making Mixtures for Both “Dry” and “Wet” Phase Equilibrium Studies. *Journal of the American Ceramic Society* **1956**, 39, (4), 145-146.
136. Schroeder, H., Properties and Applications of Oxide Layers Deposited on Glass from Organic Solutions. *Optica Acta: International Journal of Optics* **1962**, 9, (3), 249-254.
137. Iler, R. K., *The Colloid Chemistry of Silica and Silicates*. Cornell Univ. Press: 1955; p 324 pp.
138. Stöber, W.; Fink, A.; Bohn, E., Controlled Growth of Monodisperse Silica Spheres in the Micron Size Range. *Journal of Colloid and Interface Science* **1968**, 26, (1), 62-69.
139. Hench, L. L.; West, J. K., The Sol-Gel Process. *Chemical Reviews* **1990**, 90, (1), 33-72.
140. Collinson, M. M.; Moore, N.; Deepa, P. N.; Kanungo, M., Electrodeposition of Porous Silicate Films from Ludox Colloidal Silicae. *Langmuir* **2003**, 19, (18), 7669-7672.
141. Collinson, M. M., Electrochemistry: An Important Tool to Study and Create New Sol-Gel-Derived Materials. *Accounts of Chemical Research* **2007**, 40, (9), 777-783.
142. Brinker, C.; Scherer, G., *Sol-Gel Science: The Physics and Chemistry of Sol-Gel Processing*. Academic: 1990; p No pp. given.
143. Grosso, D., How to Exploit the Full Potential of the Dip-Coating Process to Better Control Film Formation. *Journal of Materials Chemistry* **2011**, 21, (43), 17033-17038.
144. Kozuka, H.; Takenaka, S.; Tokita, H.; Hirano, T.; Higashi, Y.; Hamatani, T., Stress and Cracks in Gel-Derived Ceramic Coatings and Thick Film Formation. *Journal of Sol-Gel Science and Technology* **2003**, 26, (1-3), 681-686.
145. Zhitomirsky, I., Cathodic Electrodeposition of Ceramic and Organoceramic Materials. Fundamental Aspects. *Advances in Colloid and Interface Science* **2002**, 97, (1-3), 279-317.
146. Therese, G. H. A.; Kamath, P. V., Electrochemical Synthesis of Metal Oxides and Hydroxides. *Chemistry of Materials* **2000**, 12, (5), 1195-1204.
147. Walcarius, A.; Collinson, M. M., Analytical Chemistry with Silica Sol-Gels: Traditional Routes to New Materials for Chemical Analysis. *Annual Review of Analytical Chemistry* **2009**, 2, 121-143.
148. Deepa, P. N.; Kanungo, M.; Claycomb, G.; Sherwood, P. M. A.; Collinson, M. M., Electrochemically Deposited Sol-Gel-Derived Silicate Films as a Viable Alternative in Thin-Film Design. *Analytical Chemistry* **2003**, 75, (20), 5399-5405.
149. Etienne, M.; Sallard, S.; Schroder, M.; Guillemin, Y.; Mascotto, S.; Smarsly, B. M.; Walcarius, A., Electrochemical Generation of Thin Silica Films with Hierarchical Porosity. *Chemistry of Materials* **2010**, 22, (11), 3426-3432.
150. Shacham, R.; Mandler, D.; Avnir, D., Electrochemically Induced Sol-Gel Deposition of Zirconia Thin Films. *Chemistry-a European Journal* **2004**, 10, (8), 1936-1943.

151. Sibottier, E.; Sayen, S.; Gaboriaud, F.; Walcarius, A., Factors Affecting the Preparation and Properties of Electrodeposited Silica Thin Films Functionalized with Amine or Thiol Groups. *Langmuir* **2006**, *22*, (20), 8366-8373.
152. Walcarius, A.; Sibottier, E.; Etienne, M.; Ghanbaja, J., Electrochemically Assisted Self-Assembly of Mesoporous Silica Thin Films. *Nature Materials* **2007**, *6*, (8), 602-608.
153. Sayen, S. p.; Walcarius, A., Electro-Assisted Generation of Functionalized Silica Films on Gold. *Electrochemistry Communications* **2003**, *5*, (4), 341-348.
154. Walcarius, A.; Sibottier, E., Electrochemically-Induced Deposition of Amine-Functionalized Silica Films on Gold Electrodes and Application to Cu(II) Detection in (Hydro)Alcoholic Medium. *Electroanalysis* **2005**, *17*, (19), 1716-1726.
155. Liu, L.; Toledano, R.; Danieli, T.; Zhang, J. Q.; Hu, J. M.; Mandler, D., Electrochemically Patterning Sol-Gel Structures on Conducting and Insulating Surfaces. *Chemical Communications* **2011**, *47*, (24), 6909-6911.
156. Shacham, R.; Mandler, D.; Avnir, D., Pattern Recognition in Oxides Thin-Film Electrodeposition: Printed Circuits. *Comptes Rendus Chimie* **2010**, *13*, (1-2), 237-241.
157. Luna-Vera, F.; Dong, D.; Hamze, R.; Liu, S.; Collinson, M. M., Electroassisted Fabrication of Free-Standing Silica Structures of Micrometer Size. *Chemistry of Materials* **2012**, *24*, (12), 2265-2273.
158. Tehrani, M. S.; Azar, P. A.; Mohammadiazar, S., A single Step Technique for Preparation of Porous Solid Phase Microextraction Fibers by Electrochemically Co-Deposited Silica Based Sol-Gel/Cu Nanocomposite. *Journal of Chromatography A* **2013**, *1278*, 1-7.
159. Toledano, R.; Mandler, D., Electrochemical Codeposition of Thin Gold Nanoparticles/Sol-Gel Nanocomposite Films. *Chemistry of Materials* **2010**, *22*, (13), 3943-3951.
160. Ramalingam, S.; Muralidharan, V. S.; Subramania, A., Electrodeposition and Characterization of Cu-TiO<sub>2</sub> Nanocomposite Coatings. *Journal of Solid State Electrochemistry* **2009**, *13*, (11), 1777-1783.
161. Wu, L. K.; Hu, J. M.; Zhang, J. Q.; Cao, C. N., A Silica Co-Electrodeposition Route to Highly Active Ni-Based Film Electrodes. *Journal of Materials Chemistry A* **2013**, *1*, (41), 12885-12892.
162. Wu, L. K.; Hu, J. M.; Zhang, J. Q., Electrodeposition of Zinc-Doped Silane Films for Corrosion Protection of Mild Steels. *Corrosion Science* **2012**, *59*, 348-351.
163. Liu, L.; Mandler, D., Electro-Assist Deposition of Binary Sol-Gel Films with Graded Structure. *Electrochimica Acta* **2013**, *102*, 212-218.
164. Raveh, M.; Liu, L.; Mandler, D., Electrochemical Co-Deposition of Conductive Polymer-Silica Hybrid Thin Films. *Physical Chemistry Chemical Physics* **2013**, *15*, (26), 10876-10884.
165. Camurlu, P., Polypyrrole Derivatives for Electrochromic Applications. *Rsc Advances* **2014**, *4*, (99), 55832-55845.
166. Cosnier, S.; Holzinger, M., Electrosynthesized Polymers for Biosensing. *Chemical Society Reviews* **2011**, *40*, (5), 2146-2156.

167. Dutta, K.; Kundu, P. P., A Review on Aromatic Conducting Polymers- Based Catalyst Supporting Matrices for Application in Microbial Fuel Cells. *Polymer Reviews* **2014**, 54, (3), 401-435.
168. Li, C.; Bai, H.; Shi, G. Q., Conducting Polymer Nanomaterials: Electrosynthesis and Applications. *Chemical Society Reviews* **2009**, 38, (8), 2397-2409.
169. Novák, P.; Müller, K.; Santhanam, K. S. V.; Haas, O., Electrochemically Active Polymers for Rechargeable Batteries. *Chemical Reviews* **1997**, 97, (1), 207-282.
170. Gangopadhyay, R.; De, A., Conducting Polymer Nanocomposites: A Brief Overview. *Chemistry of Materials* **2000**, 12, (3), 608-622.
171. Jung, Y. J.; Singh, N.; Choi, K. S., Cathodic Deposition of Polypyrrole Enabling the One-Step Assembly of Metal-Polymer Hybrid Electrodes. *Angewandte Chemie-International Edition* **2009**, 48, (44), 8331-8334.
172. Koh, J. Y.; Jung, Y., Nanoscale Morphology Control of Conducting Polymers by Cathodic Polymerization Route. *International Journal of Electrochemical Science* **2013**, 8, (7), 10080-10085.
173. Nam, D.-H.; Kim, M.-J.; Lim, S.-J.; Song, I.-S.; Kwon, H.-S., Single-Step Synthesis of Polypyrrole Nanowires by Cathodic Electropolymerization. *Journal of Materials Chemistry A* **2013**, 1, (27), 8061-8068.
174. Hnida, K. E.; Socha, R. P.; Sulka, G. D., Polypyrrole–Silver Composite Nanowire Arrays by Cathodic Co-Deposition and Their Electrochemical Properties. *The Journal of Physical Chemistry C* **2013**, 117, (38), 19382-19392.
175. Sakai, T.; Alexandridis, P., High-Yield Synthesis of Gold Microplates Using Amphiphilic Block Copolymers: Are Lyotropic Liquid Crystals Required? *Macromolecular Symposia* **2010**, 289, 18-24.
176. Wang, L. Y.; Chen, X.; Chai, Y. C.; Hao, J. C., Controlled Formation of Gold Nanoplates and Nanobelts in Lyotropic Liquid Crystal Phases with Imidazolium Cations. *Colloids and Surfaces a-Physicochemical and Engineering Aspects* **2007**, 293, (1-3), 95-100.
177. Jiang, J. H.; Wang, X. Y., Fabrication of High-Surface Nanoporous Gold Microelectrode. *Electrochemistry Communications* **2012**, 20, 157-159.
178. Dong, H.; Cao, X. D., Nanoporous Gold Thin Film: Fabrication, Structure Evolution, and Electrocatalytic Activity. *Journal of Physical Chemistry C* **2009**, 113, (2), 603-609.
179. Elias, J.; Gizowska, M.; Brodard, P.; Widmer, R.; deHazan, Y.; Graule, T.; Michler, J.; Philippe, L., Electrodeposition of Gold Thin Films with Controlled Morphologies and Their Applications in Electrocatalysis and SERS. *Nanotechnology* **2012**, 23, (25).

## Chapter 2: Characterization Techniques

## 2.1 Introduction

The unique properties of nanoporous materials are dependent of their chemical, physical and structural characteristics. As a result, characterization of the nanoporous materials is of a particular importance not only to determine the nanoporous material properties but also to understand the mechanism behind its formation and to explore possible potential applications. In this regard, the following chapter will provide a brief review on the main characterization techniques used in this research work. The chapter begins with the discussion of cyclic voltammetry, the major electroanalytical technique used in this work to study the electrochemical properties of the prepared nanoporous electrodes and to measure their electrochemically active surface area. Then, the electrochemical technique, chronoamperometry, used in the co-electrodeposition of the nanocomposite and alloys thin films (from them the nanoporous materials were prepared) will be discussed. The electrochemical characterization will be followed by discussion of scanning electron microscopy, the main technique used to investigate the microstructure and surface morphology of the prepared nanoporous structures. X-ray techniques used to determine the bulk and surface chemical composition of the as-prepared nanocomposites, alloys and the corresponding nanoporous films. Surface profilometry technique used to measure the thickness and investigate the surface roughness of the as-prepared nanocomposites and the corresponding nanoporous films will be the close of this chapter.

## 2.2 Electrochemical Techniques

For all the studied systems, preparation of the nanocomposite and alloy films and determination of the electrochemical characteristics of the corresponding nanostructured porous electrodes were carried out with a CHI-1000A multichannel potentiostat in a conventional three-electrode electrochemical cell.

**Voltammetry** is a series of controlled potential electrochemical techniques and it serves at the heart of the modern electroanalytical chemistry.<sup>1, 2</sup> Voltammetry involves measuring the current flowing through an electrochemical cell as a function of the applied potential to the working electrode. The current versus potential curve is called a voltammogram and it provides valuable information about a redox reaction taking place at the working electrode. The history of voltammetry dates back to the twenties of the nineteenth century where a Czech chemist “Jaroslav Heyrovský” invented the first voltammetric techniques named polarography in 1922 for which he awarded the 1959 Nobel Prize in chemistry.<sup>3</sup> Based on the nature of the applied potential function and the working electrode material, different types of voltammetric techniques are distinguished.<sup>1, 2</sup> Among the different types of voltammetric methods, I will focus only on the two techniques used in this work: cyclic voltammetry and chronoamperometry.

Voltammetry experiments are typically undertaken in a three-electrode electrochemical cell, such as that shown in **Figure 2.1**. The electrochemical cell consists of a working/indicator electrode (WE), reference electrode (RE), and counter/auxiliary electrode (CE).

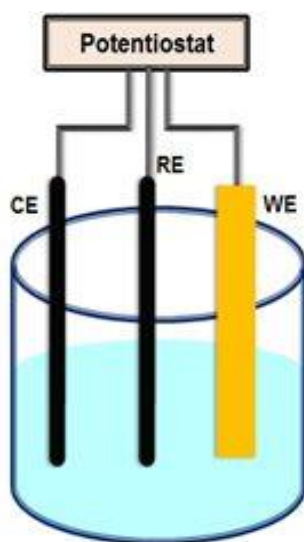


**Figure 2.1.** Three-electrode electrochemical cell



The working electrode should allow electron transfer because on its surface the electrochemical reaction of interested (reduction or oxidation) takes place and it should be inert within the electrochemical reaction potential window (potential range at which the working electrode, supporting electrolyte and solvent are electrochemically inactive) to avoid its oxidation or reduction and to prevent its interaction with the redox species. Usually, working electrodes are constructed from noble metals (e.g. gold or platinum) or conductive carbon materials such as glassy carbon electrodes. Reference electrodes are designed to have a well-known and constant/stable potential such as silver/silver chloride Ag/AgCl electrode and saturated calomel electrode (SCE) Hg/HgCl. The applied potential to the working electrode is determined with respect to the reference electrode. The auxiliary (or counter) electrode is used to avoid current flow through the reference electrode during the voltammetric measurements and to complete the electric circuit where the current flowing between the working electrode and the counter electrode is recorded. An electrochemical reaction opposite to that occurring at the working electrode is taking place at the auxiliary electrode, this is why the two electrodes should be far apart from each other and to avoid any inference with the working electrode reaction. The most common counter electrodes are made from platinum such as Pt wire, Pt mesh and Pt foil electrodes, carbon and gold are other examples of the counter electrodes.

In this work, planar gold, planar platinum, nanoporous gold, and nanoporous platinum electrodes were used as working electrodes. A silver/silver chloride Ag/AgCl wire or frit electrodes (Ag/AgCl (1.0 M KCl)) were used as reference electrodes. The counter electrodes used in this work are platinum wire, platinum mesh and platinum wire coated with polypyrrole electrodes.

### 2.2.1 Cyclic Voltammetry

Cyclic Voltammetry (CV) is a widely used electroanalytical technique to study oxidation-reduction (redox) reactions.<sup>1, 2</sup> The importance of CV measurements originate from their ability to provide not only rapid qualitative and quantitative information about electrochemical systems (e.g. chemical identity, redox potential and concentration of the electroactive species) but also valuable information about the electrochemical reaction mechanism, electron transfer kinetics, thermodynamic parameters and diffusion coefficients of the electroactive species. In the current study, CV was used to measure the electrochemically active surface area of the nanoporous metal electrodes (e.g. Au and Pt) and to study the electrochemical response of the nanoporous electrodes towards  $K_3[Fe(CN)_6]$ , ferrocenemethanol and ascorbic acid before and after exposure to fibrinogen, a common biofouling agent.

Cyclic voltammetry is a reversal sweep technique, so in a typical CV experiment the potential at the working electrode is linearly changed between two potential limits ( $E_{initial}$  and  $E_{final}$ ) in isosceles triangle potential waveform fashion.<sup>1, 2</sup> As can be seen in **Figure 2.2**, the potential of the working electrode is ramped linearly versus time till it reached the set point (end of the forward scan,  $E_{final}$ ) at which the potential sweep is reversed in direction to return back to the initial potential value (end of the backward scan and so the CV cycle,  $E_{initial}$ ). The point at which the potential changed its direction is called the switching potential and it has enough voltage to induce reduction or oxidation of the analyte (species of interest).

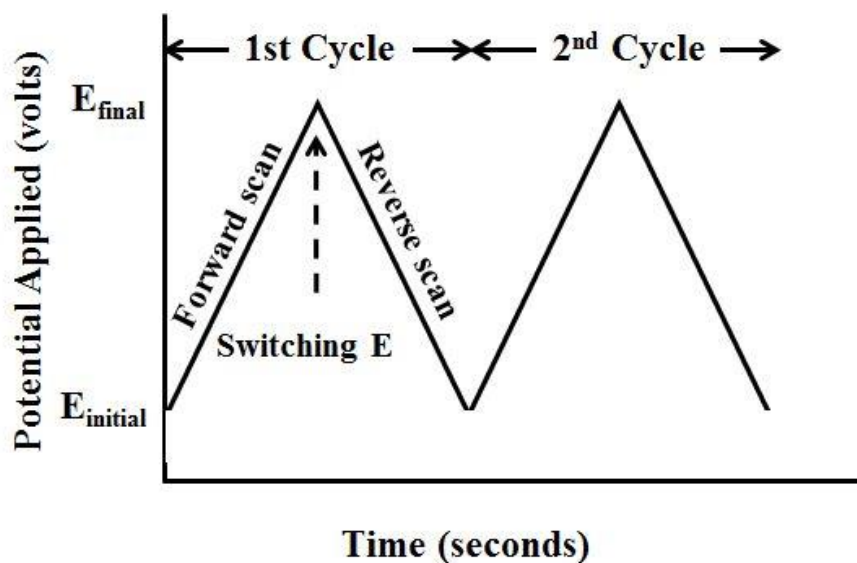


**Figure 2.2.** Potential waveform for cyclic voltammetry. (Adopted from ref. 1).

A typical CV of a reversible redox couple undergoing a single electron redox process, with an oxidized and reduced forms that are stable during the CV experiment, is shown in **Figure 2.3.**

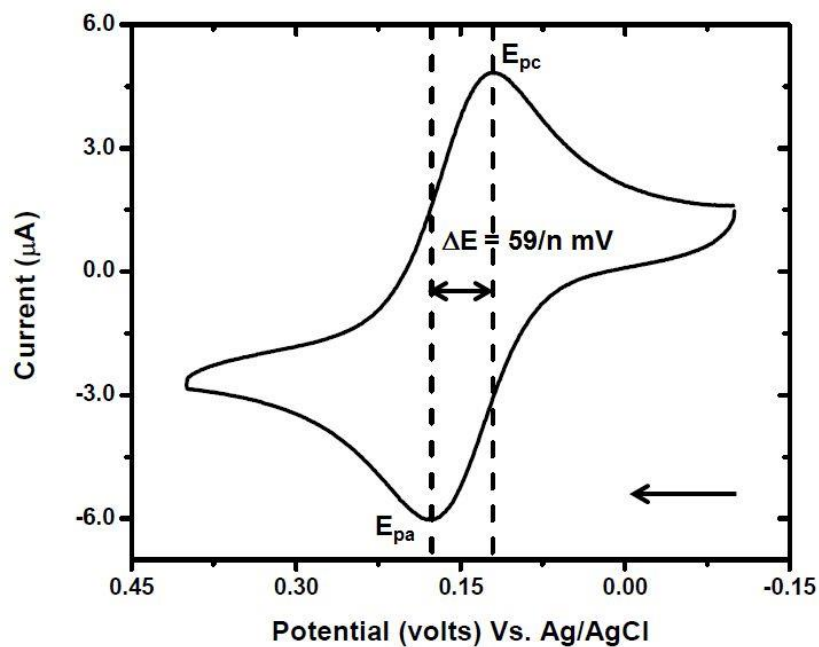


**Figure 2.3.** Typical cyclic voltammogram of a reversible redox couple, 1 mM FcCH<sub>2</sub>OH/ 0.1 M KCl on NPG electrode at 10 mV/s.

For a typical reversible redox couple the initial and the final potentials are identical, the ratio of the cathodic peak current ( $i_{pc}$ ) to the anodic peak current ( $i_{pa}$ ) is one and the peak separation is given by  $\Delta E_p = 59/n$  mV in case of a Nernstian behavior.<sup>1, 2</sup> Although, the peak splitting is independent of the scan rate for electrochemically reversible electrochemical reactions, it depends on the scan rate in case of the quasi-reversible electrochemical reactions which characterized with  $\Delta E > 59/n$  mV. Irreversible electrochemical reactions display only one peak (either oxidation or reduction) where the product of the redox reaction is unstable. An example is the oxidation of ascorbic acid and the electrochemical generation of OH<sup>-</sup> ions.<sup>1, 2</sup>

For a reversible electrochemical reaction, many useful information could be obtained from the CV. For example, the aforementioned peak separation ( $\Delta E_p$ ) can be used to determine the number of the electrons ( $n$ ) that participate in the electrochemical reaction. Also, a  $\Delta E_p$  of  $59/n$  volts implies that the electrochemical reaction follows Nernstian behavior. Under those conditions, the formal potential ( $E^{o'}$ ) of a reversible redox couple can be calculated according to the following relation:<sup>1, 2</sup>

$$E^{o'} = \frac{E_{pa} + E_{pc}}{2} \quad (2.1)$$

The peak current for reversible redox couple at 25 °C is governed by Randles-Sevcik equation:<sup>1, 2</sup>

$$i_p = (2.69 \times 10^5) n^{3/2} A C D^{1/2} v^{1/2} \quad (2.2)$$

where A is the electrode area in cm<sup>2</sup>, C is the molar concentration of the electroactive species, D is the diffusion coefficient in cm<sup>2</sup>/s and v is the scan rate in V/s.

### 2.2.2 Chronoamperometry

Chronoamperometry is another electrochemical technique used in this work to co-electrodeposit metal-metal alloys, metal-silica and polymer-silica nanocomposites. In a typical experiment, the potential of the working electrode is held constant/stepped and the resulting current-time transient is recorded. Ideally, the potential applied at the working electrode is stepped between two values  $E_1$  and  $E_2$  as shown in **Figure 2.4 a**, where  $E_1$  is the initial potential of the electrode and at which no Faradaic reactions occur while  $E_2$  is the potential at which a Faradaic process occurs (oxidation or reduction). Upon the application of  $E_2$  the concentration of the electroactive species at the electrode surface is depleted as a result a concentration gradient is formed and the current decreases with time as we can see in **Figure 2.4 b and c**.

For a reaction in which the mass transport is controlled only by diffusion (stationary planar electrode and unstirred solution), the current decays (current-time relationship) is controlled by Cottrell equation:<sup>1,2</sup>

$$i = \frac{nFAC_0D^{1/2}}{\pi^{1/2} t^{1/2}} \quad (2.3)$$

where  $n$  is the number of electrons involved in the redox reaction,  $F$  is Faraday's constant,  $A$  is the electrode surface area,  $C_0$  is the molar concentration of the electroactive species,  $D$  is the diffusion coefficient and  $t$  is the reaction time. In the present dissertation work, gold-silica nanocomposites prepared at a reaction time between 5 to 30 min, polypyrrole-silica nanocomposites electrodeposited for 30 min, and silver-rich platinum alloys obtained at a deposition time of 10 min.

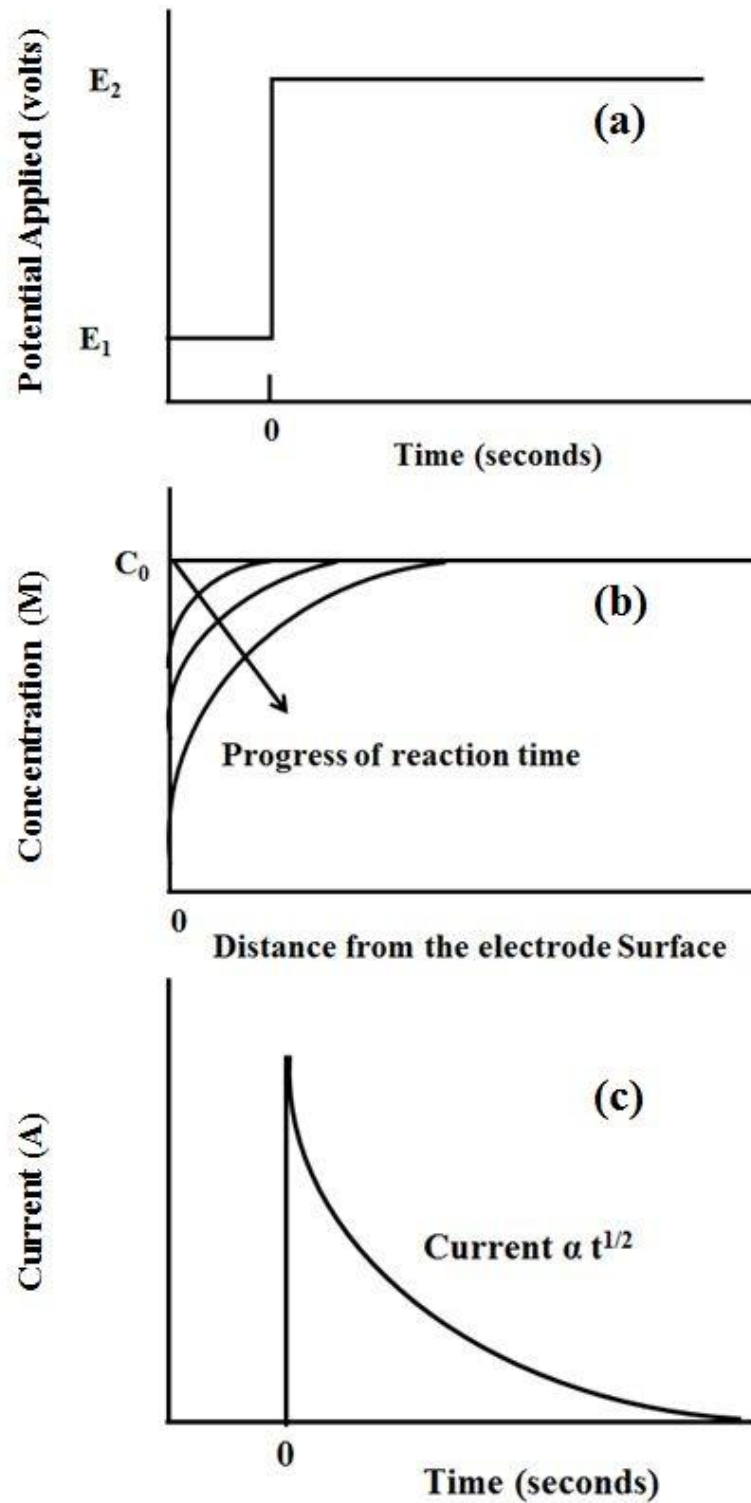


**Figure 2.4.** Typical chronoamperometric potential waveform (a), the corresponding concentration gradient profile as the reaction time proceeds (b) and the resulting current-time response (c). (Adopted from ref. 1).

### 2.3 Scanning Electron Microscopy (SEM)

In general, advanced electron microscopic/imaging techniques are required to study the microstructure, surface morphology and chemical composition of the nanostructured materials in order to determine their properties and potential applications. In this arena, *Scanning Electron Microscopy* (SEM) is a powerful tool to study such interesting characteristics. In the present work field, emission scanning electron microscopes (FE-SEM, HITACHI SU-70) equipped with energy dispersive X-ray spectrometer was used to study the nanoscale features/microstructure and chemical composition of the prepared nanocomposite and alloy materials and the corresponding nanoporous structures.

Ernst Abbe's law and microscope resolution: the resolution limits (e.g. minimum distance at which two structures can be seen as two distinct and separate entities.) of human eye and regular optical microscope are  $\sim 100 \mu\text{m}$  and  $0.2 \mu\text{m}$ , respectively, according to Ernst Abbe's law<sup>4,5</sup> which stated that the resolution limit of a microscope ( $d$ ) is dependent of the wavelength of the imaging radiation ( $\lambda$ ):

$$d = \frac{0.612 \lambda}{NA} \quad (2.4)$$

where  $NA$  is the numerical aperture and it equals " $n \sin \alpha$ " where  $n$  is refraction index of the medium and  $\alpha$  is half aperture angle. In the early 1930s, an electron-beam and focusing electromagnetic condenser lens were introduced to the field of microscopy and in 1931 the first transmission electron microscope (TEM) was invented by Max Knoll and Ernst Ruska in Germany.<sup>4,6</sup> Six years later, in 1937, Manfred Von Ardenne introduced the first scanning electron microscope which became commercially available in 1965 by Cambridge Scientific Instrument Company.<sup>4,6</sup> The resolution limit of the images dramatically enhanced, due to the shorter wavelength of the electron-beam with respect to the light photons, to be 0.1 nm in the

TEM and 1 nm in the SEM. In SEM, the images are produced by a raster scan (point by point scan) similar to that in the TV.<sup>4-7</sup>

It is important to know the modes of matter interactions with the high energy focused electron-beam and the main components of the SEM microscope to better understand how the SEM images are collected. Although bombardment of the sample surface with a focused electron-beam leads to the generation of many signals<sup>4-7</sup> due to the elastic and inelastic interactions of the electron-beam with the sample as can be seen in **Figure 2.5**, only three types of signals will be addressed here.

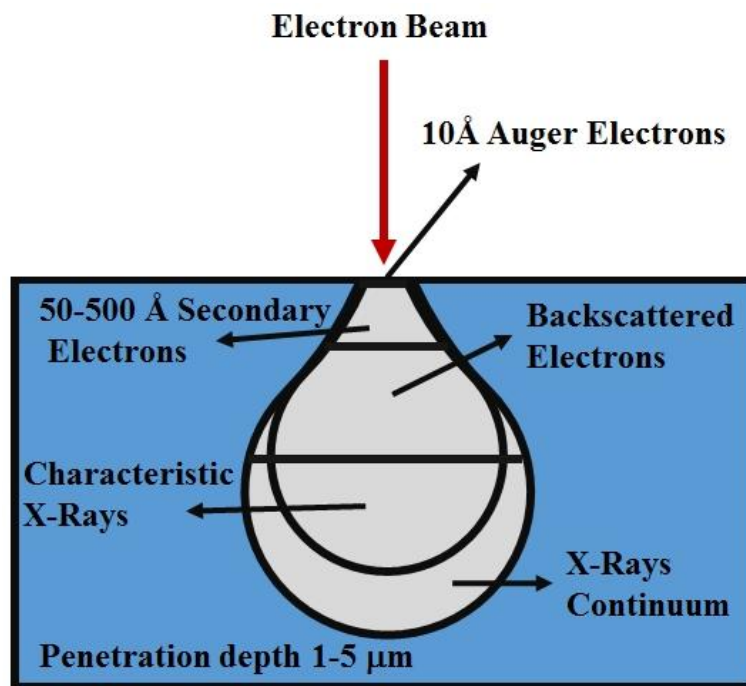


**Figure 2.5.** Illustration of the different signals generated by the electron beam-sample interactions in the scanning electron microscope. (Adopted from ref. 7).

The first type of signal is from the backscattered electrons (BSEs) and they are used to provide SEM images of different color intensities to provide valuable information about the sample composition (number of phases). BSEs are high energy electrons ( $E \geq 50$  eV) produced



from the elastic interaction between incident electron-beam and the electric field of the sample atomic nucleus.<sup>4-6</sup> The number of BSEs is dependent on the chemical nature of the sample elements. An element with a higher atomic number will produce more BSEs than a lighter one due to the presence of more positive charges in its nucleus. The BSEs SEM image shows contrasts in composition where lighter elements appear darker than the heavy ones. The most important type of signals in SEM is the secondary electrons, which are low energy electrons (e.g. 3-5 eV) emitted due to the inelastic interactions between the incident electron-beam and the sample surface electrons. Typically, loosely bound electrons escape within few nanometers from the sample's surface. The secondary electron's SEM image provides important information about the sample surface topography. The third type of signals is the characteristic X-rays photons produced during the inelastic collision between the incident electron-beam and the sample atoms. By analyzing the characteristic X-rays using energy-dispersive X-ray spectroscopy, the elemental composition of the sample can be determined. Usually the SEM instruments are equipped with energy-dispersive X-ray probe.<sup>4-7</sup>

**Figure 2.6** shows the main components of the scanning electron microscope. Electrons are produced by an electron gun (e.g. W-hairpin or LaB<sub>6</sub>) and accelerated to an energy of 0.1-30 keV. The accelerated electron-beam is characterized by a large diameter and cannot produce a high resolution images. Two sets of electromagnetic condenser lenses work in conjunction with the condenser and objective apertures to eliminate the high-angle electrons and focus the electrons beam into a defined spot on the sample surface. The focused electron beam is scanned/swept by a set of coils in a raster fashion. The scanned electron's beam is focused on a specific part of the sample through the objective lens. The produced electrons due to the electron-beam interactions with the sample surface are processed by the detectors.<sup>4-7</sup>

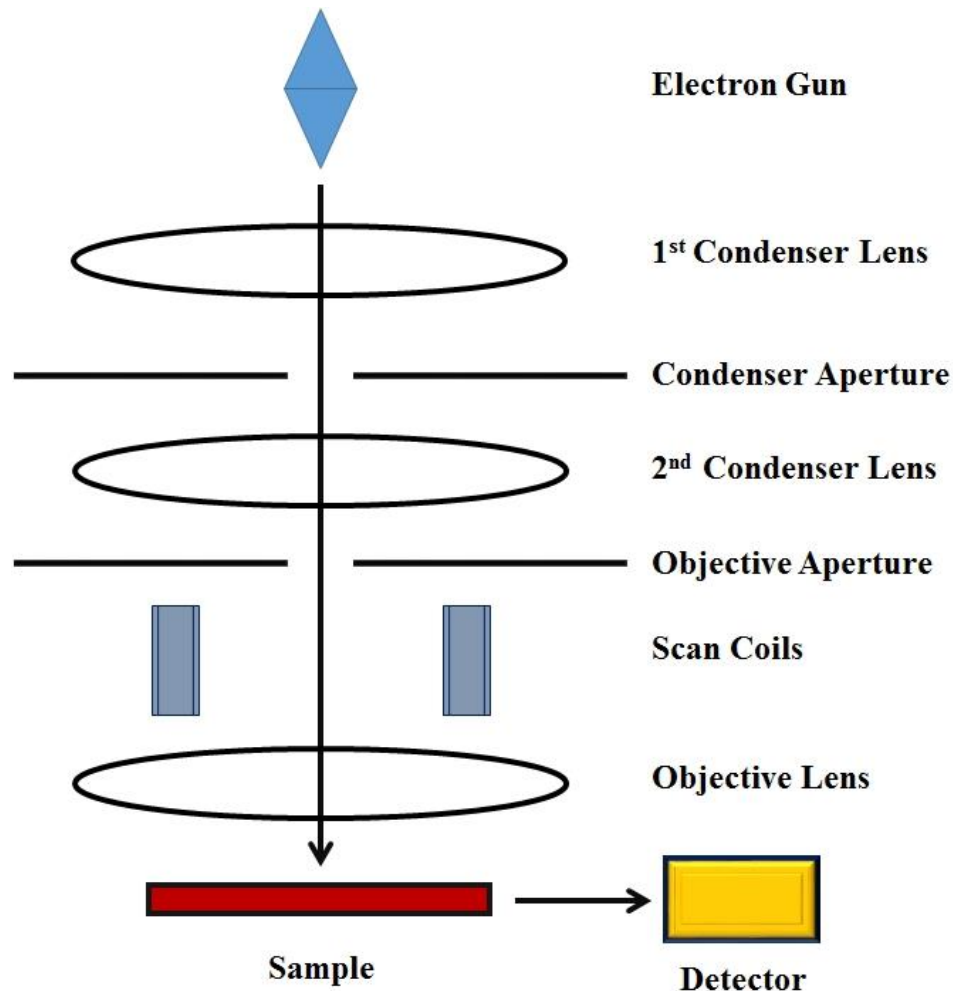


**Figure 2.6.** Schematic illustration of the scanning electron microscope. (Adopted from ref. 6).

## 2.4 Energy-Dispersive X-ray Spectroscopy (EDS)

Although we can obtain some useful information about the sample chemical composition such as number of different phases in the sample and their spatial distribution from the compositional contrast BSEs images, there is still a need to identify those elements and determine their percent composition (atomic or weight %). Elemental analysis of a sample can be done using energy dispersive X-ray spectroscopy (EDS), sometimes called energy dispersive X-ray microanalysis, which is usually integrated into the SEM instrument.<sup>5,8</sup> For the purpose of this

work, EDS was used to determine the elemental composition of the as-prepared thin film and the corresponding nanoporous structures to confirm the success of the newly developed co-electrodeposition strategies and examine the efficiency of the new dealloying/etching techniques used in this work. EDS elemental mapping was used to study the spatial distribution of the different phases in the as-prepared thin films. EDS is based on the fact that each element has a unique atomic structure differs from that of the other elements. As a result each element displays a characteristic X-ray emission spectrum. In EDS the sample is bombarded with a high energy electron-beam then the number and energy of the characteristics X-ray photons emitted are measured and used to determine the elemental composition of the sample.<sup>5, 8</sup>

**Figure 2.7** describes the fundamental basics of the energy-dispersive X-ray spectroscopy (EDS). An electron hole is generated when the incident high energy electron transfers its energy to an inner shell electron. The inner shell electron gets excited and eventually ejected from the atom when the transferred energy from the incident electron-beam is high enough. An inner shell electron hole is formed in the same position where the ejected electron was. Once the inner shell electron hole is created, the atom becomes unstable and an outer shell higher energy electron falls down to fill the hole. The excited atom will restore its stability/ground state by emitting the superfluous energy, which is the energy difference between the higher and lower energy levels, in the form of X-ray photons. The energy of the emitted X-ray is characteristic of the two energy levels from which it is derived and of the atomic number of the sample element. Due to the unique atomic number/structure of each element, different elements in a sample can be identified by analyzing the emitted characteristic X-rays.<sup>5, 8</sup>

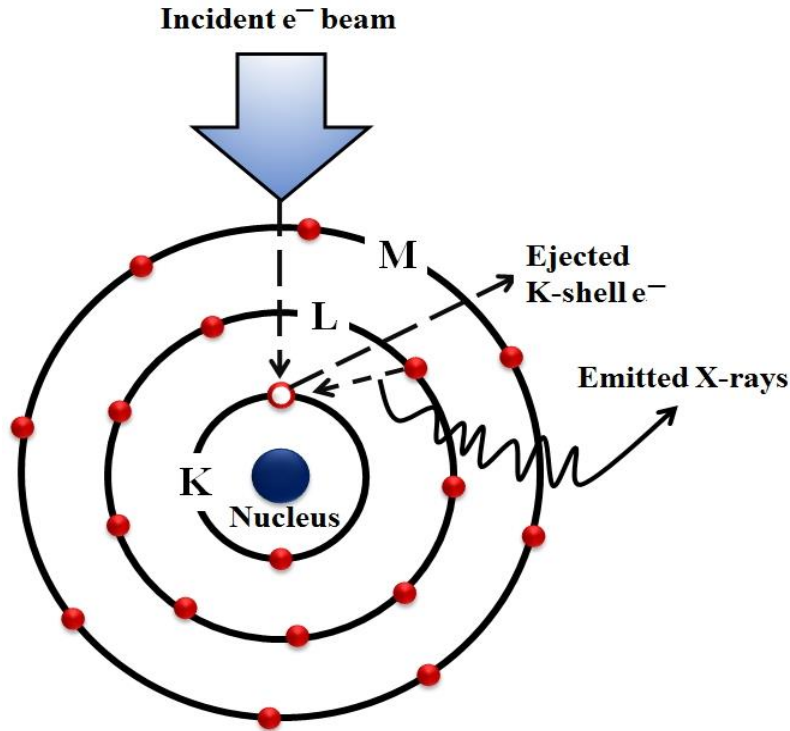


**Figure 2.7.** Schematic representation of the X-ray production through the ejection of an inner-shell electron. (Adopted from ref. 8)

The EDS setup consists of four main parts. First, the excitation source, which is an electron-beam source in case of EDS integrated with TEM or SEM. Second, X-ray detector such as the Si(Li) crystals or the more advanced silicon drift detectors. The Si(Li) crystals detector works at low voltages and needs cooling from a liquid nitrogen dewar while the new silicon drift detector does not need the liquid nitrogen cooling. The energy of the characteristic X-ray is converted into voltage signals by the detector which sends them to a pulse processor. The measured voltage signals by the pulse processor are sent to the data analyzer.<sup>5,8</sup>

## 2.5 X-ray Diffraction (XRD)

X-ray diffraction (XRD) is a rapid, reliable and non-destructive characterization technique that can provide valuable information about a material based on its diffraction pattern when it interacts with an X-ray beam.<sup>9-11</sup> In this work, X-ray diffraction patterns were recorded at room

temperature in  $\theta$ - $2\theta$  geometry by a PANalytical X'Pert Pro MPD series diffractometer equipped with a Pixcel detector and Cu  $K\alpha$  radiation ( $\lambda = 1.54060 \text{ \AA}$ ) at an operating voltage of 45 kV and 40 mA current to determine purity, crystallinity, crystal structure and number of phases (phase identification) in the prepared nanocomposite films and the corresponding nanoporous structures. In other words, XRD was used to examine the efficiency of the newly developed co-electrodeposition and etching strategies. The fundamentals of XRD are based on Bragg's law:

$$n\lambda = 2d \sin\theta \quad (2.5)$$

where  $d$  is the spacing between atom layers/crystal planes,  $n$  is an integer,  $\theta$  and  $\lambda$  are the angle and wavelength of the incident X-ray beam, respectively.<sup>11</sup>

When a beam of monochromatic X-rays bombard a sample, they (X-rays) are partially scattered in all directions due to their interaction with the sample's atoms. Diffraction occurs when the wave length of the incident X-rays beam is close to the spacing between crystal planes (atom layers) in the sample where a series of constructive and destructive interferences take place by the scattered X-rays. This diffraction is governed by Bragg's law and is similar to that obtained when a beam of light diffracted by a grating. An X-ray diffraction peak is obtained when the angle of the incident beam obeys Bragg's law and a constructive interference occurs as shown in **Figure 2.8**. Interference of the diffracted X-rays by out of phase atom layers are destructive and do not produce a peak in the diffraction pattern.<sup>9-11</sup>

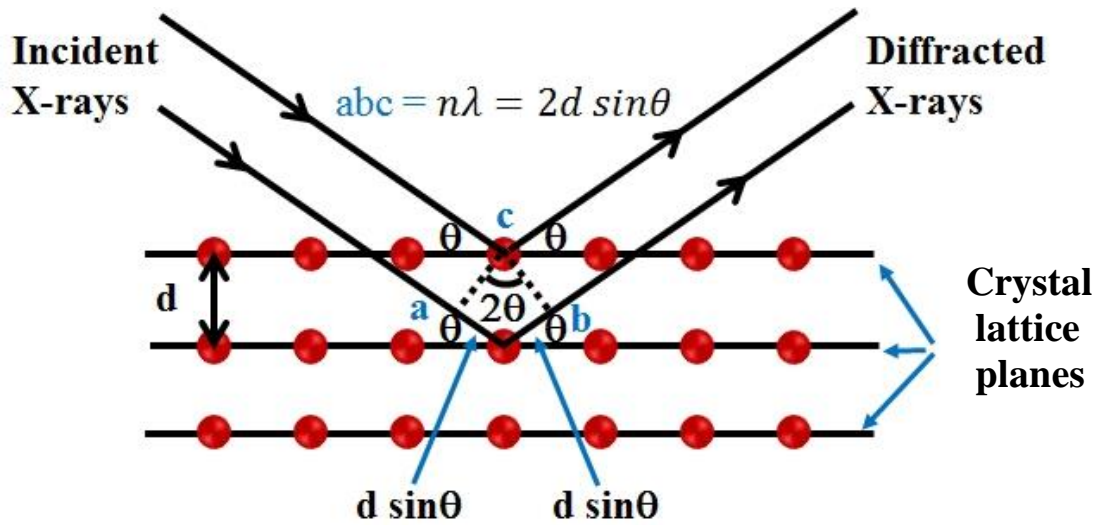


**Figure 2.8.** Graphical representation of Bragg's law for the X-ray diffraction. (Adopted from ref. 11).

In a typical XRD experiment, the angle of the incident monochromatic X-rays beam is systematically changed/scanned in order to detect all possible diffractions from the sample's atom layers. The detected diffractions are processed and counted to construct an XRD diffraction pattern which is a plot of the counts (intensity) versus the detector angle ( $2\theta$ ). The detected diffraction pattern is a reflection of the samples d-spacings and so it is characteristic of the material. Typically, phase identification is carried out by comparing the studied material diffraction pattern with reference standards such as the International Center for Diffraction Data (ICDD) standards and the Joint Committee on Powder Diffraction Standards (JCPDS).

There are three main components in any modern X-ray diffractometer as depicted in **Figure 2.9:** An X-ray tube responsible for the X-ray generation, a sample stage to mount the sample, and a detector for the diffracted X-rays. The X-ray tube consists of metal filament cathode (e.g. W) and metal target anode. The most common metal target anode is copper with  $\text{Cu K}\alpha$  radiation of  $1.5418\text{\AA}$ . Upon the application of high enough voltage the metal filament cathode gets hot and starts bombarding the metal target with electrons. Then X-ray emission occurs using

the same principle previous explained in the EDS. The diffractometer is equipped with goniometer to control the angle on the incident beam. The most common diffractometer is Bragg-Brentano para-focusing diffractometer.

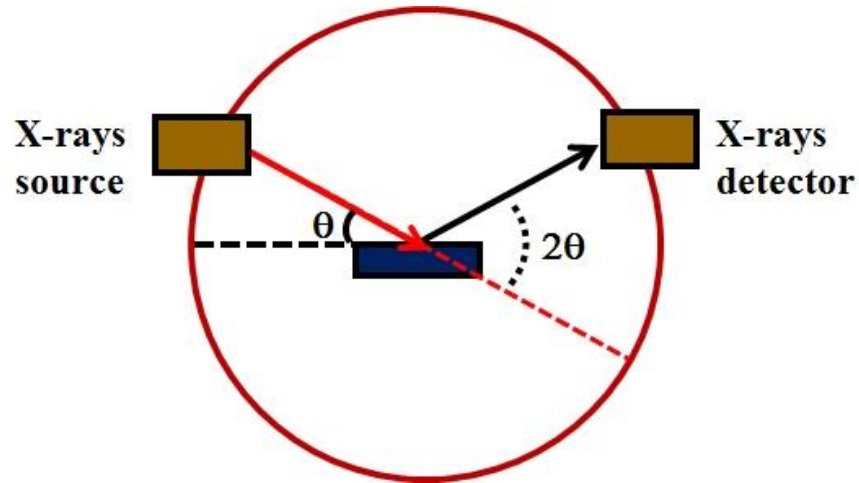


**Figure 2.9.** Schematic representation of the X-ray diffractometer. (Adopted from ref. 11).

## 2.6 X-ray Photoelectron Spectroscopy (XPS)

X-ray photoelectron spectroscopy (XPS) is a non-destructive highly surface-sensitive spectroscopic technique that can provides quantitative and qualitative information about the surface chemistry of a sample. Typically, valuable information such as elemental composition, electronic and chemical states can be obtained for the elements that exist in the top surface layers of the sample (2-10 nm).<sup>12-14</sup> Nowadays, XPS is considered the most widely used technique to study the surface chemistry of any material. In the present work, X-ray photoelectron spectroscopy analysis was performed on a ThermoFisher ESCALAB 250 imaging X-ray photoelectron spectrometer using monochromatic Al  $K_{\alpha}$  (1486.68 eV) X-ray source equipped with a hemispherical analyzer to determine the oxidation states and surface composition of the as-prepared nanoporous metal electrodes. An internal flood gun (2 eV electrons) and a low-

energy Ar+ external flood gun were used for charge compensation during the data collection. The spectra were corrected using the aliphatic hydrocarbon C 1s peak at 284.6 eV as a base. For XPS data analysis and peak fitting Thermo Scientific AdvantageXPS 4.40 and CasaXPS 2.3.16 programs were used.

XPS is based on the photoelectric effect, discovered by Heinrich Rudolf Hertz in 1887 and explained by Albert Einstein in 1905.<sup>12-14</sup> About fifty years later, the first high resolution XPS spectrum was obtained by K. Siegbahn's research group in 1954. K. Siegbahn is a physicist from Uppsala University in Sweden and he is the laureate of the 1981 Nobel Prize in Physics for his potential contributions in the development of the XPS or what he named ESCA "electron spectroscopy for chemical analysis".<sup>12-14</sup> In 1969 he collaborated with Hewlett-Packard company in the USA to build the first commercial monochromatic XPS instrument.<sup>12-14</sup>

XPS works in ultrahigh vacuum environment where a photoelectron (core/inner-shell electron) is generated when a monochromatic soft X-ray with an energy  $h\nu$  that is greater than the binding energy of the core electron illuminates the sample surface as displayed in **Figure 2.7**. The kinetic energy ( $E_{kinetic}$ ) of the escaped photoelectrons is calculated in XPS using a concentric hemispherical electron energy analyser (CHA).<sup>12-14</sup> The binding energy ( $E_{binding}$ ) of the emitted photoelectron/core electron can be calculated from the known energy of the incident monochromatic X-ray (e.g.  $E_{photon}$  for Al  $K_{\alpha}$  X-ray is 1486.7 eV) and the measured  $E_{kinetic}$  of the emitted core-electron by using Einstein and Ernest Rutherford relationships:

$$E_{photon} = h\nu \quad (2.6)$$

$$E_{binding} = E_{photon} - E_{kinetic} - \Phi \quad (2.7)$$

where  $\Phi$  is the work function of the CHA and  $E_{binding}$  is characteristic of the element from which it originated.<sup>12-14</sup> The XPS spectrum is a representation of intensity (number of counts) of the



emitted photoelectrons as a function of their binding energy. For an element, the peak shape and position are reflections of its chemical state while the peak area normalized by appropriate sensitivity factor gives the element percent composition with parts per thousand (0.1 at %) detection limit. In order to determine the peak position with high accuracy, it is recommended to use charge referencing material to compensate any charge induced shift. The C (1s) XPS peak located at 284.6 eV is the most widely used charge correction reference.<sup>12-14</sup>

**Figure 2.10** shows the main components of the XPS instrument: (a) X-ray source such as Al  $K_{\alpha}$  (1486.6eV) and Mg  $K_{\alpha}$  (1253.6eV) (b) ultrahigh vacuum environment and (c) electron energy analyzer.<sup>12-14</sup>

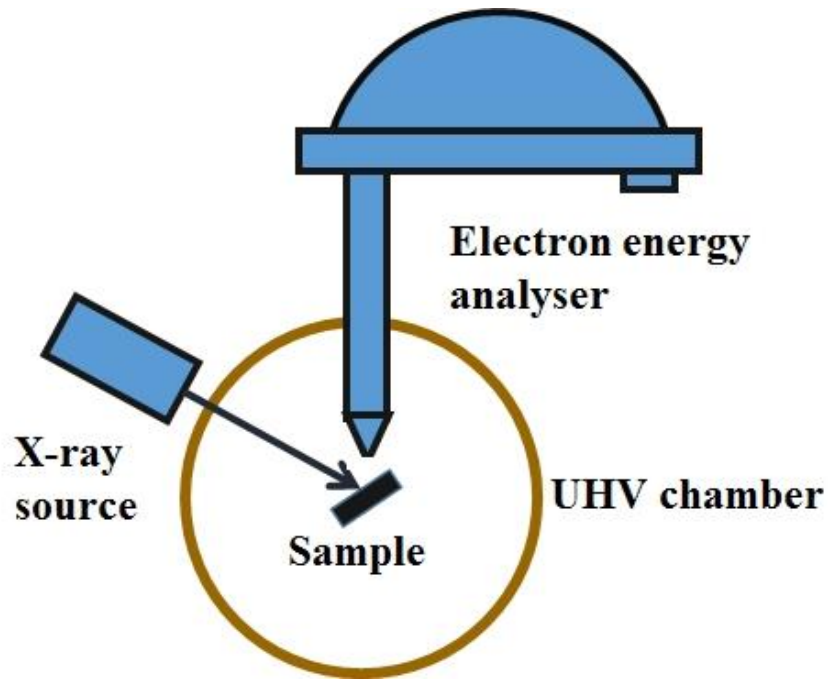


**Figure 2.10.** Graphical representation of the main components of the XPS system. (Adopted from ref. 13)

## 2.7 Contact Surface Profilometry Analysis

In order to study and quantify the surface roughness and measure the thickness of the as-prepared thin films, contact/stylus-based surface profilometry measurements were conducted on a sharp edge of the target films. For all the thickness and roughness measurements, a stylus-based surface profilometer (Surface Profiler, KLA-Tencor Co., San Jose, CA) was used to collect the surface profiles as depicted in **Figure 2.11**. The contact profilometer is equipped with a fine-tip diamond stylus that moves for a specific distance across the film and with a specific contact force to record the sample surface profile, where there is a linear relationship between the stylus vertical displacement and the roughness (height variations) of the surface.<sup>15</sup> A standard diamond stylus with 5  $\mu\text{m}$  radius was used in the present work. Typically, surface features with height ranged from 10 nm to 1.0 mm can be measured.<sup>15</sup>

The contact surface profilometry is inexpensive, easy to implement and an acceptable standard by most of the world's surface finish manufacturers. Being in contact with the surface is advantageous for many reasons. First, the measurement is not sensitive to surface color, reflectance or contaminants, which enables studies to be performed on variety of substrates even in dirty environments. Second, the measurement is direct and no modeling is required to construct the surface profile of a sample. Furthermore, it has a better resolution than the white-light optical profilometer.

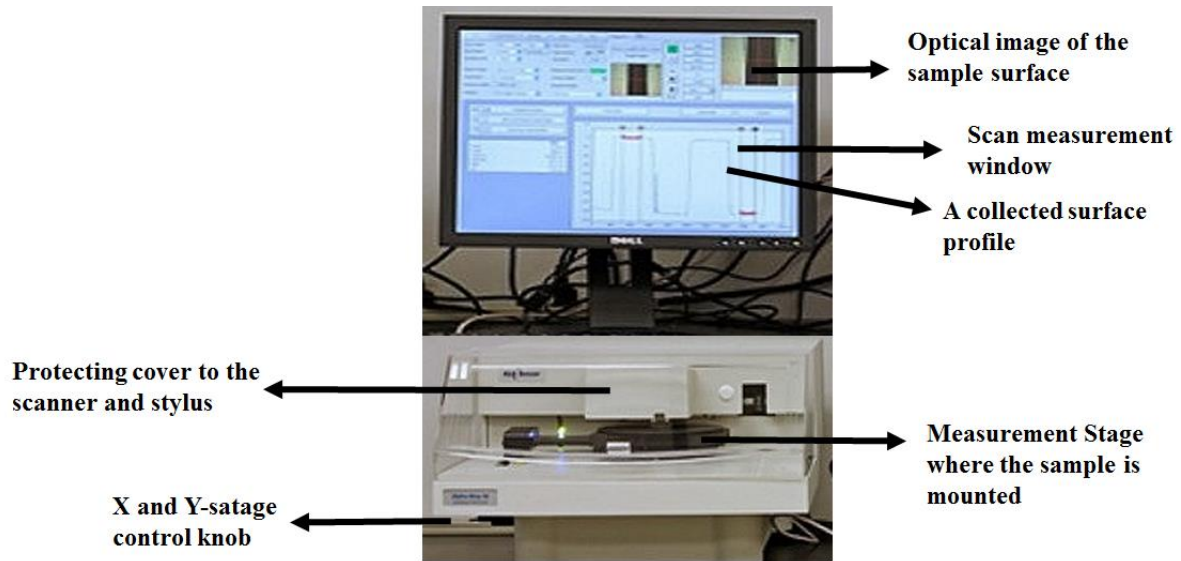


**Figure 2.11.** Photograph of the KLA-Tencor Alpha-Step IQ surface profiler.

## 2.8 References

1. Wang, J., *Analytical Electrochemistry*. Wiley-VCH: 2000.
2. Bard, A. J.; Faulkner, L. R., *Electrochemical Methods: Fundamentals and Applications*. Wiley: 1980.
3. Barek, J.; Zima, J., Eighty Years of Polarography—History and Future. *Electroanalysis* **2003**, 15, (5-6), 467-472.
4. Wells, O. C.; Boyde, A.; Lifshin, E.; Rezanowich, A., *Scanning Electron Microscopy*. McGraw-Hill: 1974.
5. Bai, C., *Scanning Tunneling Microscopy and its Application*. Springer Science & Business Media: 2000; Vol. 32.
6. Zhou, W.; Wang, Z. L., *Scanning Microscopy for Nanotechnology: Techniques and Applications*. Springer science & business media: 2007.
7. Sivasankar, B., *Instrumental Methods of Analysis*. Oxford University Press: 2012.
8. Bell, D.; Garratt-Reed, A., *Energy Dispersive X-ray Analysis in the Electron Microscope*. Garland Science: 2003; Vol. 49.
9. Skoog, D. A.; West, D. M., *Principles of Instrumental Analysis*. Saunders College Philadelphia: 1980; Vol. 158.
10. Dann, S. E., *Reactions and Characterization of Solids*. Royal Society of Chemistry: 2000; Vol. 2.
11. Pecharsky, V. K.; Zavalij, P. Y., *Fundamentals of Powder Diffraction and Structural Characterization of Materials*. Springer: 2009; Vol. 69.
12. Tilinin, I. S.; Jablonski, A.; Werner, W., Quantitative Surface Analysis by Auger and X-ray Photoelectron Spectroscopy. *Progress in surface science* **1996**, 52, (4), 193-335.
13. Watts, J. F.; Wolstenholme, J., An introduction to surface analysis by XPS and AES. *An Introduction to Surface Analysis by XPS and AES, by John F. Watts, John Wolstenholme, pp. 224. ISBN 0-470-84713-1. Wiley-VCH, May 2003.* **2003**, 1.
14. Crist, B. V., *Handbook of Monochromatic XPS Spectra, 3 Volume* 2000.
15. Schmit, J.; Creath, K.; Wyant, J., Surface Profilers, Multiple Wavelength, and White Light Interferometry. *Optical Shop Testing* **2007**, 667755.

## **Chapter 3: Fabrication of Nanostructured Porous Gold**

### 3.1. Introduction

This chapter is reprinted with permission from reference 1. Copyright 2014 American Chemical Society.<sup>1</sup> Electrochemical deposition is an attractive and versatile approach to prepare metal and/or metal oxides films and nanostructures on substrates of varying geometry and size, both patterned and unpatterned.<sup>2-5</sup> Advantages include low cost, simplicity, and ability to tailor the properties of the material such as its composition, thickness, and porosity through variations in process parameters such as time, potential, and concentration. Metal electrodeposition can take place at the electrode/solution interface by a number of different routes including the direct reduction of a metal ion/metal ion complex and/or via electrogeneration of base leading to deposition.<sup>3</sup> A known example of the former is the three-electron reduction of  $\text{AuCl}_4^-$  to metallic gold whereas an example of the latter is the precipitation of nickel hydroxide on the electrode surface via the electrogeneration of  $\text{OH}^-$  in a nickel nitrate solution.<sup>3</sup>

Metal oxide films can also be formed from sol-gel monomers through electrochemically assisted precipitation<sup>6-8</sup> or via electrogeneration of  $\text{OH}^-$ .<sup>9</sup> In the latter case, the production of  $\text{OH}^-$  at the electrode surface hydrolyzes and/or condenses the monomeric precursors near the electrode surface leading to the formation of a relatively porous film.<sup>9-15</sup> The electroassisted sol-gel route, in particular, has opened up new avenues for the formation of porous silica structures on a variety of different substrates that couldn't otherwise be made using conventional spin coating or dip coating techniques including patterned surfaces and printed circuits.<sup>16-18</sup> Furthermore, when combined with electrochemical reduction of easily reducible metal salts, the

electroassisted sol-gel route provides a unique and powerful approach to fabricate metal-metal oxide nanocomposites.<sup>19</sup> Such nanocomposites are interesting and valuable materials because their physical and chemical properties are different than those of the pure components, often enhancing the capabilities of the material allowing new potential applications to be pursued.<sup>20</sup> Examples of reported work include the formation of gold nanoparticle-SiO<sub>2</sub>,<sup>21</sup> Au/SiO<sub>2</sub> nanoparticles,<sup>22</sup> Cu-SiO<sub>2</sub>,<sup>19, 20</sup> Cu-TiO<sub>2</sub>,<sup>23</sup> Ni-SiO<sub>2</sub>,<sup>24</sup> Zn-SiO<sub>2</sub><sup>25</sup> composite films and most recently TiO<sub>2</sub>-SiO<sub>2</sub><sup>26</sup> and polymer-SiO<sub>2</sub> composite films<sup>27</sup>.

What is unique about these nanocomposite films is that they can be prepared in a single step from two independent redox reactions occurring at or near the same point in time utilizing a very simple, low cost electrochemical technique.<sup>19, 24</sup> The chemical and physical properties can be tailored by varying the ratio of precursors and electrodeposition parameters, and furthermore, the method can be extended to conductive supports of varying types and dimensions.<sup>19</sup> Surprisingly, however, only limited attention has been given to the formation of metal/sol-gel derived nanocomposite coatings using this novel co-electrodeposition approach.<sup>19-25</sup>

In this work, we report the co-electrodeposition of gold/sol-gel nanocomposite thin films and introduce a novel, robust and reliable strategy for the fabrication of high surface area - nanostructured porous gold (NSPG) frameworks from these nanocomposites. The as-prepared Au-SiO<sub>2</sub> films possess an interconnected three-dimensional porous framework with different silica – gold ratios depending on the deposition solutions and parameters. By treating these nanocomposite materials as heterogeneous alloys, one component (e.g., silica) can be selectively

removed from the film to produce high surface area conductive materials with a coral-like open porous nanostructure. The surface area, morphology and the thickness of these nanostructured gold thin films can be fine-tuned via variations in the deposition potential, deposition time, sol-gel monomer concentration and gold ion concentration. High surface area nanostructured electrodes have attracted considerable interest in the field of analytical and materials chemistry where these conductive 3D porous frameworks can give rise to increased sensitivity, lower detection limits, and better signal-to-noise ratios compared to unmodified planar electrodes.<sup>28-35</sup> The work described herein presents a simple, cost-effective strategy for making such materials from an electrodeposited metal-metal oxide porous nanocomposite.

## **3.2. Experimental Section**

### **3.2.1. Reagents and Materials**

Potassium tetrachloroaurate (III) ( $\text{KAuCl}_4$ , 98%), tetramethoxysilane (TMOS, 99%), potassium chloride (KCl), hydrofluoric acid (HF, 48-50 w/w%), and absolute ethyl alcohol (EtOH, 200 proof, ACS/USP grade) were purchased and used as received. Ultrapure type-I water was obtained using a Millipore Milli-Q purification system. Gold-coated glass slides with a 5 nm-titanium adhesion layer were obtained from EMF, Ithaca NY.

### **3.2.2. Co-Electrodeposition of Gold/Sol-Gel ( $\text{Au-SiO}_2$ ) Nanocomposite Thin Films**

Gold-coated slides were cut to produce rectangular electrodes of 1 x 2.5 cm. The electrodes were cleaned by successive sonication in ethanol and water, three times, and then dried at room temperature, flushed with nitrogen and plasma cleaned (PE2000 RF Plasma Etcher, South Bay



Technology) at 30 W, DC bias of -280 V and 150 mtorr for 3 min. An electrode area of 0.32 cm<sup>2</sup> was defined by a ¼ in. circle in a piece of UHMW Polyethylene tape (CS Hyde) placed over the surface of the gold-coated slide. The co-electrodeposition of Au-SiO<sub>2</sub> nanocomposite thin films was carried out in a standard three-electrode electrochemical cell in the absence of stirring. The reference electrode was a silver chloride-coated silver wire (Ag/AgCl) while a platinum wire was utilized as a counter electrode. Different silica sols were prepared by stirring the assigned amounts of absolute ethanol (2.45 to 2.1 mL), sol-gel monomer (TMOS, 0.05 to 0.4 mL), and KCl (supporting electrolyte, 2.5 mL) at 400 rpm (via a Magstir genie magnetic stirrer) for 50 min. The multicomponent electroplating solution was prepared by mixing the prehydrolyzed silica sol with the desired amount KAuCl<sub>4</sub> (5-40 mg) at 400 rpm for 25 min. In all the experiments, the concentration of KCl and the volume of the electroplating solution were kept constants at 0.2 M and 5 mL, respectively.

The co-electrodeposition of Au-SiO<sub>2</sub> nanocomposite films was conducted under an amperometric mode by a CHI 1000A potentiostat. Negative potentials (-0.6, -0.8, -1.0 and -1.2 volts) were applied for a specific period of time (5, 10, 15, 20, 25 and 30 min) to produce four sets of Au-SiO<sub>2</sub> nanocomposite films. As soon as electrodeposition was complete, the as-prepared thin films were promptly removed from the electroplating solution and washed with deionized water three times and then slowly and gently dried to avoid cracking of the films for 12 hrs. For comparison, electrodeposited planar gold films were obtained by following the same methodology but in the absence of the sol-gel monomer (TMOS) at -0.8 volts for 15 min.

### 3.2.3. Fabrication of Coral-Like Nanostructured Porous Gold (NSPG) Thin Films

Dissolution of silica in the as-prepared Au-SiO<sub>2</sub> nanocomposite thin films was achieved by chemical etching in hydrofluoric acid (Caution: HF is an extremely hazardous and highly corrosive material. A fume hood, protective clothing, goggles and gloves must be used). The etching strategy consisted of four stages: wetting by immersing the films in deionized water for 5 min followed by gentle etching in a 0.5 % HF solution for 5 min, additional etching in 2.5 % HF for 5 min to completely remove the silica, followed by washing with deionized water (2X) and drying in air.

### 3.2.4. Characterization

The crystal structure and chemical composition of the etched and non-etched nanostructured porous films were examined by X-ray diffraction (XRD) on the powdered samples removed from the gold-coated substrates. Multiple films prepared under the same conditions were collected and used in the XRD measurements. The XRD data was acquired at room temperature by X'Pert Philips Materials Research diffractometer with an operating voltage and current of 45 kV and 40 mA, respectively, using Cu K<sub>α</sub> radiation ( $\lambda = 1.54060 \text{ \AA}$ ) in  $\theta$ - $2\theta$  geometry. Crystal phase identification was conducted using X'Pert Highscore Plus software, which utilized the ICDD/ JCPDS database. The surface morphology and bulk composition of the co-electrodeposited nanocomposite films were investigated before and after the etching process using a field-emission scanning electron microscope (FE-SEM, HITACHI SU-70) equipped with Energy dispersive X-ray spectroscopy (EDS). In order to avoid charging effects, the non-etched

films were sputter coated with a thin layer of platinum prior to the SEM imaging. X-ray photoelectron spectroscopy (XPS) analysis was performed on a ThermoFisher ESCALAB 250 imaging X-ray photoelectron spectrometer using monochromatic Al K $\alpha$  (1486.68 eV) X-ray source equipped with a hemispherical analyzer. An internal flood gun (2 eV) and a low-energy Ar<sup>+</sup> external flood gun were used for charge compensation during the data collection. The spectra were corrected using the C1s peak at 284.6 eV. For XPS data analysis and peak fitting, CasaXPS 2.3.16 was used. The thickness and roughness of the Au-SiO<sub>2</sub> nanocomposite and coral-like NSPG films was measured by a surface profilometer (Alpha-Step IQ Surface Profiler, KLA-Tencor Co., San Jose, CA) from sharp edges on scratched films. The electrochemically active surface area of the coral-like NSPG electrodes was determined via cyclic voltammetry (CV) using a Ag/AgCl (1 M KCl) reference electrode and a Pt wire auxiliary electrode.

### **3.3. Results and Discussion**

#### **3.3.1. Sol-Gel (Au-SiO<sub>2</sub>) Nanocomposite Films**

A graphical representation of the strategy used to fabricate Au-SiO<sub>2</sub> nanocomposite films and the coral-like NSPG electrodes is shown in **Figure 3.1**. The fabrication strategy is a combination of sol-gel chemistry and electroassisted codeposition<sup>19</sup> and is explained as follow:

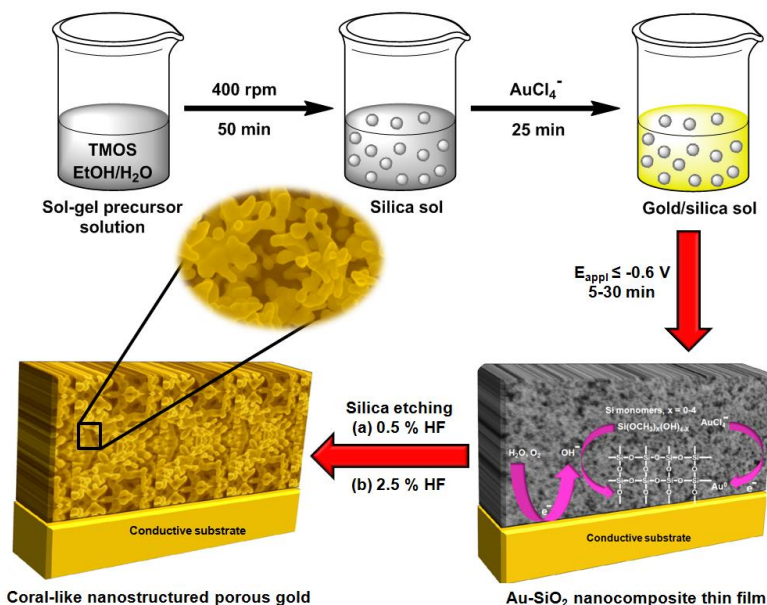


**Figure 3.1.** Schematic illustration (not drawn to scale) of the fabrication of Au-SiO<sub>2</sub> nanocomposite films and coral-like nanostructured porous gold (NSPG) through the electroassisted deposition of silica from a partially hydrolyzed silica sol and the concurrent reduction of gold ions. Reprinted with permission from reference 1. Copyright 2014 American Chemical Society.

hydrolysis of the sol-gel monomer (TMOS) takes place by stirring at 400 rpm using a digital magnetic stir plate for 50 min to produce the silica sol. The two-component electroplating solution was obtained upon addition of the gold precursor (KAuCl<sub>4</sub>) to the silica sol. The color of the solution turned yellow indicative of the formation of a gold/silica sol. Application of potentials in the range of -0.6 to -1.2 volts to the electrode surface increased the pH of the solution through the electrogeneration of OH<sup>-</sup> at the electrode/electrolyte interface from the reduction of oxygen and/or solvent (H<sub>2</sub>O in EtOH/H<sub>2</sub>O system).<sup>10</sup> Previous work estimates the pH at the interface to be ~ 8.5.<sup>10, 12</sup>



The electrogenerated  $\text{OH}^-$  catalyzes the polycondensation of the silica monomers and so the polymerization of the hydrolyzed sol-gel monomer takes place in the vicinity of the electrode surface leading to the deposition of silica.<sup>10-13</sup> Concurrently, the gold ions were electrochemically reduced to form metallic gold.<sup>36</sup>



As the co-electrochemical deposition proceeds, the color of the entire conductive substrate surface changes from golden yellow to brown and the degree of the brownish color increases as the reaction time grows. At more negative potentials, the color transformation occurs faster, and a similar effect has been observed at higher gold ion concentrations. Upon drying, the color of the Au-SiO<sub>2</sub> nanocomposite film turns grey to white depending on the deposition conditions. The color changes observed during the thin film formation are indicative of the co-electrodeposition of Au-SiO<sub>2</sub> nanocomposite films where an electrodeposited silica film is characterized by a white appearance.<sup>18</sup> Upon removal of silica (see below), the film becomes brown consistent with the presence of gold. The coverage of the entire substrate surface with a continuous nanocomposite film implies that the gold deposition occurs through the porous structure of the hard template.

**Figure 3.2 (a, b, c)** depicts SEM images of a representative as-prepared Au-SiO<sub>2</sub> nanocomposite film formed at -0.8 volts for 15 min. The microstructure of the as-prepared Au-SiO<sub>2</sub> films is rough consisting of aggregates of colloidal particles/clusters that extended over the

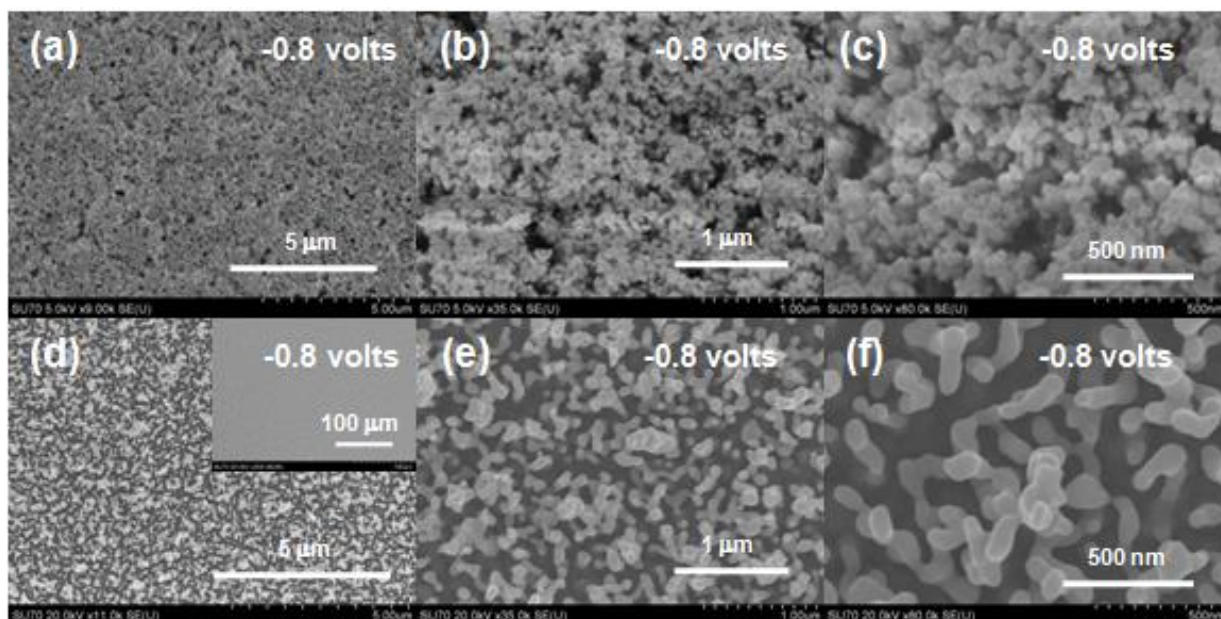


**Figure 3.2.** SEM images of the as-prepared Au-SiO<sub>2</sub> nanocomposite films (a, b, and c) electrodeposited at -0.8 volts for 15 min from a solution containing KAuCl<sub>4</sub> (5.29 mM) and TMOS (0.14 mM) and the coral-like NSPG (d, e and f) after etching in HF. The inset in (d) is a low magnification of SEM image of a crack-free NSPG film. Reprinted with permission from reference 1. Copyright 2014 American Chemical Society.

entire surface of the conductive substrate. These aggregates are linked together to produce an interconnected three-dimensional porous framework. The morphological features displayed in the microstructure of the nanocomposites are similar to that of silica films prepared under base-catalyzed polycondensation of the sol-gel monomers,<sup>10, 13, 18 15</sup> metal foams,<sup>37</sup> or a silica xerogel monolith.<sup>38-40</sup> As a result, the Au-SiO<sub>2</sub> nanocomposites are ‘porous’ like an electrodeposited sol-

gel film<sup>10, 13, 15, 18</sup> but unlike an electrodeposited gold film (which is rough, and not porous, as shown in **Figure 3.3**.

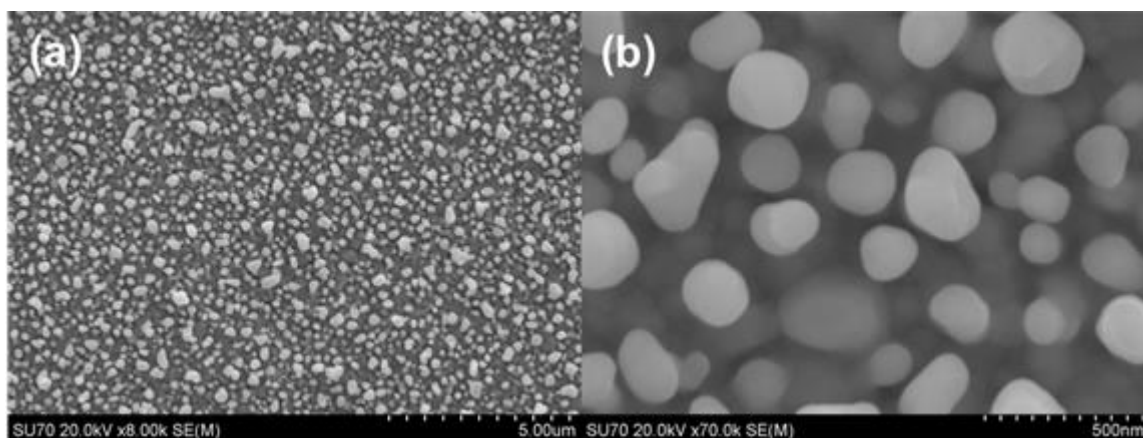


**Figure 3.3.** SEM images of a planar gold film electrodeposited at -0.8 volts for 15 min in 5.29 mM KAuCl<sub>4</sub>. Scale bars are 5 mm and 500 nm for (a) and (b), respectively. Reprinted with permission from reference 1. Copyright 2014 American Chemical Society.

Changes in the applied potential and/or deposition time leads to distinct changes in the microstructure, thickness, and color of the electrodeposited nanocomposite. At more negative potentials and long deposition, the films are whiter in color consistent with a higher content of silica whereas at a very short deposition time (e.g., 5 min) the films are grey. The surface roughness and film thickness of the as-prepared nanocomposite films were further verified using surface profilometry. The collected surface profiles displayed in **Figure 3.4** and **Figure 3.5**, are characterized by the presence of large spikes/oscillations indicative of a very rough surface, and further supporting the colloidal nature of the Au-SiO<sub>2</sub> nanocomposite films evident in the SEM

images. The average height of the oscillations significantly increases as the applied potential becomes more negative, **Figure 3.5**. This is not unexpected because of the rapid increase in the production of hydroxide ions that leads to the formation of colloidal-like silica.<sup>10, 13, 18</sup> The as-prepared Au-SiO<sub>2</sub> films are also relatively thick, ranging from 8 to 15 μm depending on the applied potential and deposition time. Concurrent with this increase in roughness and film

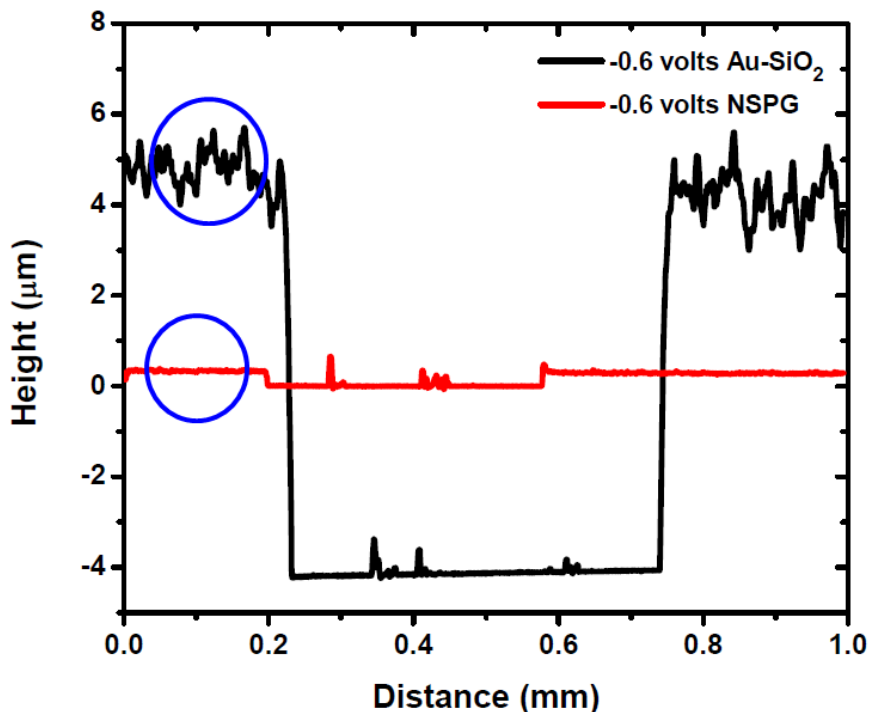


**Figure 3.4.** Surface profiles of an as-prepared Au-SiO<sub>2</sub> nanocomposite film and coral-like NSPG obtained after etching in HF. Electrodeposition potential = -0.6 volts for 15 min. [KAuCl<sub>4</sub>] = 5.29 mM; [TMOS] = 0.14 M. The films were scratched to create sharp edges. The blue circles display the decrease in the surface roughness after etching in HF. Reprinted with permission from reference 1. Copyright 2014 American Chemical Society.



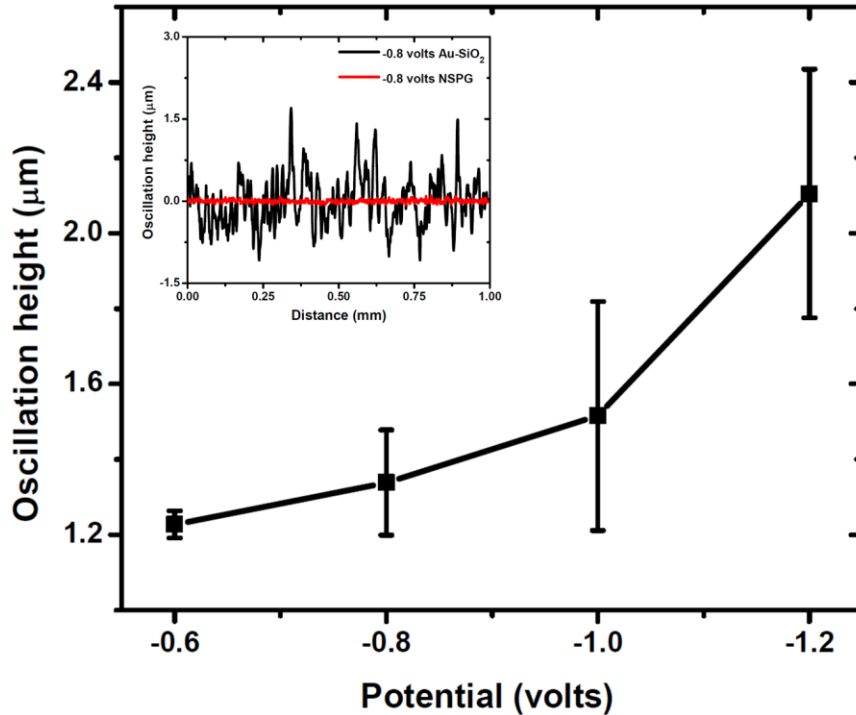


**Figure 3.5.** The average height of the oscillations (surface roughness indicator) recorded from the surface profiles acquired on Au-SiO<sub>2</sub> nanocomposite films electrodeposited at different potentials for 15 min. Inset is a surface profile of an as-prepared Au-SiO<sub>2</sub> nanocomposite film at -0.8 volts for 15 min and after etching (NSPG). [KAuCl<sub>4</sub>] = 5.29 mM; [TMOS] = 0.14 M. Reprinted with permission from reference 1. Copyright 2014 American Chemical Society.

thickness is an increase in the amount of silica (Si and O) relative to Au as reported by SEM-EDX, **Figure 3.6**, upon application of an increasing negative potential and/or deposition time.

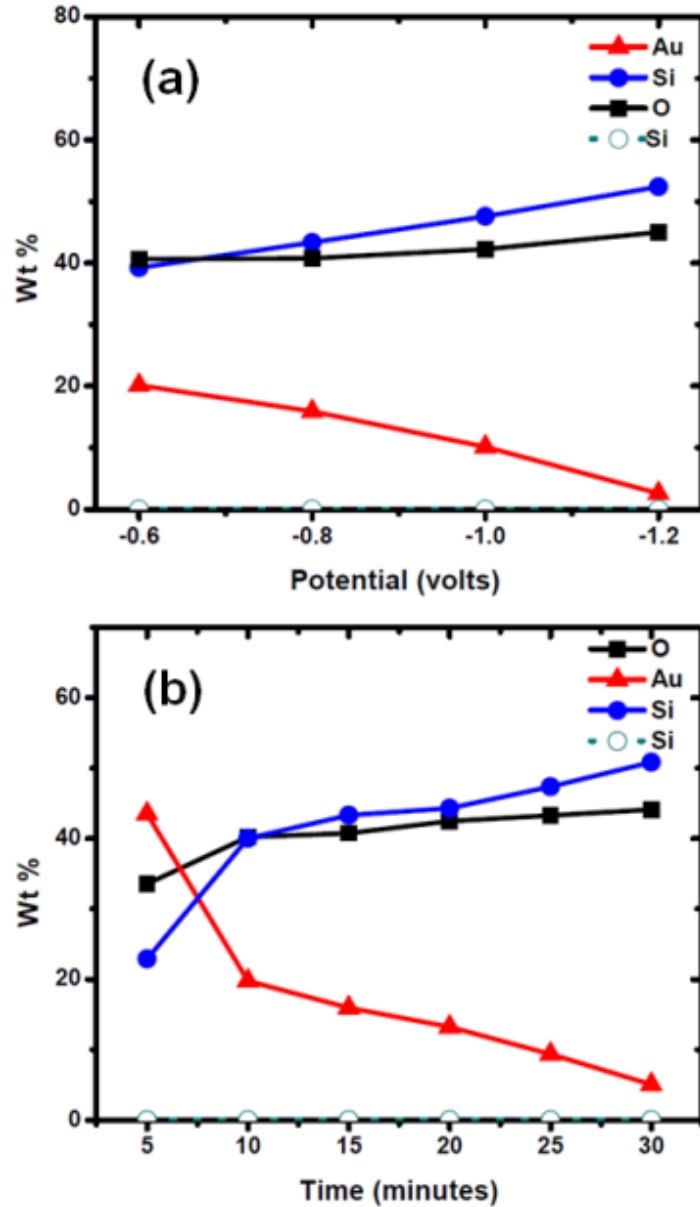


**Figure 3.6.** Composition of the as-prepared Au-SiO<sub>2</sub> nanocomposite films (solid lines) and coral-like NSPG (dashed line, open points) at (a) different deposition potentials (-0.6, -0.8, -1.0 and -1.2 volts) for 15 min and (b) different deposition times (05, 10, 15, 20, 25 and 30 min) at -0.8 volts. [KAuCl<sub>4</sub>] = 5.29 mM; [TMOS] = 0.14 M. A small amount (<1 wt%) of potassium originating from the supporting electrolyte was observed in some of the Au-SiO<sub>2</sub> nanocomposite films. Reprinted with permission from reference 1. Copyright 2014 American Chemical Society.

The colloidal nature, roughness, large thickness and composition of the nanocomposite films can be interpreted based on differences in the mechanism and kinetics for the reduction of metal ions and the polycondensation of silica monomers via electrochemical formation of  $\text{OH}^-$ .<sup>19</sup> Upon the application of a sufficiently negative potential, gold ions will be directly reduced at the electrode surface whereas silica polymerization will take place at and beyond the electrode surface as the electrogenerated  $\text{OH}^-$  begins to diffuse into the bulk of solution encountering silica monomers. Depending on the magnitude of the applied potential and the deposition time, very different nanocomposites are formed, ultimately leading to nanostructured porous gold with different porous frameworks (see below).

Generally, in a metal/silica sol system the reduction of the solvent (e.g.  $\text{H}_2\text{O}$  in  $\text{EtOH}/\text{H}_2\text{O}$  mixture) to form  $\text{OH}^-$  occurs at a more negative potential with respect to metal ions reduction.<sup>19</sup> At relatively low potentials (e.g., -0.6 volts), sol-gel polymerization will be slow due to the limited production of hydroxide ions. Gold ions, however, will be easily reduced at the electrode surface. As the reaction time proceeds (e.g. 15 min), the concentration of gold ions at the electrode surface will drop as depletion sets in while the electrogenerated base catalyst will increase as it continues to diffuse beyond the electrode surface into the bulk of the solution leading to an increase in sol-gel monomer polycondensation and the generation and growth of colloidal silica. Eventually the silica will aggregate and deposit when the critical concentration fulfills. The net result will be the formation of gold-rich nanocomposite films at the early stages of the electrochemical deposition reaction and a more silica-rich film at longer deposition times.

Contemporaneously, the gold deposition will continue to occur through the pores of the nanocomposite microstructure but at a slower rate due to the partial blockage of the electrode surface by non-conductive silica aggregates resulting in the formation of a very rough and thick particulate-like silica-rich nanocomposite at longer deposition periods. The observed differences in film composition, thickness and roughness as the applied potential became more negative can also be attributed to differences in the nucleation and growth rates of electrochemically deposited nanocomposite films. The rate of the water/oxygen reduction to  $\text{OH}^-$  will increase as the applied potential becomes more negative while the diffusion-controlled reduction of the gold ions will decrease as depletion sets in. The net result after a 15 min deposition time is a silica-rich surface. Such behavior has been noted in co-electrodeposited Cu-SiO<sub>2</sub> and Au nanoparticle-SiO<sub>2</sub> nanocomposites.<sup>19, 21</sup>

The silica and gold precursors act synergistically in that without both being present in solution at the same time and concurrently deposited, an Au-SiO<sub>2</sub> nanocomposite would not be formed. Successive (in contrast to co-) electrodeposition of silica first followed by gold would be challenging without the use of some type of ‘nanogluе’ to improve the adhesion of silica to gold.<sup>41, 42</sup> Likewise, gold electrodeposition followed by silica electrodeposition would not yield a Au-SiO<sub>2</sub> nanocomposite film. The high stability of the dry Au-SiO<sub>2</sub> nanocomposite films (> 6 months at ambient conditions) and the good adhesion to the conductive substrate surface is attributed to the presence of the gold corals, which work as a “backbone” supporting the nanocomposite microstructure. The as-prepared nanocomposite films are visually crack-free.

However, films prepared at long deposition times ( $\geq 30$  min) and/or large negative potentials ( $\leq -1.2$  volts) may crack and/or partially flake off when quickly dried or placed under vacuum.

### 3.3.2. Nanostructured Porous Gold (NSPG) Films

The Au-SiO<sub>2</sub> nanocomposite films can be used as a building block to form a porous nanostructured gold electrode by simply chemically etching the silica in hydrofluoric acid (HF). In this experiment, the co-electrodeposited Au-SiO<sub>2</sub> films were immersed in diluted hydrofluoric acid using a gentle two-step etching procedure outlined in the experimental section. The resulting porous gold films were brownish in color and adhered well to the conducting substrate.

SEMs of an etched film at different magnifications are shown in **Figure 3.2 (d, e, f)**. As can be seen, the morphology of the as-prepared Au-SiO<sub>2</sub> nanocomposite films drastically changed after the etching process. Chemical etching resulted in the formation of coral-like NSPG films characterized by a much more open framework with respect to the Au-SiO<sub>2</sub> nanocomposite films. The low magnification SEM image shows that the NSPG films are crack-free (inset of **Figure 3.2 (d)**). The circular-like pores in the Au-SiO<sub>2</sub> composite films were replaced by pores of irregular shape resulting from the cross-linkage of the gold corals. Both the thickness and roughness of the nanocomposite films also decreased significantly after the etching process as depicted in **Figure 3.4**. At -1.0 volts, for example, the film thickness decreased from  $\sim 12$   $\mu\text{m}$  to 550 nm after etching. The thickness of the nanocomposite films prepared at different deposition potentials was reduced by almost the same magnitude with the NSPG films being  $\sim 22$  times thinner than the corresponding AuSiO<sub>2</sub> nanocomposite films. Since the surface of the composite

films is predominately colloidal silica (see below), the significant decrease in film thickness and roughness is attributed to the removal of the silica over-layer. As can be seen in an SEM image acquired on an edge of a scratched NSPG, the nanostructure is continuous from the bottom (at the underlying gold substrate) to the top, **Figure 3.7**. SEM-EDX acquired over an area of  $100 \mu\text{m}^2$  confirmed the removal of silica, **Figure 3.8**.

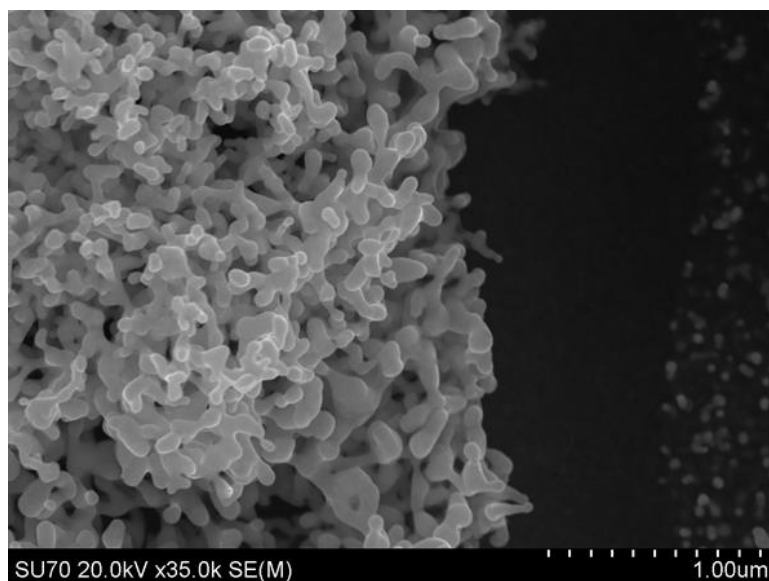


**Figure 3.7.** SEM image of a scratched NSPG prepared from an Au-SiO<sub>2</sub> nanocomposite film electrodeposited at -0.8 volts for 15 min from a solution containing 5.29 mM KAuCl<sub>4</sub> and 0.54 M TMOS. The image reflects the continuous formation of the gold corals at the conductive substrate surface (dark area). Reprinted with permission from reference 1. Copyright 2014 American Chemical Society.

The chemical nature and electronic structure of the as-prepared Au-SiO<sub>2</sub> nanocomposite and NSPG films were examined in more detail using XPS and powder XRD. **Figure 3.9** shows

a representative Au  $4f$  and Si  $2p$  high-resolution core-level spectra for the Au-SiO<sub>2</sub> nanocomposite films before and after etching. The Au  $4f$  spectrum consists of two peaks due to the spin orbit coupling of gold, with a separation of 3.7 eV.<sup>43</sup> The Si  $2p$  peak at 103.5 eV with a FWHM of 2.3 eV is consistent with Si<sup>IV</sup> such as SiO<sub>2</sub> (103.9 eV) or a suboxide (~ 102 eV).<sup>44</sup> Before etching (**Figure 3.9 (a)**), the Au peaks are very small and the Si peaks are very large indicating that the Si is on the outermost surface of Au. After etching in HF, the Si  $2p$  photoelectron peak corresponding to the presence of silica is absent (**Figure 3.9 (b)**) as is the O  $1s$  peak, further proving the effectiveness of the etching protocol in silica removal.

Upon close examination of the Au  $4f$  high resolution spectra before and after etching, a broadening and shift ( $\geq 1.0$  eV) to higher binding energy values for the Au-SiO<sub>2</sub> nanocomposite relative to metallic gold can be observed (**Figure 3.9 (a)**). However, they have the same peak separation of 3.7 eV. Before etching (Au-SiO<sub>2</sub> nanocomposite), two photoelectron peaks of Au  $4f_{7/2}$  at 84.5 eV (FWHM = 2.4 eV) and Au  $4f_{5/2}$  at 88.2 eV (FWHM = 2.7 eV) are observed. After etching, the two photoelectron peaks shifted to 83.7 (FWHM= 0.76) and 87.4 eV (FWHM = 0.78), which are in accordance with the reported literature values for metallic gold.<sup>45, 46</sup> The positive shift in the binding energies of the Au  $4f$  photoelectron peaks could arise from a number of factors including differential charging<sup>47-49</sup> and the presence of a trace amount of gold in a different oxidation state originating from the plating solution, for example. The broadening of the Au  $4f$  peaks in the nanocomposite film with respect to the NSPG may be attributed to interactions between gold and silica in the nanocomposite film.<sup>50</sup>

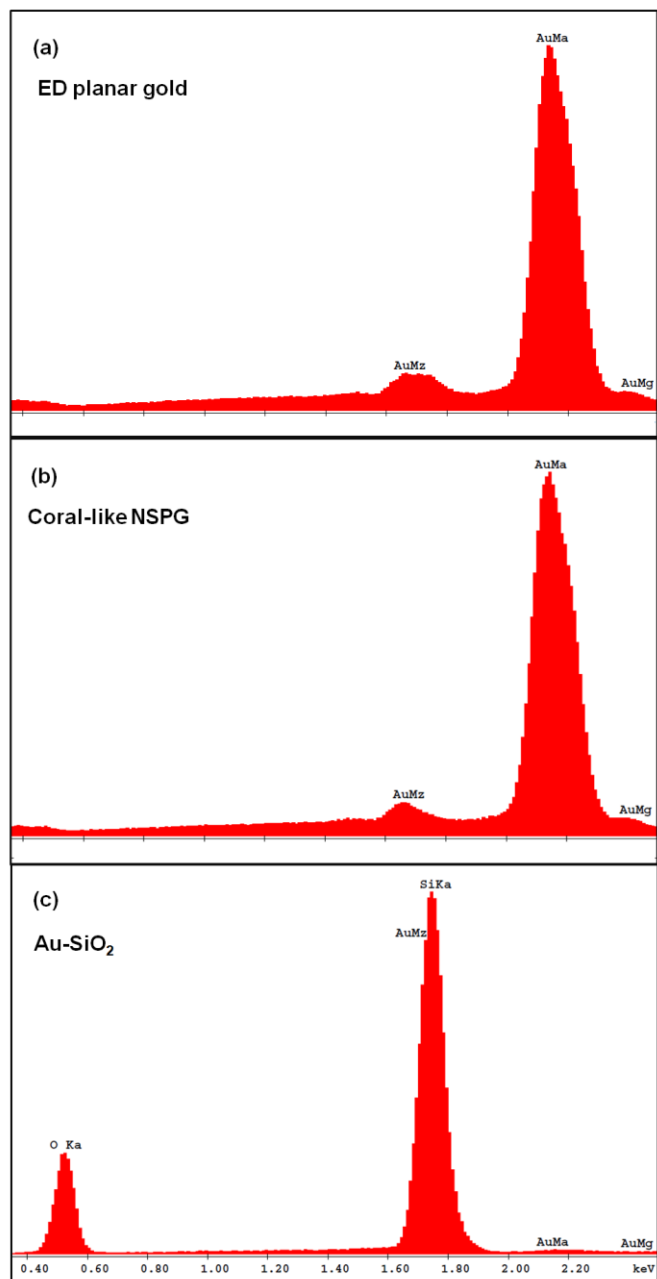


**Figure 3.8.** EDX spectra of (a) electrodeposited (ED) planar gold film (b) coral-like NSPG and (c) Au-SiO<sub>2</sub> nanocomposite film electrodeposited at -0.8 volts for 15 min in 5.29 mM KAuCl<sub>4</sub> and 0.14 M TMOS (b, c only). Reprinted with permission from reference 1. Copyright 2014 American Chemical Society.



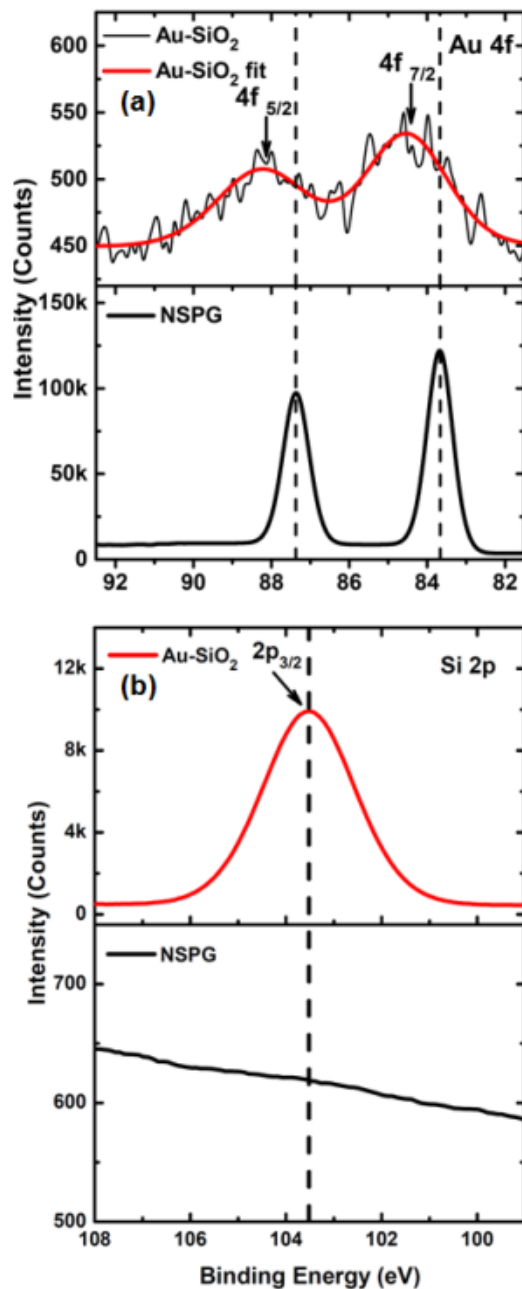


**Figure 3.9.** XPS spectra of (a) the Au 4f core-level and (b) Si 2p core-level from the Au-SiO<sub>2</sub> nanocomposite films electrodeposited at -0.8 volts for 15 min and coral-like NSPG obtained after the 2-step etching in HF. [KAuCl<sub>4</sub>] = 5.29 mM; [TMOS] = 0.14 mM. Reprinted with permission from reference 1. Copyright 2014 American Chemical Society.

X-ray diffraction patterns of the as-prepared Au-SiO<sub>2</sub> nanocomposite thin films before and after the etching process are displayed in **Figure 3.10**. XRD pattern of the non-etched film displayed two different sets of diffraction peaks. The first set consisted of five diffraction peaks which can be indexed to the diffraction from the (111), (200), (220), (311), and (222) planes of cubic metallic gold with FCC structure (JCPDS, card no. 03-065-8601). The second set was represented by two diffraction peaks located at 22.38° and 28.29° corresponding to the (100) and (101) planes of hexagonal silicon oxide (JCPDS card no. 01-070-3315), respectively. The appearance of the gold and silica diffraction peaks in the XRD pattern of the non-etched film confirmed the formation of a mixed phase gold-silica nanocomposite films.

The disappearance of the characteristic silica peaks in the XRD pattern of the etched sample is again consistent with the removal of silica as indicated by SEM-EDX and XPS. The significant increase in the intensity of the (111) peak and the large decrease in the intensities of the (200), (220), and (311) peaks could be attributed to the oriented rearrangement of the gold atoms in the (111) direction after the selective dissolution of silica. Furthermore, in the face centered cubic structure of nanoporous gold the (111) and (222) planes are parallel to each other and this could explained the observed increase in the intensity of (222) peak.<sup>51</sup> However, the differences in magnitudes of the intensity increase between the (111) and (222) peaks might be attributed to the differences in the d-spacing values where at higher 2-theta degree values the d-spacing decreases.<sup>52</sup>

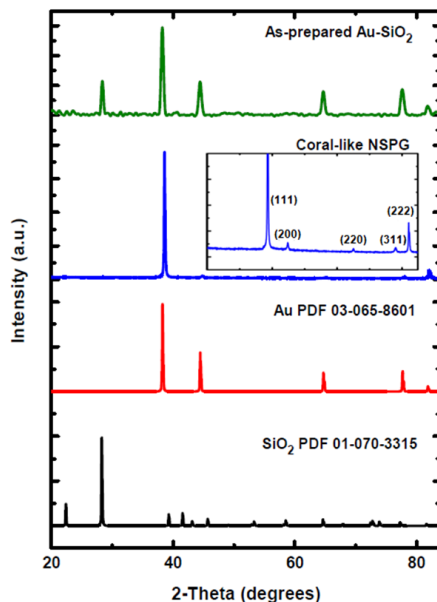


**Figure 3.10.** Powdered XRD patterns of as-prepared Au-SiO<sub>2</sub> and the coral-like NSPG obtained via electrodeposition at -0.8 volts for 15 min from a solution containing 5.29 mM KAuCl<sub>4</sub> and 0.14 mM TMOS. Reprinted with permission from reference 1. Copyright 2014 American Chemical Society.

An important characteristic of any porous gold electrode is its surface area.<sup>29</sup> The electrochemically active surface area or the so-called real surface area of the coral-like NSPG electrode was determined by cyclic voltammetry in 0.5 M H<sub>2</sub>SO<sub>4</sub> by integrating the area underneath the cathodic peak at ~0.8 volts and assuming a specific charge of 400  $\mu\text{C cm}^{-2}$  for the reduction of the gold oxide monolayer.<sup>53-56</sup> A typical cyclic voltammogram (CV) characteristic of gold in an acidic solution is shown in **Figure 3.11**. As can be seen, the stripping peak at ~0.8 volts in the CV of the coral-like NSPG electrodes is significantly larger than that observed at an electrodeposited planar gold electrode, **Figure 3.11 (a)**. For an electrode prepared at -0.8 volts,

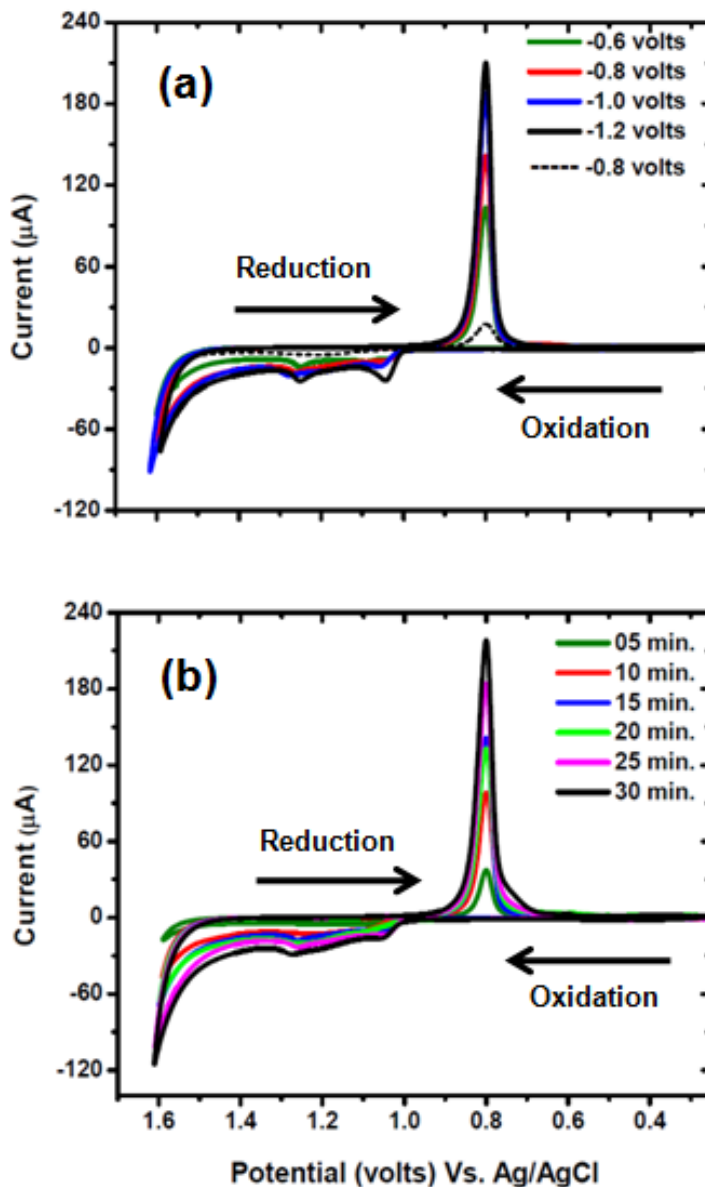


**Figure 3.11.** Cyclic voltammograms of NSPG electrodes (solid lines) in 0.5 M H<sub>2</sub>SO<sub>4</sub> at a scan rate of 10 mV/s. The NSPG electrodes were obtained by etching Au-SiO<sub>2</sub> nanocomposite films electrodeposited at (a) different deposition potentials and (b) different deposition times. The dashed line in (a) was obtained at a planar gold electrode electrodeposited at -0.8 volts for 15 min. Reprinted with permission from reference 1. Copyright 2014 American Chemical Society.

the surface area was 1.63 cm<sup>2</sup>; the geometric area is 0.079 cm<sup>2</sup>. Given a film thickness of ~ 520 nm, the surface area per unit volume is ~ 4 x 10<sup>7</sup> m<sup>2</sup>/m<sup>3</sup>. The roughness factor (RF), defined as the ratio of the real surface area (RSA) to the geometrical surface area (GSA),  $RF = RSA/GSA$ , was 20.6. The values of RF (see below) compare well with other routes for the formation of high surface area gold that include dealloying gold leaf in concentrated nitric acid,<sup>29, 57</sup> dealloying a Au-Zn alloy electrochemically,<sup>54</sup> surface rebuilding,<sup>58</sup> and roughening in HCl.<sup>56</sup>

### 3.3.3. Nanostructured Porous Gold (NSPG) Films: Morphology Control

An important characteristic of any new method for the fabrication of high surface area electrodes is the ability to control electrode morphology, surface area, and film thickness. In this work, we demonstrate morphological control by tailoring the deposition parameters, such as the potential, time, sol-gel monomer concentration, and gold ion concentration.

#### 3.3.3.1. Deposition Potential and Time

**Figure 3.12** and **Figure 3.13** displays the SEM micrographs of the coral-like NSPG films obtained at different deposition potentials (-0.6, -1.0 and -1.2 volts) and times (5, 10, 20, 25, and 30 min), respectively. For all samples the KAuCl<sub>4</sub> and sol-gel monomer (TMOS) concentrations were kept constant at 5.29 mM and 0.14 mM, respectively. As can be seen, the morphology of the film and the thickness of the coral branches/ligaments are strongly dependent on the value of the applied potential and the deposition time.

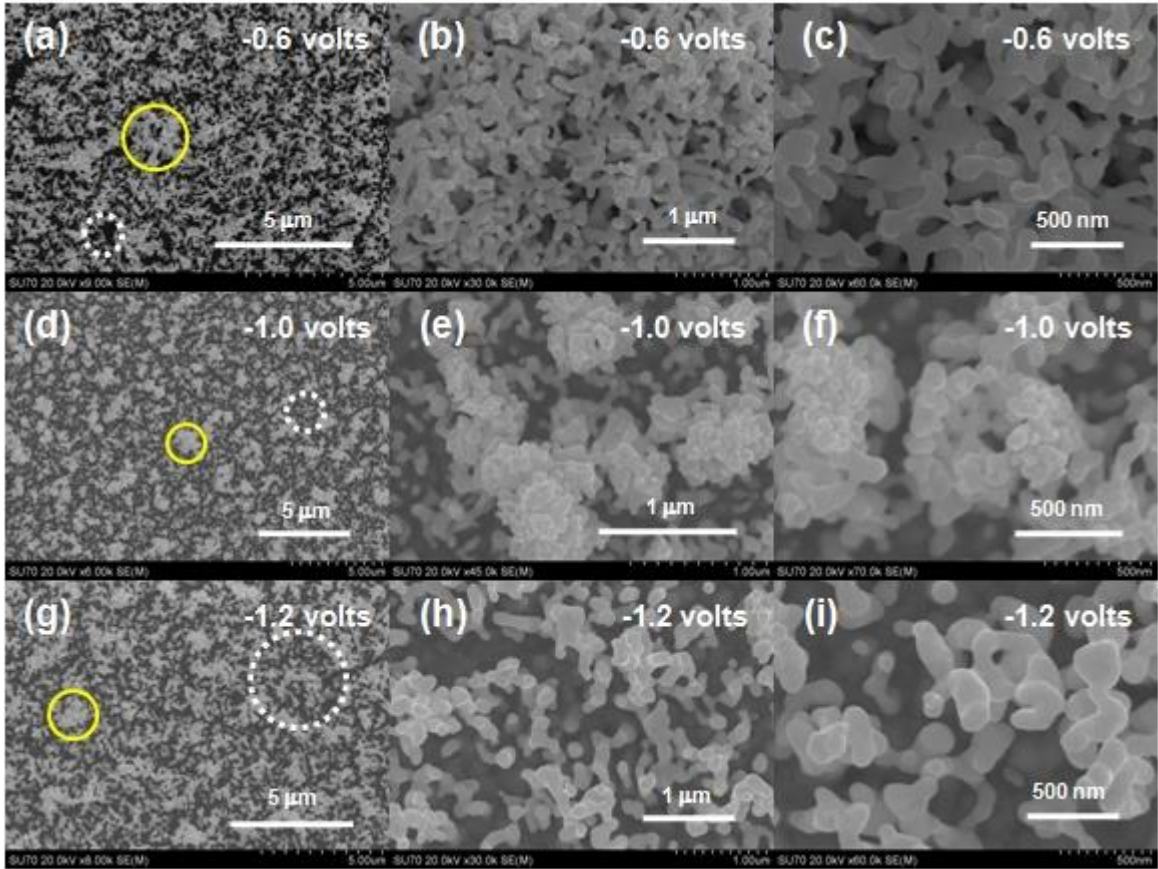


**Figure 3.12.** SEM images of coral-like NSPG prepared from Au-SiO<sub>2</sub> nanocomposite films electrodeposited at -0.6, -1.0 and -1.2 volts for 15 min. [KAuCl<sub>4</sub>] = 5.29 mM; [TMOS] = 0.14 M. The white and yellow circles indicate relatively low density gold agglomerates and higher density gold agglomerates, respectively. Reprinted with permission from reference 1. Copyright 2014 American Chemical Society.

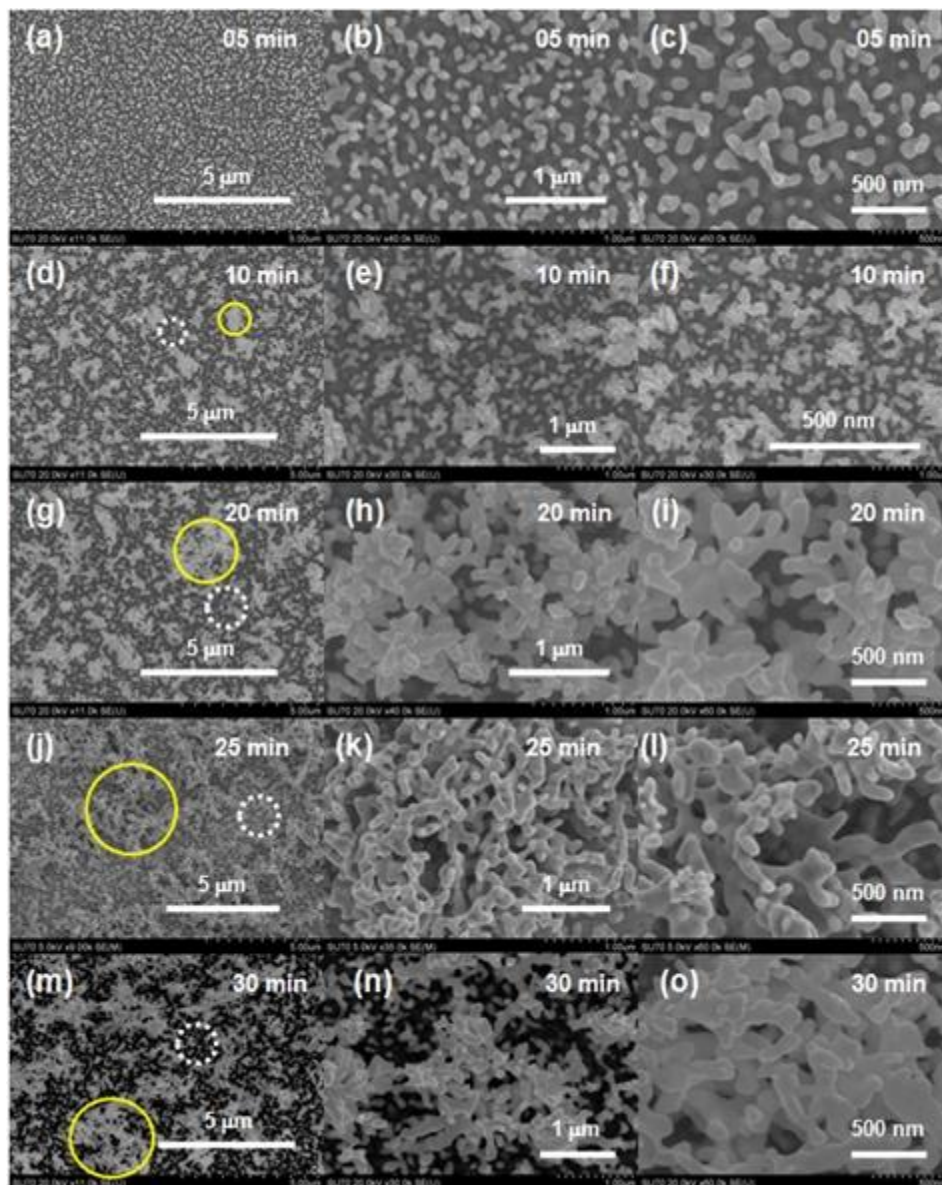


**Figure 3.13.** SEM images of coral-like NSPG prepared from Au-SiO<sub>2</sub> nanocomposite films electrodeposited at -0.8 volts for different deposition times. [KAuCl<sub>4</sub>] = 5.29 mM; [TMOS] = 0.14 mM. The white and yellow circles indicate relatively low density gold agglomerates and higher density gold agglomerates, respectively. Reprinted with permission from reference 1. Copyright 2014 American Chemical Society.

In the low magnification SEM images shown in **Figure 3.12** and **Figure 3.13**, two coral-like gold structures are evident and indicated by the yellow circles: high density agglomerates and low density agglomerates. Upon application of sufficiently negative potentials, a large number of nucleation sites at which the gold grew to produce gold-rich areas surrounded by silica-rich areas were produced. Upon chemical etching, high density and low density coral gold agglomerates were generated. From the high magnification images, it can be seen that as the applied potential becomes more negative and/or deposition time increases, the overall size of the agglomerates increases and the width of the individual fingers that make up the coral branches increases.

The increase in the reaction time/ negative potentials was accompanied by not only a continuous growth of gold but also an increase in the degree of cross-linkage of the gold coral branches, resulting in the formation of thick porous films (**Figure 3.12** and **Figure 3.13**). In **Figure 3.14**, the variation in film thickness and the roughness factor with potential and time can be seen. A near linear increase in film thickness and roughness factor as the applied potential becomes more negative or the deposition time increases was evident. An increase in RF up to 31 times has been achieved at an applied potential of -1.2 volts. The dependence of surface area per unit volume on potential and time is shown in **Figure 3.15**. In these plots, the real surface area was normalized to the volume of the film defined by the geometric area and average film thickness. With the exception of short deposition times ( $\leq 5$  min), the values obtained are nearly constant giving rise to an average value of  $4.4 \times 10^7 \text{ m}^2/\text{m}^3$ . The porosity of the coral-like NSPG films coupled with the higher degree of cross-linkage and increased thickness at longer



deposition times helps to explain the observed increase in the real surface area and roughness factor of the NSPG electrodes. Roughness factors in the range of 5-38 were obtained reflecting the large increase in the electrode surface area as the deposition potential increased.

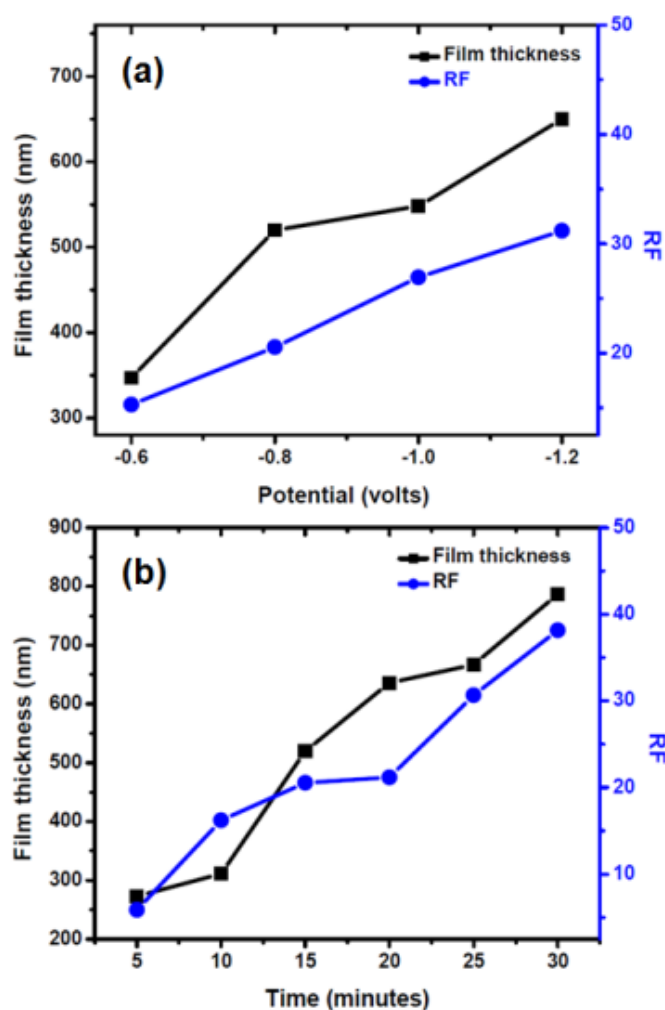


**Figure 3.14.** Thickness and the roughness factors (RF) of NSPG prepared from Au-SiO<sub>2</sub> nanocomposite films electrodeposited (a) for 15 min at different deposition potentials and (b) at -0.8 volts for different deposition times. [KAuCl<sub>4</sub>] = 5.29 mM; [TMOS] = 0.14 mM. Reprinted with permission from reference 1. Copyright 2014 American Chemical Society.

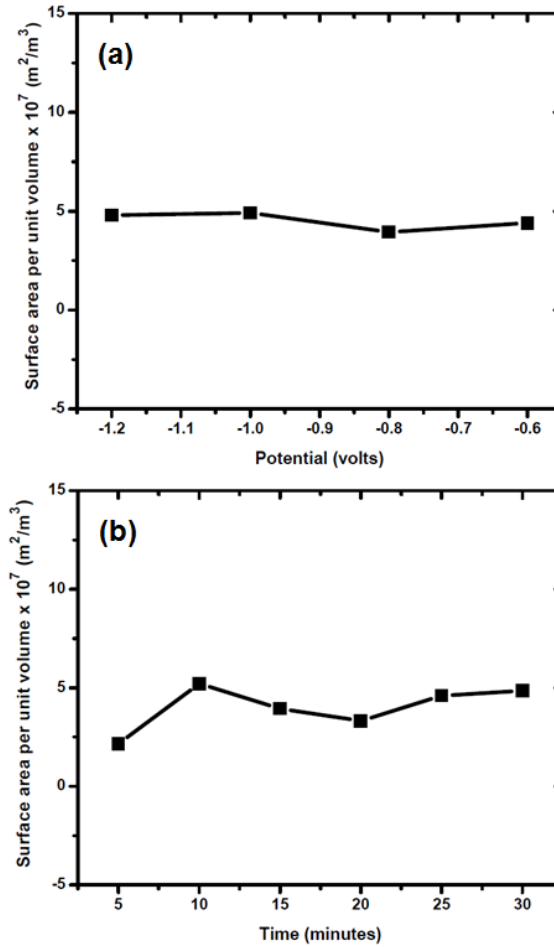


**Figure 3.15.** Variation in normalized surface area of NSPG electrodes with potential (a) and time (b). Reprinted with permission from reference 1. Copyright 2014 American Chemical Society.

### 3.3.3.2. Precursor concentration

The morphology of the NSPG electrodes was also highly dependent on the concentration of gold ions in the deposition solution (**Figure 3.16**) and the concentration of TMOS (**Figure 3.17**). As depicted in the low resolution SEM images in **Figure 3.16**, an increase in the concentration of

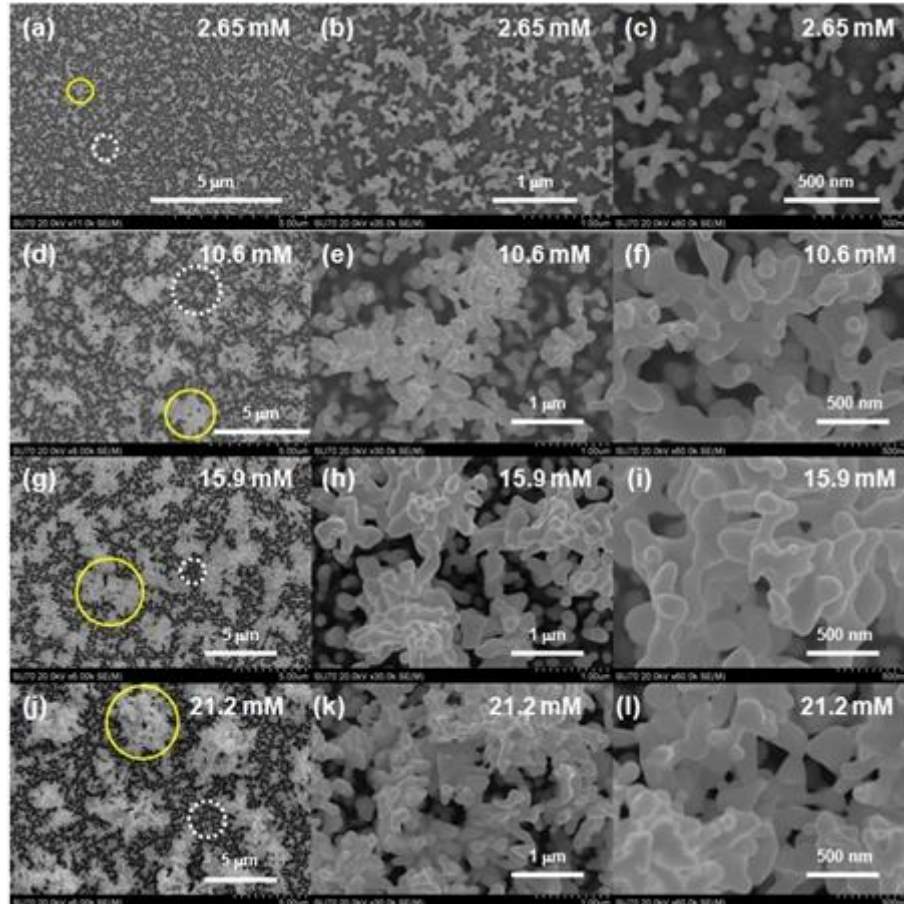


**Figure 3.16.** SEM images of coral-like NSPG prepared from Au-SiO<sub>2</sub> nanocomposite films electrodeposited at -0.8 volts for 15 min from solutions containing 0.14 mM TMOS and different concentrations of gold ions. The white and yellow circles indicate relatively low density gold agglomerates and higher density gold agglomerates, respectively. Reprinted with permission from reference 1. Copyright 2014 American Chemical Society.

HAuCl<sub>4</sub> was accompanied by an increase in the size of the gold agglomerates due to the diffusion-controlled deposition of gold. From high resolution SEM images, it can be seen that the density, size and degree of cross-linkage within the coral-shaped colonies increased with an increase of gold ion concentration (**Figure 3.16**). In addition to a change in morphology, an

increase in  $\text{HAuCl}_4$  also leads to an increased film thickness, **Figure 3.18 (a)**. The average thickness of the NSPG electrodes ranged from 0.22 to 2.25  $\mu\text{m}$ . Likewise, a significant increase in the surface area of the as-prepared coral-like NSPG electrode was noted. Through adjustment of  $[\text{HAuCl}_4]$ , up to 57 times increase in the real surface area over the geometric area was achieved.

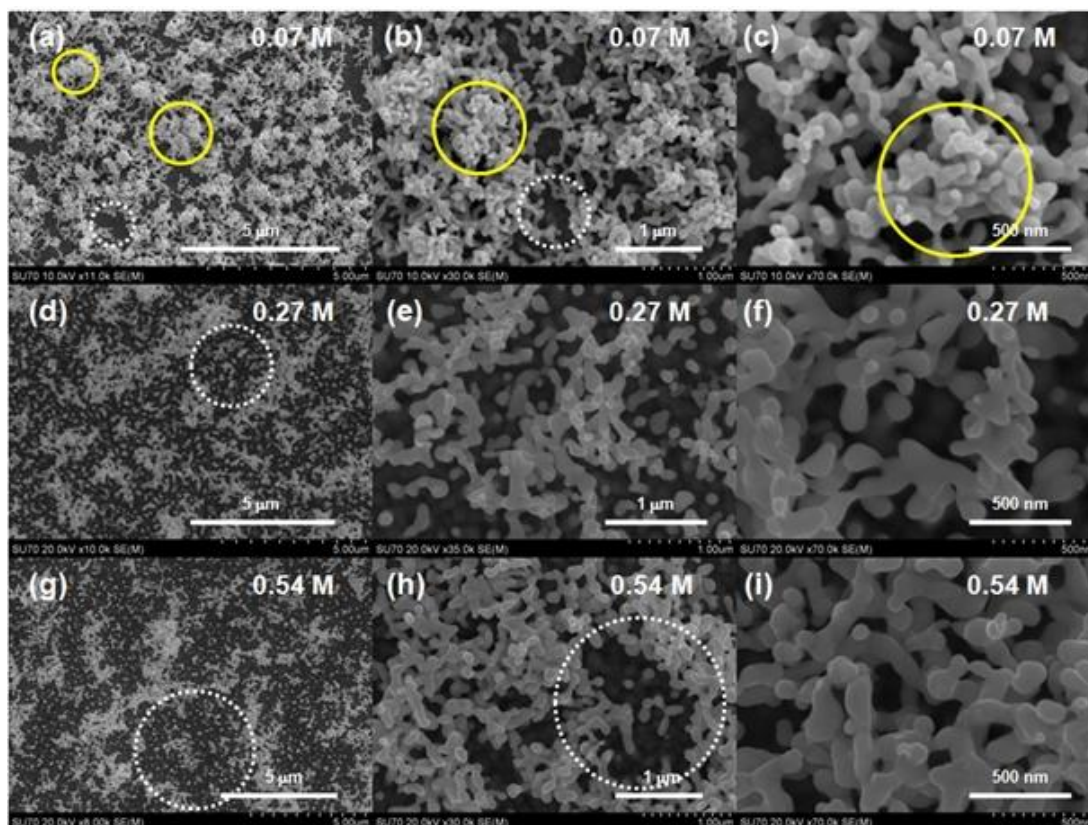


**Figure 3.17.** SEM images of coral-like NSPG prepared from Au-SiO<sub>2</sub> nanocomposite films electrodeposited at -0.8 volts for 15 min from solutions containing 5.29 mM KAuCl<sub>4</sub> and different concentrations of TMOS. The white and yellow circles indicate relatively low density gold agglomerates and higher density gold agglomerates, respectively. Reprinted with permission from reference 1. Copyright 2014 American Chemical Society.

The concentration of sol-gel monomer (TMOS) in the electroplating solution also had a significant effect on the morphology, thickness, and surface area of coral-like NSPG. From low magnification SEM images in **Figure 3.17**, it can be seen that at low TMOS concentration, the NSPG films are made up of a high density well-packed gold agglomerates. As the concentration of TMOS was increased by a factor of  $\sim 4$ , the number of these gold agglomerates decreased significantly and increased in size, **Figure 3.17 (a)** vs **(d)**.

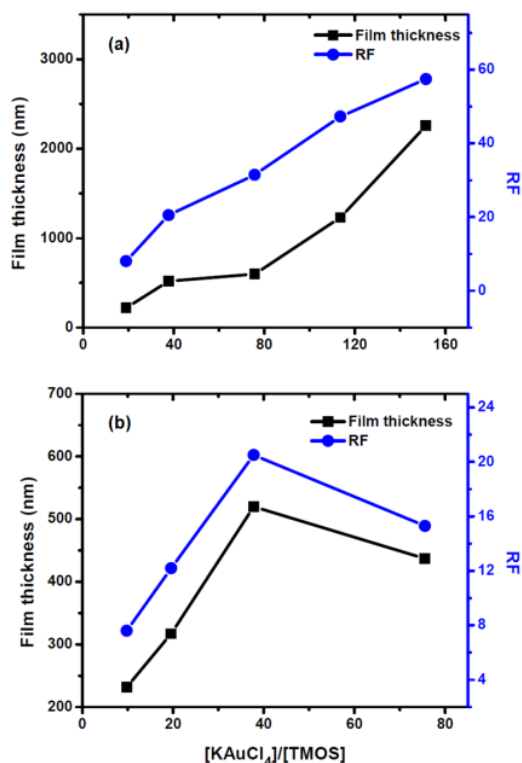


**Figure 3.18.** Thickness and the roughness factors (RF) of NSPG prepared from Au-SiO<sub>2</sub> nanocomposite films electrodeposited at -0.8 volts for 15 min as a function of (a) gold ions concentration (2.65, 5.29, 10.6, 15.9, and 21.2 mM), and (b) sol-gel monomer concentration (0.07, 0.14, 0.27, and 0.54 mM). Reprinted with permission from reference 1. Copyright 2014 American Chemical Society.

**Figure 3.18** shows the correlation in film thickness and roughness factor with the concentration ratio of gold salt to sol-gel monomer. Based on the study of the different deposition parameters mentioned above, it was expected that an increase in the concentration of TMOS will result in an increase in silica deposition at the expense of gold ion reduction and thus lead to a decrease in the film thickness of NSPG. However, an unexpected slight increase in film thickness was observed as the concentration of TMOS increased from 0.07 to 0.14 mM (or a when the ratio of  $[\text{AuCl}_4^-]/[\text{TMOS}]$  decreased from 75 to 38) followed by the expected decrease when the concentration of TMOS was further increased to 0.54 mM, **Figure 3.18 (b)**. These findings imply that there is a critical sol-gel monomer concentration (CSGC) at which the electrodeposited silica around the gold coral will be able to stabilize the coral-like gold structures and suppress the aggregation of the deposited gold. For Au-SiO<sub>2</sub> system studied herein, the CSGC concentration is ~ 0.14 mM. Above the CSGC, the coral-like gold nanostructures should be stable while below the CSGC the coral-like gold nanostructures are unstable and subject to aggregation as indicted by the yellow circles in **Figure 3.17 (a-c)**. The electrochemically active surface area and the roughness factor measurements support the assumption of CSGC where they decreased below and above the CSGC as shown in **Figure 3.18 (b)**. The observed decrease in the surface area and roughness factor below the CSGC could be attributed to the decrease in the film thickness and the aggregation of the deposited gold. The decrease in the kinetics of the gold deposition and film thickness above the CSGC might account for the observed decrease in the surface area of the electrodes.

### 3.3.3.3. Reproducibility

To examine the reproducibility of the introduced strategy for the fabrication of NSPG electrodes, four different samples were selected in order to represent the different parameters affecting the deposition process. The preparation of each sample was repeated 3 times on the same day and the roughness factor was measured in each case. The mean and the standard deviation of the roughness factor measurements were calculated and plotted as a function of the deposition parameters as displayed in **Figure 3.19**. The obtained data reflected a high degree of reproducibility.

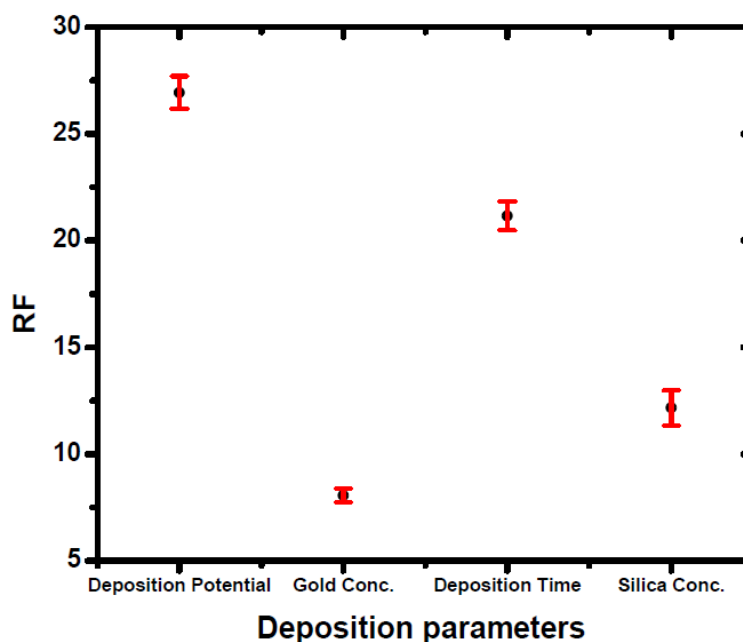


**Figure 3.19.** Reproducibility of the method at different deposition parameters. The error bars signify  $\pm 1\sigma$ .  $N = 3$ . Reprinted with permission from reference 1. Copyright 2014 American Chemical Society.

### 3.4. Conclusion

Porous Au-SiO<sub>2</sub> nanocomposites and corresponding coral-like nanostructured gold electrodes have been successfully prepared via the co-electrodeposition of KAuCl<sub>4</sub> and TMOS on a conducting substrate. Application of a sufficiently negative potential leads to the simultaneous reduction of gold ions and the formation of hydroxide ions, which subsequently catalyzes the condensation of TMOS derived monomers. The as-prepared Au-SiO<sub>2</sub> nanocomposite films are colloidal in nature with an open porous framework and good stability. Immersing the Au-SiO<sub>2</sub> composite films in a diluted hydrofluoric acid solution leads to the selective dissolution of silica and the evolution of coral-like NSPG. The nanostructured porous gold films are stable and displayed high electrochemically active surface areas (RF up to 57) and thus are excellent candidates for applications requiring high surface area conductive supports, particularly in catalysis and chemical sensing. The electrochemical gold/sol gel composite route for the formation of porous gold electrodes has several distinguishing features that include good reproducibility, low cost via the use of very dilute gold ion solutions, utilization of environmentally friendly solvents (H<sub>2</sub>O and C<sub>2</sub>H<sub>5</sub>OH), and does not require expensive equipment, vacuum, or toxic gold cyanide electrolytes. As a result, the electrochemical gold/sol-gel composite strategy for fabricating nanoporous gold is a promising candidate for a large scale production. Generalization of the method to produce other nanoporous metals is currently underway.



### 3.5. References

1. Farghaly, A. A.; Collinson, M. M., Electroassisted Codeposition of Sol–Gel Derived Silica Nanocomposite Directs the Fabrication of Coral-like Nanostructured Porous Gold. *Langmuir* **2014**, 30, (18), 5276-5286.
2. Zhitomirsky, I., Cathodic Electrodeposition of Ceramic and Organoceramic Materials. Fundamental Aspects. *Advances in Colloid and Interface Science* **2002**, 97, (1-3), 279-317.
3. Therese, G. H. A.; Kamath, P. V., Electrochemical Synthesis of Metal Oxides and Hydroxides. *Chemistry of Materials* **2000**, 12, (5), 1195-1204.
4. Sattayasamitsathit, S.; Gu, Y. E.; Kaufmann, K.; Minter, S.; Polsky, R.; Wang, J., Tunable Hierarchical Macro/Mesoporous Gold Microwires Fabricated by Dual-Templating and Dealloying Processes. *Nanoscale* **2013**, 5, (17), 7849-7854.
5. Yamauchi, Y.; Kuroda, K., Rational Design of Mesoporous Metals and Related Nanomaterials by a Soft-Template Approach. *Chemistry-an Asian Journal* **2008**, 3, (4), 664-676.
6. Bookbinder, D. C.; Wrighton, M. S., Thermodynamically Uphill Reduction of a Surface-Confining N,N'-Dialkyl-4,4'-Bipyridine Derivative on Illuminated Para-Type Silicon Surfaces. *Journal of the American Chemical Society* **1980**, 102, (15), 5123-5125.
7. Bookbinder, D. C.; Wrighton, M. S., Electrochromic Polymers Covalently Anchored to Electrode Surfaces - Optical and Electrochemical Properties of a Viologen-Based Polymer *Journal of the Electrochemical Society* **1983**, 130, (5), 1080-1087.
8. Leventis, N.; Chung, Y. C., New Complementary Electrochromic System Based on Polypyrrole Prussian Blue Composite, a Benzylviologen Polymer, and Poly(vinylpyrrolidone) Potassium Sulfate Aqueous Electrolyte. *Chemistry of Materials* **1992**, 4, (6), 1415-1422.
9. Collinson, M. M., Electrochemistry: An Important Tool to Study and Create New Sol-Gel-Derived Materials. *Accounts of Chemical Research* **2007**, 40, (9), 777-783.
10. Deepa, P. N.; Kanungo, M.; Claycomb, G.; Sherwood, P. M. A.; Collinson, M. M., Electrochemically Deposited Sol-Gel-Derived Silicate Films as a Viable Alternative in Thin-Film Design. *Analytical Chemistry* **2003**, 75, (20), 5399-5405.
11. Etienne, M.; Sallard, S.; Schroder, M.; Guillemin, Y.; Mascotto, S.; Smarsly, B. M.; Walcarius, A., Electrochemical Generation of Thin Silica Films with Hierarchical Porosity. *Chemistry of Materials* **2010**, 22, (11), 3426-3432.
12. Shacham, R.; Avnir, D.; Mandler, D., Electrodeposition of Methylated Sol-Gel Films on Conducting Surfaces. *Advanced Materials* **1999**, 11, (5), 384-388.
13. Sibottier, E.; Sayen, S.; Gaboriaud, F.; Walcarius, A., Factors Affecting the Preparation and Properties of Electrodeposited Silica Thin Films Functionalized with Amine or Thiol Groups. *Langmuir* **2006**, 22, (20), 8366-8373.
14. Walcarius, A.; Sibottier, E.; Etienne, M.; Ghanbaja, J., Electrochemically Assisted Self-Assembly of Mesoporous Silica Thin Films. *Nature Materials* **2007**, 6, (8), 602-608.

15. Goux, A.; Etienne, M.; Aubert, E.; Lecomte, C.; Ghanbaja, J.; Walcarius, A., Oriented Mesoporous Silica Films Obtained by Electro-Assisted Self-Assembly (EASA). *Chemistry of Materials* **2009**, 21, (4), 731-741.
16. Liu, L.; Toledano, R.; Danieli, T.; Zhang, J. Q.; Hu, J. M.; Mandler, D., Electrochemically Patterning Sol-Gel Structures on Conducting and Insulating Surfaces. *Chemical Communications* **2011**, 47, (24), 6909-6911.
17. Shacham, R.; Mandler, D.; Avnir, D., Pattern Recognition in Oxides Thin-Film Electrodeposition: Printed Circuits. *Comptes Rendus Chimie* **2010**, 13, (1-2), 237-241.
18. Luna-Vera, F.; Dong, D.; Hamze, R.; Liu, S.; Collinson, M. M., Electroassisted Fabrication of Free-Standing Silica Structures of Micrometer Size. *Chemistry of Materials* **2012**, 24, (12), 2265-2273.
19. Toledano, R.; Shacham, R.; Avnir, D.; Mandler, D., Electrochemical Co-Deposition of Sol-Gel/Metal Thin Nanocomposite Films. *Chemistry of Materials* **2008**, 20, (13), 4276-4283.
20. Tehrani, M. S.; Azar, P. A.; Mohammadiazar, S., A Single Step Technique for Preparation of Porous Solid Phase Microextraction Fibers by Electrochemically Co-Deposited Silica Based Sol-Gel/Cu Nanocomposite. *Journal of Chromatography A* **2013**, 1278, 1-7.
21. Toledano, R.; Mandler, D., Electrochemical Codeposition of Thin Gold Nanoparticles/Sol-Gel Nanocomposite Films. *Chemistry of Materials* **2010**, 22, (13), 3943-3951.
22. Liu, X. Q.; Li, B. H.; Wang, X.; Li, C. Y., One-Step Construction of an Electrode Modified with Electrodeposited Au/SiO<sub>2</sub> Nanoparticles, and Its Application to the Determination of NADH and Ethanol. *Microchimica Acta* **2010**, 171, (3-4), 399-405.
23. Ramalingam, S.; Muralidharan, V. S.; Subramania, A., Electrodeposition and Characterization of Cu-TiO<sub>2</sub> Nanocomposite Coatings. *Journal of Solid State Electrochemistry* **2009**, 13, (11), 1777-1783.
24. Wu, L. K.; Hu, J. M.; Zhang, J. Q.; Cao, C. N., A Silica Co-Electrodeposition Route to Highly Active Ni-Based Film Electrodes. *Journal of Materials Chemistry A* **2013**, 1, (41), 12885-12892.
25. Wu, L. K.; Hu, J. M.; Zhang, J. Q., Electrodeposition of Zinc-Doped Silane Films for Corrosion Protection of Mild Steels. *Corrosion Science* **2012**, 59, 348-351.
26. Liu, L.; Mandler, D., Electro-Assist Deposition of Binary Sol-Gel Films with Graded Structure. *Electrochimica Acta* **2013**, 102, 212-218.
27. Raveh, M.; Liu, L.; Mandler, D., Electrochemical Co-Deposition of Conductive Polymer-Silica Hybrid Thin Films. *Physical Chemistry Chemical Physics* **2013**, 15, (26), 10876-10884.
28. Asefa, T.; Duncan, C. T.; Sharma, K. K., Recent Advances in Nanostructured Chemosensors and Biosensors. *Analyst* **2009**, 134, (10), 1980-1990.
29. Collinson, M. M., Nanoporous Gold Electrodes and Their Applications in Analytical Chemistry. *ISRN Analytical Chemistry* **2013**, 2013, 21.
30. Dai, Z. H.; Ju, H. X., Bioanalysis Based on Nanoporous Materials. *Trac-Trends in Analytical Chemistry* **2012**, 39, 149-162.

31. Guo, D. J.; Ding, Y., Porous Nanostructured Metals for Electrocatalysis. *Electroanalysis* **2012**, 24, (11), 2035-2043.
32. Guo, Y. G.; Hu, J. S.; Wan, L. J., Nanostructured Materials for Electrochemical Energy Conversion and Storage Devices. *Advanced Materials* **2008**, 20, (15), 2878-2887.
33. Menzel, N.; Ortel, E.; Kraehnert, R.; Strasser, P., Electrocatalysis Using Porous Nanostructured Materials. *Chemphyschem* **2012**, 13, (6), 1385-1394.
34. Smatt, J. H.; Sayler, F. M.; Grano, A. J.; Bakker, M. G., Formation of Hierarchically Porous Metal Oxide and Metal Monoliths by Nanocasting into Silica Monoliths. *Advanced Engineering Materials* **2012**, 14, (12), 1059-1073.
35. Zhang, J. T.; Li, C. M., Nanoporous Metals: Fabrication Strategies and Advanced Electrochemical Applications in Catalysis, Sensing and Energy Systems. *Chemical Society Reviews* **2012**, 41, (21), 7016-7031.
36. Monzon, L. M. A.; Byrne, F.; Coey, J. M. D., Gold Electrodeposition in Organic Media. *Journal of Electroanalytical Chemistry* **2011**, 657, (1â€²2), 54-60.
37. Tappan, B. C.; Steiner, S. A.; Luther, E. P., Nanoporous Metal Foams. *Angewandte Chemie International Edition* **2010**, 49, (27), 4544-4565.
38. Kanamori, K.; Nakanishi, K., Controlled Pore Formation in Organotrialkoxysilane-Derived Hybrids: from Aerogels to Hierarchically Porous Monoliths. *Chemical Society Reviews* **2011**, 40, (2), 754-770.
39. Ciriminna, R.; Fidalgo, A.; Pandarus, V.; Beland, F.; Ilharco, L. M.; Pagliaro, M., The Sol-Gel Route to Advanced Silica-Based Materials and Recent Applications. *Chemical Reviews* **2013**, 113, (8), 6592-6620.
40. Inayat, A.; Reinhardt, B.; Uhlig, H.; Einicke, W. D.; Enke, D., Silica Monoliths with Hierarchical Porosity Obtained from Porous Glasses. *Chemical Society Reviews* **2013**, 42, (9), 3753-3764.
41. Sayen, S. p.; Walcarius, A., Electro-Assisted Generation of Functionalized Silica Films on Gold. *Electrochemistry Communications* **2003**, 5, (4), 341-348.
42. Walcarius, A.; Sibottier, E., Electrochemically-Induced Deposition of Amine-Functionalized Silica Films on Gold Electrodes and Application to Cu(II) Detection in (Hydro)Alcoholic Medium. *Electroanalysis* **2005**, 17, (19), 1716-1726.
43. Kundu, S.; Jayachandran, M., The Self-Assembling of DNA-Templated Au Nanoparticles into Nanowires and Their Enhanced SERS and Catalytic Applications. *Rsc Advances* **2013**, 3, (37), 16486-16498.
44. He, J. W.; Xu, X.; Corneille, J. S.; Goodman, D. W., X-ray Photoelectron Spectroscopic Characterization of Ultra-thin Silicon-Oxide Films on a MO(100) Surface. *Surface Science* **1992**, 279, (1-2), 119-126.
45. Sivakumar, M.; Venkatakrishnan, K.; Tan, B., Characterization of MHz Pulse Repetition Rate Femtosecond Laser-irradiated Gold-Coated Silicon Surfaces. *Nanoscale Research Letters* **2011**, 6.

46. Radnik, R.; Mohr, C.; Claus, P., On the Origin of Binding Energy Shifts of Core Levels of Supported Gold Nanoparticles and Dependence of Pretreatment and Material Synthesis. *Physical Chemistry Chemical Physics* **2003**, 5, (1), 172-177.
47. Karadas, F.; Ertas, G.; Suzer, S., Differential Charging in SiO<sub>2</sub>/Si System as Determined by XPS. *Journal of Physical Chemistry B* **2004**, 108, (4), 1515-1518.
48. Ulgut, B.; Suzer, S., XPS studies of SiO<sub>2</sub>/Si System Under External Bias. *Journal of Physical Chemistry B* **2003**, 107, (13), 2939-2943.
49. Tunc, I.; Demirok, U. K.; Suzer, S.; Correa-Duarte, M. A.; Liz-Marzan, L. M., Charging/Discharging of Au (core)/silica (Shell) Nanoparticles as Revealed by XPS. *Journal of Physical Chemistry B* **2005**, 109, (50), 24182-24184.
50. Matmor, M.; Ashkenasy, N., Peptide Directed Growth of Gold Films. *Journal of Materials Chemistry* **2011**, 21, (4), 968-974.
51. Callister, W. D., Jr., *Fundamentals of Materials Science and Engineering: An Interactive E-Text, 2nd Edition*. Wiley: 2004.
52. Davey, W. P., Precision Measurements of the Lattice Constants of Twelve Common Metals. *Phys. Rev.* **1925**, 25, 753-61.
53. Trasatti, S.; Petrii, O. A., Real Surface-Area Measurements in Electrochemistry. *Pure and Applied Chemistry* **1991**, 63, (5), 711-734.
54. Jia, F. L.; Yu, C. F.; Ai, Z. H.; Zhang, L. Z., Fabrication of Nanoporous Gold Film Electrodes with Ultrahigh Surface Area and Electrochemical Activity. *Chemistry of Materials* **2007**, 19, (15), 3648-3653.
55. Huang, J. F.; Sun, I. W., Fabrication and Surface Functionalization of Nanoporous Gold by Electrochemical Alloying/Dealloying of Au-Zn in an Ionic Liquid, and the Self-Assembly of L-Cysteine Monolayers. *Advanced Functional Materials* **2005**, 15, (6), 989-994.
56. Deng, Y. P.; Huang, W.; Chen, X.; Li, Z. L., Facile Fabrication of Nanoporous Gold Film Electrodes. *Electrochemistry Communications* **2008**, 10, (5), 810-813.
57. Seker, E.; Reed, M. L.; Begley, M. R., Nanoporous Gold: Fabrication, Characterization, and Applications. *Materials* **2009**, 2, (4), 2188-2215.
58. Huang, W.; Wang, M. H.; Zheng, J. F.; Li, Z. L., Facile Fabrication of Multifunctional Three-Dimensional Hierarchical Porous Gold Films via Surface Rebuilding. *Journal of Physical Chemistry C* **2009**, 113, (5), 1800-1805.

## **Chapter 4: Fabrication of Strata-Like Mesoporous Polypyrrole- Silica Nanostructures**

## 4.1. Introduction

This work has been submitted to *Langmuir*.<sup>1</sup> Conducting polymers have fascinated scientists due to their important properties and potential technological applications in energy storage, electrocatalysis, and chemical sensing, as well as in the fabrication of flexible electronics, supercapacitors, batteries, etc.<sup>2-6</sup> However, reduced mechanical properties, stability and processability of the conductive polymer materials have often limited such applications. Doping the conductive polymer material with inorganic components through the formation of organic–inorganic hybrid composites has been an appealing route to overcome these problems.<sup>7-12</sup> Silica is a potential candidate as the inorganic component in such hybrid composites due to its improved mechanical strength, chemical and thermal stability, tunable structure and ease of preparation.<sup>13-15</sup> Indeed, many studies aimed toward the preparation of silica-polymer core-shell particles, silica-polymer nanofibers, polymer-silica films and coatings, and other composite materials have been reported in the literature.<sup>16-25</sup>

Polymer-silica nanocomposites can be prepared in a number of different ways as described in various reviews.<sup>9, 20, 25</sup> Conducting polymers as well as silica xerogels can be prepared *chemically* via addition of an oxidizing agent or condensation catalyst, respectively.<sup>13-15, 26-29</sup> Alternatively, they can be prepared *electrochemically* via direct oxidation of monomers<sup>5</sup> or electrogeneration of the condensation catalyst, respectively.<sup>30-37</sup> The advantage that an electrochemical method provides is the ability to control and fine-tune the film thickness and nanoscale morphology of the composite material by simply varying the applied potential.<sup>36, 37</sup> However, the simultaneous electrochemical formation of the polymer and the silica network at or near the same point in time to form a homogeneous nanocomposite film has proved elusive. This is due in part because polymer films are electrochemically deposited anodically through application of a sufficiently large positive potential while silicate films are electrochemically deposited cathodically through application of a large enough negative potential.

In recent work by Mandler and coworkers, polymer-silica nanocomposite films were prepared via application of alternating potentials.<sup>19</sup> Polypyrrole was deposited upon application of an anodic potential pulse while silica was deposited during the cathodic pulse. A composite film was thus produced, with the morphology and extent of homogeneity of the deposits dependent on the applied potentials, the order of their application, deposition time and electrode material.<sup>19</sup> Ideally, it would be advantageous to be able to co-electrodeposit the polymer and the silica via a single-potential-step. Not only would this greatly simplify the fabrication of polymer-silica nanocomposites but it would likely improve the homogeneity of the deposit since the silica and polymer will be simultaneously produced. Morphology and film thickness can be tuned via changes in the potential applied to the electrode surface.

To be able to form the polymer-silica nanocomposite in a single-potential-step, e.g., cathodically, it will be necessary to generate an oxidizing agent electrochemically via application of sufficiently reductive potentials. In recent work, however, Choi and co-workers.<sup>38</sup> demonstrated the ability to form a conducting polymer, e.g., polypyrrole cathodically by coupling the electrogeneration of the nitrosonium ion ( $\text{NO}^+$ ), as an oxidizing agent with the oxidative polymerization of the pyrrole monomers.  $\text{NO}^+$  ions were generated through the electrochemical reduction of  $\text{NO}_3^-$  ions in a strongly acidic environment. A particulate-like polypyrrole thin film was then cathodically deposited on a copper substrate by the interaction of the electrogenerated oxidizing agent  $\text{NO}^+$  ions and pyrrole monomers at the electrode surface.<sup>38</sup> The applied cathodic potential required to initiate these chemical reactions is similar to that required to produce the sol-gel based catalyst ( $\text{OH}^-$ ), therefore we hypothesized that it may actually be feasible to prepare homogeneous polymer-silica composite films with a single-potential-step.

Herein, we demonstrate the fabrication of polypyrrole-silica ( $\text{Ppy-SiO}_2$ ) and polypyrrole-silica-metal ( $\text{Ppy-SiO}_2\text{-M}$ ) hybrid nanocomposite films on oxidizable (Ag) and non-oxidizable (Au) substrates using a one-step single-potential cathodic deposition process for the first time. The mechanism of the electropolymerization process under cathodic conditions is different from

that occurring under anodic potentials, which allows for the formation of new structures and morphologies and provides new avenues for material synthesis that cannot be achieved using conventional anodic methods including the formation of free-standing films. By controlling the reaction parameters, the morphology of the resulting nanostructured hybrid films can be fine-tuned from particulate-like to wire-like. A novel growth mechanism of Ppy-SiO<sub>2</sub> nanocomposite films is proposed based on understanding the relation between two competing redox reactions, OH<sup>-</sup> and NO<sup>+</sup> electrogenerations, which take place simultaneously at the electrode surface, and the resultant morphology of the electrodeposited Ppy-based materials.

## 4.2. Experimental Section

### 4.2.1. Reagents and Materials

Pyrrole (99%, extra pure) and tetramethoxysilane (TMOS, 99%) were purchased from Acros Organics. Silver nitrate (AgNO<sub>3</sub>, 99.9995% (metals basis), Premion) and sodium nitrate (NaNO<sub>3</sub>, 98+%) were obtained from Alfa Aesar. The hydrofluoric acid (HF, 48-50%), and nitric acid (HNO<sub>3</sub>, 69.3%), were obtained from Fisher Scientific (*CAUTION*: these acids are highly corrosive and must be handled with extreme caution in a fume hood. Gloves, protective clothing, and safety glasses must be used). Potassium ferricyanide K<sub>3</sub>[Fe(CN)<sub>6</sub>] was purchased from Sigma-Aldrich. All the electrodeposition solutions were prepared using ultrapure type-I water (Millipore Milli-Q purification system, 18.2 MΩ·cm at 25 °C) and 200 proof ethyl alcohol (CH<sub>3</sub>CH<sub>2</sub>OH, ACS/USP grade, Pharmco-AAPER). Chemicals were used as received without any further purification. A 100 nm-thick gold-coated glass slides with a 5 nm-thick adhesive layer of titanium were purchased from EMF, Ithaca NY.



#### 4.2.2. Co-electrodeposition of Polypyrrole-Silica-Silver (Ppy-SiO<sub>2</sub>-Ag@Au) and Polypyrrole-Silica (Ppy-SiO<sub>2</sub>@Ag) Hybrid Nanocomposite Films on Gold and Silver Substrates, Respectively

The gold electrodes (1 cm x 2.5 cm) were cleaned by successive sonication in soap, water, ethanol and water, each for 10 min followed by drying under nitrogen stream. The electrodes were then plasma cleaned (PE2000 RF Plasma Etcher, South Bay Technology) at 30 W, DC bias of -400 V and 140 mtorr in oxygen for 5 minutes. The electrodeposition solution was prepared as follow: first, the silica sol was obtained by a continuous stirring of 1250  $\mu$ L of 1.6 M NaNO<sub>3</sub>, 1120  $\mu$ L of H<sub>2</sub>O, 180  $\mu$ L of HNO<sub>3</sub> (69.3%), 400  $\mu$ L of TMOS, and 6.05 mL of EtOH for 8 h at 800 rpm using a digital stir plate. Then 20 mg of AgNO<sub>3</sub> were added to the hydrolyzed silica sol and stirred for 15 min. After that, 200  $\mu$ L of pyrrole were injected into the silver-silica sol and stirred for 2 min to produce a transparent electrodeposition solution with a pH of 1.4. For the preparation of Ppy-SiO<sub>2</sub>-Ag@Au (**sample A**), the as-prepared electrodeposition solution was transferred into a conventional three-electrode electrochemical cell housing a silver chloride-coated silver wire in 1.0 M KCl (Ag/AgCl/1.0M KCl) reference electrode, a polypyrrole pre-coated platinum wire as a counter electrode and a gold slide as the working electrode. A  $\frac{1}{4}$  in circle in a piece of tape (UHMW polyethylene tape, CS Hyde) defines the electrode area to be 0.32 cm<sup>2</sup>. The co-electrodeposition experiment was carried out at room temperature under an amperometric mode using an applied potential of -1.0 volts without stirring and controlled by a CHI-1000A potentiostat. Deposition took place for 30 min to produce a dark-navy-blue nanocomposite thin film (Ppy-SiO<sub>2</sub>-Ag@Au). The electrode was removed from the electrodeposition solution while the potential was still applied to avoid further deposition of silica, possible over-oxidation of polypyrrole by the electrogenerated nitrosyl ions or dissolution of Ag nanoparticles by HNO<sub>3</sub>. The Ppy-SiO<sub>2</sub>-Ag@Au thin film was carefully rinsed with deionized water and kept in a moisture-rich environment (e.g. desiccator bottom filled with hot water) for at least a week to slowly dry before further treatment. (*CAUTION: drying the as-prepared nanocomposite thin film in air and/ or not keeping it for enough time in the moisture-*

*rich environment will lead to its destruction in the subsequent treatments*). The properly dried Ppy-SiO<sub>2</sub>-Ag@Au nanostructured thin films were air-stable (no cracks nor peeling from the substrate was observed) for more than 8 months. For the preparation of Ppy-SiO<sub>2</sub>@Ag nanocomposite thin film (**sample B**), the same methodology was used but AgNO<sub>3</sub> was absent in the deposition solution and a silver-coated gold substrate was used. The silver-coated gold substrate was obtained by depositing silver from a 7 mM AgNO<sub>3</sub> in 0.1 M HNO<sub>3</sub> plating solution on a clean gold electrode at -0.6 volts for 500 sec. For comparison, a Ppy thin film was deposited under anodic potential of +1.0 volts for 400 sec from the same electrodeposition solution but in absence of the silane monomer (TMOS) and AgNO<sub>3</sub>. The kinetics of the electrodeposition reaction were investigated by carrying out the Ppy-SiO<sub>2</sub>-Ag@Au electrodeposition at -1.0 volts for 1, 2 and 4 min. In addition, the effect of the applied potential (-0.6 and -0.8 volts) was also investigated.

To confirm that electropolymerization of pyrrole monomers was induced only by the *in situ* electrochemically generated nitrosonium ions, several electrodeposition solutions were allowed to age for 30 min in closed glass vials without applying any potential and the color of the electrodeposition solution was monitored. No change in color was observed. To investigate the reaction mechanism, five sets of control experiments were performed in addition to the above-mentioned time- and potential-based control experiments. Electrodeposition of Ppy-SiO<sub>2</sub>-Ag@Au was repeated under the following conditions (a) absence of the silane monomer (TMOS), (b) low sodium nitrate concentration of 0.08 M, (c) low pH obtained by increasing the HNO<sub>3</sub> concentration to 1.0 M, (d) low pyrrole monomer concentration of 0.08 M, (e) absence of ethanol in a pure aqueous environment.

#### **4.2.3. Fabrication of Free-Standing and Transferable Polypyrrole Thin Films**

A new multistep etching strategy for the dissolution of silica or silver from the nanocomposite hybrid thin films was developed and named localized drop-cast dealloying (LDCD) (**Figure 4.1**). Typically, LDCD was carried out as follow: the nanocomposite film was

completely covered with 3-5 drops of 3.0% HF and allowed to incubate for 10 min. During the incubation time, the film released from the electrode surface and the used HF carefully and safely discarded using a disposable pipet to allow the released film to re-settle on the substrate as displayed in **Figure 4.1 (d)**. To completely etch the silica, the released film was carefully transferred into a Teflon beaker filled with 5.0% HF (the HF level should be 1-2 cm above the film surface) and allowed to settle for 10 min. The free-standing film on a gold slide was transferred into a deep plastic dish filled with deionized water and allowed it to sit 10 min, **Figure 4.1 (e)**. This step was repeated two times. The free-standing film was transferred to a suitable substrate (e.g. gold, glass, stainless steel, ITO, etc., (**Figure 4.1 (f)**) and dried in a moisture-rich environment for at least two days before characterization or further treatment. To remove the silver particles from the nanocomposite thin films or to dissolve the underlying silver substrate by LDCD, the nanocomposite thin films were first covered with few drops of 2% HNO<sub>3</sub> for 30 min followed by full immersion in 1:1 HNO<sub>3</sub> for 30 min. They were then immersed twice in deionized water for 10 min and transferred into a moisture-rich environment for at least two days. Application of the LDCD technique to Ppy-SiO<sub>2</sub>-Ag@Au and Ppy-SiO<sub>2</sub>@Ag nanocomposite films resulted in the fabrication of several free-standing nanostructured thin films listed in **Table 4.1**. The resulting free-standing thin films stored in moisture-rich environments are stable for more than 8 months.

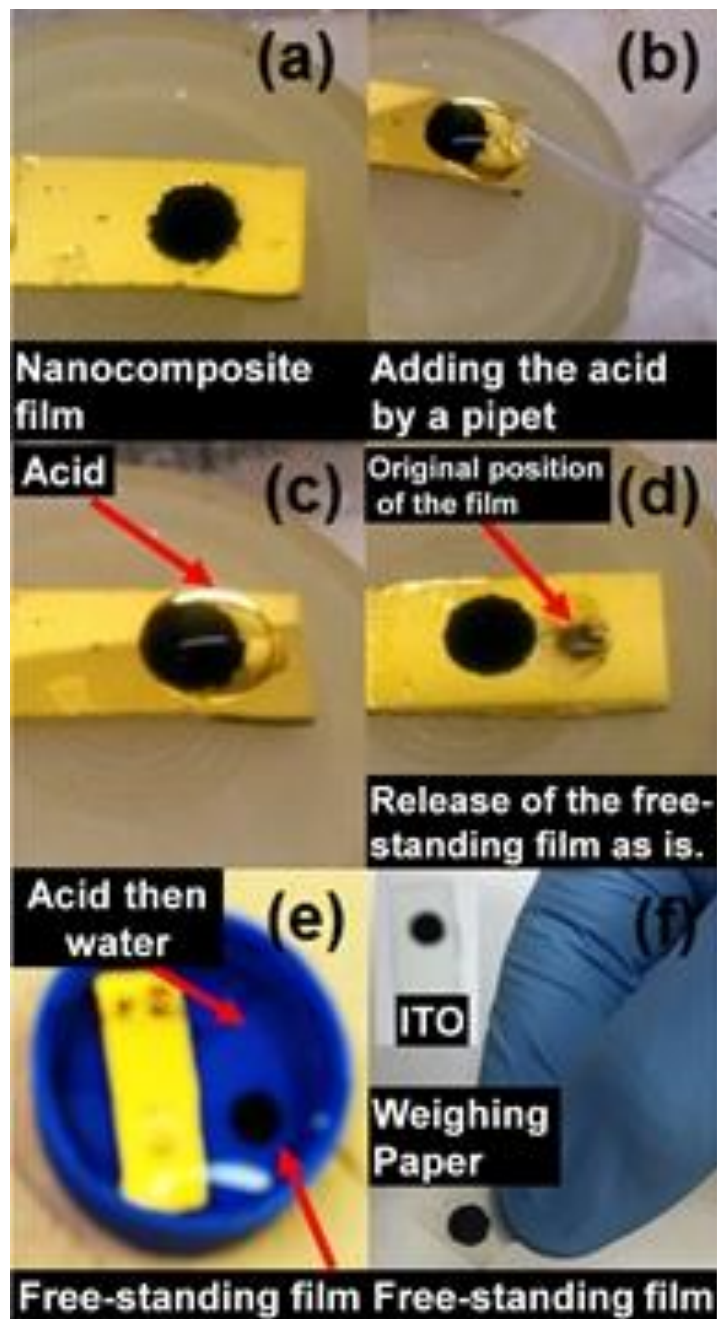


**Figure 4.1.** Fabrication of free-standing and transferable polypyrrole-based thin films by the localized drop-cast dealloying (LDCD) technique (a-e). Loading the free-standing film on ITO electrode and weighing paper (f).

**Table 4.1.** Polypyrrole and polypyrrole hybrid nanocomposite thin films.

Number	Sample	Chemical composition	Preparation	Mounting nature
1	Ppy-SiO <sub>2</sub> -Ag@Au	Polypyrrole-silica-silver	Electrodeposition, main sample <b>A</b>	Deposited on gold substrate
2	Ppy-SiO <sub>2</sub> @Ag	Polypyrrole-silica	Electrodeposition, main sample <b>B</b>	Deposited on silver substrate
3	Ppy-Ag	Polypyrrole-silver	Treating sample <b>A</b> with HF	Free-standing film
4	Ppy	Polypyrrole	Treating sample <b>A</b> with HF and HNO <sub>3</sub> successively	Free-standing film
5	Ppy	Polypyrrole	Treating sample <b>B</b> with HF	Free-standing film
6	Ppy	Polypyrrole	Treating sample <b>B</b> with HF and HNO <sub>3</sub> successively	Free-standing film
7	Ppy-SiO <sub>2</sub>	Polypyrrole-silica	Treating sample <b>B</b> with HNO <sub>3</sub>	Free-standing film
8	Ppy	Polypyrrole	Treating sample <b>B</b> with HNO <sub>3</sub> and HF successively	Free-standing film

#### 4.2.4. Characterization

The morphological aspects and chemical composition of the electrodeposited and free-standing films were examined by field emission scanning electron microscopes (FE-SEM, HITACHI SU-70 and HITACHI S4300) equipped with energy dispersive X-ray spectrometer (EDX). Film thickness was measured using a surface profilometer (Alpha-Step IQ Surface Profiler, KLA-Tencor Co., San Jose, CA) on samples captured on glass or gold-coated glass slides. X-ray diffraction (XRD) patterns were recorded at room temperature in  $\theta$ - $2\theta$  geometry by a PANalytical X'Pert Pro MPD series diffractometer equipped with a Pixcel detector and Cu K $\alpha$  radiation ( $\lambda = 1.54060 \text{ \AA}$ ) at an operating voltage of 45 kV and 40 mA current to determine the crystal nature and phase composition of the as-prepared thin films. A total of 20 thin films prepared under the same conditions were collected, grounded, and the powder loaded on a no background, low volume holder for the XRD measurements. X'Pert HighScore Plus software with ICDD/ JCPDS database was used to analyze the XRD data and identify the crystal-phase composition in the as-prepared thin films. The average crystallite size for each crystalline phase was determined by Scherrer equation. A Micromeritics model ASAP-2020 surface area and pore size analyzer was utilized to acquire the N<sub>2</sub> adsorption-desorption isotherms at 77 K. The nanocomposite samples were outgassed under vacuum at 80 °C for 24 h prior to the measurements. The surface areas of the as-prepared nanocomposites were calculated by fitting the collected isotherm data using Brunauer, Emmett, and Teller (BET) model. The desorption isotherms data were fitted by Barrett, Joyner, and Halenda (BJH) model to calculate the average pore diameters, and pore-size distribution. Electrochemical characteristics of the free-standing Ppy-SiO<sub>2</sub> thin films were investigated by means of cyclic voltammetry and compared to Ppy thin films deposited under an anodic potential of +1.0 volts for 400 sec.

### 4.3. Results and Discussion

#### 4.3.1. Synthesis of Conducting Polymer-Silica (Ppy-SiO<sub>2</sub>-Ag@Au & Ppy-SiO<sub>2</sub>@Ag) Nanocomposite Thin Films

To date, there is no available strategy to simultaneously synthesize conducting polymer-silica hybrid nanocomposites via a single deposition potential process. **Figure 4.2** is a graphical illustration of the nanocomposite and free-standing films fabrication strategy. The mechanism of

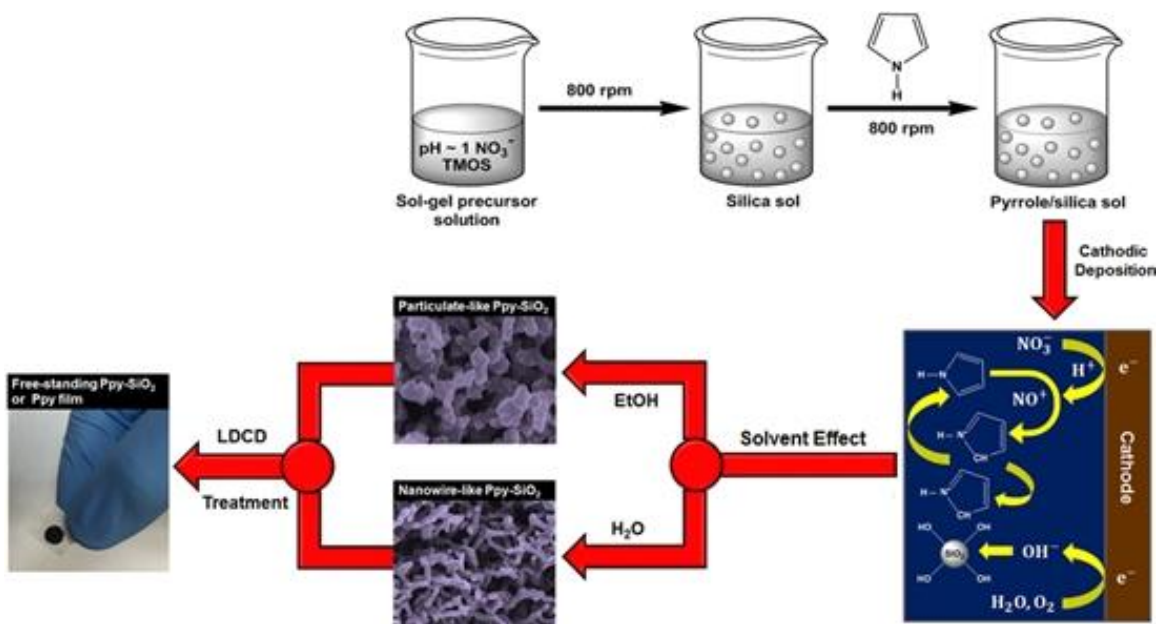
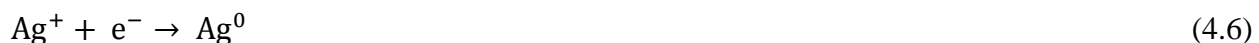


**Figure 4.2.** Schematic Illustration (Not Drawn to Scale) of the Fabrication of Ppy-SiO<sub>2</sub> Mesoporous Nanostructured Composite Films through the Cathodic Co-Deposition of Ppy and SiO<sub>2</sub> from Pyrrrole-Silica Sol and the Application of the LCD Etching Strategy to Produce Ppy-SiO<sub>2</sub> and Ppy Free-Standing Films.

the single-step co-electrodeposition of Ppy-SiO<sub>2</sub>-Ag@Au and Ppy-SiO<sub>2</sub>@Ag hybrid films is complicated. The synthesis strategy is based on the combination of electrodeposition, electrochemical reduction, sol-gel chemistry and free-radical polymerization processes in a strongly acidic environment. Although each of these processes involve multiple steps, the main stage during the formation of hybrid nanocomposite thin films is the *in situ* electrogeneration of two catalysts simultaneously: one for the hydrolyzed sol-gel monomers polycondensation (e.g., OH<sup>-</sup>),<sup>34</sup> and the second for pyrrole monomers oxidation and polymerization (e.g., NO<sup>+</sup>).<sup>38-41</sup> The reaction conditions were optimized to generate appreciable amounts of both catalysts.

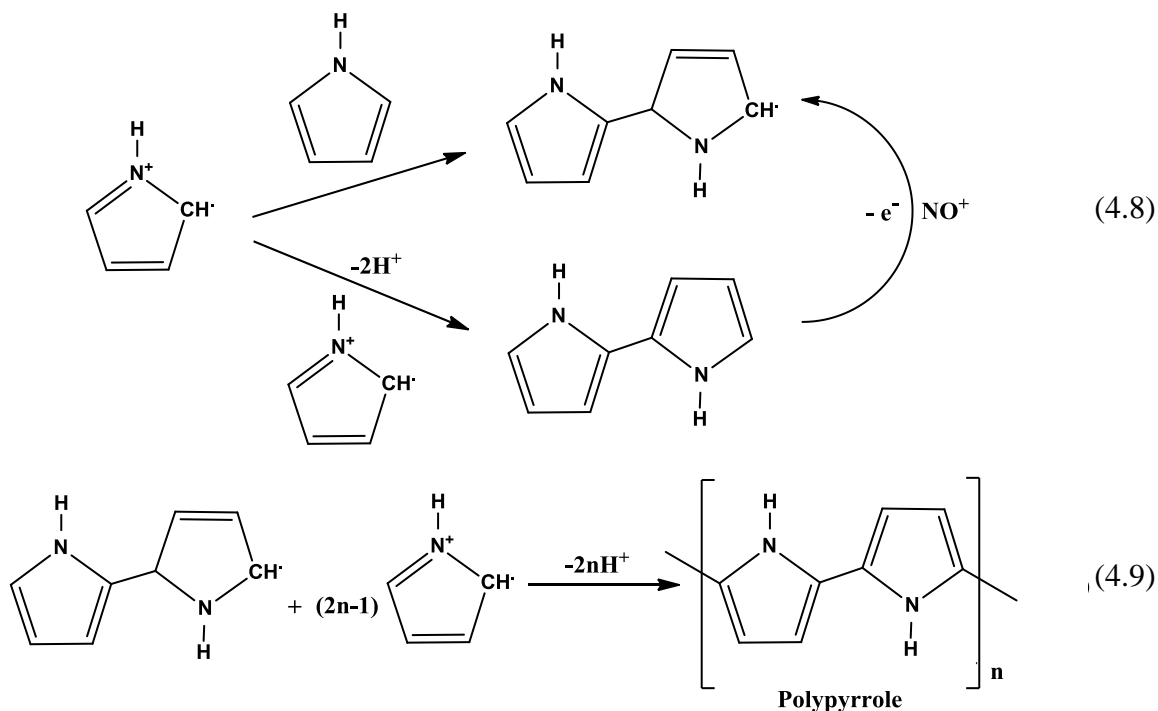
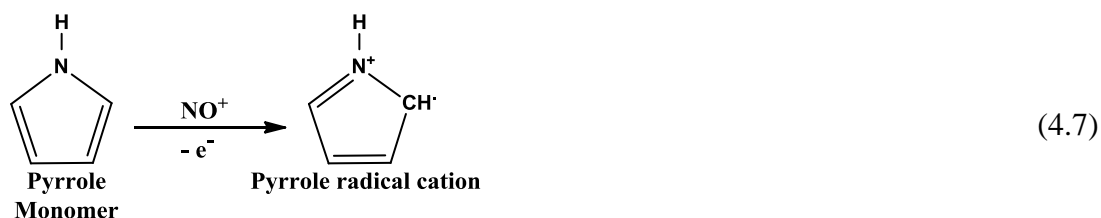
The multi-step reaction begins with silica sol formation through the acid catalyzed hydrolysis of TMOS (silane monomer) for 8 h. The strongly acidic reaction medium (pH ~ 1) and prolonged reaction time ensures a nearly complete hydrolysis of the silica monomer. The silver precursor (AgNO<sub>3</sub>, zero or 20 mg) and the pyrrole monomer were added successively to the silica sol to produce a transparent two/three-component electrodeposition solution. The electrodeposition solution retained its transparency and its color did not change after aging for 30 min at ambient conditions in a closed vial. This finding indicated that the pyrrole monomers did

not undergo any polymerization and reflected the stability of the electrodeposition solution within the time frame of the electrodeposition reaction. Furthermore, it confirms that electropolymerization of pyrrole monomers is achieved only by the *in situ* electrogenerated oxidation catalyst, NO<sup>+</sup>. Upon the application of a large enough negative potential (e.g., -1.0 volts) to the electrode surface, simultaneous redox reactions promptly take place at the electrode/electrolyte interface as shown in **equations (1-6)**. First, the electrochemical reduction of the nitrate ions (NO<sub>3</sub><sup>-</sup> from NaNO<sub>3</sub> and HNO<sub>3</sub>) in a strong acidic medium (pH ~ 1) to produce nitrous acid (HNO<sub>2</sub>, pKa = 3.3) which is kinetically unstable under the reaction conditions and undergoes a dissociation reaction to produce a strong oxidizing agent and electrophile, the nitrosonium ion (NO<sup>+</sup>, E<sup>o</sup><sub>red</sub> = 1.50 volts vs. SCE) as previously demonstrated.<sup>38, 41</sup> Second, the reduction of oxygen and/or water in the system<sup>31-35</sup> yields the sol-gel polycondensation base catalyst (OH<sup>-</sup>). The third reaction is the electrodeposition of silver particles through the electrochemical reduction of the silver ions.



Pyrrole monomers are chemically oxidized at vicinity of the electrode surface by the *in situ* electrogenerated nitrosonium ions (NO<sup>+</sup>) in a free radical polymerization process and eventually Ppy deposits on the electrode surface as shown in **equations 7-9, Figure 4.3, and Figure 4.2.**<sup>41, 42</sup>





The hydrolyzed silica monomers undergo a polycondensation reaction catalyzed by the *in situ* electrogenerated base catalyst ( $\text{OH}^-$ ) at the electrode/solution interface.<sup>31-36</sup> As a result colloidal silica particles are immediately deposited at the electrode surface via a base-catalyzed sol-gel process taking place at the electrode/solution interface.<sup>31-36</sup> The color of electrodeposited Ppy-SiO<sub>2</sub> nanocomposite films is deep-navy-blue with a black appearance as displayed in **Figure 4.1**.

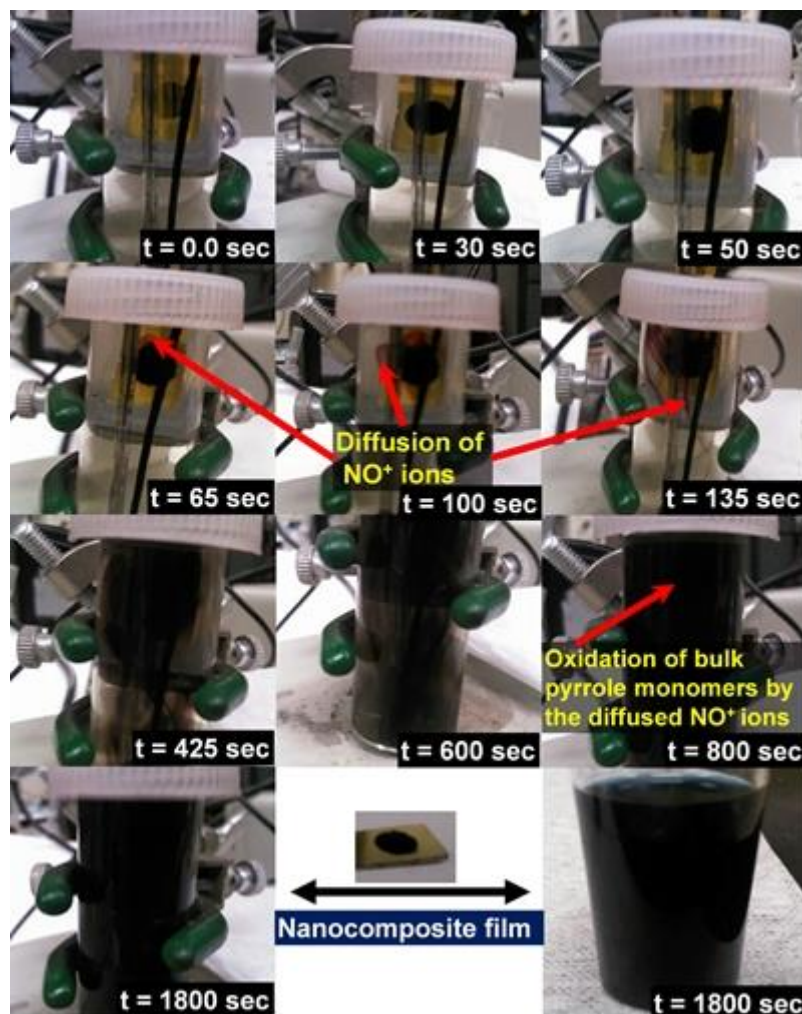


**Figure 4.3.** Photographs at different intervals during the co-electrodeposition of the nanocomposite film. The electrogenerated nitrosonium  $\text{NO}^+$  ions started to diffuse beyond the electrode surface at  $t = 60$  sec and complete diffusion was achieved at  $t = 600$  sec. The pyrrole monomers in the bulk oxidized at  $t = 800$  sec. The progress of reaction indicates that Ppy deposited within and around the silica mesopores.

#### 4.3.2. Surface Morphology

**Figure 4.4** shows the scanning electron micrographs of Ppy-SiO<sub>2</sub>-Ag@Au and Ppy-SiO<sub>2</sub>@Ag nanocomposite films fabricated by cathodic co-deposition of Ppy, SiO<sub>2</sub> and Ag at -1.0 volts for 30 min from an ethanolic solution containing 0.3 M TMOS, 0.22 M NaNO<sub>3</sub>, 0.31 M HNO<sub>3</sub>, 13.08/0.0 mM AgNO<sub>3</sub>, and 0.33 M pyrrole. All the presented SEM micrographs were collected from the as-prepared thin films without application of a conductive coating such as gold or platinum. Typically, an electrodeposited silica film displays severe charging problems

during the imaging process due to its non-conductive nature and thus has to be coated with a thin conductive film (e.g. Au, C or Pt) before the imaging event.<sup>34</sup> In the present work, no significant charging effects were observed suggesting that Ppy was homogeneously deposited within and around the colloidal silica particles. Additional details about the chemical composition of the films are provided in later sections.

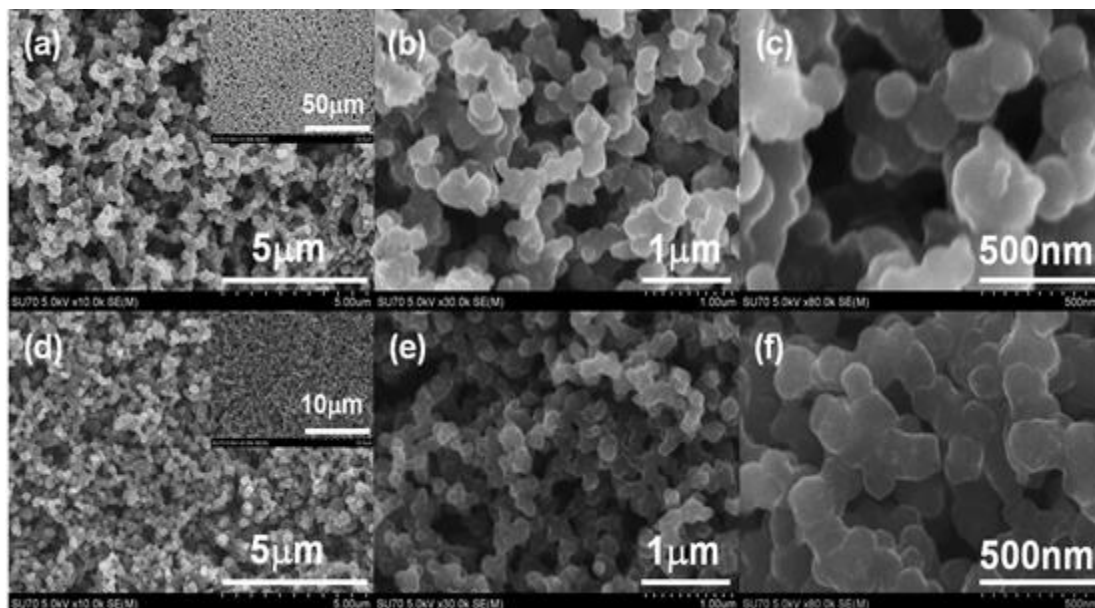


**Figure 4.4.** SEM images of the as-prepared Ppy-SiO<sub>2</sub>-Ag@Au (a-c, sample A) and Ppy-SiO<sub>2</sub>@Ag (d-f, sample B) nanocomposite films electrodeposited at -1.0 volts for 30 min.

Under low magnification, the SEM images reveal the formation of porous thin films (**inset of Figure 4.4 (a, d)**) that cover the surface completely while at high magnification, the microstructure of the co-deposited hybrids is rough, and particulate/colloidal in nature. The particulate-like structure is composed of quasi-spherical aggregates that are interconnected to each other in such a fashion as to create a multimodal porous structure composed of small mesopores and much larger macropores. The surface of the quasi-spherical aggregates themselves is rough and characterized by the presence of superficial nanoparticles. The size of the co-electrodeposited nanocomposite aggregates ranged from 70-470 and 30-380 nm in diameter for Ppy-SiO<sub>2</sub>-Ag@Au and Ppy-SiO<sub>2</sub>@Ag, respectively. The observed large diameter ( $d \geq 200$  nm) of some aggregates could be attributed to the fact that these aggregates consist of two

or more fused spherical or quasi-spherical particles. Overall, the morphology of the two as-prepared films are very similar.

To understand the morphology and ultimately the composition of the films in more detail, the deposition potential, deposition time, and the concentrations of the most important reagents were varied. For this study, only one reaction parameter was changed at a time while all the others were kept constant. The SEM images of the nanocomposite hybrid films prepared at different deposition times (0.5, 1, 2 and 4 min) are shown in **Figure 4.5** while that deposited at longer deposition time (30 min) is displayed in **Figure 4.4**. It is clearly evident that the morphology of the as-prepared hybrid films strongly depends on the deposition time. For a deposition time of 0.5 or 1 min, the electrodeposited particles have a near perfect spherical shape and start to interconnect; the deposited film is composed of a number of nanocomposite clusters. The observation of spherical particles at the early stages of the electrodeposition reaction is in agreement with the previous reports which stated that formation of the Ppy nanowire-based films started with the cathodic deposition of a thin layer of Ppy nanospheres.<sup>38, 41</sup> As the reaction time proceeds beyond 1.0 min, the interconnected particles are no longer near perfect spheres and the nanocomposite clusters became more and more cross-linked and span the entire surface, resulting in the formation of a three-dimensional open network with a multimodal porosity (**Figure 4.5 (e-h)**). At longer deposition times, the degree of the cross-linkage increases and the film becomes thicker (**Figure 4.4**). It is worth pointing out that nanocomposite films formed at deposition times  $\geq 2.0$  min have aerogel-like microstructures.<sup>43</sup>

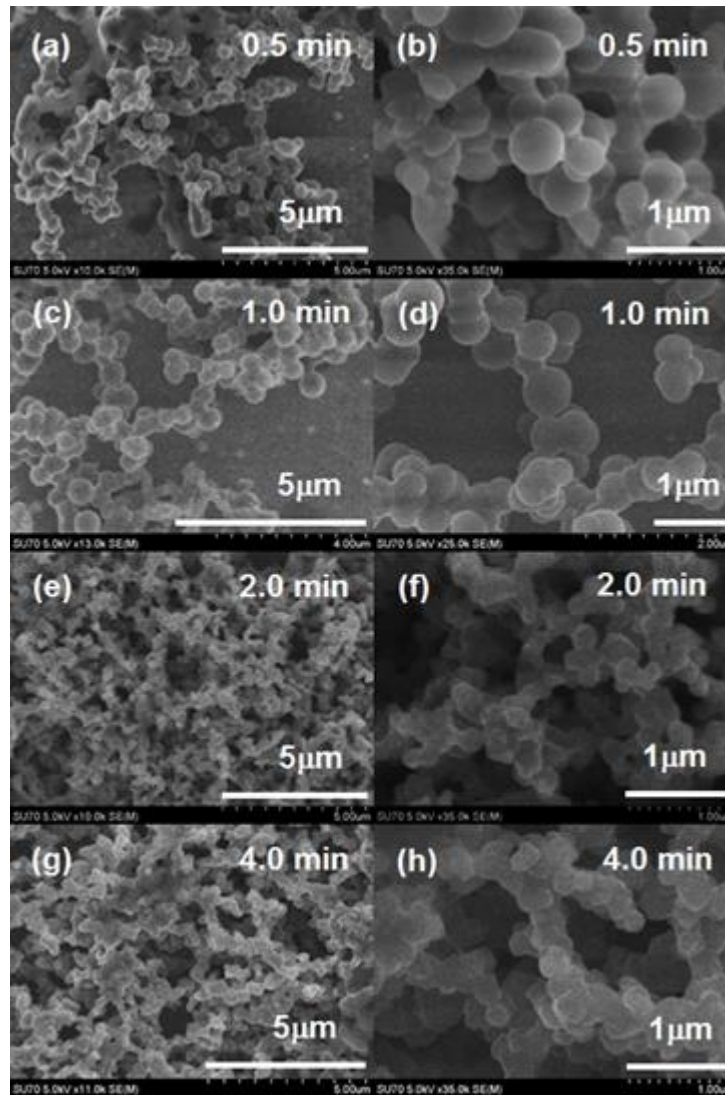


**Figure 4.5.** SEM images of Ppy-SiO<sub>2</sub>-Ag@Au nanocomposite films prepared at different deposition times at -1.0 volts. At early stages of the reaction ( $t \leq 60$  sec) spherical nanoparticles formed. At  $t \geq 2$  min the 3D open framework forms and the film continues to grow thicker with time.

The microstructure of the co-electrodeposited films also depends on the magnitude of the applied potential. **Figure 4.4** and **Figure 4.6** show SEM micrographs of materials obtained at -1.0, -0.8 and -0.6 volts. The electrodeposited hybrid films are particulate in nature and have a three-dimensional open framework structure that depends on the deposition potential. Upon careful examination of the low and high magnification SEM images, it can be noted that the pores of the film deposited at -1.0 volts are smaller than those of the film deposited at -0.6 volts.

In addition, the size of the nanocomposite aggregates decreases as the potential is made more negative. The films deposited at -0.6 and -0.8 volts are also weakly adhered to the conductive substrate, consistent with reduced crosslinking, and could be destroyed upon the removal of the deposited film from the electrodeposition solution. Careful attention is required in handling such films.

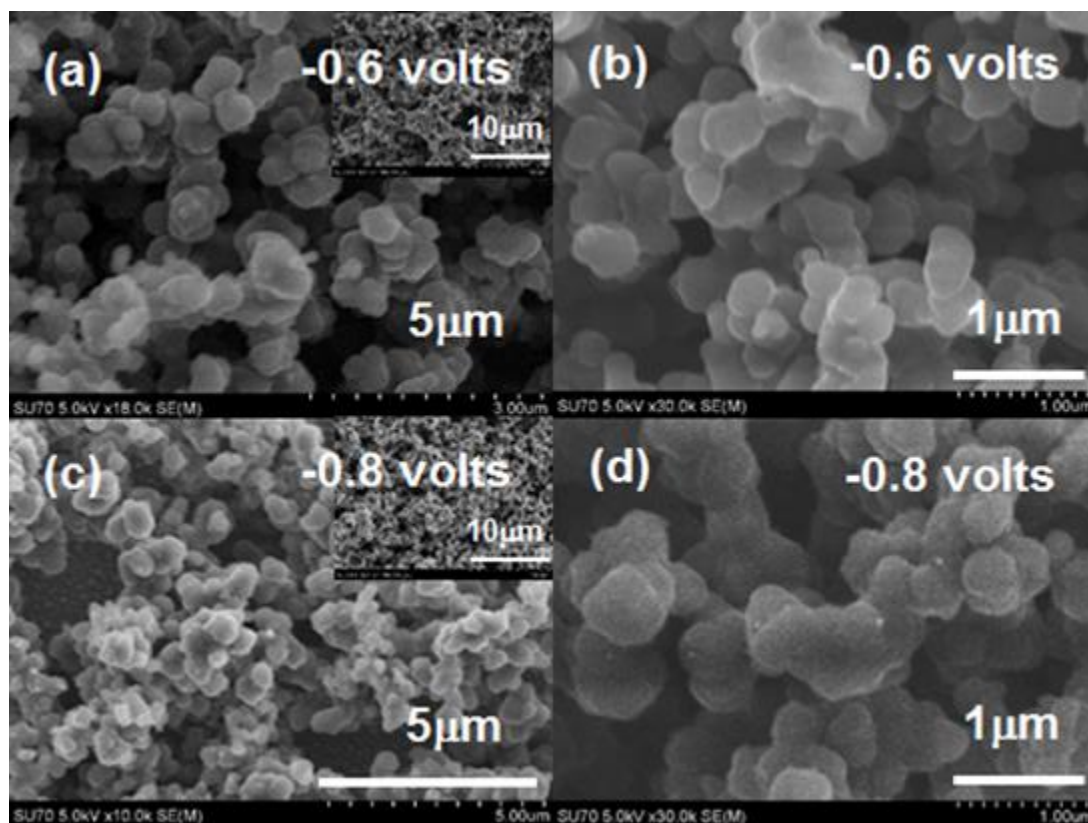


**Figure 4.6.** SEM images of Ppy-SiO<sub>2</sub>-Ag@Au nanocomposite films prepared at: -0.6 volts (a & b) and -0.8 volts (c & d) for 30 min.

The individual effects of changes in either the concentration of sol-gel monomer (TMOS), pyrrole monomer, nitric acid, or sodium nitrate can be seen in **Figure 4.7**. In all cases the SEM images depict a porous open framework consisting of interconnected clusters of irregular shaped particles. It was surprising that even in the absence of TMOS, a particulate-like Ppy nanostructured film was obtained instead of the expected nanowire-like film as reported before by Koh et al. at seemingly comparable conditions, **Figure 4.7 (a, b)**.<sup>40</sup> Of the four parameters that were varied, the one that gave rise to the largest change in morphology was the

concentration of the acid. Compared with the lower  $\text{HNO}_3$  concentration, the nanocomposite film prepared at higher  $\text{HNO}_3$  concentration is strongly adhered to the conductive substrate, highly cross-linked, rich in the small pores and rougher than the film prepared at lower  $\text{HNO}_3$  concentration, **Figure 4.7 (e, f)**.

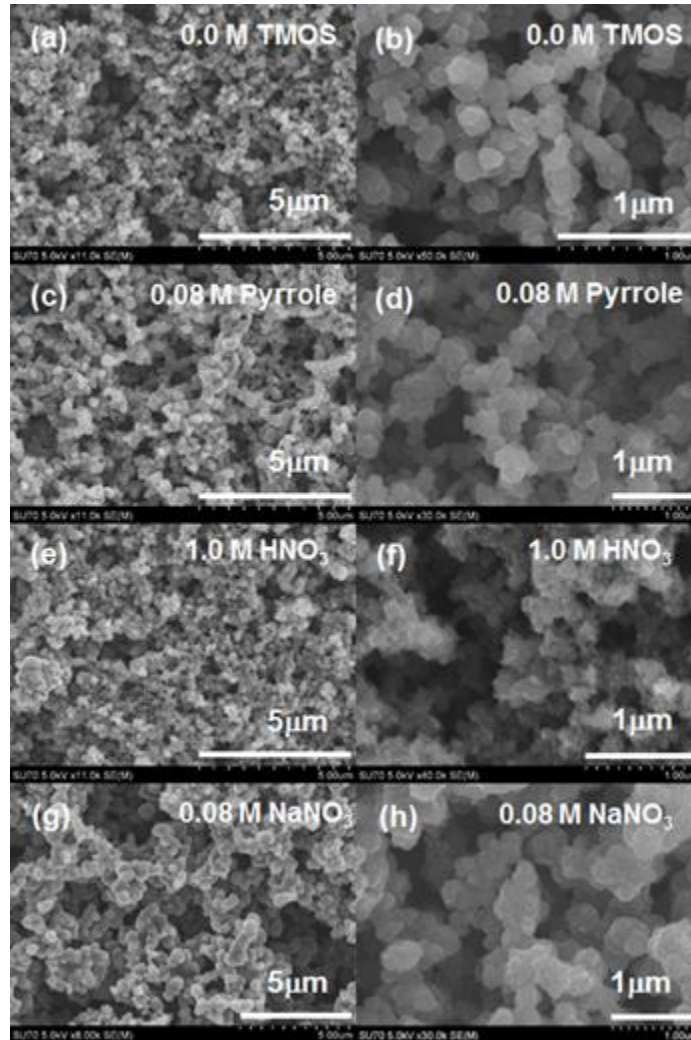


**Figure 4.7.** SEM images reflect the effect of different concentration parameters on the morphology of Ppy-SiO<sub>2</sub>-Ag@Au nanocomposite films electrodeposited at -1.0 volts for 30 min.

#### 4.3.3. Free Standing and Transferable Composite Films by LDCD

A variety of porous, conductive, and free-standing films can easily be made by using the new multistep etching strategy termed localized drop-cast dealloying (LDCD), **Figure 4.1**.

Selective dissolution of silica and/or silver in the as-prepared Ppy-SiO<sub>2</sub>-Ag@Au and Ppy-SiO<sub>2</sub>@Ag nanocomposite thin films with diluted HF and HNO<sub>3</sub> acids leads to a series of free-standing and transferable pure and hybrid Ppy thin films, **Table 4.1**. The co-electrodeposited hybrid films release during the HF acid treatment without cracking or damage, suggesting a strata-like structure with the portion of the film deposited closest to the electrode surface is silica-rich (see below). The deep-navy-blue color of the acid-etched free-standing films is similar to that of the non-etched nanocomposite films, which reflects the uniformity in composition of the electrodeposited nanocomposite films. **Figure 4.8** and **Figure 4.9** show SEM images of the free-standing Ppy-SiO<sub>2</sub>, Ppy-Ag and Ppy thin films obtained after the dissolution and selective chemical etching of silica and/or silver. The materials are more porous and maintained the original particulate-like three-dimensional microstructure of the co-electrodeposited nanocomposite films. It also appears that the as-prepared nanocomposite films are rougher than the corresponding free-standing films.

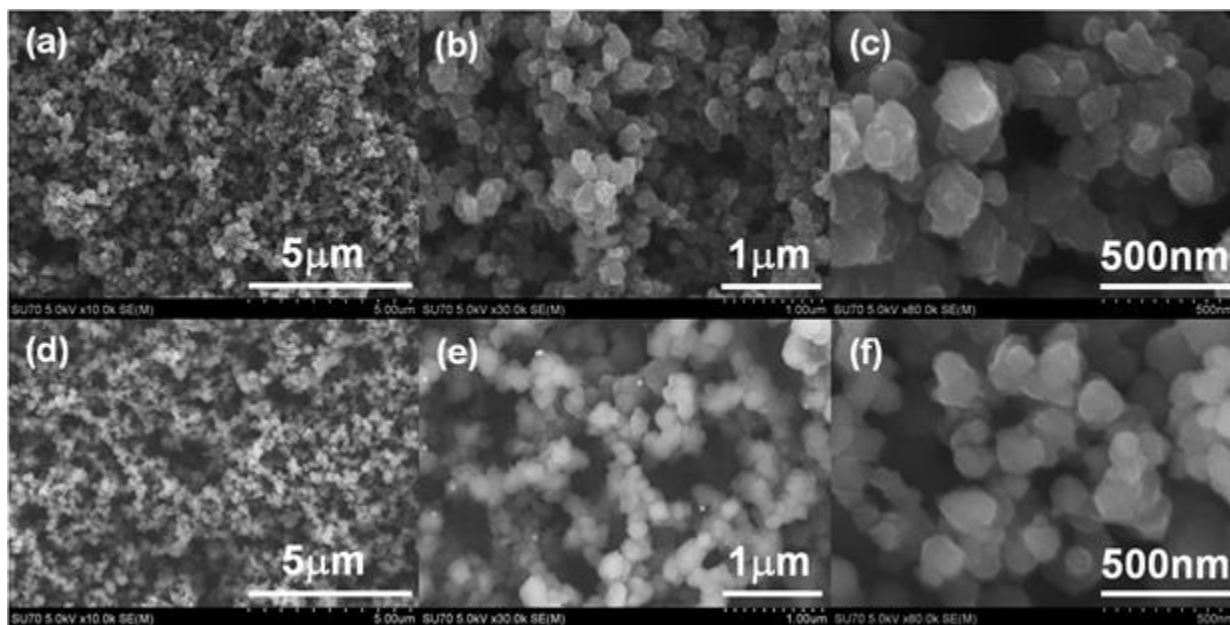


**Figure 4.8.** SEM micrographs of the Ppy-Ag free-standing film obtained by treating sample A with HF (a-c) and Ppy free-standing film obtained by treating sample A with HF and HNO<sub>3</sub>, successively (d-f).



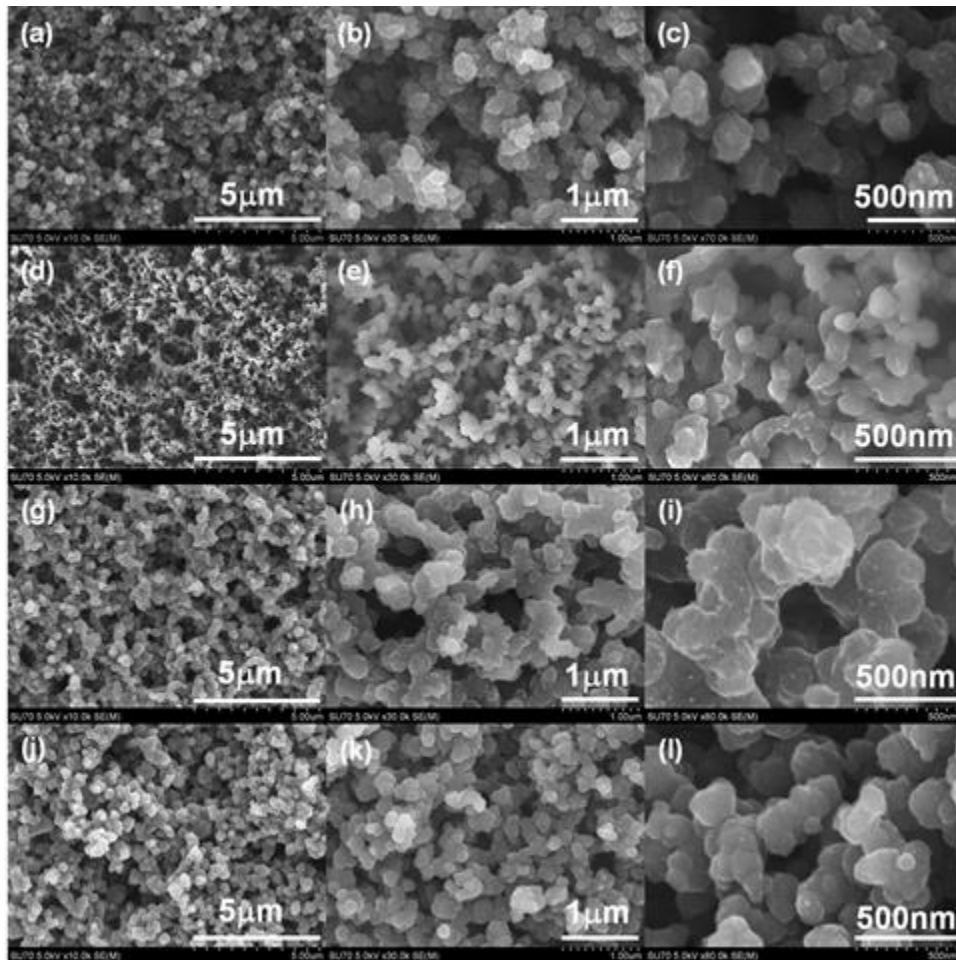


**Figure 4.9.** SEM images of Ppy@Ag thin film obtained by treating sample B with HF (a-c). Ppy free-standing free obtained by treating sample B with HF and HNO<sub>3</sub>, successively (d-f). Ppy-SiO<sub>2</sub> free-standing film obtained by treating sample B with HNO<sub>3</sub> (g-i). Ppy free-standing film obtained by treating sample B with HNO<sub>3</sub> and HF, successively (j-l). The non-destruction of the film reflects its homogeneity.

To better evaluate surface roughness and film thickness, surface profilometry was undertaken. **Figure 4.10** shows the surface profiles across a sharp edge of the as-prepared Ppy-SiO<sub>2</sub>-Ag@Au nanocomposite film and the corresponding Ppy-Ag and Ppy free-standing films. The surface profile of the as-prepared nanocomposite film is characterized by the presence of larger spikes/oscillations, which is indicative of a rougher surface. The decrease in magnitude and number of oscillations in the surface profile of the free-standing films compared with those

in surface profile of the mother nanocomposite film might be attributed to the presence of superficial particles that dissolve during the acid treatment. The SEM measurements demonstrated the presence of such superficial particles in the electrodeposited nanocomposite films as pointed out earlier. It is interesting and noteworthy to point out that thickness of the co-deposited nanocomposite film did not change significantly in the corresponding free-standing films obtained after silica and silver removal. This finding reflects the homogeneity in composition of the electrodeposited nanocomposite films. A non-homogeneous film such as a film with large silica or Ppy aggregates or a film formed by the layer-by-layer deposition technique in which the silica and Ppy layers are segregated<sup>19</sup> will either be destroyed or show a significant decrease in thickness upon the acid treatment.

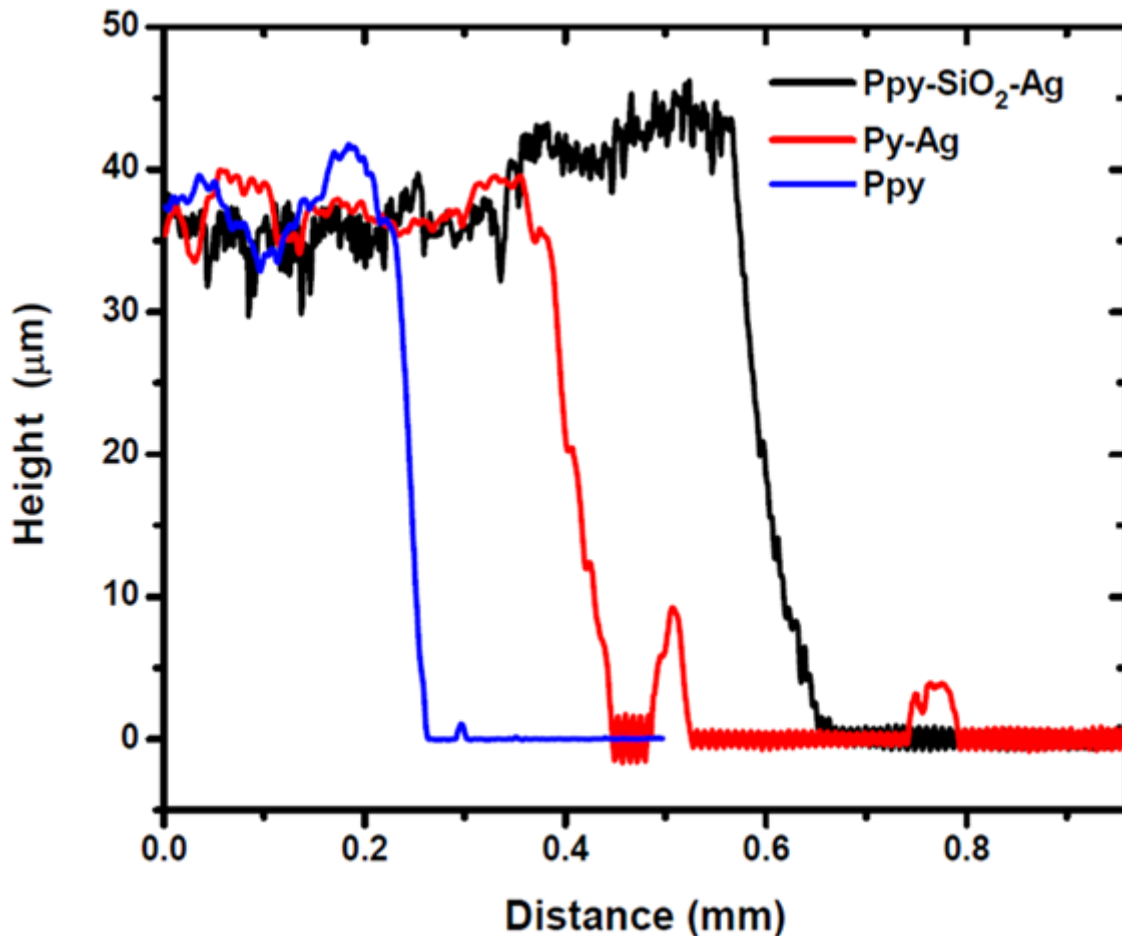


**Figure 4.10.** Surface profiles of the as-prepared Ppy-SiO<sub>2</sub>-Ag@Au nanocomposite film (sample A), Ppy-Ag free-standing nanocomposite film (sample A + HF) and Ppy free-standing

film (sample A + HF + HNO<sub>3</sub>). The homogeneity of the deposited nanocomposite film is evident.

To obtain additional quantitative information about the porosity of the nanostructured composite films, nitrogen adsorption/desorption measurements were undertaken. In these experiments, multiple films were combined to obtain enough powder to perform the measurements. **Figure 4.11** shows the isotherms, which reveal a type IV curve characteristic of mesoporous structures.<sup>44, 45</sup>

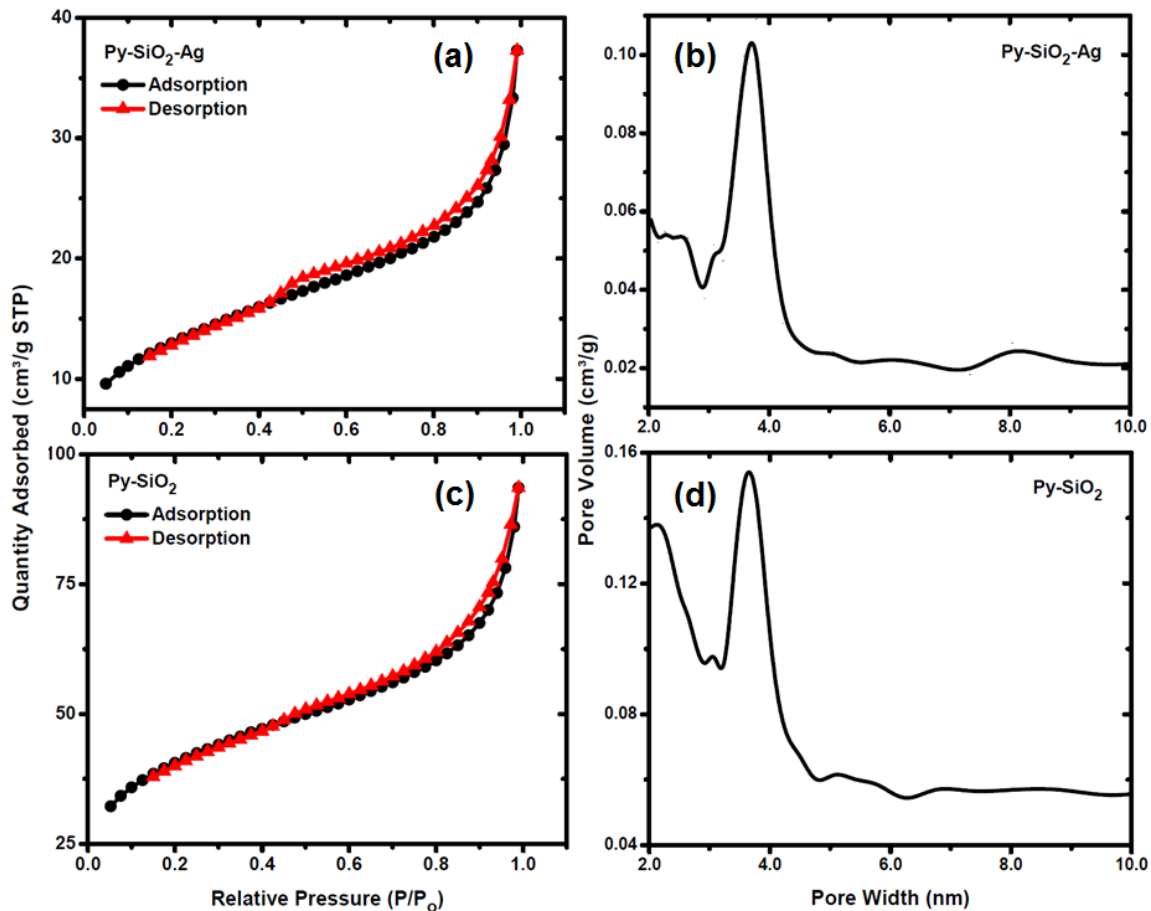


**Figure 4.11.** Nitrogen adsorption/desorption isotherms of the as-prepared Ppy-SiO<sub>2</sub>-Ag@Au (sample A) and the Ppy-SiO<sub>2</sub> (obtained by applying the LDCD etching strategy to sample A) nanocomposite films and the corresponding BJH-modeled pore size distribution.

The specific surface areas calculated using the BET model were found to be 45 and 136 m<sup>2</sup>/g for the electrodeposited Ppy-SiO<sub>2</sub>-Ag and the chemically etched Ppy-SiO<sub>2</sub> nanocomposite films,

respectively. These values are significantly higher than BET specific surface areas reported for anodically electrodeposited Ppy films (4.8 m<sup>2</sup>/g) and chemically synthesized Ppy (6.0-21.1m<sup>2</sup>/g) which are mainly non-porous.<sup>28, 29</sup> The Barrett-Joyner-Halenda (BJH) model was used to determine the average pore diameters and pore sizes distribution from the nitrogen desorption isotherms.<sup>44, 45</sup> Both Ppy-SiO<sub>2</sub>-Ag and Ppy-SiO<sub>2</sub> hybrid films displayed average pore diameters of 6.0 nm with a relatively narrow pore sizes distribution centered at 3.7 nm, indicative of the mesoporous nature of the nanocomposite films. Additionally, upon removal of the Ag, a new peak centered near 2.1 nm appears in the pore size distribution plot of the Ppy-SiO<sub>2</sub> hybrid film. These pores are attributed to the formation of micro-mesopores upon the silver dissolution and consistent with the increase in surface area observed for the Ppy-SiO<sub>2</sub> nanocomposite film.

#### 4.3.4. Chemical Composition

The success of Ppy and silica co-electrodeposition, efficiency of the LDCD etching strategy, elemental composition, spatial distribution and crystallinity of the different phases in the nanocomposite films were examined by X-ray diffraction and energy dispersive X-ray microanalysis. **Figure 4.12** presents the X-ray diffraction scans of the as-prepared Ppy-SiO<sub>2</sub>-Ag nanocomposite film and the free-standing Ppy-SiO<sub>2</sub> and Ppy thin films obtained by applying the LDCD etching strategy. The success of the co-electrodeposition process is further confirmed through the presence of two different sets of diffraction peaks in the XRD pattern of the Ppy-SiO<sub>2</sub>-Ag nanocomposite film. First, silver in the nanocomposite film displayed five sharp diffraction peaks that can be assigned to face-centered cubic (FCC) structure of metallic silver phase crystallizing in Fm-3m space group (JCPDS, card no. 03-065-2871). These peaks are corresponding to (111), (200), (220), (311), and (222) crystalline planes in the FCC silver crystal which indicates the deposition of highly crystalline silver phase.

The average crystallite size of silver in the nanocomposite film was estimated to be 45.4 nm by applying Scherrer's formula to the XRD data. Second, the amorphous nature of both silica and Ppy in the nanocomposite film is reflected in the observation of a broad peak centered at  $2\theta = 24.4^\circ$ . Furthermore, the high efficiency of the LDCD etching strategy is clearly pronounced in the XRD scans of the free-standing films where the sharp silver peaks disappeared and the broad peak components shifted to lower 2-theta angles ( $2\theta = 21.06^\circ, 25.90^\circ$  with FWHM of 4.21, 3.44 Å, respectively in Ppy film), which is consistent with the silver and silica dissolution/removal.

The observed Ppy free-standing film peak positions and d-spacings are matched well with the reported literature values for Ppy films.<sup>46-48</sup>

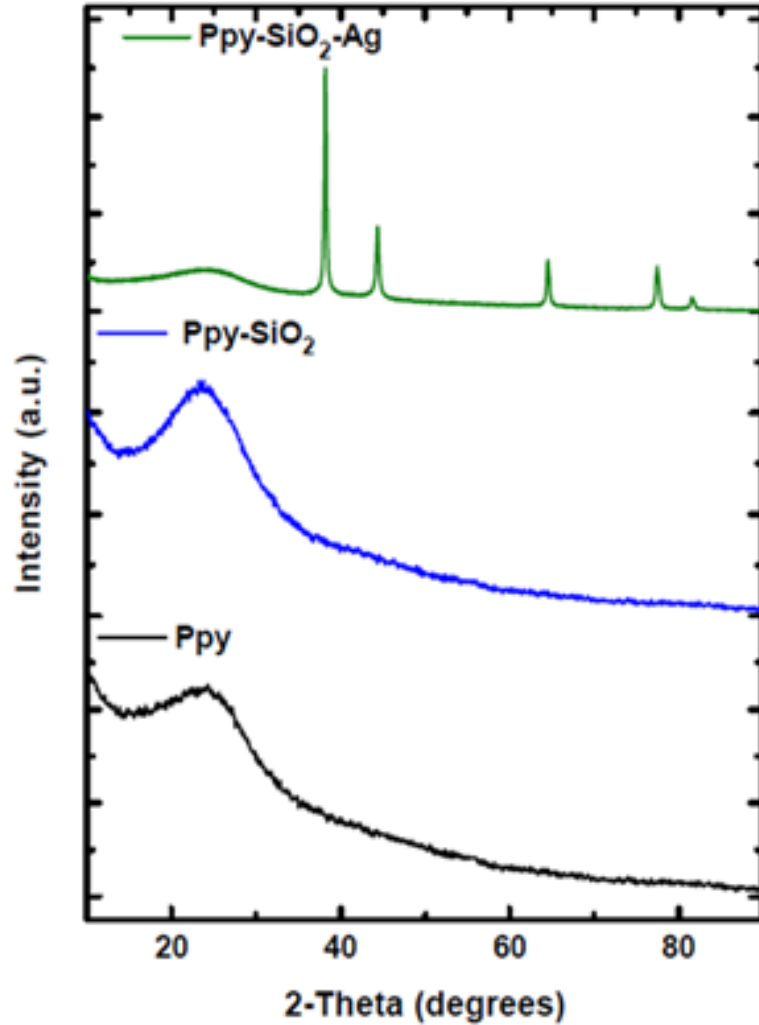


**Figure 4.12.** X-ray diffraction patterns of the as-prepared Ppy-SiO<sub>2</sub>-Ag@Au nanocomposite film (sample A) and the free-standing Ppy-SiO<sub>2</sub> and Ppy films obtained by applying the LDCD etching strategy.

Energy dispersive X-ray (EDX) analysis was conducted to determine the chemical composition of the as-prepared nanocomposite and free-standing films, further examine the efficiency of the LDCD etching strategy and achieve a better understanding of the reaction mechanism and kinetics. The performed SEM-EDX analysis included EDX spectra recorded over an area of 100  $\mu\text{m}^2$ , elemental mapping, cross-sectional EDX line scan profile, cross-

sectional EDX line scan elemental mapping, cross-sectional selected area EDX and single point-scan EDX. The EDX spectral data shown in **Figure 4.13**, confirm the formation of Ppy-SiO<sub>2</sub>-Ag@Au and Ppy-SiO<sub>2</sub>@Ag nanocomposite films where characteristic Ppy (C and N), SiO<sub>2</sub> (Si and O) and Ag peaks were observed. The absence of silica and/or silver peaks in the EDX spectra of the etched samples further reflects the high efficiency of the LDCD etching technique. The higher silica content (more than 3 times) in Ppy-SiO<sub>2</sub>@Ag compared with that in Ppy-SiO<sub>2</sub>-Ag@Au could be attributed to the lower over-potential for the reduction of water/oxygen to OH<sup>-</sup>, which can lead to an increase in the condensation and deposition of silica on silver vs. gold.

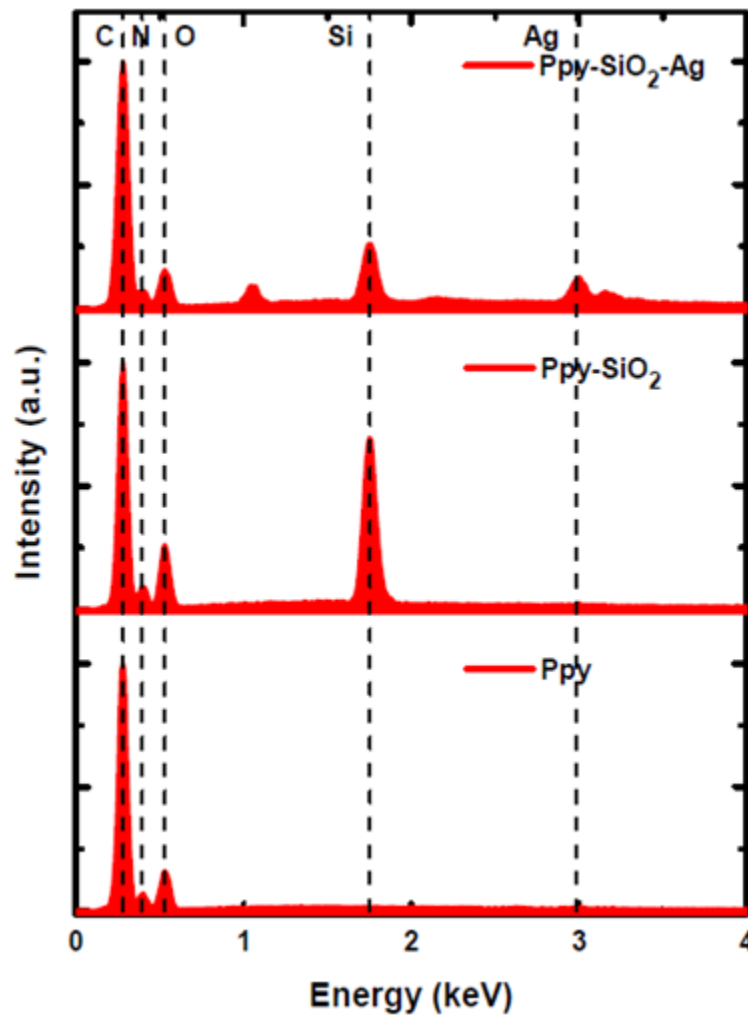


**Figure 4.13.** EDX spectra of the as-prepared Ppy-SiO<sub>2</sub>-Ag@Au (sample A), Ppy-SiO<sub>2</sub> (sample B, after Ag substrate removal) free-standing film and Ppy free-standing film obtained by treating sample A with HNO<sub>3</sub> and HF, successively. The success of the co-electrodeposition process and the LDCD etching strategy is evident.

EDX elemental maps were collected to investigate the spatial distribution of Ppy (C and N), and SiO<sub>2</sub> (Si and O) in the co-electrodeposited nanostructured composite films and further evaluate film homogeneity. The elemental maps of the as-prepared hybrid films shown in **Figure 4.14** and **Figure 4.15**, consist of different colors, with each color corresponding to a different element. By careful examination of each elemental map and superimposing the EDX maps of the different elements, it can be seen that carbon, nitrogen, oxygen and silicon are near uniformly distributed over the entire surface of the conductive substrate. The Ag EDX map (**Figure 4.14**) shows some aggregates that are distributed across the film. The fast deposition rate of silver with respect to that of Ppy and silica could account for the observation of some silver aggregates.

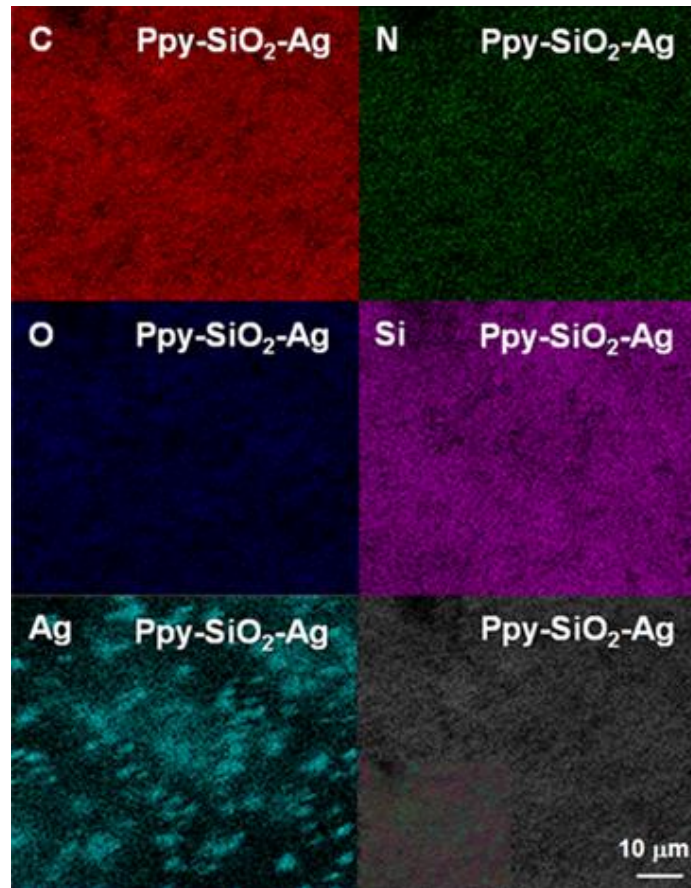


**Figure 4.14.** EDX elemental mapping images of the as-prepared Ppy-SiO<sub>2</sub>-Ag@Au (sample A). The bottom right SEM image shows the area over which the EDX elemental maps were collected. The inset in the bottom right SEM image is an overlay of all the collected elemental maps.

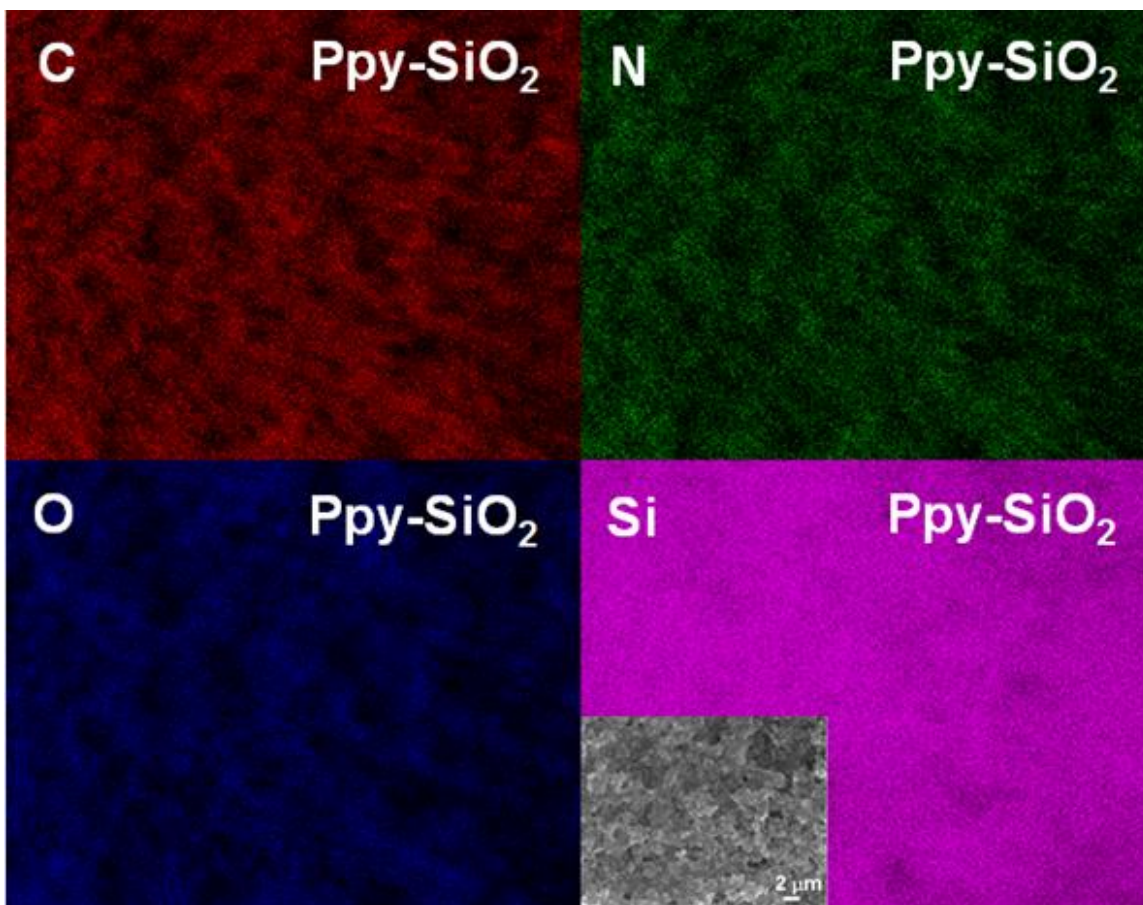


**Figure 4.15.** EDX elemental mapping images of the as-prepared Ppy-SiO<sub>2</sub>@Ag (sample B). The inset SEM image in the bottom right displays the area over which the maps collected.

Analysis of elemental maps of the free-standing films shown in **Figure 4.16**, **Figure 4.17**, and **Figure 4.18**, indicates that the isotropic distribution of different elements in the co-electrodeposited films did not change/disturb after the acid treatment, which further confirm the high efficiency and reliability of the LCDC technique. Examining the nanoparticles on the rough surface of the nanocomposite aggregates in the Ppy-SiO<sub>2</sub> hybrid films by single point-scan EDX indicated that they possess the same composition as that of the mother film, **Figure 4.19**.



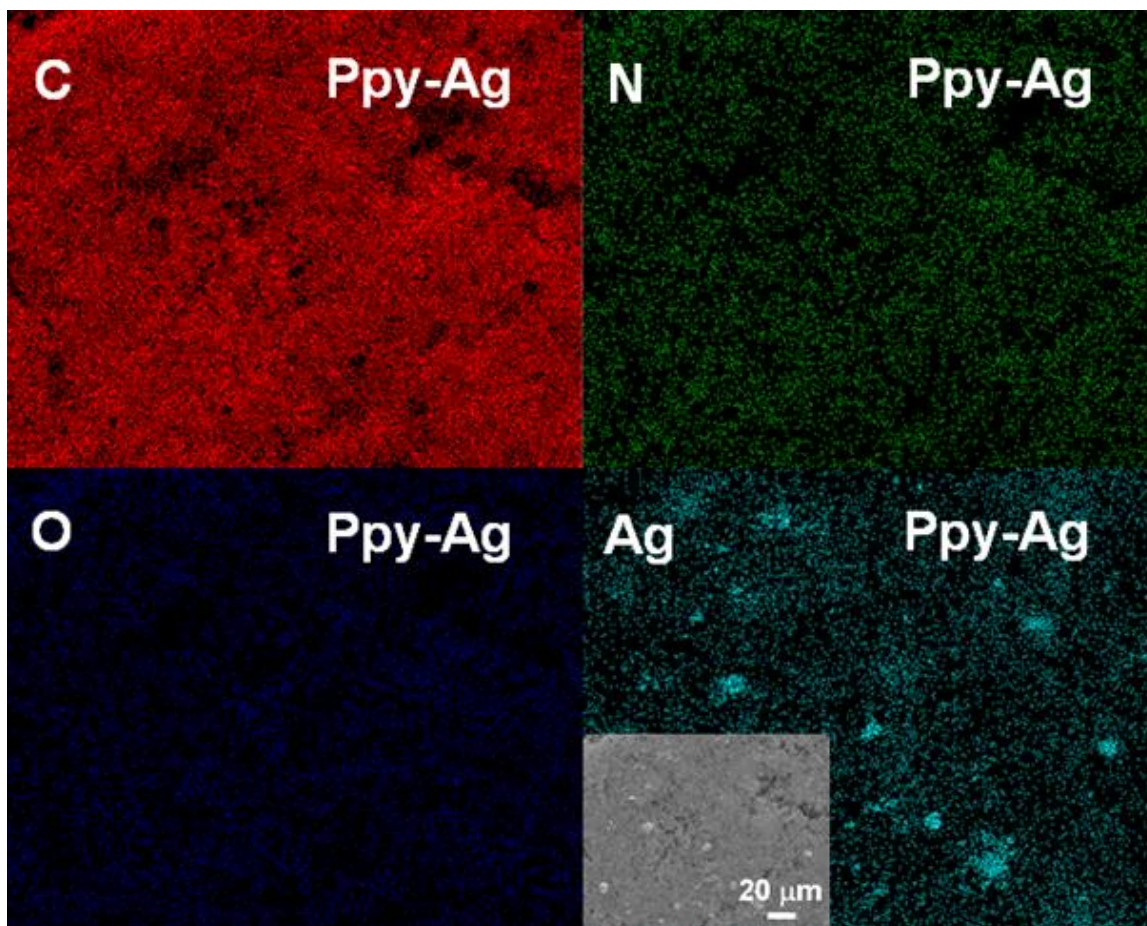


**Figure 4.16.** EDX elemental mapping images of the free-standing Ppy-Ag hybrid film obtained by treating sample A with HF. The inset SEM image in the bottom right displays the area over which the maps collected.

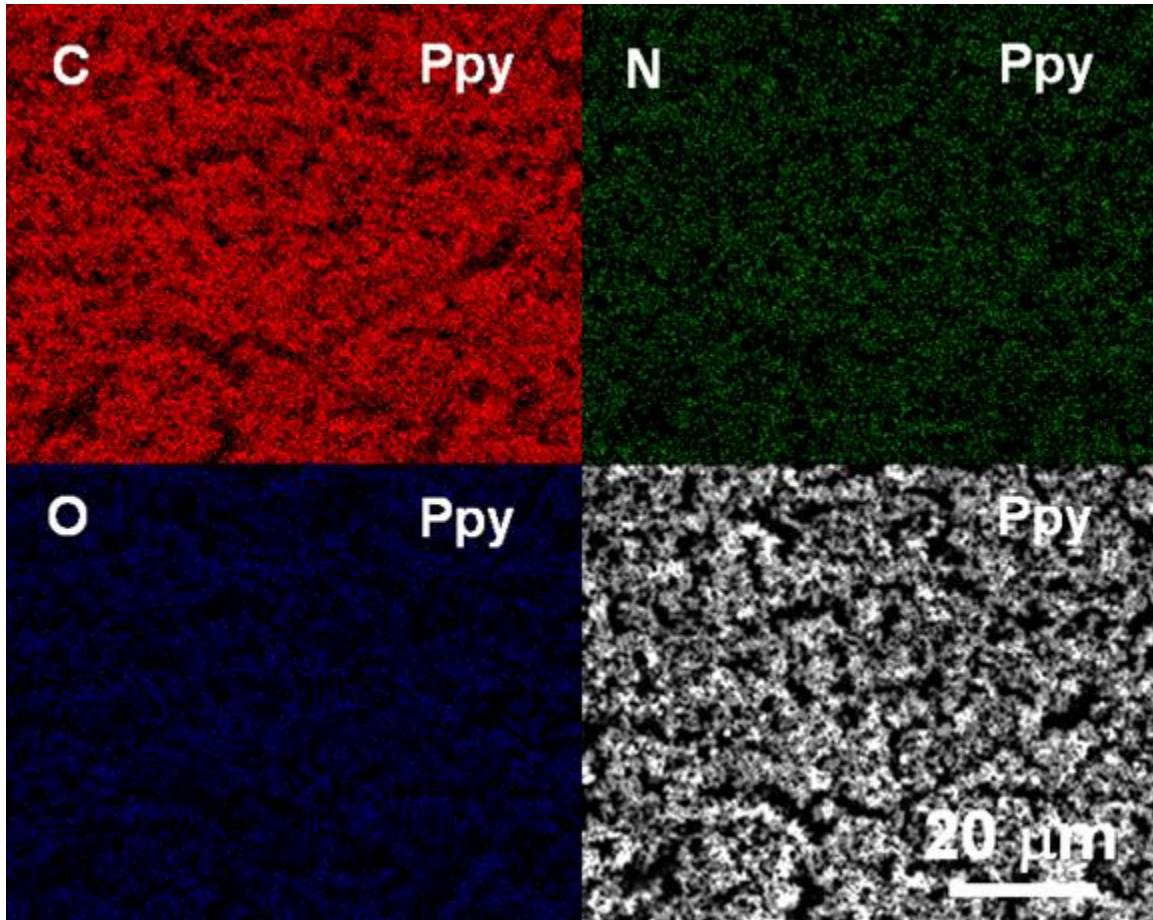


**Figure 4.17.** EDX elemental mapping images of the free-standing Ppy film obtained by treating sample A with  $\text{HNO}_3$  and HF, successively. The SEM image in the bottom displays the area over which the maps collected.

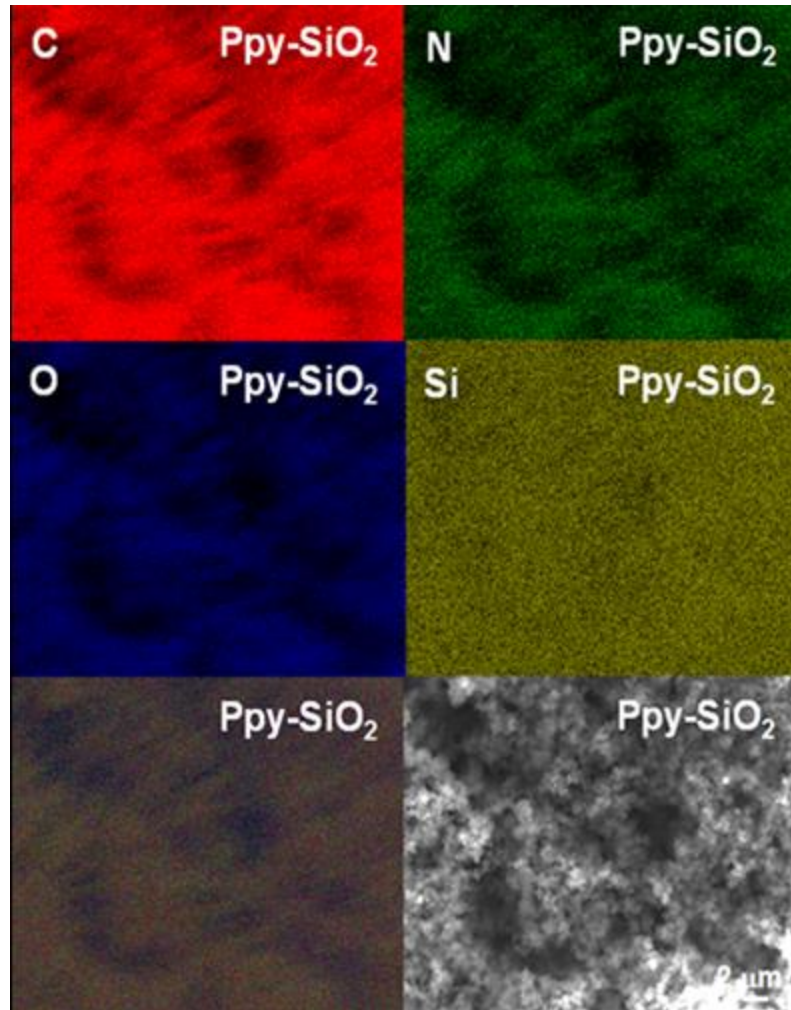


**Figure 4.18.** EDX elemental mapping images of the free-standing Ppy-SiO<sub>2</sub> film obtained by treating sample B with HNO<sub>3</sub>. The SEM image in the bottom right displays the area over which the maps collected. The bottom left image is an overlay of all the elemental maps. Note: the color of the Si map in this figure is different from that in the other figures due to the fact that the elemental maps for this sample were collected on a different SEM-EDS instrument.

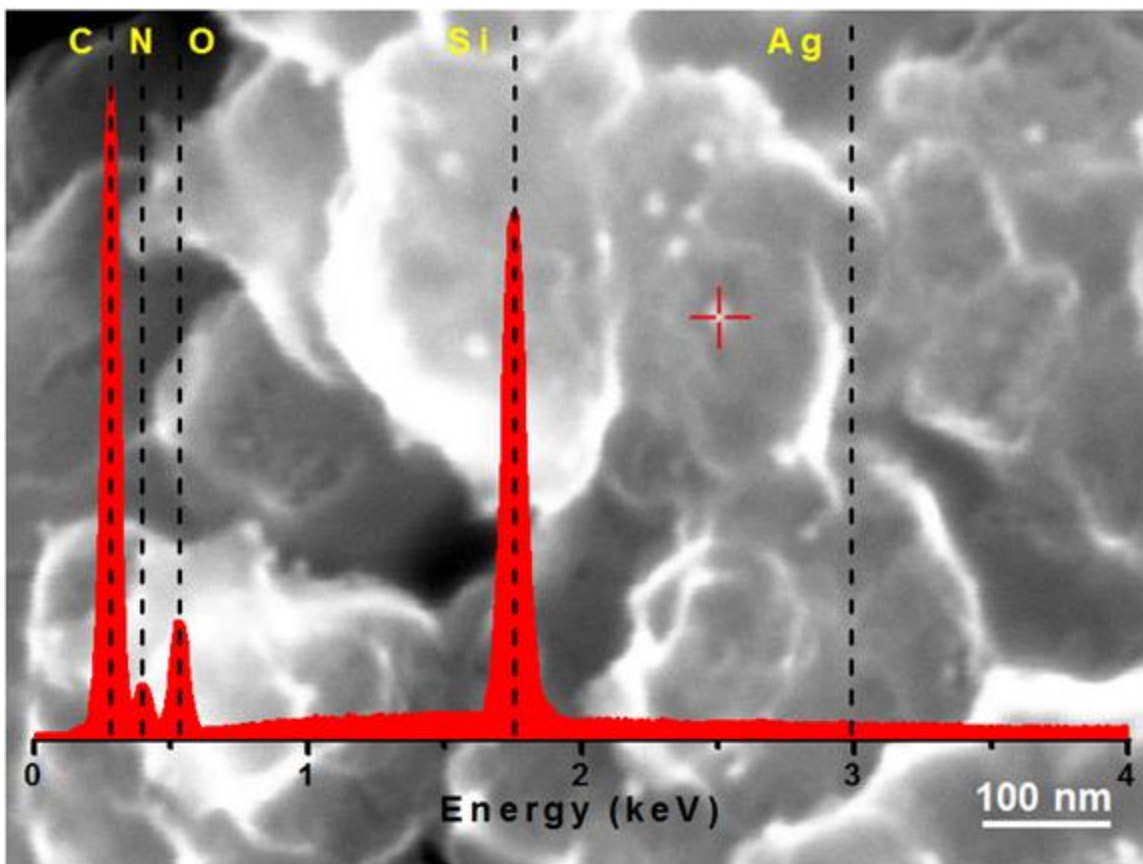


**Figure 4.19.** Single point-scan EDX spectrum of Ppy-SiO<sub>2</sub> free-standing film obtained by treating sample B (Ppy-SiO<sub>2</sub>@Ag) with HNO<sub>3</sub>.

#### 4.3.5. Electrochemical Measurements

One of the unique features of these particular electrodeposited materials is the ability to obtain a free-standing film that can be captured on any surface. In this work, we captured a Ppy-SiO<sub>2</sub> free-standing films on a planar gold electrode and a planar ITO electrode. **Figure 4.20** shows the cyclic voltammograms collected in supporting electrolyte (1.0 M Na<sub>2</sub>SO<sub>4</sub>) at a Ppy-SiO<sub>2</sub> modified gold electrode. The capacitive current increases with increasing scan rate as expected. When compared to a CV obtained at an unmodified planar gold electrode, the capacitive current is 7 times larger, which is attributed in part to the greater surface area of nanocomposite film modified electrode.

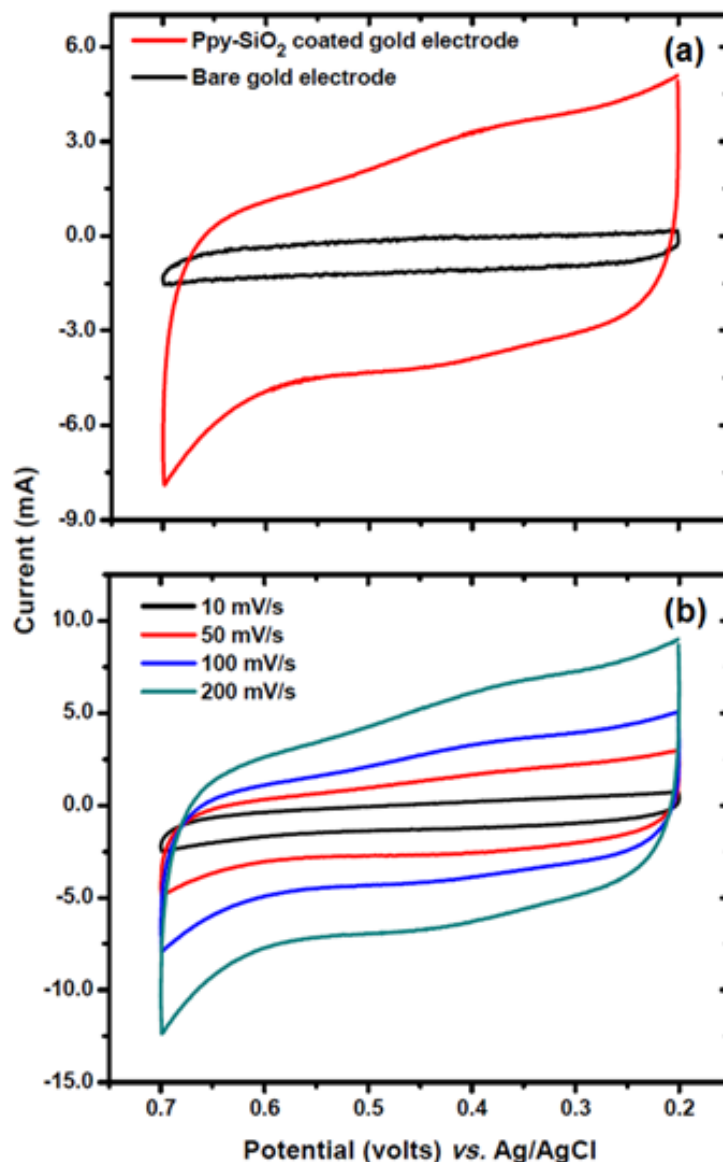


**Figure 4.20.** Cyclic voltammograms of the Ppy-SiO<sub>2</sub> free-standing film loaded on gold substrate and bare gold electrode in 1.0 M Na<sub>2</sub>SO<sub>4</sub> at a scan rate of 1000 mV/s (a). CVs of Ppy-SiO<sub>2</sub> free-standing film loaded on gold substrate in 1.0 M Na<sub>2</sub>SO<sub>4</sub> at different scan rates (b).

**Figure 4.21 (a)** shows the CV obtained when the Ppy-SiO<sub>2</sub> free-standing film was captured on ITO and the modified electrode immersed in 10 mM [Fe(CN)<sub>6</sub>]<sup>3-</sup> in 0.2 M KCl (pH ~ 7). The monoelectronic redox system [Fe(CN)<sub>6</sub>]<sup>3-</sup> did not display any characteristic redox peaks in the collected CV over the nanocomposite film indicative of the rejection of anionic ferricyanide anions by the negatively charged film. A similar trend was reported before for electrodeposited silica and pyrrole by our group and others.<sup>32, 36, 49</sup> In addition, Ppy anodically

deposited on ITO also did not show any redox peaks in the obtained  $[\text{Fe}(\text{CN})_6]^{3-}$  CV as shown in **Figure 4.21 (b)**. In comparison, bare ITO displayed two peaks characteristic of the monoelectronic redox system  $[\text{Fe}(\text{CN})_6]^{3-}$ . Full electrochemical characterization of the Ppy-SiO<sub>2</sub> nanocomposites and their potential applications as potentiometric and amperometric sensors is currently undergoing and it will be the subject of another publication.

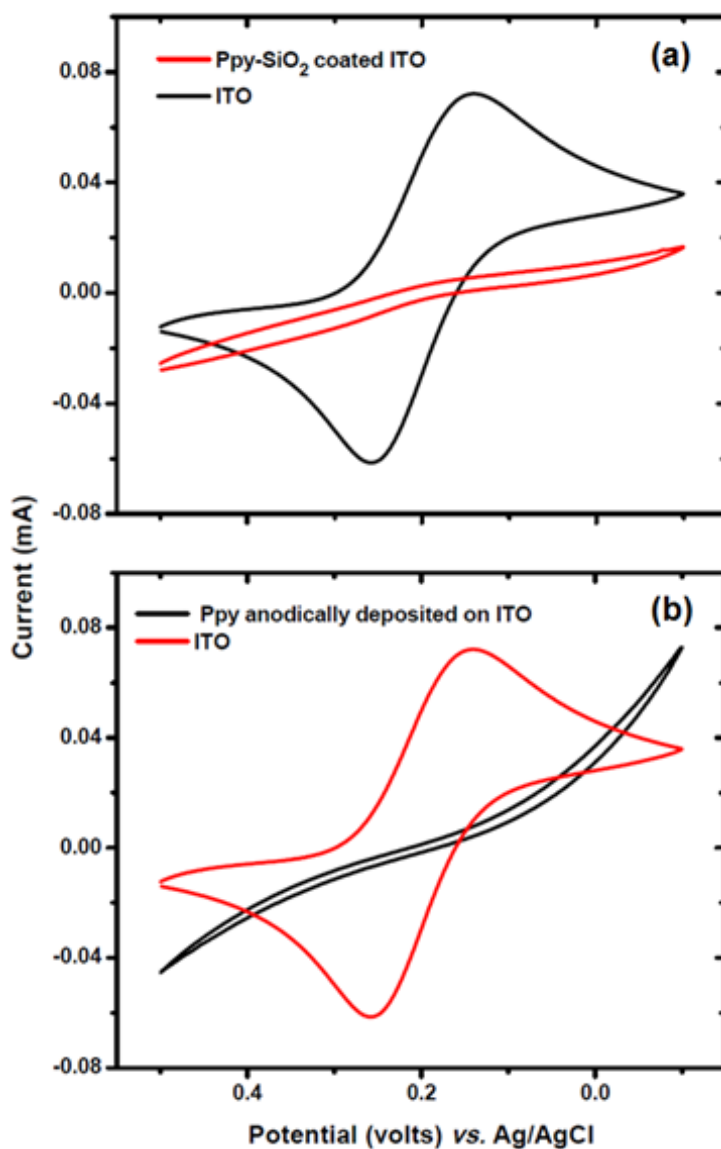


**Figure 4.21.** Cyclic voltammograms of the Ppy-SiO<sub>2</sub> free-standing film loaded on ITO substrate (red solid line, a), anodically deposited Ppy on ITO substrate (red solid line, b) and bare ITO electrode (black solid line in a, b) in 10 mM  $[\text{Fe}(\text{CN})_6]^{3-}$  in 0.2 M KCl (pH ~ 7) at a scan rate of 20 mV/s<sup>-1</sup>.

#### 4.3.6. Strata-Like Mesoporous Structure

In order to examine the microstructure of the as-prepared nanocomposite hybrid film in more detail, a cross-sectional SEM image was recorded and is shown in **Figure 4.22**. Interestingly, the nanocomposite film has a strata-like microstructure constructed of three regions with different particle density, cross-linkage and porosity. The inner region adjacent to the electrode surface and the most outer region exposed to solution are significantly less porous, denser, and more cross-linked compared to the middle region. All three regions are composed of quasi-spherical particles. The size of the particles in the middle stratum ranged from 68 to 376 nm while those in the inner and outer strata, measured at the middle stratum boundaries, are having an average size of 106 and 85 nm, respectively.

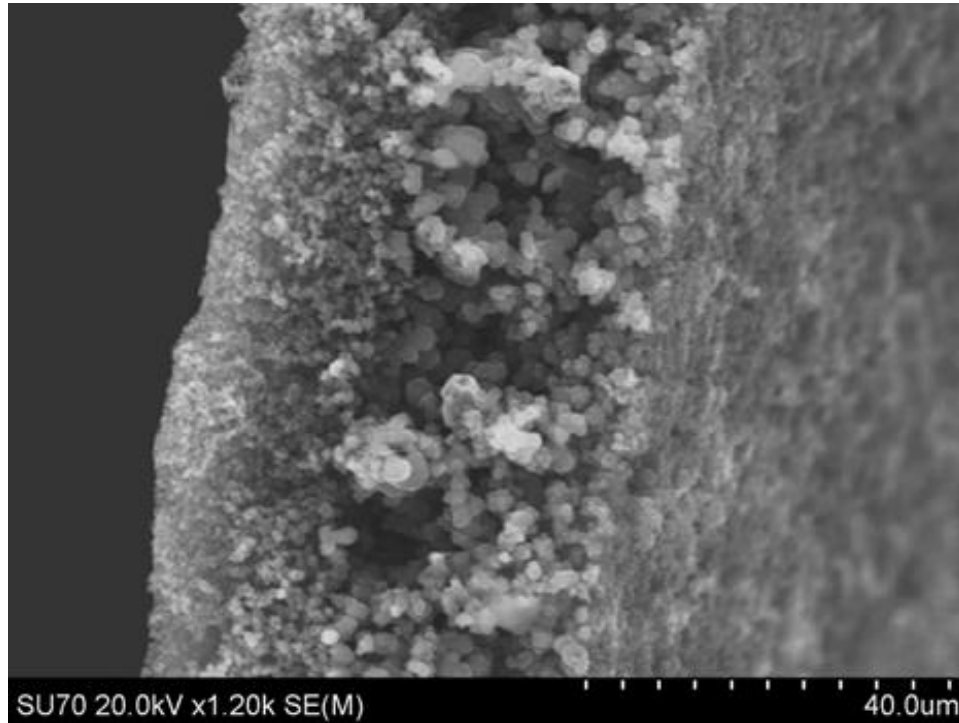


**Figure 4.22.** Cross-sectional SEM micrograph of the as-prepared Ppy-SiO<sub>2</sub>-Ag@Au nanocomposite film (sample A) at -1.0 volts for 30 min. The nanocomposite film has a strata-like structure with the middle stratum being more porous than the inner and outer strata.

Cross-sectional selected area EDX, cross-sectional EDX line scan profile, cross-sectional EDX line scan elemental mapping were recorded to further investigate the chemical composition

of each of the three layers and further understand the kinetics of the co-electrodeposition reaction. **Figure 4.23** and **Figure 4.24** display cross-sectional selected area EDX data of the as-prepared Ppy-SiO<sub>2</sub>-Ag@Au nanocomposite film. The uniform distribution of color in the cross-sectional elemental color maps supports the notion that Ppy and silica simultaneously deposit during film formation. The observation of three regions of different color intensity in all the collected cross-sectional elemental maps supports the formation of the strata-like microstructure. First, the color intensity in C and N elemental maps increased gradually during the inner stratum formation, being very weak at the early stages of the reaction (close to the substrate) indicative of slow kinetics of Ppy deposition. Then the color intensity dropped in the middle highly porous section of the growing hybrid film and then increased during the outer portion of the film growth. On the other hand, an opposite trend for the color intensity was observed in the Si and O elemental maps. Close to the substrate surface, the color intensity in Si and O maps is high and increases to reach its maximum in the inner stratum indicative of relatively fast kinetics of silica formation at the beginning of the co-electrodeposition reaction. The strata-like structure is obvious in the overlay of the elemental maps and the color intensity increases in the order middle stratum (least intense, low Ppy and silica contents), outer stratum (highest Ppy content), and inner stratum (most intense, highest silica content) as depicted in **Figure 4.23**.

These elemental maps and cross sectional images provide important clues regarding the kinetics of the individual processes that lead to the formation of the strata-like Ppy-SiO<sub>2</sub> mesoporous hybrid film: pyrrole oxidative polymerization vs. silica condensation. At the initial stages of the co-electrodeposition reaction, close to the electrode interface, the EDX line scan profile of silica is significantly higher than that of Ppy, indicative of an initial prominent fast rate of silica deposition and a relatively slower rate of Ppy deposition. A more silica-rich inner stratum thus forms at the electrode interface. Due to the non-conductive nature of electrodeposited silica on and around the conductive Ppy nanoparticles, it may be first expected that film deposition would stop. But this was not the case. The porous nature of base-catalyzed electrodeposited films ensures there is access to the electrode surface where reduction of water/oxygen and NO<sub>3</sub><sup>-</sup> can still take place to form the two catalysts (OH<sup>-</sup>, NO<sup>+</sup>) that diffuse away from the electrode surface. For the specific case of electrogenerated NO<sup>+</sup>, it is also possible that a second scenario takes place at and within the mesoporous of the electrodeposited silica through the interaction between the electrogenerated HNO<sub>2</sub> (**eq. 1**) and the labile hydrogen



protons from the surface hydroxyl groups of silica as shown in **equations 10-11**.<sup>39</sup> The low isoelectric point of silica ( $P_{zc} = 1.7-3.5$ ) makes the hydrogen protons of its surface hydroxyl groups accessible to the amphoteric  $HNO_2$ .<sup>39, 50</sup> This assumption is supported by the observed large uniformity in the composition of the as-prepared nanocomposite film as evidenced by vision, EDX mapping and the non-charging nature of the co-deposited film during the SEM imaging.

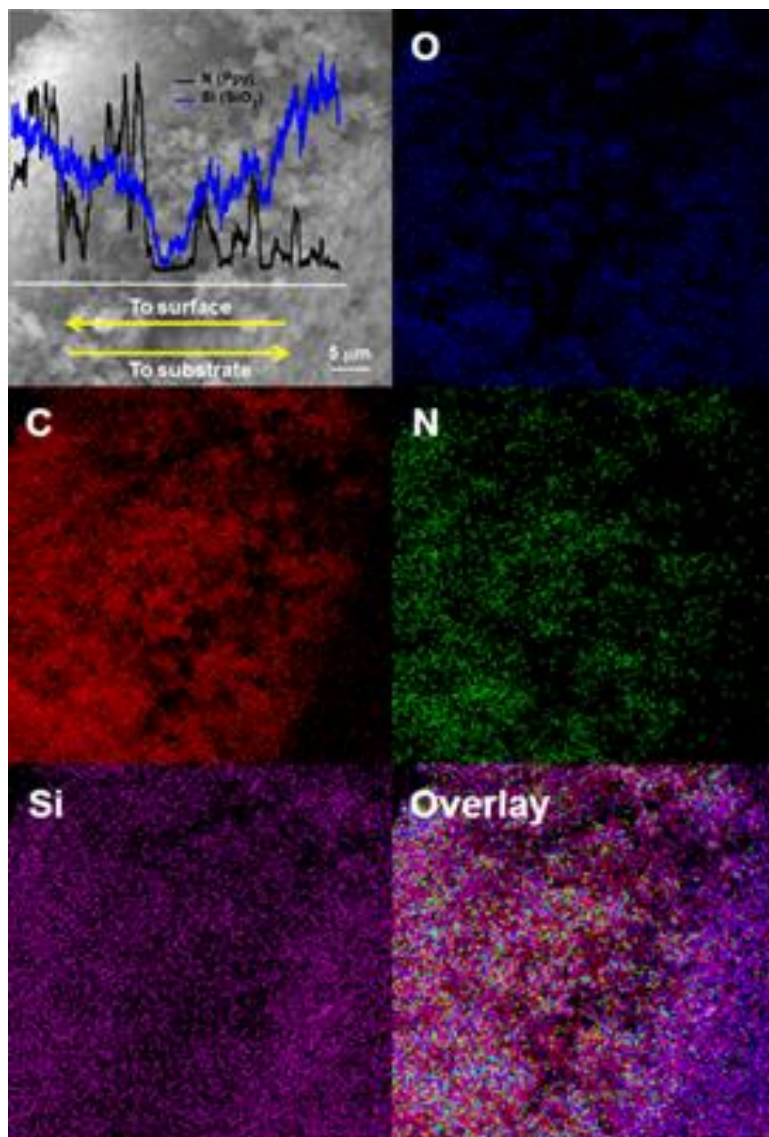
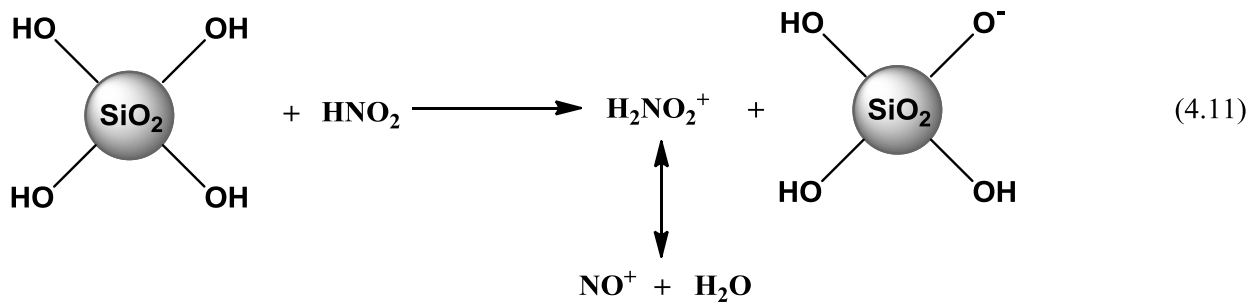
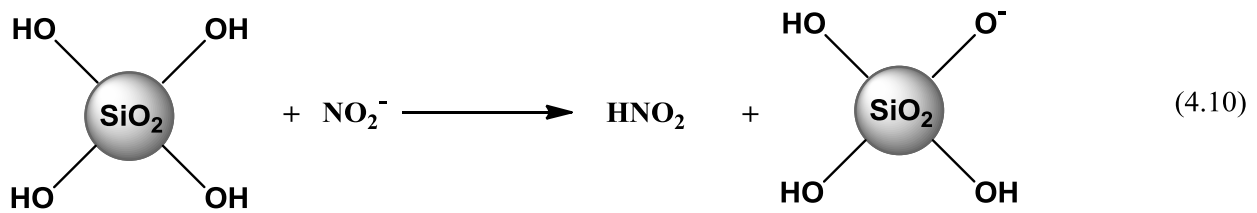


**Figure 4.23.** Cross-sectional EDX line scan profile and cross-sectional EDX line scan elemental mapping of the as-prepared Ppy-SiO<sub>2</sub>-Ag@Au nanocomposite film (sample A). The different Ppy and silica electrodeposition kinetics are evident.

During further growth of the nanocomposite film, the rate of Ppy formation increases and a more porous stratum obtained. The electrodeposited film becomes darker and darker producing polymer-rich nanocomposite films and the color of the entire solution becomes dark-blue within 10-12 min due to the chemical oxidation of the pyrrole monomers in the bulk solution by the diffused  $\text{NO}^+$  ions. Afterwards, there is a simultaneous increase in silica and Ppy line scan profiles during the formation of the denser outer stratum. This increase reflects an enhancement in Ppy and silica deposition rates due to the increase in number of the nucleation sites, which can be explained based on the continuous deposition of Ppy at and within the mesopores of the pre-deposited silica and on the uncoated electrode surface according the proposed reaction mechanism. During the outer stratum formation, the deposited Ppy provides extra nucleation sites for the silica deposition and so the rate of the silica formation increases and the intensity of Si and O colors increases as well.



Additional structural and kinetics information can be obtained by closely examining the morphology and chemical composition of the hybrid films prepared at different deposition times. EDX spectra of films prepared at different deposition times (0.5, 1, 2, 4 and 30 min) were collected and the results are shown in **Figure 4.24**. As can be seen in **Figure 4.24 (c)**, the co-electrodeposited nanocomposite film at 0.5 min is relatively silica-rich with Si content of 16.1%. The increase in the deposition time from 0.5 to 1 min was accompanied by an enhancement in the silica content, a decrease in the Ppy content, and a relatively silica-rich film was obtained with Si content of 21.6% These results support the assumption that silica deposition is

characterized by fast kinetics at the preliminary stages of the reaction. This high silica content is significantly comparable to the highest silica content demonstrated by the cross-sectional selected area EDX measurements, which may imply that the life-time for the inner stratum formation is approximately 1 min. Thereafter, as the deposition time passed 1 min, the rate of silica deposition reduced and silica content in the growing nanocomposite film decreased continuously with the progress of the reaction time while the rate of Ppy formation was increasing to produce Ppy-rich nanocomposite film.

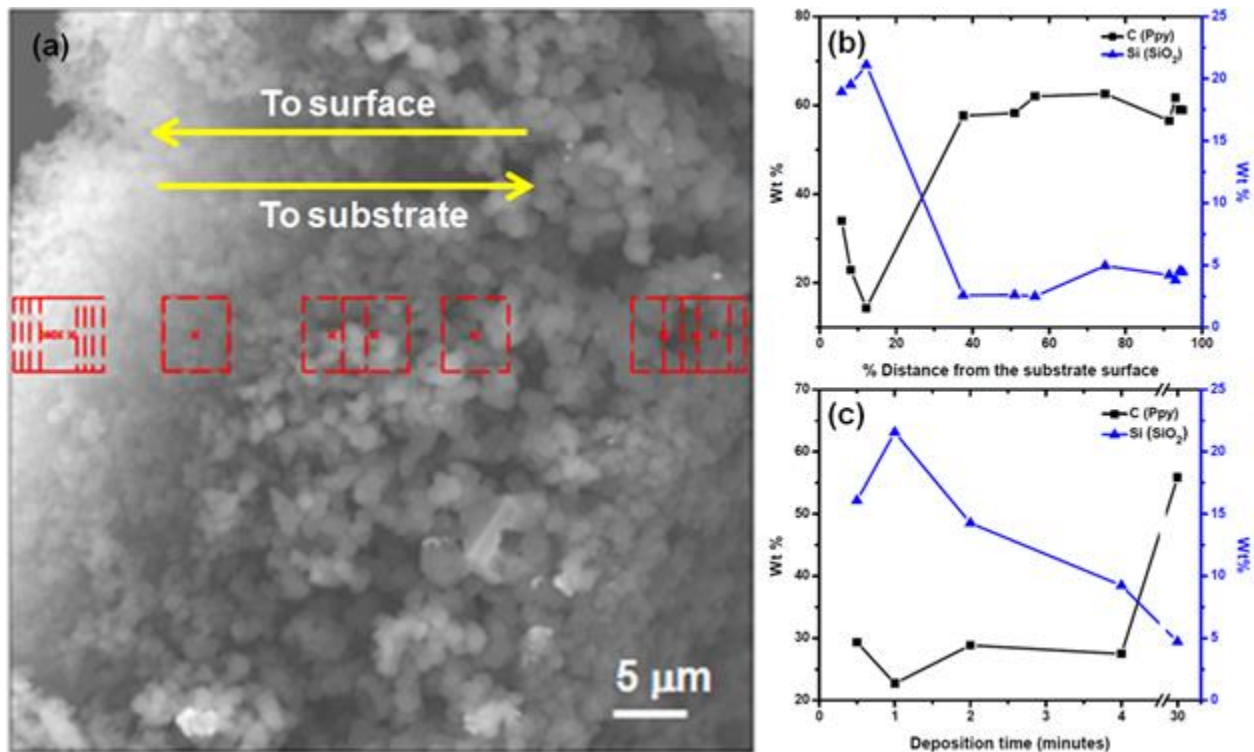


**Figure 4.24.** Kinetics of Ppy and silica electrodeposition during the formation of Ppy-SiO<sub>2</sub>-Ag@Au nanocomposite film (sample A) as presented by (a and b) the cross-sectional selected area EDX data and (c) EDX spectral data (Wt%) collected at different deposition times.

In case of Ppy-SiO<sub>2</sub>-Ag nanocomposite, the rate of silver deposition gradually increased by time and so the Ag content in the nanocomposite film increased linearly in the early and middle stages of the reaction due to the fast deposition kinetics of silver with respect to that of silica and Ppy, then it decreased due to the consumption/deposition of most of the Ag<sup>+</sup> ions and the massive deposition of Ppy at the final stages of the reaction as can be seen in **Figure 4.25**.

In Ppy-SiO<sub>2</sub>-Ag@Au nanocomposite thin films, silver nanoparticles, silica and Ppy are concurrently deposited on the conductive substrate. The electrodeposited silver particles are conductive and so they work as active centers for the deposition of Ppy and/or silica. The simultaneously deposited silica and Ppy on and around the silver particles stabilized them and suppress the formation of large silver agglomerates. As a result, the electrodeposited nanocomposite thin films are characterized by the presence of dispersed silver particles as can be seen in **Figure 4.14**. It is worthwhile, to mention that co-electrodeposition of Ppy-SiO<sub>2</sub> nanocomposite thin films on a gold conductive substrate failed due to the weak adhesion of the electrodeposited film where the deposited film flaked off and destroyed upon the removal of the electrode from the electrodeposition solution. On the other hand, the success of Ppy-SiO<sub>2</sub>-Ag@Au coelectrodeposition could be attributed to the presence of silver particles, which serve as anchors to stabilize the deposited film and increase its adhesion to the conductive gold substrate. Similar effect was reported by our group during the co-electrodeposition of Au-SiO<sub>2</sub> nanocomposite films on gold conductive substrates.<sup>34</sup> The success of Ppy-SiO<sub>2</sub>@Ag coelectrodeposition could be attributed to the rough nature of silver conductive substrate which enhances the adhesion of the deposited film a similar effect was observed when Ppy cathodically deposited on nodular copper substrate.<sup>41</sup> The weak adhesion of the electrodeposited nanocomposite thin film and the need for an adhesion enhancer such as silver particles or a rough surface could be attributed to the pH of the electrodeposition solution (pH = 1.4). Previous reports stated that cathodic deposition of Ppy occurs only at pH below 1.5 which is on the border of the current study.<sup>38</sup>

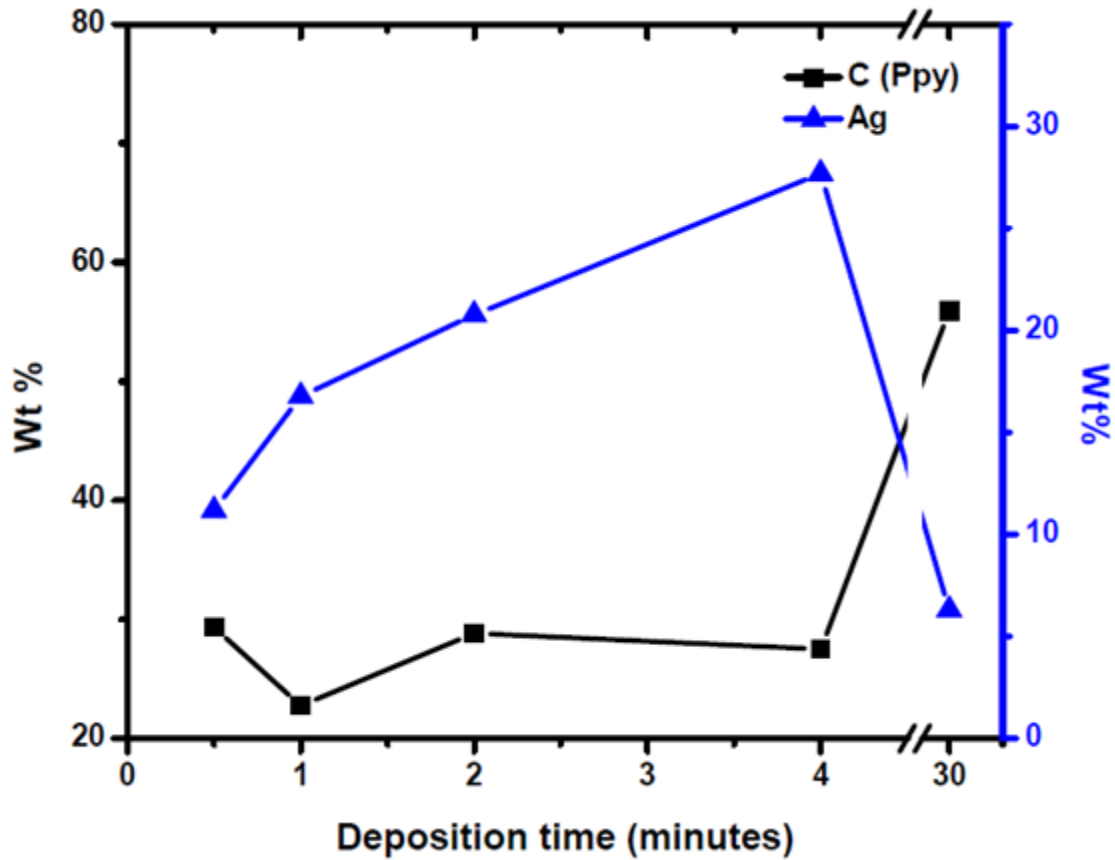


**Figure 4.25.** Kinetics of Ppy and silver electrodeposition during the formation of Ppy-SiO<sub>2</sub>-Ag@Au nanocomposite film (sample A) as presented by EDX spectral data (Wt%) collected at different deposition times.

#### 4.3.7. Proposed Reaction Mechanism

It is well established that base-catalyzed polycondensation of the hydrolyzed silica monomers is the dominant reaction during the cathodic deposition of silica and the resulting films are particulate in nature.<sup>31, 33-35</sup> The cathodic deposition of polypyrrole, however, can lead to either particle-like or wire-like nanostructures depending on experimental conditions such as the concentration of reagents and applied potential. Based on previous work, the microstructure of the polymeric film formed via cathodic electrodeposition will be determined by the reactivity/concentration of the produced pyrrole monomeric radical cations, which depend on the concentration ratio,  $C_{\text{ratio}} = \frac{[\text{NO}^+]}{[\text{pyrrole}]}$ , where  $[\text{NO}^+]$  is the concentration of the *in situ* electrogenerated nitrosonium ions and  $[\text{pyrrole}]$  is the concentration of the neutral pyrrole

monomer.<sup>41, 42, 51</sup> Step-growth polymerization is assumed to occur at high  $C_{\text{ratio}}$  value, where a large number of monomeric radical cations is produced and the highly reactive pyrrole radical cation is forced to polymerize with the closest radical cation to minimize its high energy, resulting in the formation of *particulate-like polymeric structures*. On the other side, chain growth leads to polymers with a *nanowire-like morphologies* and are obtained when a relatively low number of pyrrole radical cations is produced at low  $C_{\text{ratio}}$  value. These less reactive pyrrole monomeric radical cations preferentially polymerize with the more reactive and larger polymeric species at the electrode interface (e.g. electrodeposited polypyrrole nanospheres) rather than the less reactive neighboring monomeric radical cations.<sup>41, 42, 51</sup>

The *in situ* electrogeneration of the polycondensation base catalyst ( $\text{OH}^-$ ) will induce immediate deposition of colloidal silica at the electrode. Concomitantly, Ppy nanospheres will also be cathodically deposited at the electrode surface and on the silica nanoparticles as  $\text{NO}^+$  is produced in solution. As the pH at the interface increases, the electrogeneration of  $\text{NO}^+$  ions will decrease/suppress as will the  $[\text{NO}^+]:[\text{pyrrole}]$  ratio, which subsequently result in the formation of low number of the relatively stable pyrrole radical cations. As a result, a chain growth mechanism should then dominant the process and nanowires produced. Surprisingly, however, particulate-like nanostructures were obtained instead of the expected nanowire-like structures in the studied system regardless of the reaction conditions, e.g. high or low  $C_{\text{ratio}} = \frac{[\text{NO}^+]}{[\text{pyrrole}]}$ ,  $\text{NO}_3^-$  concentration,  $\text{HNO}_3$  concentration, magnitude of the applied cathodic potential (-0.6, -0.8 and -1.0 volts), pyrrole monomer concentration, reaction time (1, 2, 4 up to 30 min) and absence or presence of the silane monomer (TMOS), as can be seen in **Figures 4.4-4.9**. This leads us to the conclusion that the microstructure of the electrodeposited materials also depends on another factor, which has not been discussed before: nature of the reaction medium or what we called the “*solvent effect*”.

In aqueous **acidic** environment, the pyrrole monomers slowly dissolve due to their weak basic character<sup>52</sup>. In **neutral** aqueous media, pyrrole monomers are very slightly soluble<sup>52</sup> and so they are difficult to undergo an electro-assisted polymerization reaction. Previous studies on the cathodic electrodeposition of polypyrrole have been exclusively undertaken in *highly acidic aqueous* condition, where the  $C_{\text{ratio}} = \frac{[\text{NO}^+]}{[\text{pyrrole}]}$  controls the morphology of the electrodeposited polymers as described.<sup>38, 40, 41</sup> Our work employed a mixed solvent, ethanol:water (2.5:1 vol

ratio). Ethanol not only improves the miscibility of TMOS with water, but will also improve the solubility of pyrrole monomers as the electrodeposition and the production of OH<sup>-</sup> near the electrode surface commences. Notwithstanding, the improved/complete solubility of pyrrole monomers along with a slightly faster diffusion rate in the less viscous alcohols and alcohol-rich environments, with respect to aqueous environments, facilitate the formation of active pyrrole radical cations where the *in situ* electrogenerated nitrosonium ions (NO<sup>+</sup>) become more accessible by a large number of the pyrrole monomers. Under such “solvent effect” conditions, the  $C_{\text{ratio}} = \frac{[\text{NO}^+]}{[\text{pyrrole}]}$  is no longer governing the morphology of the electrodeposited Ppy or Ppy composites and the reaction mechanism proceeds in a step-growth fashion to produce particulate-like Ppy-based thin films. In other words, the presence of ethanolic-based silica sol in the reaction medium and the subsequent silica deposition directed the pyrrole free radical polymerization to occur through a step-growth mechanism rather than the expected chain-growth mechanism.

The validity of this hypothesis has been examined and demonstrated by carrying out the co-electrodeposition of the Ppy-SiO<sub>2</sub> nanocomposite film using a pure aqueous medium while keeping all the other deposition parameters constant. In absence of ethanol, a nanocomposite film consisting of nanowires was obtained as shown in **Figure 4.26**. On the contrary, in the presence of ethanol and no matter what the reaction conditions were, a particulate-like nanocomposite films were obtained as depicted in **Figures 4.4-4.9**. The present work demonstrates for the first time the “*solvent effect*” on controlling the morphology and directing the reaction mechanism of the electrodeposited Ppy-based materials.

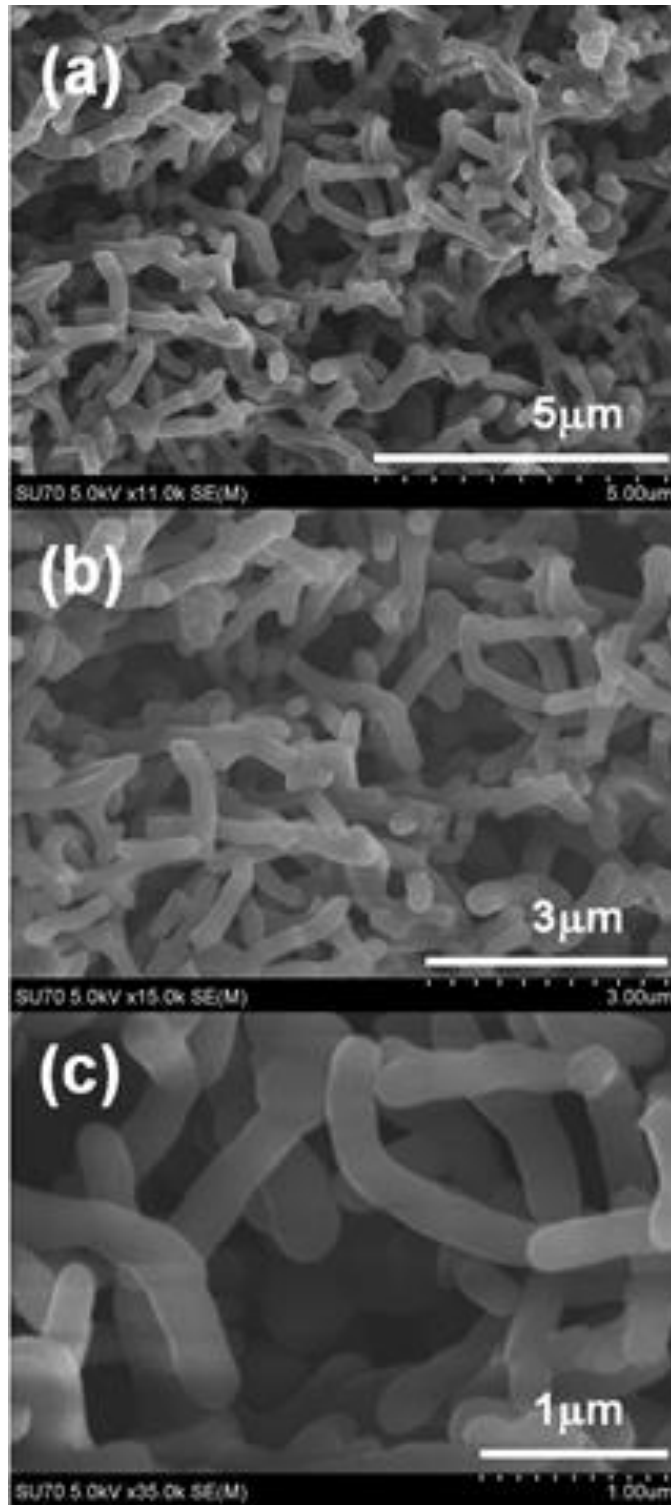


**Figure 4.26.** SEM images of Ppy-SiO<sub>2</sub>-Ag@Au nanowires prepared from the original electrodeposition solution but in absence of ethanol at -1.0 volts 30 min. The solvent effect on the nanocomposite film morphology is clearly evident.



#### 4.4. Conclusions

Polypyrrole-Silica (Ppy-SiO<sub>2</sub>) nanocomposite films characterized by a multimodal porous structure were prepared using a single-step co-electrodeposition route. The synthesis strategy was based on the combination of electrodeposition, sol-gel chemistry and electro-assisted polymerization processes in a strongly acidic environment. Upon the application of a sufficiently large negative potential (e.g., -1.0 volts) to a gold or silver coated gold electrode, simultaneous redox reactions promptly took place at the electrode/electrolyte interface ultimately yielding two catalysts, NO<sup>+</sup> and OH<sup>-</sup>. The former oxidized the pyrrole monomers while the latter condensed hydrolyzed silica monomers. A new morphology determining factor the “*solvent effect*” was demonstrated, through which the microstructure of the resulting nanocomposite films can be fine-tune between particulate-like and nanowire-like. The fast rate of silica deposition commencing at the beginning of the electrodeposition reaction, competition between the electrogenerated catalysts at the electrode surface, and their subsequent diffusion into the reaction bulk are responsible for the formation of a strata-like nanostructured hybrid thin film. Moreover, the silica-rich inner stratum allowed for the formation of free-standing Ppy and Ppy-SiO<sub>2</sub> films through the silica dissolution when the film treated with HF acid. The uniform distribution of silica and Ppy within the strata-like nanocomposite film and the absence of any silica or Ppy large aggregates were confirmed through the elemental mapping measurements which reflects the homogenous co-deposition of silica and Ppy during the film growth and accounts for the non-destruction/survival of the free-standing film during the acid treatment. The present preparation strategy can be extended to produce other conductive polymer-sol-gel nanocomposite thin films of various morphologies. These unique structural features of the nanocomposite thin films, particularly their meso- and macro-porosity and ability to be transferred to different substrates make them potential candidate in a wide range of application including electrochemical sensing, energy storage, miniaturized electronics and catalysis.

## 4.5. References

1. Farghaly, A. A.; Collinson, M. M., Mesoporous Hybrid Polypyrrole-Silica Nanocomposite Films with a Strata-Like Structure. *Submitted to Langmuir* **2016**.
2. Camurlu, P., Polypyrrole Derivatives for Electrochromic Applications. *Rsc Advances* **2014**, 4, (99), 55832-55845.
3. Cosnier, S.; Holzinger, M., Electrosynthesized Polymers for Biosensing. *Chemical Society Reviews* **2011**, 40, (5), 2146-2156.
4. Dutta, K.; Kundu, P. P., A Review on Aromatic Conducting Polymers- Based Catalyst Supporting Matrices for Application in Microbial Fuel Cells. *Polymer Reviews* **2014**, 54, (3), 401-435.
5. Li, C.; Bai, H.; Shi, G. Q., Conducting Polymer Nanomaterials: Electrosynthesis and Applications. *Chemical Society Reviews* **2009**, 38, (8), 2397-2409.
6. Novák, P.; Müller, K.; Santhanam, K. S. V.; Haas, O., Electrochemically Active Polymers for Rechargeable Batteries. *Chemical Reviews* **1997**, 97, (1), 207-282.
7. Camargo, P. H. C.; Satyanarayana, K. G.; Wypych, F., Nanocomposites: Synthesis, Structure, Properties and New Application Opportunities. *Materials Research-Ibero-American Journal of Materials* **2009**, 12, (1), 1-39.
8. Chujo, Y.; Saegusa, T., Organic Polymer Hybrids With Silica-Gel Formed By Means Of The Sol-Gel Method. *Advances in Polymer Science* **1992**, 100, 11-29.
9. Gangopadhyay, R.; De, A., Conducting polymer nanocomposites: A brief Overview. *Chemistry of Materials* **2000**, 12, (3), 608-622.
10. Maity, A.; Biswas, M., Recent Progress in Conducting Polymer, Mixed Polymer-Inorganic Hybrid Nanocomposites. *Journal of Industrial and Engineering Chemistry* **2006**, 12, (3), 311-351.
11. Mammeri, F.; Bourhis, E. L.; Rozes, L.; Sanchez, C., Mechanical Properties of Hybrid Organic-Inorganic Materials. *Journal of Materials Chemistry* **2005**, 15, (35-36), 3787-3811.
12. Zhu, T.; Row, K. H., Preparation and Applications of Hybrid Organic-Inorganic Monoliths: A Review. *Journal of Separation Science* **2012**, 35, (10-11), 1294-1302.
13. Brinker, C. J.; Scherer, G. W., *Sol-Gel Science: the Physics and Chemistry of Sol-Gel Processing*. Academic press: 2013.
14. Ciriminna, R.; Fidalgo, A.; Pandarus, V.; Beland, F.; Ilharco, L. M.; Pagliaro, M., The Sol-Gel Route to Advanced Silica-Based Materials and Recent Applications. *Chemical Reviews* **2013**, 113, (8), 6592-6620.
15. Hench, L. L.; West, J. K., The Sol-Gel Process. *Chemical Reviews* **1990**, 90, (1), 33-72.
16. Maeda, S.; Armes, S. P., Preparation And Characterization Of Novel Polypyrrole-Silica Colloidal Nanocomposites. *Journal of Materials Chemistry* **1994**, 4, (6), 935-942.
17. Maeda, S.; Gill, M.; Armes, S. P., Surface Characterization Of Conducting Polymer-Silica Nanocomposites By X-Ray Photoelectron-Spectroscopy. *Langmuir* **1995**, 11, (6), 1899-1904.
18. Perruchot, C.; Chehimi, M. M.; Mordenti, D.; Briand, M.; Delamar, M., The Role of a Silane Coupling Agent in the Synthesis of Hybrid Polypyrrole Silica Gel Conducting Particles. *Journal of Materials Chemistry* **1998**, 8, (10), 2185-2193.
19. Raveh, M.; Liu, L.; Mandler, D., Electrochemical Co-Deposition of Conductive Polymer-Silica Hybrid Thin Films. *Physical Chemistry Chemical Physics* **2013**, 15, (26), 10876-10884.
20. Ribeiro, T.; Baleizao, C.; Farinha, J. P. S., Functional Films from Silica/Polymer Nanoparticles. *Materials* **2014**, 7, (5), 3881-3900.
21. Roux, S.; Audebert, P.; Pagetti, J.; Roche, M., Design of a New Bilayer Polypyrrole-Xerogel Hybrid Coating for Corrosion Protection. *Journal of Materials Chemistry* **2001**, 11, (12), 3360-3366.
22. Sayari, A.; Hamoudi, S., Periodic Mesoporous Silica-Based Organic - Inorganic Nanocomposite Materials. *Chemistry of Materials* **2001**, 13, (10), 3151-3168.
23. Schmid, A.; Tonnar, J.; Armes, S. P., A New Highly Efficient Route to Polymer-Silica Colloidal Nanocomposite Particles. *Advanced Materials* **2008**, 20, (17), 3331-3336.

24. Zandi-zand, R.; Ershad-langroudi, A.; Rahimi, A., Silica Based Organic-Inorganic Hybrid Nanocomposite Coatings for Corrosion Protection. *Progress in Organic Coatings* **2005**, 53, (4), 286-291.
25. Zou, H.; Wu, S.; Shen, J., Polymer/Silica Nanocomposites: Preparation, Characterization, Properties, and Applications. *Chemical Reviews* **2008**, 108, (9), 3893-3957.
26. Boeva, Z. A.; Sergeyev, V. G., Polyaniline: Synthesis, Properties, and Application. *Polymer Science Series C* **2014**, 56, (1), 144-153.
27. Shu, X.; Li, Z. X.; Xia, J. B., Synthetic Methods for Poly(thiophene)s. *Progress in Chemistry* **2015**, 27, (4), 385-394.
28. Nishio, K.; Fujimoto, M.; Ando, O.; Ono, H.; Murayama, T., Characteristics of Polypyrrole Chemically Synthesized by Various Oxidizing Reagents. *Journal of applied electrochemistry* **1996**, 26, (4), 425-429.
29. Sharma, M.; Waterhouse, G. I.; Loader, S. W.; Garg, S.; Svirskis, D., High Surface Area Polypyrrole Scaffolds for Tunable Drug Delivery. *International journal of pharmaceutics* **2013**, 443, (1), 163-168.
30. Walcarius, A.; Sibottier, E.; Etienne, M.; Ghanbaja, J., Electrochemically Assisted Self-Assembly of Mesoporous Silica Thin Films. *Nature Materials* **2007**, 6, (8), 602-608.
31. Sibottier, E.; Sayen, S.; Gaboriaud, F.; Walcarius, A., Factors Affecting the Preparation and Properties of Electrodeposited Silica Thin Films Functionalized with Amine or Thiol Groups. *Langmuir* **2006**, 22, (20), 8366-8373.
32. Shacham, R.; Avnir, D.; Mandler, D., Electrodeposition of Methylated Sol-Gel Films on Conducting Surfaces. *Advanced Materials* **1999**, 11, (5), 384-388.
33. Luna-Vera, F.; Dong, D.; Hamze, R.; Liu, S.; Collinson, M. M., Electroassisted Fabrication of Free-Standing Silica Structures of Micrometer Size. *Chemistry of Materials* **2012**, 24, (12), 2265-2273.
34. Farghaly, A. A.; Collinson, M. M., Electroassisted Codeposition of Sol-Gel Derived Silica Nanocomposite Directs the Fabrication of Coral-like Nanostructured Porous Gold. *Langmuir* **2014**, 30, (18), 5276-5286.
35. Etienne, M.; Sallard, S.; Schroeder, M.; Guillemin, Y.; Mascotto, S.; Smarsly, B. M.; Walcarius, A., Electrochemical Generation of Thin Silica Films with Hierarchical Porosity. *Chemistry of Materials* **2010**, 22, (11), 3426-3432.
36. Deepa, P. N.; Kanungo, M.; Claycomb, G.; Sherwood, P. M. A.; Collinson, M. M., Electrochemically Deposited Sol-Gel-Derived Silicate Films as a Viable Alternative in Thin-Film Design. *Analytical Chemistry* **2003**, 75, (20), 5399-5405.
37. Collinson, M. M., Electrochemistry: An important Tool to Study and Create New Sol-Gel-Derived Materials. *Accounts of Chemical Research* **2007**, 40, (9), 777-783.
38. Jung, Y. J.; Singh, N.; Choi, K. S., Cathodic Deposition of Polypyrrole Enabling the One-Step Assembly of Metal-Polymer Hybrid Electrodes. *Angewandte Chemie-International Edition* **2009**, 48, (44), 8331-8334.
39. Jung, Y.; Spray, R. L.; Kim, J. H.; Kim, J. M.; Choi, K. S., Selective Polymerization of Polypyrrole in Silica Mesopores using an In Situ Generated Oxidizing Agent on a Silica Surface. *Chemical Communications* **2010**, 46, (35), 6566-6568.
40. Koh, J. Y.; Jung, Y., Nanoscale Morphology Control of Conducting Polymers by Cathodic Polymerization Route. *International Journal of Electrochemical Science* **2013**, 8, (7), 10080-10085.
41. Nam, D.-H.; Kim, M.-J.; Lim, S.-J.; Song, I.-S.; Kwon, H.-S., Single-Step Synthesis of Polypyrrole Nanowires by Cathodic Electropolymerization. *Journal of Materials Chemistry A* **2013**, 1, (27), 8061-8068.
42. Hnida, K. E.; Socha, R. P.; Sulka, G. D., Polypyrrole-Silver Composite Nanowire Arrays by Cathodic Co-Deposition and Their Electrochemical Properties. *The Journal of Physical Chemistry C* **2013**, 117, (38), 19382-19392.
43. Liu, W.; Herrmann, A.-K.; Bigall, N. C.; Rodriguez, P.; Wen, D.; Oezaslan, M.; Schmidt, T. J.; Gaponik, N.; Eychmüller, A., Noble Metal Aerogels—Synthesis, Characterization, and Application as Electrocatalysts. *Accounts of Chemical Research* **2015**, 48, (2), 154-162.

44. Gregg, S. J.; Sing, K. S. W., *Adsorption, Surface Area and Porosity. 2nd Ed.* Academic Press: 1982; p 303 pp.
45. Webb, P. A.; Orr, C., *Analytical Methods in Fine Particle Technology.* Micromeritics Instrument Corp: 1997.
46. Cheah, K.; Forsyth, M.; Truong, V. T., Ordering and Stability in Conducting Polypyrrole. *Synthetic Metals* **1998**, 94, (2), 215-219.
47. Wynne, K. J.; Street, G. B., Poly(pyrrol-2-ylum tosylate), Electrochemical Synthesis and Physical and Mechanical Properties. *Macromolecules* **1985**, 18, (12), 2361-2368.
48. Li, X.-G.; Li, A.; Huang, M.-R.; Liao, Y.; Lu, Y.-G., Efficient and Scalable Synthesis of Pure Polypyrrole Nanoparticles Applicable for Advanced Nanocomposites and Carbon Nanoparticles. *The Journal of Physical Chemistry C* **2010**, 114, (45), 19244-19255.
49. Debiemme-Chouvy, C.; Gallois, M., Characterization of a Very Thin Overoxidized Polypyrrole Membrane: Application to H<sub>2</sub>O<sub>2</sub> Determination. *Surface and Interface Analysis* **2010**, 42, (6-7), 1144-1147.
50. Jolivet, J.-P.; Henry, M.; Livage, J.; Bescher, E., *Metal Oxide Chemistry and Synthesis: From Solution to Solid State.* John Wiley & Sons, Ltd.: 2000; p No pp. given.
51. Nam, D.-H.; Lim, S.-J.; Kim, M.-J.; Kwon, H.-S., Facile Synthesis of SnO<sub>2</sub>-Polypyrrole Hybrid Nanowires by Cathodic Electrodeposition and Their Application to Li-Ion Battery Anodes. *RSC Advances* **2013**, 3, (36), 16102-16108.
52. Plimmer, R. H. A., *Practical Organic and Bio-Chemistry.* Longmans, Green & Co.: 1918.

## **Chapter 5: Bicontinuous Nanoporous Platinum**

## 5.1 Introduction

An invention disclosure and manuscript have been written based on the work included in this chapter.<sup>1</sup> Porous nanomaterials generally, and nanostructured porous noble metals specifically, have fascinated scientists due to their superior chemical and physical properties over nanoparticles and bulk counterparts. Nanoporous metals possess an interesting combination of properties owing to their metallic nature and the nanoscale features or the so-called “finite-size effect”.<sup>2,3</sup> These intriguing properties are of particular interest from the fundamental research and technological applications points of view. Among the different types of porous metals, porous platinum nanostructures have received a considerable attention due to their chemical stability, excellent biocompatibility, high surface-to-volume ratio, excellent electrical and thermal conductivities, good mechanical stability, low density, high catalytic activity, feasibility of functionalization and large surface area.<sup>4,5</sup> These characteristics have placed them at the forefront as potential candidates for a wide range of technological applications including sensing, catalysis, filtration and energy related devices (e.g. state-of-the-art electrode materials in fuel cells are platinum-based nanomaterials).<sup>2, 3, 6-8</sup>

A number of approaches have been developed to fabricate porous platinum nanostructures such as lyotropic liquid crystals soft template technique,<sup>9</sup> hard templating of mesoporous silica,<sup>10</sup> porous alumina,<sup>11</sup> sol-gel assembly of prefabricated metals nanoparticles to produce aerogels,<sup>4</sup> dealloying techniques,<sup>12</sup> and electrochemical deposition.<sup>13, 14</sup> Although the aforementioned fabrication techniques possess merits and have been proven to be suitable routes to prepare a

variety of porous platinum nanostructures, they suffer from some drawbacks. For example, templating approaches are time consuming, multistep processes that are difficult to implement for the large-scale production due to the necessity to adopt many factors in the templating process (e.g. concentration, temperature, pH, etc.), the limitation to produce one-dimensional porous structures at most (e.g. array of tubes), and the absence of dynamic control over the length scale are disadvantageous.<sup>15</sup> Dealloying of an electrodeposited Pt-Cu and Pt-Si binary alloys failed to produce bicontinuous porous platinum structures and instead gave platinum films composed of randomly cracked spheres<sup>13</sup> or isolated pores via ligaments of different sizes.<sup>12, 16</sup>

The presence of continuous, non-intersecting and oriented plane (e.g. vertical, horizontal, etc.) within a volume furnishes continuously interpenetrated sub-volumes. This partition fashion called bicontinuous partitioning. A 3D structure composed of a bicontinuously partitioned sub-volumes each of them is filled with a distinguished and connected phase of matter (e.g. solid, gas, or liquid) is called a 3D bicontinuous structure.<sup>17</sup> For example, a sponge and nanoporous gold are composed of a connected solid phase and connected gas phase across the sample.

For applications in electrochemical sensing and electrocatalysis, there are many factors that need to be considered.<sup>5, 7, 18</sup> For example: (a) porous platinum materials need to be in the form of an electrode. Porous platinum nanostructures prepared by wet chemical approaches are in most situations particle-based materials,<sup>19</sup> not attached to any conductive substrates and so they need to undergo an additional electrode fabrication process before use<sup>20</sup> (b) stability of the electrode. Generally, electrodes fabricated from particle-based materials suffer from stability issues for many

reasons such as the weak contact between the material particles and the current collector surface, partial deterioration of the electrode during the measurement due to the inadequate adhesion between the active electrode material and conductive support;<sup>21</sup> (c) mass transport and electron transfer limitations are a reflectance of the electrode efficiency and reproducibility so a control over the pore diameter and electrode microstructure needs to be achieved to avoid mass transport and electron transfer problems, ensure access of the electroactive species being detected into the inner surface of the electrode and to prevent the fouling of the electrode surface when it is used in complex fouling environments.<sup>18, 22, 23</sup>

In order to address all of these considerations, there is a continued necessity to discover new porous platinum structures, develop existing fabrication strategies and/ or find a new ones. An ideal platform that can satisfy these considerations is a three-dimensional bicontinuous nanostructured porous platinum (3D-BC-NP-Pt) prepared by dealloying an electrodeposited platinum alloy thin film. A strongly adhered platinum based-film to a conductive substrate can be obtained in a one-step process by the application of the electrodeposition technique.<sup>24</sup> Dealloying of the electrodeposited noble metal alloys represents a simple and promising route for the fabrication of three-dimensional bicontinuous structures (e.g. nanoporous gold).<sup>18, 22</sup> The 3D-BC-NP-Pt electrodes are expected to overcome the mass transport and electron transfer issues and display excellent electrochemical sensing and catalytic performance even in complex fouling environments due to the unique sieving-like mechanism of the bicontinuous nanoporous structures (e.g. nanoporous gold) and the nano-confinement related features.<sup>16, 22, 25, 26</sup>



Although for the first glance, the fabrication strategy of 3D-BC-NP-Pt thin film electrodes by dealloying an electrochemically deposited platinum alloy looks simple, the non-existence of such structure reflects the fact that fabrication of 3D-BC-NP-Pt structure is a challenge. In order to address this challenge, we reasoned that electrodeposition of silver-rich platinum binary alloy thin films and selective chemical dissolution of silver would allow the fabrication of three-dimensional bicontinuous nanoporous platinum (3D-BC-NP-Pt) structures. In this work, we report the first the fabrication of high surface area three-dimensional bicontinuous nanoporous platinum (3D-BC-NP-Pt) thin film electrodes with a nanoporous gold-like microstructure from electrochemically deposited Pt–Ag binary alloy thin films. We demonstrated that the microstructure of the resulting 3D-BC-NP-Pt thin films can be fine-tuned by tailoring the electrodeposition reaction parameters. Moreover, we demonstrated that the new 3D-BC-NP-Pt structure possess excellent electrochemical sensing properties in complex biofouling environments and remarkable catalytic activity toward the methanol electro-oxidation compared with conventional planar platinum electrodes. The present fabrication strategy is facile, reliable, reproducible, scalable and conducive to microfabrication. These findings will open the gates for the development of high performance and reliable electrodes for energy, catalysis, sensing, and miniaturized device (e.g. implantable neural electrodes) applications. The as-prepared 3D-BC-NP-Pt structures will enrich the field of electrochemical sensing and electrocatalysis research via introducing a new bicontinuous porous high surface area electrode that can be fabricated easily and reliably.

## 5.2 Experimental section

### 5.2.1 Reagents and Materials

Potassium tetrachloroplatinate (II)  $K_2PtCl_4$  46-47% Pt, ACROS Organics™, methanol,  $CH_3OH$  99.9%, Extra Dry, AcroSeal™, ACROS Organics™, bovine fibrinogen (90% clottable, MP Biomedicals), nitric acid  $HNO_3$  69.3%, potassium chloride KCl, potassium hydroxide KOH, potassium phosphate monobasic  $KH_2PO_4$ , and potassium phosphate dibasic  $K_2HPO_4$ , were purchased from Fisher Scientific (*CAUTION*:  $HNO_3$  is a highly corrosive acid and must be handled with caution using gloves, safety glasses and protective clothing in a fume hood). Potassium ferricyanide  $K_3[Fe(CN)_6]$  was purchased from Sigma-Aldrich. Elevate® Platinum 7810 RTU and Techni Silver 1025 RTU were obtained from Technic Inc. US. All chemicals were used as received without any further purification. The electrochemical measurement were performed using ultrapure type-I water (18.2 MΩ.cm at 25 °C) obtained from Millipore Milli-Q water purification system. Nitrogen gas was obtained from AirGas Company, Richmond, VA. Gold mirror conductive substrates made of a 100 nm-thick gold and 5 nm-thick titanium adhesion layer on glass were purchased from EMF Corporation, Ithaca NY.

### 5.2.2 Preparation of the Conductive Substrate

EMF gold mirror slides were cut to produce rectangular planar gold electrodes of 1 cm x 2.5 cm. The electrodes were sonicated successively in deionized water, soap, deionized water, ethanol and deionized water for cleaning and dried with nitrogen gas. The clean and dry gold slides were subject to oxygen plasma cleaning (PE2000 RF Plasma Etcher, South Bay Technology) for

5 min at 30 W, 140 mtorr and DC bias of -400 V and were left in air accessible clean chamber for 30 min before use.

### **5.2.3 Fabrication of Three-Dimensional Bicontinuous Nanoporous Platinum Thin Films**

Three-dimensional bicontinuous nanoporous platinum (3D-BC-NP-Pt) electrodes with different morphologies were fabricated as follow:

#### **5.2.3.1 Electrodeposition of Pt–Ag Thin Films**

Pt–Ag binary alloy thin films were co-electrodeposited on hanged gold working electrodes from solutions containing  $[\text{Ag}(\text{CN})_2]^-$  and  $[\text{PtCl}_4]^{2-}$  complex ions of varying molar ratios in the presence of Elevate<sup>®</sup> Platinum 7810 RTU (Tech. Inc.) as a supporting electrolyte and extra platinum source. The geometrical area of the working electrodes was defined by a 1 cm x 1 cm square using CS Hyde UHMW polyethylene tape positioned on the gold mirror electrode surface. A three-electrode electrochemical cell housing platinum gauze as the counter electrode, and a silver chloride-coated silver reference electrode positioned close to the gold slide working electrode was used to carry out the electrodeposition experiments at room temperature from stirred solutions. The electrochemical deposition experiments were performed under an amperometric mode using a CHI-1000A potentiostat at a constant potential of  $-1.0$  V for a desired period of time (10 min) to produce Pt–Ag binary alloy thin films of varying compositions. The electrodeposited alloy films were rinsed with copious amounts of deionized water three times and dried at  $60$  °C for 30 min then annealed at  $300$  °C for 6 h at  $2$  °C/min heating rate.

### 5.2.3.2 Dealloying Pt–Ag Thin Films and Evolution of the Three-Dimensional Bicontinuous Nanoporous Platinum Structures

Three-dimensional bi-continuous nanoporous platinum structures were obtained by chemically dealloying the as-prepared Pt–Ag binary alloy thin films for 30 min in 1:1 nitric acid (*CAUTION*:  $\text{HNO}_3$  is a highly corrosive and dangerous acid and must be handled with extreme caution using protective equipment such as gloves, safety glasses and protective clothing in a fume hood). The resulting porous electrodes were immersed in deionized water for 15 min, four times to remove any trace amounts of nitric acid from the evolved porous platinum networks. Then the 3D-BC-NP-Pt electrodes were dried under a gentle stream of nitrogen gas. The as-prepared 3D-BC-NP-Pt electrodes are air stable for more than 4 months.

In a typical experiment, 3D-BC-NP-Pt thin films with hierarchical porosity and on purposely designed micro-cracks were prepared by dealloying a Pt–Ag thin film electrodeposited at -1.0 V for 10 min from a bi-component electroplating solution. The electroplating solution was prepared by adding 20 mg  $\text{K}_2\text{PtCl}_4$  to 9.0 mL of the supporting electrolyte and stirring the mixture for 2 min followed by sonication for 10 min and finally the desired amount of  $[\text{Ag}(\text{CN})_2]^-$  was added, 200  $\mu\text{L}$  of Techni Silver 1025 RTU, Tech. Inc. (*CAUTION*: cyanide based salts are highly toxic and must not subject to heat, acid or light. Extreme care, use of protective equipment and running the electrodeposition experiment in an acid-free closed chamber equipped with an efficient ventilation system are a must). This sample has been chosen a model example to investigate the characteristics of the 3D-BC-NP-Pt thin films in electrochemical sensing and methanol electro-

oxidation. While nanorods-based 3D-BC-NP-Pt thin films were obtained as follow: first a plating solution composed of 20 mg  $K_2PtCl_4$ , 9.0 mL of the supporting electrolyte and 75  $\mu L$  of  $[Ag(CN)_2]^-$  was prepared. The chemical composition of the plating solution was modified/adjusted by depositing a Pt–Ag thin film for 2 min. The resulting electrode after 2 min was discarded while the modified electroplating solution was used to deposit Pt–Ag thin film on a new gold electrode at -1.0 V for 10 min. Upon dealloying 3D-BC-NP-Pt nanorods with circular apex and ice-cream-cone like structures were obtained. (*NOTE*: always the electrodeposited Pt–Ag thin films annealed at 300 °C for 6 h before the dealloying process).

**Table 5.1** summarized the experimental details for preparing the different nanoporous platinum structures.

**Table 5.1.** Experimental details for preparing the nanoporous platinum structures.

Electroplating solution for	$K_2PtCl_4$ , mg	Elevate Platinum 7810 RTU, mL	Techni Silver 1025 RTU, $\mu L$	Deposition Potential, volts	Deposition time, min
Sample A	20	9.0	75	-1.0	10
Sample B	20	9.0	100	-1.0	10
Sample C	20	9.0	200	-1.0	10
Sample D*	20	9.0	75	-1.0	10

\*: for sample D deposition was carried out for 2 min then the substrate was replaced and deposition carried out on a new substrate for 10 min.

#### 5.2.4 Characterization of 3D-BC-NP-Pt Electrodes

The surface morphology of the electrodeposited Pt–Ag binary alloy thin films and the resulting 3D-BC-NP-Pt structures after the dealloying process were investigated using a HITACHI SU-70 field-emission scanning electron microscope (FE-SEM). The post-dealloying chemical composition of the BC-NP-Pt films was examined by energy dispersive X-ray spectrometer (EDX) using a HITACHI SU-70 FE-SEM. Thickness of the dealloyed films was measured via collecting cross-sectional SEM images.

Platinum and silver contents in the electroplating solutions were determined by using Varian-Vista MPX, CCD Simultaneous inductively coupled plasma-optical emission spectroscopy (ICP-OES).as follow: first, seven aqueous platinum standard solutions were prepared by the continuous dilution of the stock platinum standard (Inorganic Ventures  $1000 \pm 4 \mu\text{g/mL}$ ) using 2% trace metal grade nitric acid solution. A 1.00 mL of the stock platinum standard ( $1000 \mu\text{g/mL}$ , 1000 ppm) was diluted to 10.00 mL to produce the first platinum standard of 100 ppm concentration. Then 5.00 mL of the as-prepared platinum standard (100 ppm) was diluted to 10.00 mL to produce the second platinum standard of 50 ppm concentration. A 5.00 mL of the second platinum standard (50 ppm) was used to prepare the third platinum standard of 25 ppm concentration. The same dilution method was used to prepare 12.50, 6.25, 3.125 and 1.5625 ppm platinum standards.

Second, 10 mL of the stock silver standard (Inorganic Ventures  $100.52+0.72 \mu\text{g/mL}$ ) was used as the first silver standard solution. The second silver standard solution of 50 ppm

concentration was obtained by diluting 5.00 mL of the first standard solution to 10.00 mL using 2% trace metal grade nitric acid solution. Then 25, 12.5, 6.25, 3.125 and 1.5625 ppm silver standards were prepared by following the same dilution protocol.

The electroplating solutions correspond to samples A, B, C and D (**Table 5.1**) were diluted 200 times before the ICP measurements using 2% trace metal grade nitric acid solution. Typically, a 0.50 mL of the electroplating solution was diluted to 100.00 mL.

The obtained ICP data are summarized in **Table 5.2**, all numbers should be multiplied by 200 to get the actual concentration.

**Table 5.2.** As-obtained ICP data for the nanoporous platinum electroplating solutions.

No.	Electroplating solution for	[Platinum], ppm	[Silver], ppm
1	Sample A	9.090	1.379
2	Sample B	8.909	1.710
3	Sample C	8.081*	3.625
4	Sample D	9.133	1.293

\* This number is low because of error in the weighing of the Pt salt.

### 5.2.5 Electrochemical Measurements

The electrochemical performance and characteristics of the as-prepared 3D-BC-NP-Pt thin film electrodes relative to the commercially available planar platinum electrodes (CHI102, 2 mm diameter and BASi, 1.6 mm diameter) were examined by means of cyclic voltammetry. All electrochemical measurements were performed at room temperature in a typical 3-electrode one-

chamber electrochemical setup using a platinum wire auxiliary electrode and silver-silver chloride (1 M KCl internal filling solution) reference electrode. For all the electrochemical measurements working 3D-BC-NP-Pt electrodes with an exposing geometrical area of  $0.0792 \text{ cm}^2$  were used. Geometrical area of the working electrodes was defined by utilizing a 1/8 in. circle punched in a rectangular piece of CS Hyde UHMW polyethylene tape positioned on the 3D-BC-NP-Pt electrode surface just prior to the measurement. The planar Pt electrodes were cleaned by rinsing the electrode surface with a plenty of deionized water and gently wiping it using a Kimwipe. The dry electrode was rinsed again with deionized water three times and polished on a polishing cloth pad with  $0.5 \mu\text{m}$  alumina suspension for 2-3 min. Then, it cleaned with a plenty of deionized water three times and polished again on a clean wet cloth pad for 2-3 min. After that, the electrode rinsed with deionized water three times and sonicated in deionized water, ethanol and deionized water each for 5 min (*CAUTION*: sonication for long time may damage the electrode via the overheating). After sonication the electrode was dried by nitrogen gas. The cleaned and dry electrode was plasma cleaned for 5 min at 30 W and kept in a clean chamber overnight before use.

The electrochemical sensing and biofouling of the working electrodes experiments were conducted using a multichannel CHI-1000A electrochemical workstation while the performance of the 3D-BC-NP-Pt working electrodes toward the electro-oxidation of methanol was evaluated by cyclic voltammetry on a CHI-401 electrochemical workstation (CH Instruments Inc.) and compared to planar platinum electrode.  $10 \text{ mM K}_3[\text{Fe}(\text{CN})_6]$  in  $0.1 \text{ M KCl}$  used for the sensing



experiments. For the biofouling test 10 mM  $K_3[Fe(CN)_6]$ , 10 mM and 2 mM ascorbic acid in PBS (0.1M, 0.1 M KCl, 7.4 pH) and 1 mg/mL fibrinogen were used.

## 5.3 Results and discussion

### 5.3.1 Fabrication of Three-Dimensional Bicontinuous Nanoporous Platinum Thin Films

**Figure 5.1** is a graphical illustration of the template-less fabrication of nanorods and nanoporous gold-like 3D-BC-NP-Pt structures with and without hierarchical porosity.

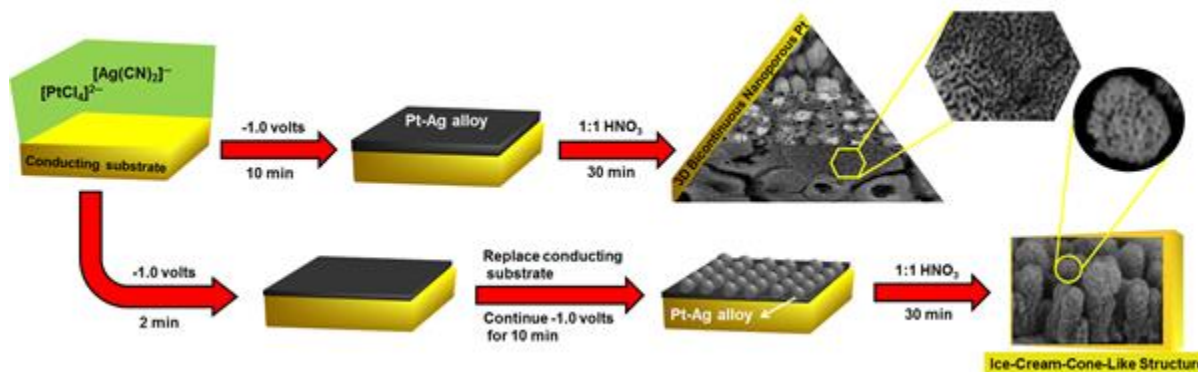


**Figure 5.1.** Schematic Illustration (Not Drawn to Scale) of the Fabrication of Three-Dimensional Bicontinuous Nanoporous Platinum (3D-BC-NP-Pt) Structures through Chemical Dealloying of the Co-Electrodeposited Pt–Ag Binary Alloy Thin Films.

The fabrication strategy of the 3D-BC-NP-Pt structures is based on the combination of the coordination chemistry, electrochemical reduction and corrosion chemistry. The fabrication strategy is composed of two main steps: (a) co-electrodeposition of a single phase silver-rich platinum binary alloy Pt–Ag thin film and (b) chemical dealloying of the electrodeposited Pt–Ag alloy thin films in nitric acid. The dealloying technique is well known since the 1920s and in which

the porous metal structure is obtained by the selective removal of the least noble component from an alloy in a corrosive medium.<sup>27-29</sup> There is a basic requirement to ensure success of the pores formation during the dealloying process, the rate of the dissolution of the more noble component in the target alloy should be significantly slower than that of the less noble component.<sup>30</sup> The challenge in the formation of 3D bicontinuous porous noble metal structures via the dealloying technique is attributed to the fact that dealloying of a given system (e.g. Au–Ag) is only possible within a narrow compositional range. Outside this range and at high percentage of the more noble metal, the complete dissolution of the less noble alloy component is impossible and random pores are obtained.<sup>31, 32</sup> While at low concentration of the more noble metal, formation of microscopic cracks or complete destruction of the resulting porous framework is possible.<sup>30</sup> However, the main challenge during the fabrication of 3D-BC-NP-Pt structures lay in the electrodeposition of a single phase Pt–Ag binary alloy thin film of a proper composition for many reasons.<sup>14</sup> Although both platinum and silver are crystallized in face cubic structures similar to gold, the Pt–Ag system has limited solid solubility opposite to Au–Ag system which has complete solid solubility across the whole composition range.<sup>33-35</sup> The large degree of immiscibility in the Pt–Ag system and the high melting points of Pt (~1772 °C) and Ag (~962 °C) hinder the control over the Pt–Ag alloy composition which is of a particular importance during the evolution of the 3D bicontinuous nanoporous structure via the dealloying process.<sup>27, 36</sup> Although Pt–Ag binary alloys is a suitable candidate for the formation porous platinum structures, the simultaneous electrodeposition of Pt and Ag is problematic. The rate of Ag electrodeposition is much faster than that of platinum and

thus a high degree of control over the electrodeposition reaction parameters and plating solution composition is required to deposit Pt–Ag alloy of a desired composition.<sup>14</sup> Due to the chemical nobility of platinum, its simple salts are not very stable and it mainly stabilized through the formation of coordination compounds such as the square planer  $[\text{PtCl}_4]^{2-}$  complex ion. There is a need to shift the reduction potential of platinum precursors to a more negative potential to avoid or minimize the spontaneous galvanic displacement reaction in the presence of  $\text{Ag}^0$  and this could be achieved by choosing a proper platinum complex.<sup>14,37</sup> Electrodeposition of platinum thin films are usually carried out from plating solutions containing chloride-, borate- or phosphate-based supporting electrolytes.<sup>14</sup> These electrolytes react with  $\text{Ag}^+$  ions forming white ( $\text{AgCl}$  or  $\text{AgBO}_2$ ) or yellow ( $\text{Ag}_3\text{PO}_4$ ) precipitates and this hinders the electrodeposition of Ag and so prevent the formation/co-electrodeposition of Pt–Ag binary alloy. Careful experimental examination of the Pt–Ag system electrodeposition (e.g. testing different precursors and different supporting electrolytes) and understanding the silver coordination chemistry led to the finding that silver cyanide complex  $[\text{Ag}(\text{CN})_2]^-$  with a formation constant of  $5.6 \times 10^{18}$  can be stable<sup>38</sup> in such environments and both Pt and Ag can simultaneously electrodeposited from a plating solution containing  $[\text{PtCl}_4]^{2-}$  and  $[\text{Ag}(\text{CN})_2]^-$  ions. The electrodeposition reaction parameters (e.g. deposition time and potential) for the Pt–Ag system were optimized to produce bicontinuous nanoporous platinum structures after the selective dissolution of Ag in acidic medium. By manipulating the Pt : Ag mole ratio in the electroplating solution bicontinuous nanoporous platinum structures with different morphologies were obtained.

**Figure 5.2** and **Figure 5.3** display the SEM micrographs of the as-prepared 3D-BC-NP-Pt structures and a representative SEM of an electrodeposited Pt–Ag binary alloy thin film, respectively. As can be seen in **Figure 5.3** the electrodeposited Pt–Ag binary alloy thin film is non-porous. Upon the acid treatment of the Pt–Ag thin film, silver is selectively dissolved and platinum atoms diffuse and aggregate at the metal/acid interface to form a 3D-BC-NP-Pt structure as shown in **Figures 5.2-5.4**.

### 5.3.2 Morphology and Pt : Ag Mole Ratio

At low Pt : Ag mole ratio of 9.27 : 2.56, the low magnification SEM images (**Figure 5.2** (a, b)) indicate that the resulting platinum thin film (**sample A**) is crack-free, porous and particulate

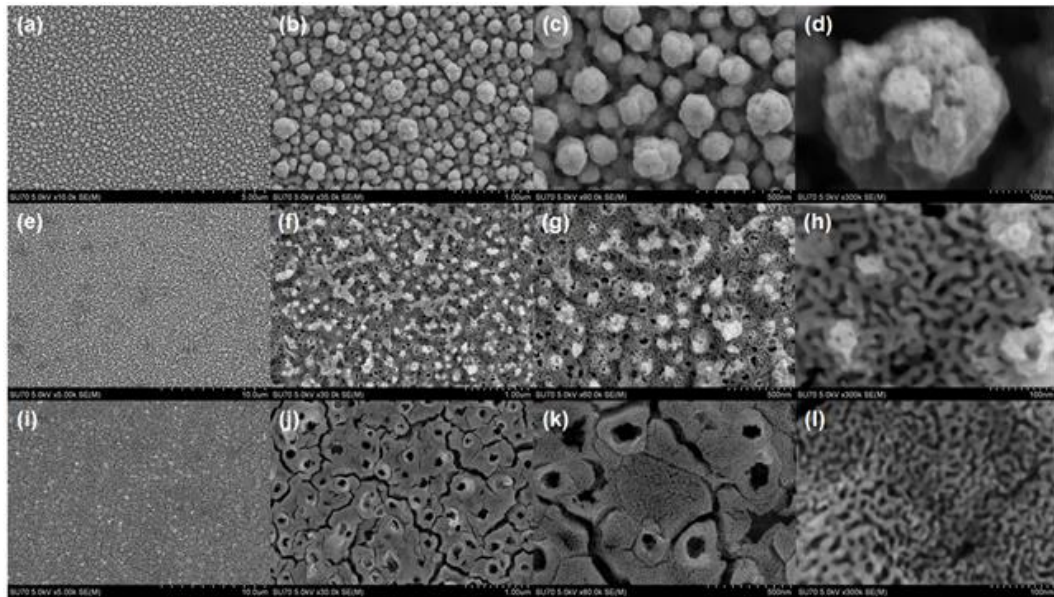


**Figure 5.2.** SEM micrographs of the post-dealloying porous platinum particulate-like structure (a-d, sample A), crack-free 3D-BC-NP-Pt structure with hierarchical porosity (e-h, sample B), and hierarchical 3D-BC-NP-Pt structure with nano-cracks (i-h, sample C). Electroplating solutions of 9.27:2.56, 9.27:3.17, and 9.27:6.72 Pt:Ag mole ratios were used to produce the pre-dealloying films corresponding to samples A, B and C, respectively.

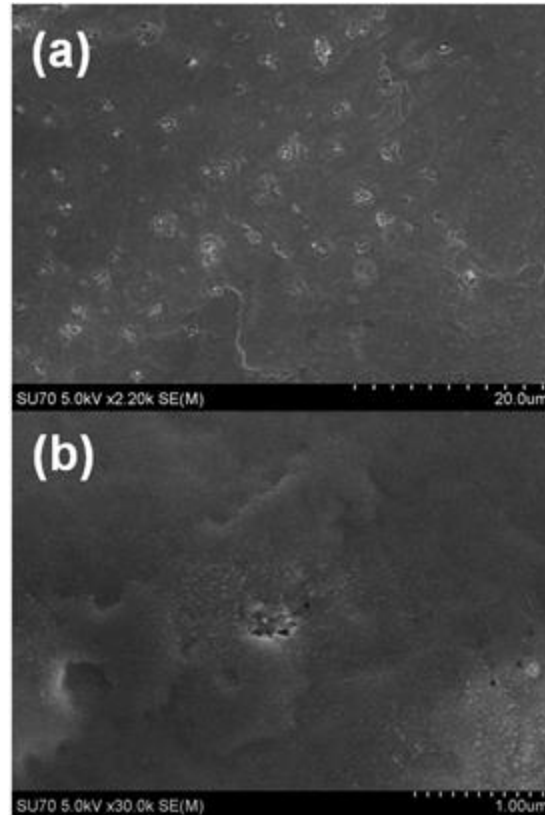


**Figure 5.3.** SEM images of the electrodeposited Pt-Ag thin film (pre-dealloying sample C) from a plating solution containing 9.27:6.72 Pt:Ag mole ratio at -1.0 V for 10 min.

in nature. While, the high magnification SEM images (**Figure 5.2** (c, d)) reflect the mesoporous nature of the film where the particles at the film upper interface are characterized by the presence of a large number of interconnected mesopores and the underneath particles are arranged and connected with each other in such a fashion to create a mesopores-rich rough blanket with some macropores. The formation of 3D bicontinuous porous platinum structure was not very pronounced in this film, which may imply that the concentration of silver in the electrodeposited Pt-Ag film was not high enough to produce a 3D bicontinuous porous structure upon its dissolution and/ or

the platinum content in the deposited film was high to the extent that limited/hindered the bicontinuous porous structure formation upon the silver dissolution.

Upon increasing the concentration of silver in the electroplating solution by a factor of 1.24, a 3D-BC-NP-Pt structure was obtained when the electrodeposited Pt–Ag film was treated with nitric acid, **Figure 5.2** (e-h). At low magnification (**Figure 5.2** (e)), the platinum film (**sample B**) is porous, crack-free and characterized by the presence of platinum islands/clusters at the film interface. Interestingly, closer examination of the microstructure of the resulting film after the dealloying process at high SEM magnification (**Figure 5.2** (f-h)) indicated the presence of 3D-BC-NP-Pt structure with hierarchical porosity. The observed platinum islands/clusters are themselves porous in nature and embedded within the 3D-BC-NP-Pt structure. The hierarchical 3D-BC-NP-Pt structure is composed of multimodal pores: (a) large semi-circular pores of average size  $42.4 \pm 13.6$  nm,  $N = 15$  (b) medium size bicontinuous pores with an average diameter and ligaments size of  $13.9 \pm 9.9$  nm ( $N = 22$ ) and  $11.8 \pm 3.0$  nm ( $N = 13$ ), respectively and (c) small pores within the platinum clusters of 5.7 nm diameters. The medium size bicontinuous pores are the dominant pore-type and all the pores are within the mesopores size range 2-50 nm which is indicative of the mesoporous nature of the resulting 3D bicontinuous porous platinum film. The formation of hierarchical porosity 3D-BC-NP-Pt structure is advantageous because the 3D bicontinuous small pores will effectively increase the surface area of the electrode while the semi-circular large pores will facilitate the transport of the analyte species to the smaller 3D-BC pores.<sup>23</sup>

<sup>39</sup> This will provide additional sites (active centers) for the electron exchange process and enhance

the electrode area. The net result will be an efficient mass transport and electron exchange between the redox molecules and the 3D-BC-NP-Pt electrode surface and hence enhancement in the sensitivity and electrocatalytic activity of the electrode. Here it is important to point out that no surfactants or structure directing agents were added to the electroplating solution and the resulting films after the dealloying process were not further treated except by drying with nitrogen gas.

Hierarchical 3D-BC-NP-Pt thin film (**sample C**) with multimodal porosity and nano-cracks was obtained when the concentration of silver in the electroplating solution further increased to be 6.72 mmol as can be seen in **Figure 5.2** (i-l). Examining the SEM micrographs reveal a nearly complete disappearance of the platinum islands/clusters. The effect of increasing the silver content on the microstructure of the hierarchical 3D-BC-NP-Pt structure is explicit in the high magnification SEM micrographs where cracks with an average width of  $81.8 \pm 27.6$  nm,  $N = 16$  were observed. The presence of these nano-cracks is advantageous because it enables fast kinetics release of an analyte loaded over or within the porous metal framework.<sup>40</sup> The average size of the semi-circular large pores almost doubled to be  $99.2 \pm 25.0$  nm,  $N = 17$  while the average size and thickness of the small pores and ligaments composing the bicontinuous porous structure decreased to be  $9.6 \pm 3.3$  nm ( $N = 12$ ) and  $8.9 \pm 3.1$  nm ( $N = 14$ ), respectively. Combining the merits of the multimodal hierarchical pore morphology and the fast kinetics release of an analyte through the nano-cracks makes the obtained 3D-BC-NP-Pt structure a potential platform for the drug delivery applications.<sup>40</sup> The cracks formation may be assigned to the stress, and volume contraction during the construction of the brittle continuous porous metal structure from a relatively thick alloy film

placed in a corrosive medium.<sup>40</sup> It worthwhile to mention that, in all the obtained 3D-BC-NP-Pt structures, the pores and the ligaments are of a comparable size.

### 5.3.3 Film Thickness

**Figure 5.4** and **Figure 5.5** display the cross-sectional SEM images of the as-prepared nanostructured porous platinum thin films. It is clear that the film thickness increases with the increase of the silver concentration in the electroplating solution. The porous platinum films A, B and C displayed an average thickness of  $408 \pm 104$ ,  $294 \pm 55$  and  $294 \pm 19$  nm,  $N = 15$  respectively.

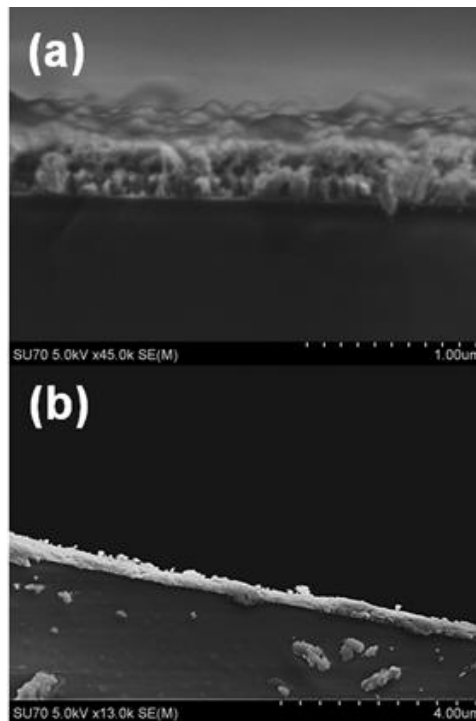


**Figure 5.4.** Cross-sectional SEM images of the post-dealloying porous platinum thin films; sample A (a) and sample B (b). The images evident the preservation of the porous microstructural features throughout the film thickness and demonstrate the increase of the films thickness with the increase of silver content in the electroplating solution.



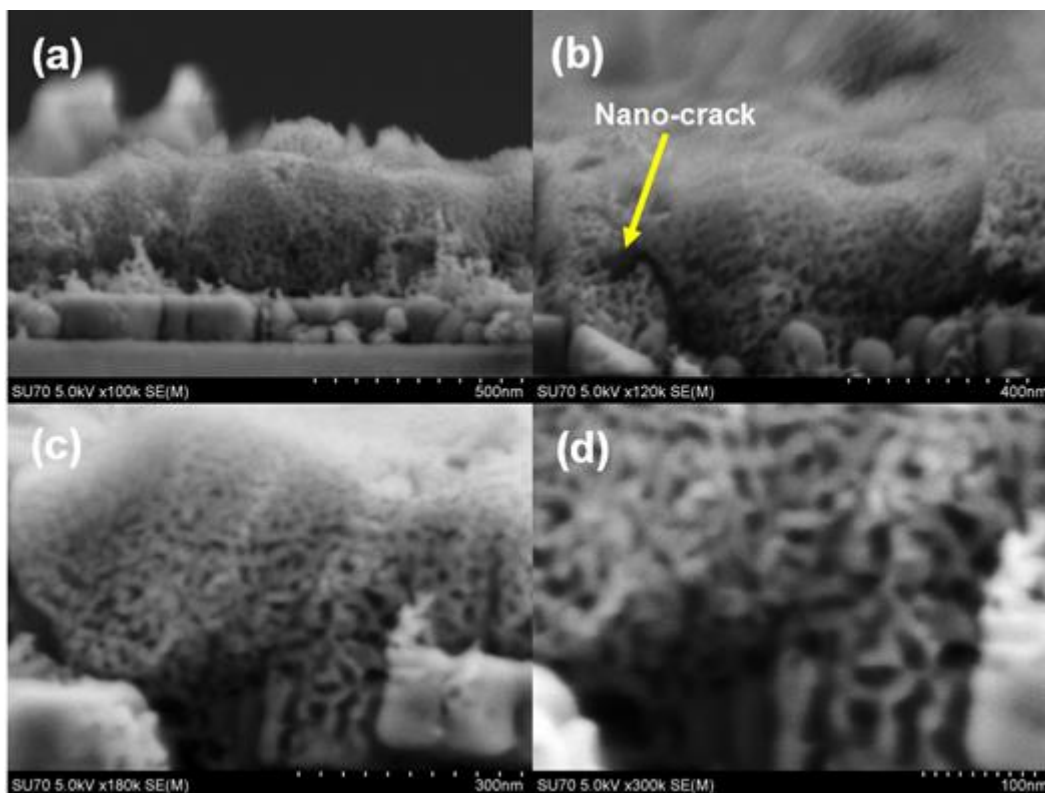


**Figure 5.5.** Cross-sectional SEM images of the hierarchical 3D-BC-NP-Pt structure with nano-cracks (sample C). The images evident the preservation of the bicontinuous porous microstructural features throughout the film thickness.

The high magnification cross-sectional SEM images of **sample C** distinctly demonstrate that the microstructural features of the hierarchical 3D-BC-NP-Pt structure observed on the dealloyed film surface are maintained throughout the film thickness as shown in **Figure 5.5**. The efficiency of the dealloying strategy as well as the remaining silver content after the dealloying process were examined by the EDX measurements. **Figure 5.6** shows a representative EDX spectra of the electrodeposited Pt–Ag film and the resulting 3D-BC-NP-Pt film after the dealloying

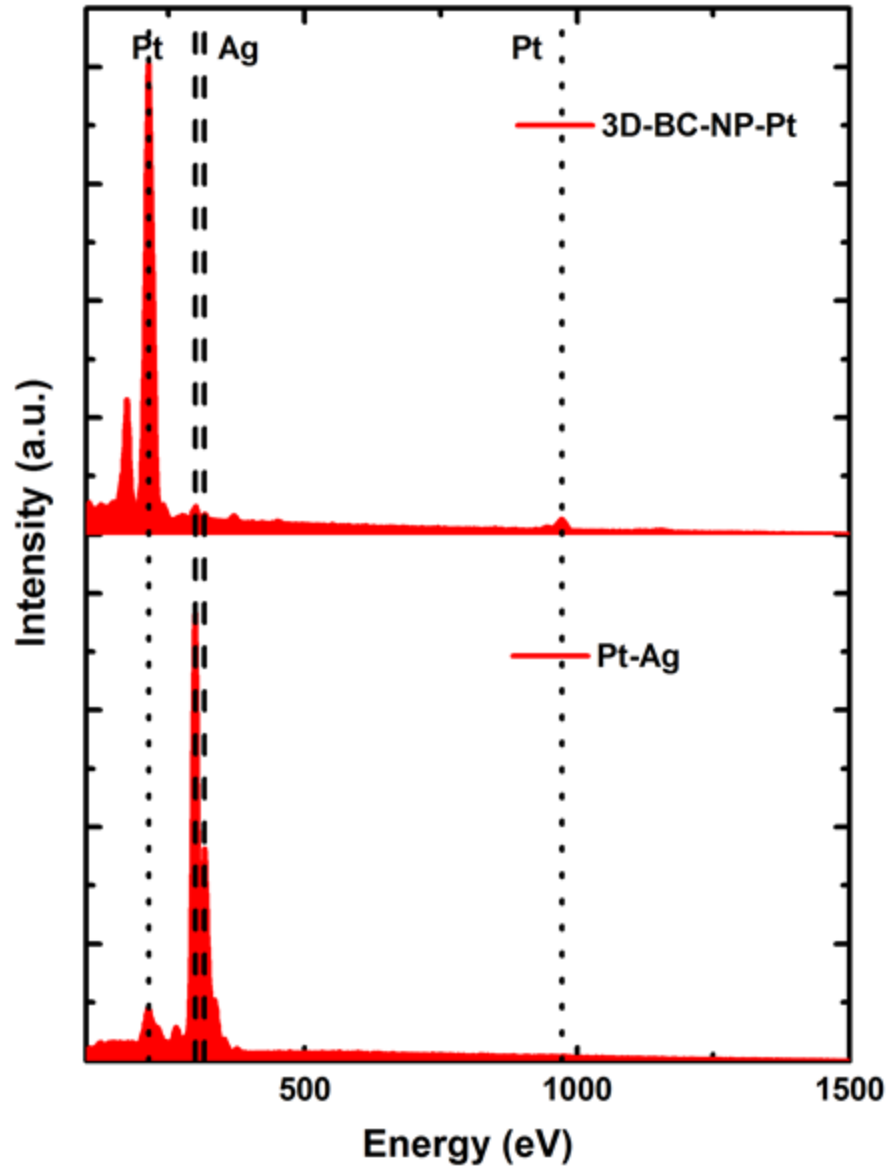


**Figure 5.6.** EDX spectra of the electrodeposited Pt-Ag thin film from a solution containing Pt:Ag mole ratio of 9.27:6.72 at -1.0 V for 10 min and the 3D-BC-NP-Pt thin film (sample C) obtained by the selective removal of Ag in HNO<sub>3</sub>. The success of the co-electrodeposition of silver-rich platinum alloy thin film and the high efficiency of the dealloying process is evident.

process. It is evident that the electrodeposited film is composed of silver-rich platinum alloy and the silver content in the post-dealloyed film is significantly reduced to be ~ 2-4 atomic%. The obtained data reflect the efficiency of the applied dealloying strategy. A similar residual silver content has been reported before for nanoporous gold prepared by dealloying silver-rich gold alloys in acid medium.<sup>25, 40</sup>

### 5.3.4 Template-Less Fabrication of 3D Bicontinuous Porous Platinum Nanorods

We postulated that the absence of continuous porosity in the post-dealloying film (**sample A**) can be tackled by tailoring Pt : Ag mole ratio in the electroplating solution. In order to examine this postulation, an extra electrodeposition step has been introduced to fine-tune the Pt : Ag mole ratio in the electroplating solution in a trail to get a continuous porous platinum structure. The composition of the electroplating solution was modified by running the electrodeposited process for 2 min at -1.0 V, the conductive substrate was then removed from the electroplating solution and discarded. A new conductive substrate was introduced into the modified plating solution and electrodeposition was carried out for 10 min at -1.0 V as shown in **Figure 5.1**. The resulting Pt–Ag film underwent the same post treatments applied to samples A, B and C.

**Figure 5.7** displays the SEM micrographs of the electrodeposited Pt–Ag film before and post the dealloying process. The electrodeposited Pt–Ag film (**Figure 5.7** (a-d)) is particulate in nature and the particles composing the film are non-porous. Two types of particles can be identified at the film surface, relatively large particles with an average size of  $160.1 \pm 37.7$  nm,  $N = 9$  and smaller particles with median particle diameter of  $50.6 \pm 11.9$  nm,  $N = 9$ . Careful examination of

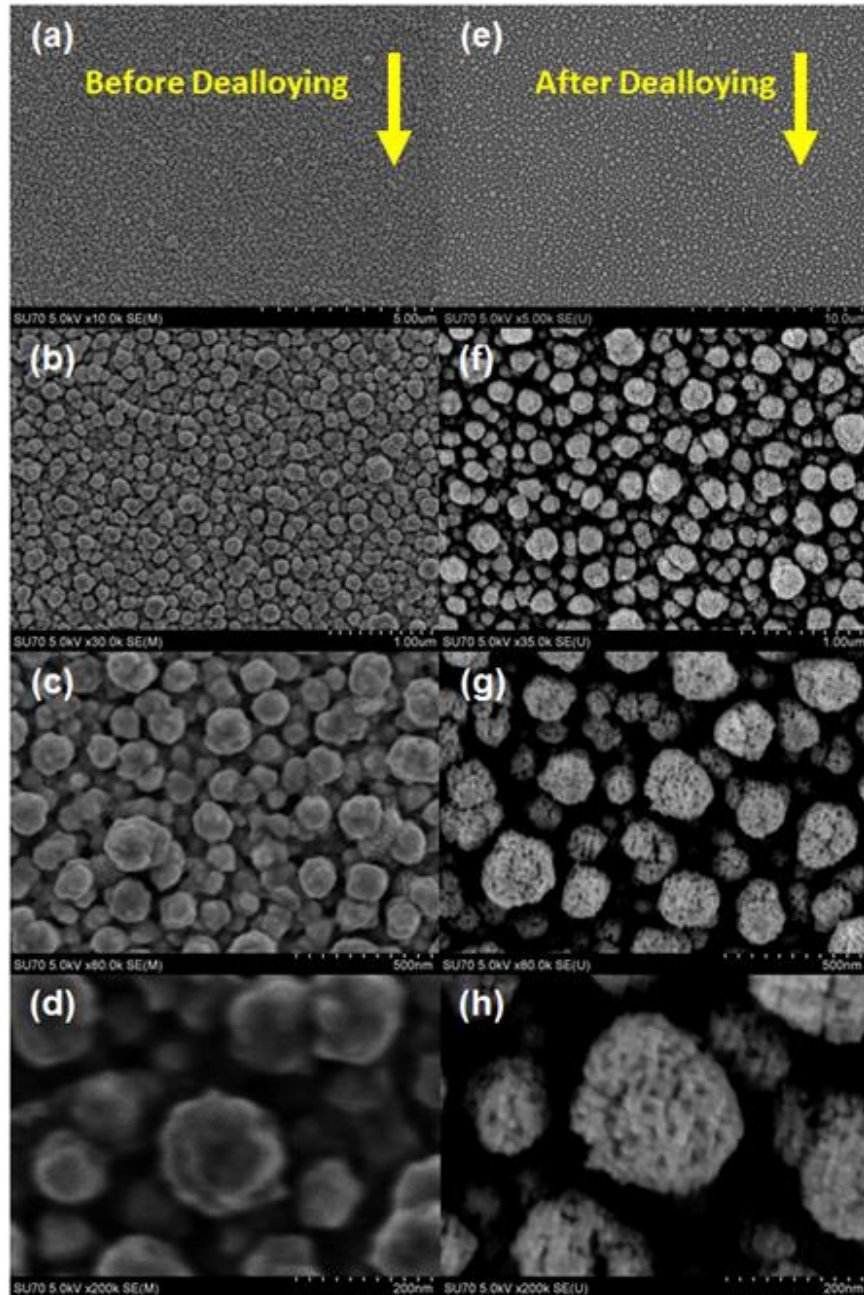


**Figure 5.7.** (a-g) SEM images of the electrodeposited Pt-Ag thin film from the same plating solution used for sample A after modifying it through depositing Pt-Ag for 2 min at -1.0 V then replacing the conductive substrate and continue the deposition for 10 min at -1.0 V. (e-h) SEM images of the resulting 3D-BC-NP-Pt structure (sample D) after the dealloying process.

the high resolution SEM image (**Figure 5.7** (d)) further confirmed the non-porous nature of the deposited particles and reveals that the as-deposited film is porous where the particles composing the film are separated from each other' and within the interstitial spaces that ranged from 19.8 to 201.3 nm small separate particles with an average size of  $50.6 \pm 11.9$  nm,  $N = 9$  can be identified. These findings are interesting and may imply that these particles grew as single entities and what the SEM images are showing is simply the top view of growing nanorods. However, further investigation is required to support this claim.

The low magnification SEM micrograph (**Figure 5.7** (e)) reveals that the post-dealloyed film (**sample D**) preserved the particulate nature of the pre-dealloyed mother film. On the other hand, the high magnification SEM micrographs distinctly demonstrate the evolution of 3D-BC-NP-Pt structure after the selective silver removal as shown in **Figure 5.7** (f-h). The microstructure of the post-dealloyed film is similar to that of the pre-dealloyed mother film and is made up of relatively large 3D-BC-NP-Pt particles with  $192.0 \pm 42.6$  nm ( $N = 9$ ),  $10.8 \pm 1.9$  nm ( $N = 11$ ) and  $14.8 \pm 5.0$  nm ( $N = 6$ ) average size, pore diameter and ligaments thickness, respectively. These porous particles are separated from each other by voids ranging from 9.5 to 239.9 nm. The voids contain smaller porous particles with an average size of  $50.7 \pm 4.8$  nm,  $N = 6$ ; these particles are separated from each other' and from the larger ones. It is worthwhile to mention that the particles and voids size increased after the dealloying process and thus the post-dealloyed film is more porous than the mother Pt-Ag film where the particles composing the film became more separated and less dense after the dealloying process as shown in **Figure 5.7** (c, g and d, f).

In order to further explore the microstructure of the dealloyed porous platinum film, cross-sectional SEM images were collected. Interestingly, the post-dealloyed platinum film (**sample D**) is composed of 3D-BC-NP-Pt nanorods as can be seen in **Figure 5.8**.

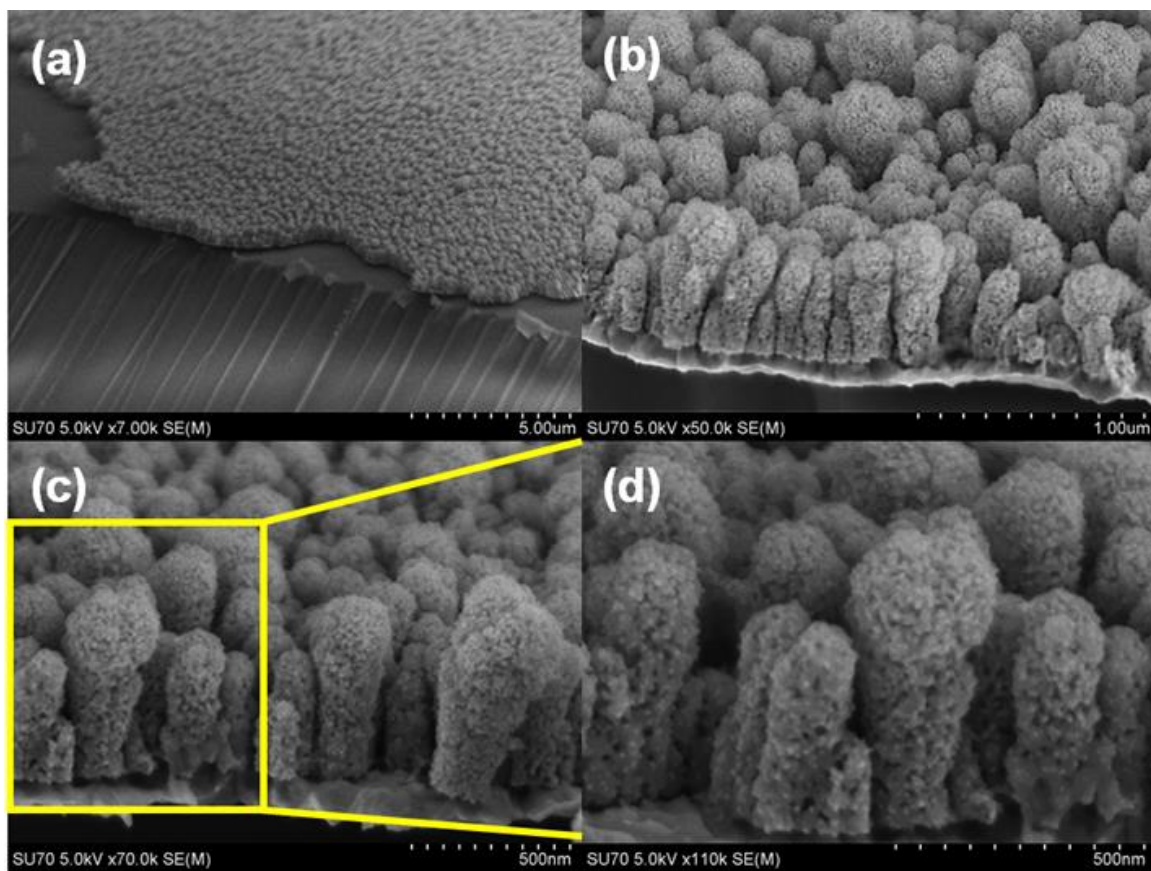


**Figure 5.8.** Cross-sectional SEM micrographs of the 3D-BC-NP-Pt structure (sample D). The images demonstrate that the post-dealloyed film is composed of 3D-BC-NP-Pt nanorods with circular apex and ice-cream-cone-like structure.

Close examination of the cross-sectional SEM micrographs at high magnification demonstrates the presence of two different types of nanorods that correspond to the two different particle sizes identified in top view SEM images. Short nanorods with circular apex ranged in height from 179.9 to 463.6 nm and longer nanorods with ice-cream-cone like structure and height scales between 458.2 and 704.3 nm. The ice-cream-cone like nanostructured porous rods correspond to the large porous spherical particles observed in the top view SEM micrographs of the post-dealloyed film. These findings clearly indicate the magnificent role of tailoring the Pt : Ag mole ratio in fine-tuning the morphology of the resulting 3D-BC-NP-Pt films.

### **5.3.5 Electrochemical Measurements**

The hierarchical 3D-BC-NP-Pt thin film with multimodal porosity and nano-cracks (**sample C**) was selected as a model to examine the electrochemical characteristics of the bicontinuous porous platinum nanostructures.

#### **5.3.5.1 Surface Area Measurement**

An important character that directly affects the electrochemical sensing and electrocatalytic performance of an electrode is its electrochemically active surface area (ECSA), which is a reflection/measure of the number of electrochemically active sites on the exposed electrode surface. The median ECSA of the as-prepared 3D-BC-NP-Pt electrode was evaluated by means of cyclic voltammetry for four 3D-BC-NP-Pt electrodes in 0.5 M H<sub>2</sub>SO<sub>4</sub> at a scan rate of 50 mV/s and compared to that of a planar platinum electrode as shown in **Figure 5.9**.

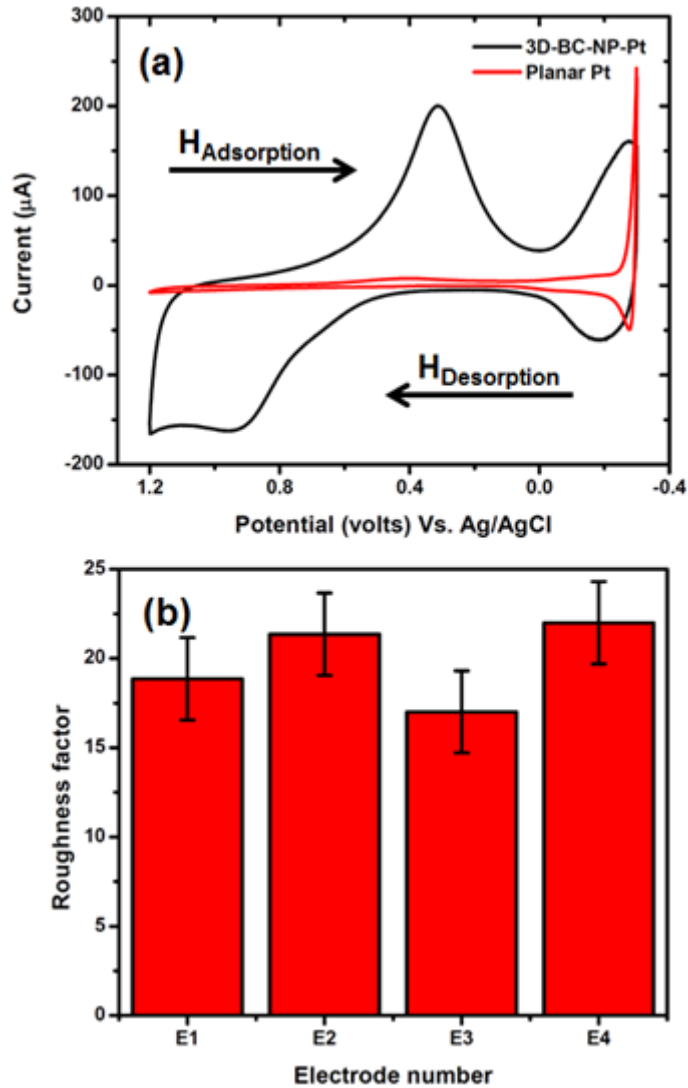


**Figure 5.9.** Cyclic voltammetric (CV) curves of the as-prepared 3D-BC-NP-Pt electrode (sample C) and planar platinum electrode in 0.5 M  $\text{H}_2\text{SO}_4$  at a scan rate of 50 mV/s (a). The roughness factor (surface area enhancement) of four different 3D-BC-NP-Pt electrodes prepared at different days was found to be  $19.81 \pm 2.31$ ,  $N = 4$ , (b).



The total charge associated with the hydrogen adsorption ( $H^+ \rightarrow H_{ad}$ ) peak around -0.27 V (vs Ag/AgCl, 1.0 M KCl) during the cathodic sweep was calculated and corrected with respect to the double layer capacity, and a conversion factor of  $210 \mu\text{C}/\text{m}^2$  was used to calculate the ECSA of the exposed electrode surface.<sup>41-45</sup> **Figure 5.9** obviously demonstrates that the charge associated with the hydrogen adsorption on the 3D-BC-NP-Pt electrode is significantly higher than that on planer platinum electrode. The roughness factor (R.F. = ECSA/ geometrical area of the electrode) for the 3D-BC-NP-Pt electrode is  $19.81 \pm 2.31$ ,  $N = 4$ . This finding indicates that the surface area of the nanoporous platinum electrode is ~ 20 times higher than that of a planer platinum electrode which has a R.F. of 1.0. The significant enhancement in the surface area of the 3D-BC-NP-Pt electrode was expected due to the presence of a large population of nanopores in the 3D bicontinuous framework.

To further examine the surface area of the as-prepared 3D-BC-NP-Pt thin films, CVs were concurrently acquired at a planar platinum electrode and three porous platinum electrodes in 0.1 M KCl at different scan rates. The measured non-Faradaic capacitive current at 0.25 V in 0.1 M KCl is directly proportional to the electrode surface area. As it obvious in **Figure 5.10**, the non-Faradaic charging current for the 3D-BC-NP-Pt electrode is significantly higher than that of the planar electrode, which is attributed to the higher surface area of the porous platinum electrode. As expected, a linear relation was found when the charging current was plotted against scan rate as can be seen in the inset of **Figure 5.10**. The high surface area of the 3D-BC-NP-Pt electrode is demonstrated through its high slope value compared to that of the planar electrode. The ratio of

the slope of the three 3D-BC-NP-Pt electrodes to the slope of the planar platinum electrode is 27.98 which means that the surface area of the porous platinum electrode is ~ 28 times higher than that of the planar electrode. This data is consistent with the surface area measurements in 0.5 M H<sub>2</sub>SO<sub>4</sub>, although it looks a slightly higher.

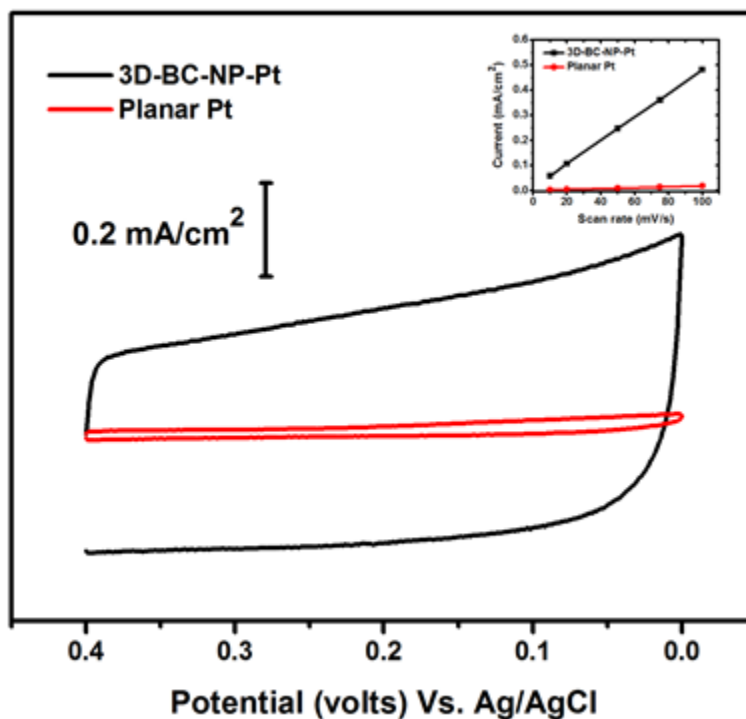


**Figure 5.10.** Cyclic voltammetric (CV) curves of 3D-BC-NP-Pt (sample C) and planar platinum electrodes obtained at 100 mV/s in 0.1 M KCl. The inset displays the relation of the non-Faradaic charging current at 0.25 V vs the scan rate. The slope the current vs scan rate curve for the is much higher than that for the planar platinum electrode which demonstrates the high surface area of the electrode, ~ 28 times higher than that of the planar electrode.

The capacitance (C, F), areal ( $C_a$ , F/cm<sup>2</sup>) and volumetric capacitances ( $C_v$ , F/cm<sup>3</sup>) of the 3D-BC-NP-Pt electrodes were calculated to be 161  $\mu$ F, 2000  $\mu$ F/cm<sup>2</sup> and 400 F/cm<sup>3</sup> from the cyclic voltammograms in 0.1 M KCl according to the equation:

$$C_x = \frac{\int_{v_1}^{v_2} I dv}{x v \Delta V}$$

where x is 1.0, geometric area or volume of the 3D-BC-NP-Pt electrode, v is the scan rate (V/s),  $\Delta V$  is the potential window for the CV measurement and  $\int_{v_1}^{v_2} I dv$  is the integration of the cyclic voltammetry curve.<sup>46-49</sup> The high volumetric capacitance of the 3D-BC-NP-Pt electrode gets back to its high surface area which make the as-prepared porous platinum structures possible platforms for battery-like supercapacitor applications.<sup>47</sup>

### 5.3.5.2 Electrochemical Sensing of a Reversible Diffusing Redox Couple [Fe(CN)<sub>6</sub>]<sup>3-</sup>

The performance of the as-fabricated 3D-BC-NP-Pt structures as a platform for electrochemical sensing applications has been investigated by simultaneously collecting CVs for a set of three 3D-BC-NP-Pt electrodes in 10 mM [Fe(CN)<sub>6</sub>]<sup>3-</sup> in 0.1 M KCl as a supporting electrolyte and compared to those acquired at a planar platinum electrode. The three porous platinum electrodes exhibited the same behavior and representative CVs collected at nanoporous and planar platinum electrodes as a function of scan rate are depicted in **Figure 5.11** and **Figure 5.12**. The CVs collected contemporarily at planar and nanostructured porous platinum electrodes displayed a well-defined redox peaks characteristic of the reversibly diffusing monoelectronic redox system [Fe(CN)<sub>6</sub>]<sup>3-</sup>. The ratio of the peak faradaic current at the forward

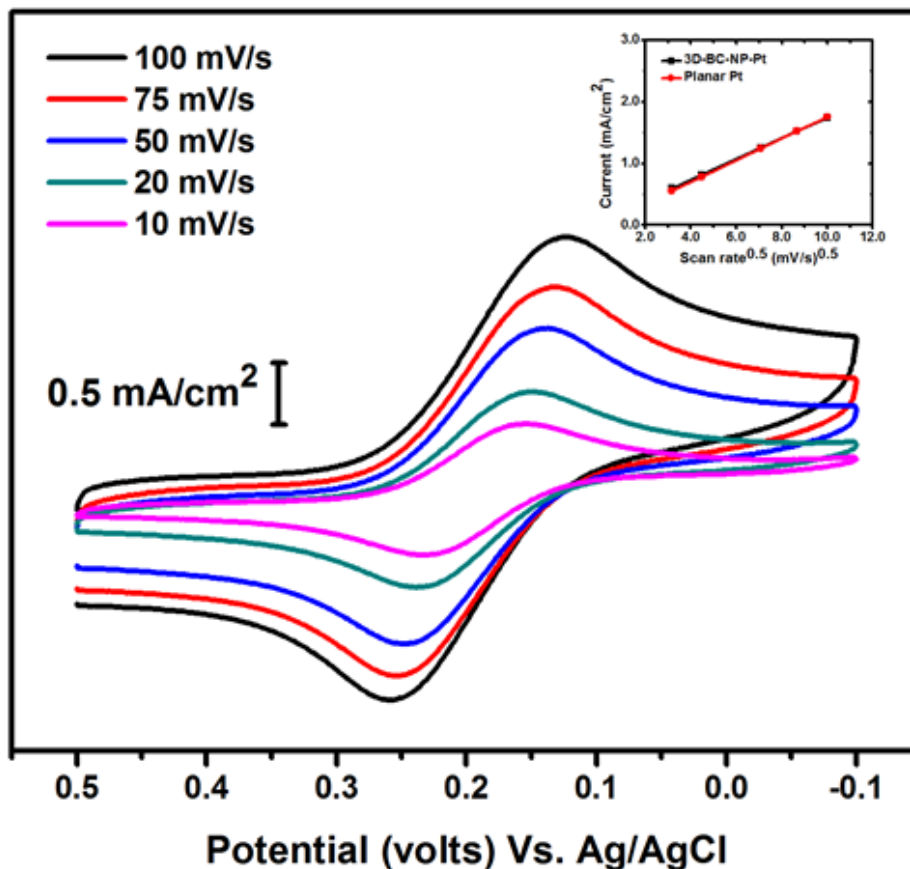


**Figure 5.11.** Cyclic voltammetric (CV) curves of 10 mM [Fe(CN)<sub>6</sub>]<sup>3-</sup> in 0.1 M KCl acquired at 3D-BC-NP-Pt electrode (sample C) at different scan rates. The inset is a plot of the peak Faradaic current as a function of the square root of scan rate. The tested electrodes displayed the same slope for the current vs the square root of scan rate curve which reveals a typical sensing behavior for the 3D-BC-NP-Pt electrode.

scan to that at the backward scan at the different scan rates was found to be  $1.19 \pm 0.03$  and  $1.16 \pm 0.03$  for 3D-BC-NP-Pt and planar electrodes, respectively which is evident of chemically stable redox system at the electrodes surface.<sup>22</sup> Furthermore, the formal reduction potential ( $E^0$ ) of the

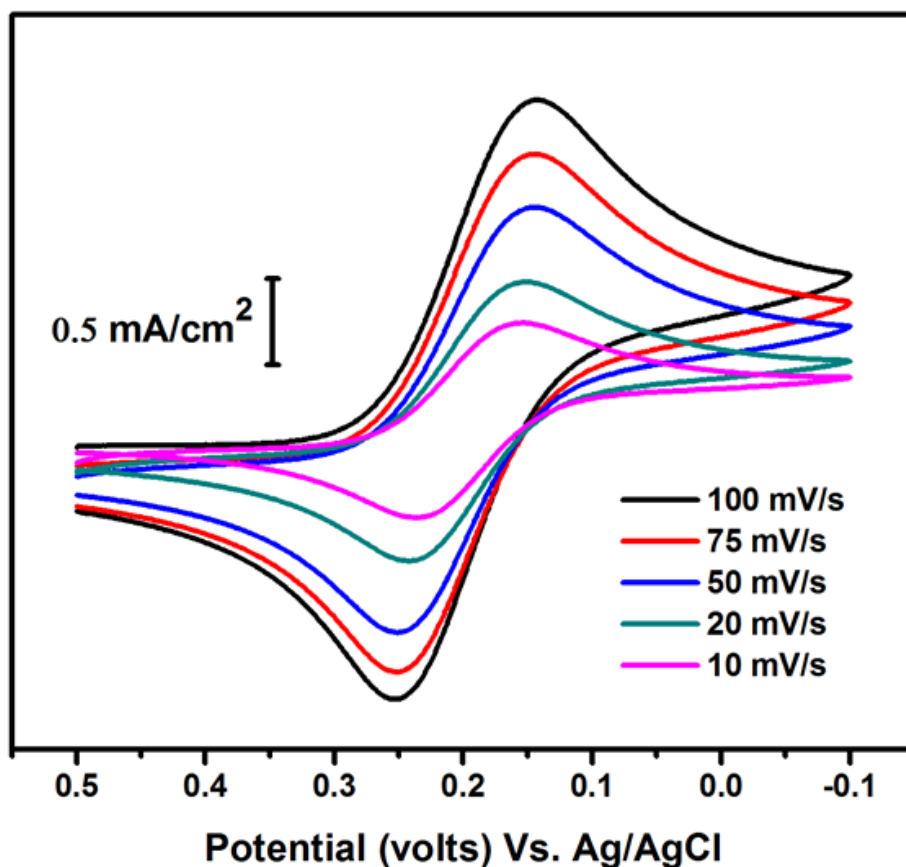


**Figure 5.12.** Cyclic voltammetric (CV) curves of 10 mM  $[\text{Fe}(\text{CN})_6]^{3-}$  in 0.1 M KCl acquired at planar Pt electrode at different scan rates.

studied redox couple at the different scan rates and a lab temperature of  $\sim 22^\circ\text{C}$  was calculated to be  $194.6 \pm 1.0$  mV for 3D-BC-NP-Pt electrode and  $197.4 \pm 1.9$  mV for planar platinum electrode. The small standard deviation ( $\sim 1$  mV) of the calculated  $E^\circ$  at different scan rates is indicative that approximately the same  $E^\circ$  value was observed for the studied redox system at the 3D-BC-NP-Pt electrode regardless of the magnitude of the applied scan rate. In addition, the tested electrodes

displayed a comparable peak splitting at different scan rates as shown in Tables 5.3 and 5.4. These findings are evident of the excellent electrochemical sensing performance of the as-prepared 3D-BC-NP-Pt electrodes that is comparable to that of commercially available platinum electrodes.

**Table 5.3.** Electrochemical characteristics of nanoporous platinum in 10 mM  $[\text{Fe}(\text{CN})_6]^{3-}$

Scan rate, mV/s	$E_{pc}$ , V	$E_{pa}$ , V	$E^{\circ}$ , mV	$\Delta E_p$ , mV	$i_{pc} * 10^{-5}$ , A	$i_{pa} * 10^{-5}$ , A	$i_{pc}/i_{pa}$
100	0.13	0.26	194	114	13.8	11.3	1.22
75	0.13	0.26	193.5	106	12.1	9.98	1.21
50	0.15	0.25	196	104	9.96	8.51	1.17
20	0.15	0.24	194.5	89	6.43	5.61	1.14
10	0.16	0.23	195	83	4.71	3.93	1.20

**Table 5.4.** Electrochemical characteristics of planar platinum in 10 mM  $[\text{Fe}(\text{CN})_6]^{3-}$

Scan rate, mV/s	$E_{pc}$ , V	$E_{pa}$ , V	$E^{\circ}$ , mV	$\Delta E_p$ , mV	$i_{pc} * 10^{-5}$ , A	$i_{pa} * 10^{-5}$ , A	$i_{pc}/i_{pa}$
100	0.14	0.25	197	128	3.785	3.29	1.15
75	0.15	0.25	199	125	3.31	2.90	1.14
50	0.15	0.25	199	98	2.75	2.40	1.15
20	0.15	0.24	197.5	89	1.85	1.59	1.16
10	0.15	0.24	194.5	76	1.39	1.14	1.22

The inset of **Figure 5.11** displays the relation between the peak Faradaic current and the square root of the scan rate for the data acquired at planar and nanoporous platinum electrodes. The morphologically different electrodes displayed a direct relation as was expected and interestingly the two plots/lines superimpose each other with the ratio between their slopes being a unit. A similar surface area was obtained for the two electrodes when their slopes were applied to the Randles–Sevcik equation. This finding indicates that not all the surface area of the nanoporous platinum electrode is used in the electrochemical reaction and only an area approximately equal to the geometric area of the electrode was used. This finding agrees with the reported literature data by Collinson et al. and others for reversible redox species with fast electron transfer kinetics at high surface area electrodes and could be attributed to the prompt consumption of the electroactive redox species at outer pore interface which prohibits the use of the underneath 3D porous network.<sup>23, 50-53</sup>

### **5.3.5.3 Electrochemical Sensing in a Complex Biofouling Environment**

One unique aspect associated with the electrode morphology is the presence of a continuous array of nanopores with diameters of ~ 10 nm, similar to that shown for nanoporous gold.<sup>22, 25, 26, 40</sup> Because of this unique geometric arrangement of nanopores, the surface can act like a biosieving membrane and allow for efficient electron transfer between a redox species in solution and the electrode surface even in the presence of biofouling proteins. To test this hypothesis, the voltammetry of potassium ferricyanide was evaluated at nanoporous (set of 3 electrodes) and planar platinum electrodes in the absence and presence of bovine fibrinogen as a

fouling agent. **Figure 5.13** and **Figure 5.14** show the CVs of 10 mM  $[\text{Fe}(\text{CN})_6]^{3-}$  in 0.1 M phosphate buffer (pH 7.4, 0.1 M KCl) before and after the addition of fibrinogen at planar and 3D-BC-NP-Pt electrodes, respectively.

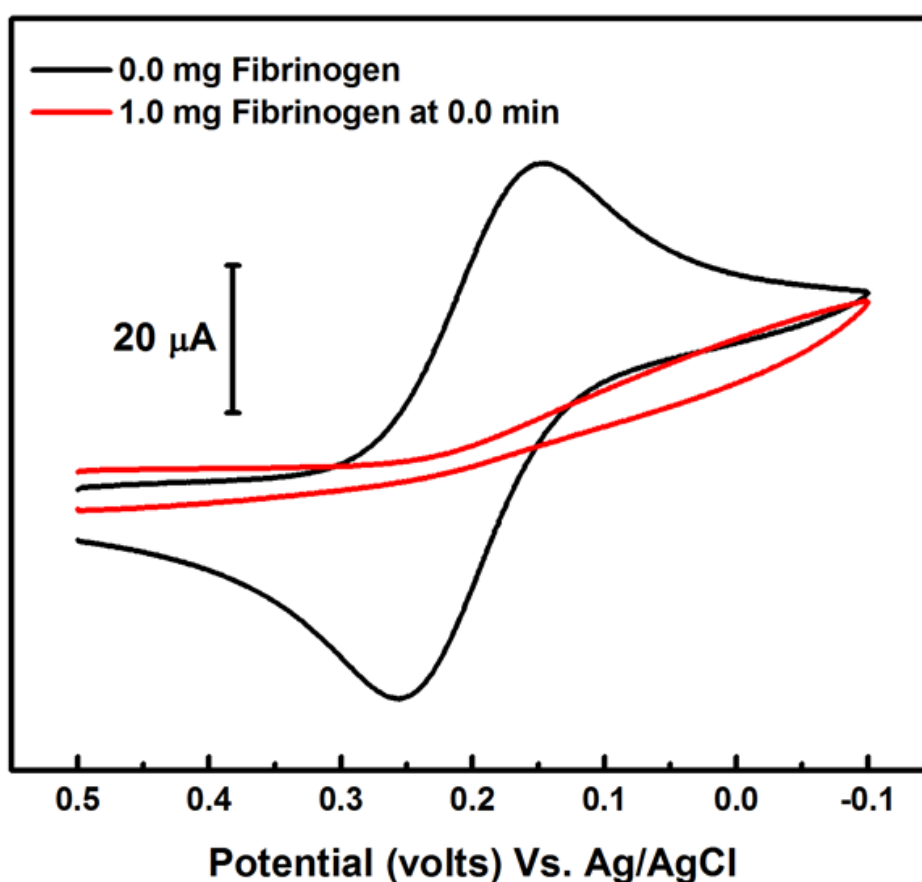


**Figure 5.13.** Cyclic voltammetric (CV) curves obtained at planar platinum electrode in 10 mM  $[\text{Fe}(\text{CN})_6]^{3-}$  in 0.1 M phosphate buffer (pH 7.4, 0.1 M KCl) before (black curve) and after (red curve) addition of bovine fibrinogen (1 mg/mL). Scan rate: 100 mV/s. The electrode was incubated for 1 min before collecting the CV. The effect of the fouling agent is pronounced where the electrode failed to produce any significant electrochemical response.



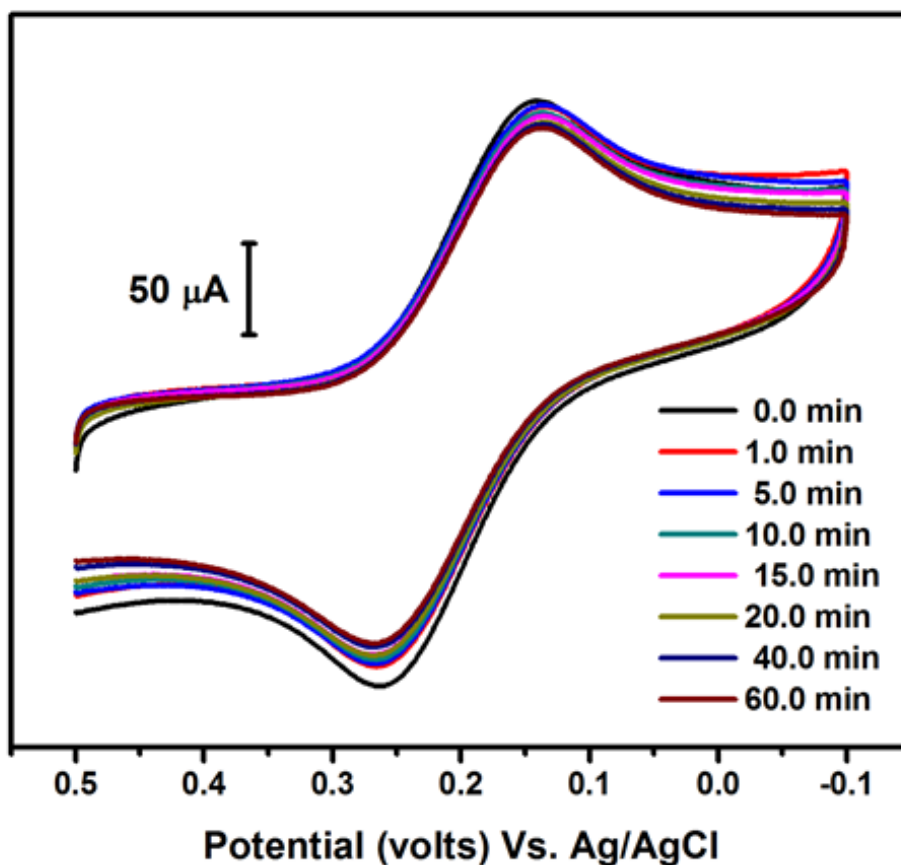


**Figure 5.14.** Cyclic voltammetric (CV) curves acquired at 3D-BC-NP-Pt electrode (sample C) in 10 mM  $[\text{Fe}(\text{CN})_6]^{3-}$  in 0.1 M phosphate buffer (pH 7.4, 0.1 M KCl) before (0.0 min) and after addition of bovine fibrinogen (1 mg/mL). Scan rate: 100 mV/s. The electrode was incubated for 1 min before collecting the CVs over a 60 min period. CVs of well-defined peaks obtained which reflecting the excellent performance of the porous platinum electrode in biofouling environments.

As can be seen, at a planar platinum electrode, the obtained CV is characteristic of an electrochemically quasi-reversible redox probe; the peak splitting is 107 mV when the scan rate was 100 mV/s. After addition of fibrinogen, the faradaic peak for the reduction of  $[\text{Fe}(\text{CN})_6]^{3-}$  decreases dramatically indicative that the surface of the electrode has been contaminated, or

biofouled by the addition of fibrinogen. In contrast, at nanoporous platinum, no significant change in the voltammetric behavior of  $[\text{Fe}(\text{CN})_6]^{3-}$  was observed after addition of fibrinogen, **Figure 5.14**. The peak splitting remains at  $124.86 \pm 1.9$  mV and minimal change in the Faradaic peak current was observed over ~22 h time period.

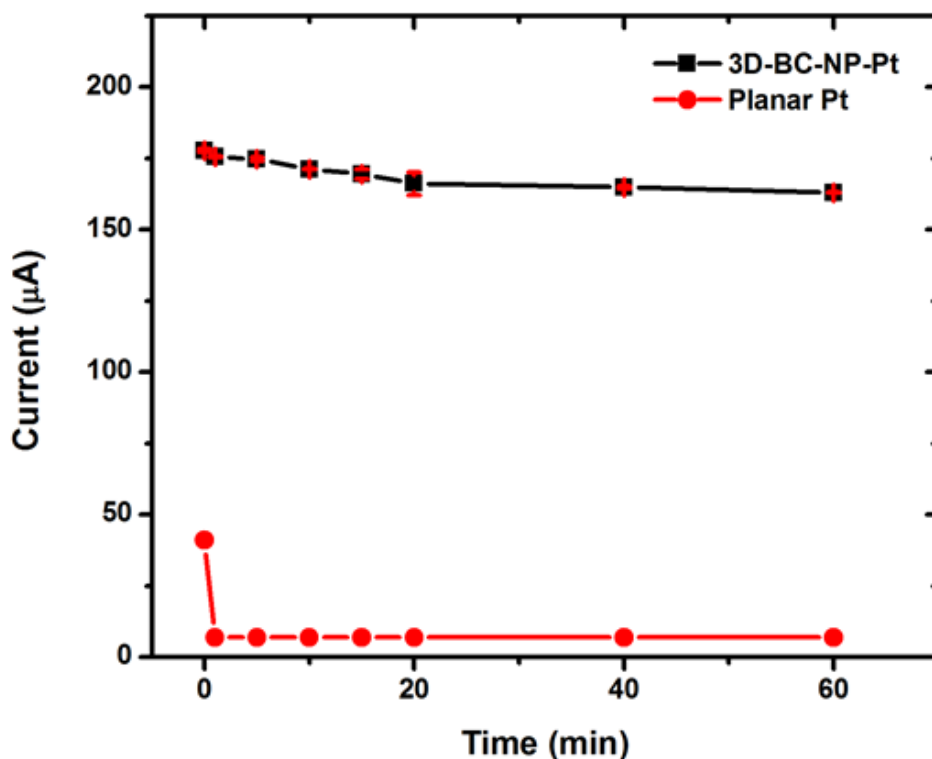


**Figure 5.15.** Peak current data acquired at 3D-BC-NP-Pt (sample C, back line) and planar platinum (red line) electrodes from a 10 mM  $[\text{Fe}(\text{CN})_6]^{3-}$  in 0.1 M phosphate buffer (pH 7.4, 0.1 M KCl) aqueous solution before ( $t = 0$ ) and after the addition of fibrinogen (1mg/mL) to the solution. Data recorded over a 60 min period at a scan rate of 100 mV/s. The error bars represent the standard deviations of the peak current data acquired simultaneously from 3 porous platinum electrodes. Planar platinum electrode peak current signal vanished in the biofouling environment while that of the porous platinum almost did not change.

To better see the change in Faradaic current of  $[\text{Fe}(\text{CN})_6]^{3-}$  following addition of fibrinogen, the current at  $\sim 138$  mV was measured and plotted vs time and the results are shown in **Figure 5.15**. Again, a significant drop in current took place at the planar Pt electrode due to the adsorption of the fibrinogen molecules on the electrode surface and electrode became no longer responsive while only a 8.3 % drop was observed at 3D-BC-NP-Pt after immersion for 60 min. Interestingly, the peak current ratio of  $[\text{Fe}(\text{CN})_6]^{3-}$  redox probe at nanoporous platinum electrode maintained the unit value over time in the biofouling environment. This proves the fast and efficient electron transfer between the nanoporous platinum electrode and the  $[\text{Fe}(\text{CN})_6]^{3-}$  ions in the solution takes place even in the presence of adsorbed fibrinogen. This results is attributed to the unique microstructure, nanoscale features and biosieving-like behavior of the nanoporous electrode. These results are very similar to nanoporous gold prepared by dealloying, which has a similar pore arrangement.<sup>25</sup>

#### 5.3.5.4 Electro-Oxidation of Methanol

The electrocatalytic activity of the as-prepared bicontinuous nanoporous platinum films (set of three electrodes) toward methanol oxidation has been evaluated by means of cyclic voltammetry under alkaline conditions and compared to a commercial planar platinum electrode. All the electrochemical measurements were conducted in a deaerated 1 M KOH aqueous solution containing 0.5 M methanol at room temperature and under nitrogen as a protection atmosphere. Activation of the tested electrodes has been done by cycling them in 1 M KOH aqueous electrolyte within the voltage range -1.0 to 0.6 V (vs Ag/AgCl) for 10 cycles at scan rate of 50 mV s<sup>-1</sup>. The as-prepared nanoporous platinum electrodes displayed an exceptionally high catalytic activity

toward the electro-oxidation of methanol compared to that of the planar platinum electrode. Representative cyclic voltammograms (CVs) for the electro-oxidation of methanol at a scan rate of  $50 \text{ mVs}^{-1}$  are depicted in **Figure 5.16**.

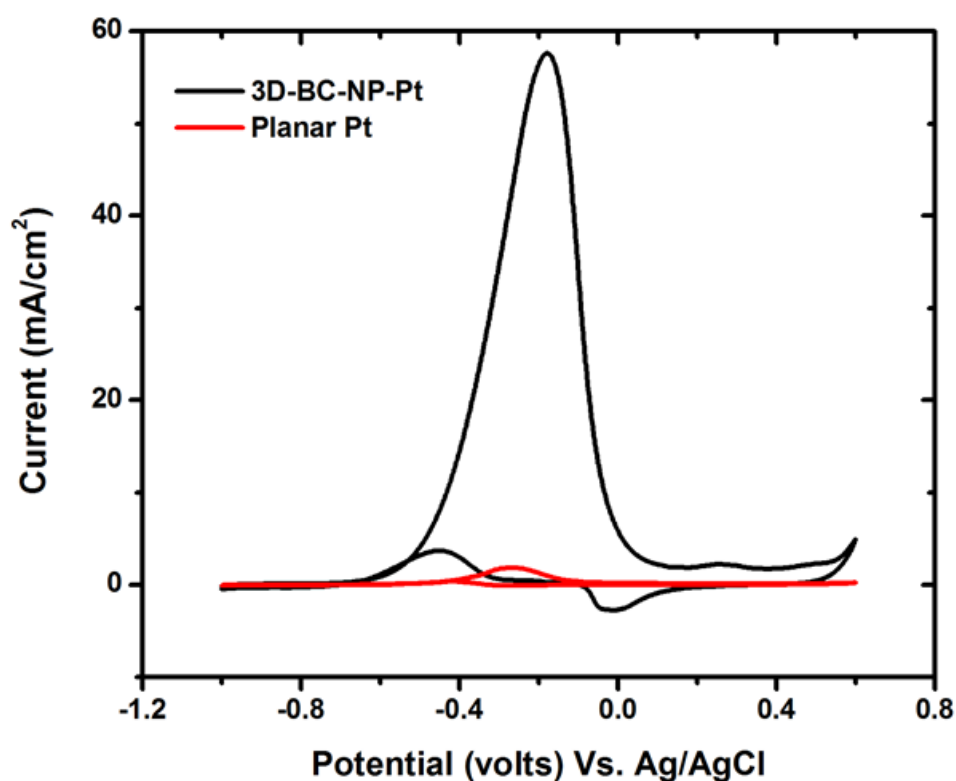


**Figure 5.16.** Comparison of the cyclic voltammetric (CV) curves for methanol electro-oxidation obtained at 3D-BC-NP-Pt electrode (sample C, black curve) and planar platinum electrode (red curve) from alkaline solution containing 0.5 M  $\text{CH}_3\text{OH}$  in 1.0 M KOH. Scan rate: 50 mVs. The high catalytic activity of 3D-BC-NP-Pt electrode toward methanol electro-oxidation is obvious and the rate of methanol electro-oxidation at BC-NP-Pt electrode is 30 times higher than that on planar platinum electrode.

The tested electrodes displayed two well-defined current peaks characteristic of methanol electro-oxidation. The symmetric anodic peak observed in the forward scan corresponds to the oxidation of freshly adsorbed methanol species. This peak shifted from -294 mV on planar platinum electrode to  $-177.6 \pm 3.2$  mV on nanoporous platinum electrodes. The significant shift of the peak potential to a less negative value may be attributed to the high surface area, nanoscale and nano-confinement features, large number of active sites and the enhanced mass transport through the porous network which facilitate/catalyze the methanol electro-oxidation. During the reverse scan, an anodic oxidation current peak around -0.4 V was recorded. This peak can be attributed to sweeping the incompletely oxidized carbonaceous organic intermediates formed on the electrode surface during the forward potential sweep. The high tolerance of the 3D-BC-NP-Pt catalyst toward the accumulation of carbonaceous organic residues on the electrode surface is pronounced in its very high  $i_f/i_b$  ratio  $\sim 19$  ( $i_f$  and  $i_b$  are the forward and reverse anodic peak current densities, respectively) which is 4 times larger than that of the planar Pt electrode. The ratio  $(i_f)_{3D-BC-NP-Pt}/(i_f)_{planar-Pt}$  was found to be 30, which demonstrates that the rate of methanol electro-oxidation at nanoporous platinum is 30 times higher than that at planar platinum. Another factor that reflects the high catalytic activity of the 3D-BC-NP-Pt electrode toward the methanol oxidation is the very low catalyst loading that lies in the microgram scale. A rough catalyst loading of  $\sim 35$  micrograms can be calculated based on the median film thickness 435 nm, diameter of the cylindrical electrode 0.32 cm, and assuming that pores and ligaments are having the same size and their ratio is 1:1 so density of nanoporous platinum will be half that of bulk Pt. These interesting findings make the

as-prepared 3D-BC-NP-Pt catalyst a potential candidate to overcome the sluggish kinetics of methanol electro-oxidation and so pave the way to its possible application in high current outputs direct methanol fuel cells.

## 5.4 Conclusion

Silver-rich platinum binary alloys thin films have been successfully prepared by the co-electrodeposition of  $[\text{Ag}(\text{CN})_2]^-$  and  $[\text{PtCl}_4]^{2-}$  complex ions on conductive substrates at ambient conditions. Bicontinuous nanoporous platinum thin film electrodes with different morphologies and microstructural features similar to that of nanoporous gold were obtained via the selective removal of silver in an acid medium. The electrochemically assisted strategy for bicontinuous porous platinum fabrication is simple, reproducible, time and cost effective where very low platinum concentrations in the mmole range are required. These merits make the developed fabrication strategy a promising candidate for the large scale production. By tailoring the composition of the electroplating solution hierarchically porous crack-free films and films with nano-crack were obtained. Thin films composed of bicontinuous porous platinum nanorods were synthesized by fine-tuning the composition of the electroplating solution in a two-step electrodeposition process. The prepared porous electrodes possess significantly high and tunable surface area with respect to that of planar electrodes. The nanoporous platinum thin film electrodes displayed a typical electrochemical behavior in aqueous medium contains electrochemical reversible redox species and retained its outstanding sensing behavior in complex biofouling environments, in which planar electrodes become irresponsive. High volumetric capacitance and

enhanced catalytic activity toward methanol electro-oxidation were demonstrated for the as-prepared porous platinum electrodes. These interesting findings coupled with the unique structural features of the nanoporous platinum thin films and easy of fabrication, make them potential platforms for many technological applications including high power outputs fuel cells, battery-like supercapacitors, energy storage, drug delivery vehicles, electrochemical sensing, catalysis, and electrocatalysis and miniaturized devices.

## 5.5 References

1. Farghaly, A. A.; Collinson, M. M., Three-Dimensional Bicontinuous Nanoporous Platinum. **2016**.
2. Erlebacher, J.; Seshadri, R., Hard Materials with Tunable Porosity. *MRS Bulletin* **2009**, 34, (08), 561-568.
3. Tappan, B. C.; Steiner, S. A.; Luther, E. P., Nanoporous Metal Foams. *Angewandte Chemie International Edition* **2010**, 49, (27), 4544-4565.
4. Liu, W.; Herrmann, A.-K.; Bigall, N. C.; Rodriguez, P.; Wen, D.; Oezaslan, M.; Schmidt, T. J.; Gaponik, N.; Eychmueller, A., Noble Metal Aerogels-Synthesis, Characterization, and Application as Electrocatalysts. *Accounts of Chemical Research* **2015**, 48, (2), 154-162.
5. Zhu, C.; Du, D.; Eychmueller, A.; Lin, Y., Engineering Ordered and Nonordered Porous Noble Metal Nanostructures: Synthesis, Assembly, and Their Applications in Electrochemistry. *Chemical Reviews* **2015**, 115, (16), 8896-8943.
6. Menzel, N.; Ortel, E.; Kraehnert, R.; Strasser, P., Electrocatalysis Using Porous Nanostructured Materials. *Chemphyschem* **2012**, 13, (6), 1385-1394.
7. Zhang, J. T.; Li, C. M., Nanoporous Metals: Fabrication Strategies and Advanced Electrochemical Applications in Catalysis, Sensing and Energy Systems. *Chemical Society Reviews* **2012**, 41, (21), 7016-7031.
8. Kloke, A.; von Stetten, F.; Zengerle, R.; Kerzenmacher, S., Strategies for the Fabrication of Porous Platinum Electrodes. *Advanced Materials* **2011**, 23, (43), 4976-5008.
9. Yamauchi, Y.; Kuroda, K., Rational Design of Mesoporous Metals and Related Nanomaterials by a Soft-Template Approach. *Chemistry-an Asian Journal* **2008**, 3, (4), 664-676.
10. Song, Y. Y.; Zhang, D.; Gao, W.; Xia, X. H., Nonenzymatic Glucose Detection by Using a Three-Dimensionally Ordered, Macroporous Platinum Template. *Chemistry-a European Journal* **2005**, 11, (7), 2177-2182.
11. Yuan, J. H.; Wang, K.; Xia, X. H., Highly Ordered Platinum-Nanotubule Arrays for Amperometric Glucose Sensing. *Advanced Functional Materials* **2005**, 15, (5), 803-809.
12. Pugh, D. V.; Dursun, A.; Corcoran, S. G., Formation of Nanoporous Platinum by Selective Dissolution of Cu from  $\text{Cu}_{0.75}\text{Pt}_{0.25}$ . *Journal of Materials Research* **2003**, 18, (1), 216-221.
13. Kloke, A.; Koehler, C.; Gerwig, R.; Zengerle, R.; Kerzenmacher, S., Cyclic Electrodeposition of PtCu Alloy: Facile Fabrication of Highly Porous Platinum Electrodes. *Advanced Materials* **2012**, 24, (21), 2916-2921.
14. Rao, C. R. K.; Trivedi, D. C., Chemical and Electrochemical Depositions of Platinum Group Metals and Their Applications. *Coordination Chemistry Reviews* **2005**, 249, (5-6), 613-631.
15. Zhang, Z. H.; Wang, Y.; Qi, Z.; Somsen, C.; Wang, X. G.; Zhao, C. C., Fabrication and Characterization of Nanoporous Gold Composites Through Chemical Dealloying of Two Phase Al-Au alloys. *Journal of Materials Chemistry* **2009**, 19, (33), 6042-6050.



16. Jung, H. Y.; Kim, D. H.; Chun, H. K.; Kim, S. H.; Lim, C. S.; Byun, J. Y.; Jung, Y. J., Towards Engineering Nanoporous Platinum Thin Films for Highly Efficient Catalytic Applications. *Advanced Energy Materials* **2011**, 1, (6), 1126-1132.
17. Scriven, L. E., Equilibrium Bicontinuous Structure. *Nature* **1976**, 263, (5573), 123-125.
18. Collinson, M. M., Nanoporous Gold Electrodes and Their Applications in Analytical Chemistry. *ISRN Analytical Chemistry* **2013**, 2013, 21.
19. Peng, Z.; Yang, H., Designer Platinum Nanoparticles: Control of Shape, Composition in Alloy, Nanostructure and Electrocatalytic Property. *Nano Today* **2009**, 4, (2), 143-164.
20. Litster, S.; McLean, G., PEM Fuel Cell Electrodes. *Journal of Power Sources* **2004**, 130, (1-2), 61-76.
21. Antolini, E., Formation, Microstructural Characteristics and Stability of Carbon Supported Platinum Catalysts for Low Temperature Fuel Cells. *Journal of Materials Science* **2003**, 38, (14), 2995-3005.
22. Farghaly, A. A.; Lam, M.; Freeman, C. J.; Uppalapati, B.; Collinson, M. M., Potentiometric Measurements in Biofouling Solutions: Comparison of Nanoporous Gold to Planar Gold. *Journal of The Electrochemical Society* **2016**, 163, (4), H3083-H3087.
23. Zhao, B.; Collinson, M. M., Hierarchical Porous Gold Electrodes: Preparation, Characterization, and Electrochemical Behavior. *Journal of Electroanalytical Chemistry* **2012**, 684, 53-59.
24. Bicelli, L. P.; Bozzini, B.; Mele, C.; D'Urzo, L., A Review of Nanostructural Aspects of Metal Electrodeposition. *International Journal of Electrochemical Science* **2008**, 3, (4), 356-408.
25. Patel, J.; Radhakrishnan, L.; Zhao, B.; Uppalapati, B.; Daniels, R. C.; Ward, K. R.; Collinson, M. M., Electrochemical Properties of Nanostructured Porous Gold Electrodes in Biofouling Solutions. *Analytical Chemistry* **2013**, 85, (23), 11610-11618.
26. Daggumati, P.; Matharu, Z.; Wang, L.; Seker, E., Biofouling-Resilient Nanoporous Gold Electrodes for DNA Sensing. *Analytical Chemistry* **2015**, 87, (17), 8618-8622.
27. Erlebacher, J.; Aziz, M. J.; Karma, A.; Dimitrov, N.; Sieradzki, K., Evolution of Nanoporosity in Dealloying. *Nature* **2001**, 410, (6827), 450-453.
28. Newman, R. C.; Sieradzki, K., Metallic Corrosion. *Science* **1994**, 263, (5154), 1708-1709.
29. Pickerin, H.; Wagner, C., Electrolytic Dissolution of Binary Alloys Containing a Noble Metal. *Journal of the Electrochemical Society* **1967**, 114, (7), 698-&.
30. Sieradzki, K.; Newman, R. C., Stress-Corrosion Cracking. *Journal of Physics and Chemistry of Solids* **1987**, 48, (11), 1101-1113.
31. Lu, X.; Balk, T. J.; Spolenak, R.; Arzt, E., Dealloying of Au-Ag Thin Films with a Composition Gradient: Influence on Morphology of Nanoporous Au. *Thin Solid Films* **2007**, 515, (18), 7122-7126.
32. Lu, X.; Bischoff, E.; Spolenak, R.; Balk, T. J., Investigation of Dealloying in Au-Ag Thin Films by Quantitative Electron Probe Microanalysis. *Scripta Materialia* **2007**, 56, (7), 557-560.
33. Ebert, H.; Abart, J.; Voitlander, J., Metastable Solid-Solutions in Ag-Pt Alloys. *Journal of the Less-Common Metals* **1983**, 91, (1), 89-96.

34. Okamoto, H., Ag-Pt (Silver-Platinum). *Journal of Phase Equilibria* **1997**, 18, (5), 485-485.
35. Elliott, R. P.; Shunk, F. A., The Ag–Au (Silver-Gold) System. *Bulletin of Alloy Phase Diagrams* **1980**, 1, (2), 45-47.
36. Erlebacher, J., An Atomistic Description of Dealloying - Porosity Evolution, the Critical Potential, and Rate-Limiting Behavior. *Journal of the Electrochemical Society* **2004**, 151, (10), C614-C626.
37. Alia, S. M.; Zhang, G.; Kisailus, D.; Li, D.; Gu, S.; Jensen, K.; Yan, Y., Porous Platinum Nanotubes for Oxygen Reduction and Methanol Oxidation Reactions. *Advanced Functional Materials* **2010**, 20, (21), 3742-3746.
38. Hill, J. W.; Petrucci, R. H.; Mosher, M. D., *General chemistry*. Pearson Prentice Hall Upper Saddle River, NJ: 2005.
39. Nyce, G. W.; Hayes, J. R.; Hamza, A. V.; Satcher, J. H., Synthesis and Characterization of Hierarchical Porous Gold Materials. *Chemistry of Materials* **2007**, 19, (3), 344-346.
40. Kurtulus, O.; Daggumati, P.; Seker, E., Molecular release from patterned nanoporous gold thin films. *Nanoscale* **2014**, 6, (12), 7062-7071.
41. Khan, A. S. A.; Ahmed, R.; Mirza, M. L., Evaluation of Catalytic Activity of Pt and Pt-Ru Catalysts for Electro-Oxidation of Methanol in Acid Medium by Cyclic Voltammetry. *Portugaliae Electrochimica Acta* **2009**, 27, (4), 429-441.
42. Stevens, D. A.; Dahn, J. R., Electrochemical Characterization of the Active Surface in Carbon-Supported Platinum Electrocatalysts for PEM Fuel Cells. *Journal of the Electrochemical Society* **2003**, 150, (6), A770-A775.
43. Lee, E. P.; Peng, Z.; Chen, W.; Chen, S.; Yang, H.; Xia, Y., Electrocatalytic Properties of Pt Nanowires Supported on Pt and W Gauzes. *Acs Nano* **2008**, 2, (10), 2167-2173.
44. Rodriguez, J. M. D.; Melian, J. A. H.; Pena, J. P., Determination of the Real Surface Area of Pt Electrodes by Hydrogen Adsorption Using Cyclic Voltammetry. *Journal of Chemical Education* **2000**, 77, (9), 1195-1197.
45. Chi Linh, D.; Thy San, P.; Ngoc Phong, N.; Viet Quan, T., Properties of Pt/C nanoparticle Catalysts Synthesized by Electroless Deposition for Proton Exchange Membrane Fuel Cell. *Advances in Natural Sciences-Nanoscience and Nanotechnology* **2013**, 4, (3).
46. El-Kady, M. F.; Strong, V.; Dubin, S.; Kaner, R. B., Laser Scribing of High-Performance and Flexible Graphene-Based Electrochemical Capacitors. *Science* **2012**, 335, (6074), 1326-1330.
47. El-Kady, M. F.; Ihns, M.; Li, M.; Hwang, J. Y.; Mousavi, M. F.; Chaney, L.; Lech, A. T.; Kaner, R. B., Engineering Three-Dimensional Hybrid Supercapacitors and Microsupercapacitors for High-Performance Integrated Energy Storage. *Proceedings of the National Academy of Sciences* **2015**, 112, (14), 4233-4238.
48. Moussa, M.; Zhao, Z.; El-Kady, M. F.; Liu, H.; Michelmore, A.; Kawashima, N.; Majewski, P.; Ma, J., Free-Standing Composite Hydrogel Films for Superior Volumetric Capacitance. *Journal of Materials Chemistry A* **2015**, 3, (30), 15668-15674.

49. Ali, G. A.; Manaf, S. A. B. A.; Kumar, A.; Chong, K. F.; Hegde, G., High performance Supercapacitor Using Catalysis Free Porous Carbon Nanoparticles. *Journal of Physics D: Applied Physics* **2014**, 47, (49), 495307.
50. Szamocki, R.; Velichko, A.; Holzapfel, C.; Muecklich, F.; Ravaine, S.; Garrigue, P.; Sojic, N.; Hempelmann, R.; Kuhn, A., Macroporous Ultramicroelectrodes for Improved Electroanalytical Measurements. *Analytical Chemistry* **2007**, 79, (2), 533-539.
51. Park, S.; Song, Y. J.; Han, J.-H.; Boo, H.; Chung, T. D., Structural and Electrochemical Features of 3D Nanoporous Platinum Electrodes. *Electrochimica Acta* **2010**, 55, (6), 2029-2035.
52. Jia, F.; Yu, C.; Ai, Z.; Zhang, L., Fabrication of Nanoporous Gold Film Electrodes with Ultrahigh Surface Area and Electrochemical Activity. *Chemistry of Materials* **2007**, 19, (15), 3648-3653.
53. Szamocki, R.; Reculosa, S.; Ravaine, S.; Bartlett, P. N.; Kuhn, A.; Hempelmann, R., Tailored Mesostructuring and Biofunctionalization of Gold for Increased Electroactivity. *Angewandte Chemie-International Edition* **2006**, 45, (8), 1317-1321.

## Chapter 6: Conclusions and Future Work

## 6.1 Conclusion

Novel, facile, reliable, scalable and reproducible strategies for the fabrication of multifunctional nanostructured porous materials have been demonstrated based on the deep understanding and correlation of inorganic-chemistry, organic-chemistry and electrochemistry. All the developed strategies were written as articles and an invention disclosure; published or submitted.

First, porous Au-SiO<sub>2</sub> nanocomposites of various compositions have been prepared by a novel one-step co-electrodeposition route of KAuCl<sub>4</sub> and TMOS on a conducting substrate and from which high surface area nanostructured porous gold electrodes have been successfully prepared. Application of a sufficient negative potential resulted in the simultaneous reduction of gold ions and the formation of hydroxide ions, which subsequently catalyzes the condensation of the pre-hydrolyzed TMOS derived monomers. The as-prepared Au-SiO<sub>2</sub> films are colloidal in nature and possess an interconnected three-dimensional porous framework with different silica – gold ratios depending on the composition of the deposition solutions and the electrodeposition reaction parameters (e.g. time and magnitude of the applied cathodic potential). Chemical etching of the nanocomposite films using hydrofluoric acid resulted in the formation of nanostructured porous gold films with coral-like structures and pores in the nanometer range. The cross-linkage of the gold coral branches resulted in the generation of a porous framework, which consequently led to the formation of high surface area porous gold electrodes. The thickness of the as-prepared Au-SiO<sub>2</sub> nanocomposite films was relatively high and varied from 8 to 15 μm by changing the

applied deposition potential while the thickness of the coral-like nanostructured porous gold films ranged from 0.22 to 2.25  $\mu\text{m}$ . The as-prepared porous gold films are stable and displayed an enhancement in the electrode's surface area up to 57 times relative to the geometric area. Thus they are potential candidates for applications that require high surface area conductive supports, particularly in catalysis and chemical sensing. The developed electrochemical route for the formation of porous gold electrodes possess several advantages that include good reproducibility, low cost via the use of very dilute gold ion solutions, utilization of environmentally friendly solvents ( $\text{H}_2\text{O}$  and  $\text{C}_2\text{H}_5\text{OH}$ ), and does not require expensive equipment, vacuum, or toxic gold cyanide electrolytes. As a result, the electrochemical gold/sol-gel composite strategy for fabricating nanoporous gold is a promising candidate for a large scale production.

Second, using a single-potential-step co-electrodeposition route, polypyrrole-silica (Ppy- $\text{SiO}_2$ ) nanocomposite films characterized by a multimodal porous structure composed of meso- and macropores were cathodically deposited from ethanolic solutions on oxidizable and non-oxidizable substrates. The developed fabrication strategy depends on the combination of electrodeposition, sol-gel chemistry and electro-assisted polymerization processes in a strongly acidic medium. The materials produced have an interesting and unique strata-like pore structure along their depth. With the exception of a silica-rich inner region, the nanocomposite films are homogeneous in composition. Because the region closest to the electrode surface is silica-rich, the fabrication of Ppy- $\text{SiO}_2$  and Ppy free-standing films become possible using a newly developed multistep etching strategy. Such films can be captured on a variety of different supports depending

on the application and they maintain their conductivity when interfaced to an electrode surface. These mesoporous composite films form through a unique mechanism that involves the simultaneous production of two catalysts,  $\text{OH}^-$  and  $\text{NO}^+$ . Through the process of understanding the reaction mechanism, we highlighted the effect of two simultaneous competing redox reactions occurring at the electrode interface on the morphology of the electrodeposited Ppy nanocomposite films and discovered a new parameter named the “*solvent effect*” that can influence the Ppy electropolymerization reaction mechanism and hence control the morphology of the final material. In an ethanolic solvent system, the pyrrole monomers undergo a step-growth polymerization and particulate-like nanostructured films were obtained even upon variation in the monomer or acid concentrations. In an aqueous based system, nanowire-like structures were produced consistent with a chain-growth mechanism. Such materials are promising candidates for a wide range of applications including electrochemical sensing, energy storage, and catalysis. The developed fabrication strategy can be extended to produce a variety of conductive polymer–sol–gel nanocomposite thin films of various morphologies and compositions.

Third, the last, most interesting and challenging project in my dissertation involved the fabrication of 3D bicontinuous porous platinum thin film electrodes with a nanoporous gold-like microstructure. Silver-rich platinum binary alloys thin films have been successfully prepared by the co-electrodeposition of  $[\text{Ag}(\text{CN})_2]^-$  and  $[\text{PtCl}_4]^{2-}$  complex ions on conductive substrates at ambient conditions. Bicontinuous nanoporous platinum thin film electrodes with different morphologies and microstructural features similar to that of nanoporous gold were obtained via

the selective removal of silver in an acid medium. The present fabrication strategy is facile, reliable, reproducible, scalable and conducive to microfabrication and thus it is a suitable for large scale production. The morphology and the porosity of the 3D-BC-NP-Pt thin films can be fine-tuned by tailoring the electrodeposition reaction parameters. Template-less fabrication of nanorods and nanoporous gold-like 3D-BC-NP-Pt thin films with and without hierarchical porosity were demonstrated. The as-prepared 3D-BC-NP-Pt structures displayed high surface area and typical electrochemical sensing properties comparable to that of commercially available planar platinum electrodes for a reversible diffusing redox couple in an aqueous medium. Exceptional electrochemical sensing capability for the 3D-BC-NP-Pt electrodes in a complex biofouling environment containing fibrinogen as a biofouling agent was evidenced while the commercial planar platinum electrodes failed to produce any reasonable signal. The 3D-BC-NP-Pt electrodes displayed remarkably high catalytic activity toward the methanol electro-oxidation that is 30 times higher than that of planar platinum electrodes and high volumetric capacitance of 400 F/cm<sup>3</sup>. These findings will pave the way toward the development of high performance and reliable electrodes for catalysis, sensing, high power outputs fuel cells, battery-like supercapacitors and miniaturized device applications.

## 6.2 Future Work

My future work will involve the generalization of the developed methods to prepare new porous structures, especially the metallic ones. Investigating the possible technological



applications of the newly developed porous structures in electrochemical sensing, electrocatalysis (e.g. alcohol fuel cells and ORR) and energy storage.

### **6.2.1 Electroassisted Fabrication of Metal/Sol-Gel Nanocomposites**

The electrochemically assisted metal/sol-gel nanocomposite fabrication route can be extended to prepare a large number of silica-metal nanocomposites and upon silica dissolution, the formation of new porous metal structure is possible. Other metal oxides (e.g.  $\text{SnO}_2$ ) and their corresponding metal nanocomposites can be prepared. For example,  $\text{SnO}_2$ -Ni and  $\text{SnO}_2$ - $\text{Ni}_x\text{O}_y$  for lithium ion battery applications.

Also, the combination of the metal/sol-gel route and the hard templating approach can be applied to fabricate hierarchical nanoporous metal structures. For example, electrodeposition of metal-metal oxide nanocomposite films within the voids of silica or polystyrene colloidal crystals.

#### **6.2.1.1 Fabrication of Hierarchical Nanoporous Metal Structures Using Colloidal Silica**

First, silica nanoparticles (500-1000 nm) will be prepared by Stöber method in which the ammonia will catalyze the hydrolysis and polycondensation of a silicon alkoxide precursor in  $\text{H}_2\text{O}/\text{C}_2\text{H}_5\text{OH}$  system.<sup>1</sup> Then the surface of the silica particle will undergo modification using amino silane.<sup>2, 3</sup> Second, a solid template will be formed through evaporation induced self-assembly technique,<sup>4, 5</sup> where a cleaned gold slide will be immersed in alcoholic or aqueous solution of cysteamine overnight to induce the formation of a self-assembled monolayer. Then the functionalized gold substrate will be transferred into a glass vial containing an alcoholic solution of the silica nanoparticles at 50 °C for 12 h to form a colloidal crystal of the silica spheres.<sup>4, 5</sup> The

M-SiO<sub>2</sub> nanocomposite will deposit by the electrochemically induced metal/sol-gel route. Chemically etching of silica in HF will result in the formation of hierarchical structures.

#### **6.2.1.2 Fabrication of Hierarchical Nanoporous Metal Structures Using Polystyrene**

Polystyrene spheres of different diameters are commercially available plus the synthesis of polystyrene spheres is a straightforward.<sup>6</sup> Hexagonal close packed template of polystyrene spheres (500-2000 nm) can be prepared by following the same procedures in 5.2.1.1 and substituting the colloidal silica spheres with the polystyrene spheres.<sup>4</sup> By electrodeposition of a metal/sol-gel derived nanocomposite followed by the dissolution of the polystyrene template using a suitable solvent (e.g. chloroform, chloroform/acetone, THF or toluene) a hierarchical structure will be evolved. The structure of the prepared nanocomposites and the efficiency of the template removal will be examined using SEM and EDX. The electrochemically active surface area of the proposed electrodes will be measured by means of cyclic voltammetry and a comparison to the geometric area and to the area of planar electrodes will be made in order to examine the success of the proposed methodologies.

#### **6.2.1.3 Fabrication of Hierarchical Nanoporous Metal Structures Using Perpendicular Silica**

A thin film of vertically oriented silica mesochannels on a conductive substrate can be prepared easily by using a modified Stöber solution (H<sub>2</sub>O, C<sub>2</sub>H<sub>5</sub>OH, NH<sub>4</sub>OH and TEOS + CTAB).<sup>7</sup> The coelectrodeposition of M-SiO<sub>2</sub> nanocomposites or M-precious metal alloys through the perpendicular silica mesochannels followed by SiO<sub>2</sub> or the less noble metal etching will result in the formation of hierarchical structures.

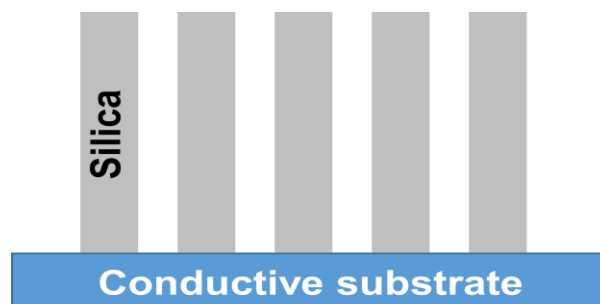


**Figure 6.1.** Graphical representation of a perpendicular silica structure

### **6.2.2 Electroassisted Fabrication of Polymer-Metal/Metal Oxide Nanocomposites**

Based on the desired application a variety of conducting polymer-metal/metal oxide nanocomposites can be easily prepared. Thermal treatment of the as-prepared nanocomposites at high temperatures (e.g. 800 °C) will produce porous carbon-metal/metal oxides nanocomposites for potential applications in fuel cells, ORR and energy storage (e.g. batteries and supercapacitors). For example, electrodeposition of polypyrrole-metal/metal oxides nanocomposites nanowires is expected to produce a high energy output capacitors and batteries. For catalysis applications, metal catalyst nanoparticles can be cathodically deposited simultaneously on and within the growing polymer framework. This will enable an efficient distribution of the catalyst nanoparticles within the porous polymer network and thus enhanced catalytic performance.

### **6.2.3 Bicontinuous Porous Platinum**

This will be my first future project. There is a lot of knowledge and information that can be gained by studying this system. For example, the different parameters affecting the electrodeposition reaction need to be studied. The formation of new morphologies are expected.

Extensive study of the applications of the newly developed porous platinum in electrochemical sensing, drug delivery, electrocatalysis and energy storage could help in the development of new sensors, efficient catalysts and portable electronics. A large variety of hierarchical nanoporous platinum structures can be also obtained by combining the developed strategy for fabricating porous platinum with the hard templating approach. For example, electrodeposition of Pt-Ag binary alloy films within the voids of silica or polystyrene colloidal crystals.

Due to the biosieving nature and excellent biocompatibility of the as-prepared porous platinum, it is expected that it will overweight the best known sensor so far in biofouling environments, bicontinuous nanoporous gold. For example, many blood storing facilities are stabilizing blood through the addition of citrate that inhibits the blood clotting mechanism. It is not ideal to examine such blood samples using nanoporous gold electrode due to adsorption of the citrate ions on the gold electrode surface. Porous platinum electrodes are expected to behave much better than gold in such complex environments.

Platinum is a powerful catalyst that can be used in many applications. The as-prepared porous platinum electrodes can be used in producing high current/energy outputs fuel cells. This is quite important for military and space applications. The high catalytic activity of platinum can also be used to develop new energy-saving sensors. For example, due to the high surface, nano-confinement and catalytic features of porous platinum it is expected that it will reduce the potential required for many electrochemical reaction, for example ascorbic acid oxidation. Such proposed sensors could be important in military and space applications when energy supplies are limited.

Due to the high volumetric capacitance of the prepared porous platinum it can be used in the production of batter-like supercapacitors especially after simple modifications such as depositing a thin layer of polymer or graphene on its surface. These capacitors are expected to beat the current market batteries because they can be charged in seconds.

### 6.3 References

1. Stöber, W.; Fink, A.; Bohn, E., Controlled Growth of Monodisperse Silica Spheres in the Micron Size Range. *Journal of Colloid and Interface Science* **1968**, 26, (1), 62-69.
2. Paunescu, D.; Puddu, M.; Soellner, J. O. B.; Stoessel, P. R.; Grass, R. N., Reversible DNA Encapsulation in Silica to Produce ROS-Resistant and Heat-Resistant Synthetic DNA 'Fossils'. *Nature Protocols* **2013**, 8, (12), 2440-2448.
3. Graf, C.; Gao, Q.; Schütz, I.; Noufele, C. N.; Ruan, W.; Posselt, U.; Korotianskiy, E.; Nordmeyer, D.; Rancan, F.; Hadam, S.; Vogt, A.; Lademann, J. r.; Haucke, V.; Rühl, E., Surface Functionalization of Silica Nanoparticles Supports Colloidal Stability in Physiological Media and Facilitates Internalization in Cells. *Langmuir* **2012**, 28, (20), 7598-7613.
4. Zhao, B.; Collinson, M. M., Well-Defined Hierarchical Templates for Multimodal Porous Material Fabrication. *Chemistry of Materials* **2010**, 22, (14), 4312-4319.
5. Heim, M.; Reculosa, S.; Ravaine, S.; Kuhn, A., Engineering of Complex Macroporous Materials Through Controlled Electrodeposition in Colloidal Superstructures. *Advanced Functional Materials* **2012**, 22, (3), 538-545.
6. Telford, A. M.; Pham, B. T. T.; Neto, C.; Hawket, B. S., Micron-Sized Polystyrene Particles by Surfactant-Free Emulsion Polymerization in Air: Synthesis and Mechanism. *Journal of Polymer Science Part A: Polymer Chemistry* **2013**, 51, (19), 3997-4002.
7. Teng, Z. G.; Zheng, G. F.; Dou, Y. Q.; Li, W.; Mou, C. Y.; Zhang, X. H.; Asiri, A. M.; Zhao, D. Y., Highly Ordered Mesoporous Silica Films with Perpendicular Mesochannels by a Simple Stober-Solution Growth Approach. *Angewandte Chemie-International Edition* **2012**, 51, (9), 2173-2177.

## Vita

AHMED A. FARGHALY, Ph.D.



1001 West Main Street, P.O. Box 842006  
Chemistry Department, Virginia Commonwealth University,  
Richmond, Virginia 23284-2006, USA

Chemistry Department, Faculty of Science, Assiut University,  
Assiut 71516, Egypt (Permanent Mailing Address)  
Tel: 001-804-300-0485; E-Mail: [abozeedfaraa@vcu.edu](mailto:abozeedfaraa@vcu.edu)

---

### *Personal Data*

Date and Place of Birth: 20 November 1980; Assiut, Egypt

### *Academic Education*

1. Ph.D. Chemistry Department, Virginia Commonwealth University, Richmond, Virginia USA. May 2016.  
Dissertation title “Fabrication of Multifunctional Nanostructured Porous Materials”.  
Advisor: Prof. Maryanne M. Collinson ([mmcollinson@vcu.edu](mailto:mmcollinson@vcu.edu)).
2. M.Sc. (*Inorganic Chemistry*) Chemistry Department, Faculty of Science, Assiut University, Assiut, Egypt February, 2008.  
Thesis title “Transition Metal Complexes of Some Ligands Containing Triazole Nucleus”.  
Advisor: Prof. Said A. Ibrahim ([saidibrahim7@yahoo.com](mailto:saidibrahim7@yahoo.com)).
3. B.Sc. (*Chemistry*) with Honors Degree, Assiut University, Egypt July, 2001 [Top Senior among my colleagues ~ 100, this based on the cumulative scores I collected during my 4-year B.Sc.].

## ***Professional Appointments and Research Experience***

Ahmed Farghaly is an electrochemist, synthetic chemist, nano and materials scientist with excellent lab and microscopic skills, expert in a wide range of characterization and electrochemical techniques and has a solid teaching and research experience (15 years). Ahmed's research motto: "There is nothing impossible; it always deserves a shot."

1. Graduate Teaching and Research Assistant: Chemistry Department, Virginia Commonwealth University, From August 2010- May 2016.
2. Associate Lecturer: Chemistry Department, Assiut University, From April 2008- July 2010 (Faculty position: **Tenured position**). **Note:** Upon my arrival to Egypt I will appointed as **Assistant Professor** at Assiut University.
3. Teaching and Research Assistant: Chemistry Department, Assiut University 2001- March 2008.
4. Excellent professional in electrodeposition and electroanalytical techniques.
5. Excellent professional in electrodes preparations for electrochemical sensing, fuel cells and supercapacitors applications.
6. Excellent professional in the nanoparticles synthesis and characterization.
7. Excellent professional in the use of high pressure reactors for the supercritical synthesis of nanomaterials.
8. Excellent professional in running reactions at high temperature and pressures using toxic and flammable gases (e.g. CO and H<sub>2</sub>).
9. Excellent professional in large scale synthesis of nanoparticles using pilot plant.
10. Mentored many undergraduate students.
11. **Opened collaborations with many research labs in Chemistry (Dr. Indika and Dr. Hani), Physics (Dr. Ye), Chemical and Life Sciences Engineering, and Biomedical Engineering Departments (Dr. Wen, Dr. Vamsi and Dr. Gupta) at VCU.**

## ***Projects***

1. DOE React (Rare-earth free permanent magnets) 2011 –2013. Design and synthesis of rare-earth free carbide based permanent magnet materials through various synthetic methods.
2. FASCDP Project for "Development of the Faculty of Science, Assiut University, Egypt".
3. DONACC Project: "Development of New Analytical Chemistry Curriculum in the Faculties of Science in Upper Egypt" ([www.donacc.edu.eg](http://www.donacc.edu.eg)).



***Material Characterization at Chemistry Department and Nanomaterials Core Characterization Facility, VCU, Richmond, VA***

Expert in materials characterization using the following techniques:

- Cyclic Voltammetry
- Potentiometry
- Open Circuit Potentiometry (OCP)
- Chronoamperometry
- Galvanostatic Charge-Discharge
- Impedance Spectroscopy
- Oxygen Reduction Reaction (ORR)
- X-ray Diffraction (XRD)
- X-ray data processing using High Score Software.
- Vibrating Sample Magnetometer (VSM)
- Energy-dispersive X-ray spectroscopy (EDS)
- X-ray photoelectron spectroscopy (XPS) and data processing using CASA software.
- Inductively Coupled Plasma - Optical Emission Spectrometry (ICP-OES)
- Inductively Coupled Plasma - Mass Spectrometry (ICP-MS)
- Transmission electron microscopy (TEM)
- High Resolution Transmission electron microscopy (HRTEM)
- Scanning Electron Microscopy (SEM)
- High Resolution Scanning Electron Microscopy (HRSEM)
- Surface Profilometry: Thin Films Thickness measurement
- BET Surface Area and Pore Size Analysis
- UV-Visible Spectroscopy,
- Raman Spectroscopy,
- Fourier transform infrared spectroscopy (FT-IR)
- Thermal analysis (TG, DTG, DTA and DSC)
- Dynamic Light Scattering (DLS)
- Nuclear Magnetic Resonance (NMR)

### ***Fields of Research Interest:***

Electroanalytical Chemistry and Electrocatalysis: Cyclic Voltammetry, Potentiometry, Chronoamperometry, Galvanostatic Charge-Discharge and Impedance Spectroscopy, **Nanoporous metal electrodes**, Electrodeposition, Fuel Cells, Supercapacitors, Oxygen Reduction Reaction (ORR) and sensing.

Material science: Nanoporous materials, nanocomposites, conducting polymers, nanoparticle and nanostructure synthesis and characterization (special focus on metallic and magnetic nanoparticles).  
Supercritical fluids synthesis of nanoparticles and Digestive Ripening.  
HOMO and LUMO energy levels and band gap measurements for polymeric materials and organic compounds using electrochemical methods.  
Thin film preparation using chemical and physical methods.  
Colloidal crystal assembly (e.g. polystyrene).

Inorganic Chemistry: Nanomaterials & Synthesis and characterization of coordination compounds by spectrometric, magnetic and thermal techniques.

Organic Chemistry: Hyperbranched polymers (e.g. polyethylene), polystyrene spheres synthesis and conducting polymers electrosynthesis, chelating agents and coordinating ligands synthesis (e.g. triazole thiols).

Catalysis and electrocatalysis: C-C coupling reactions (Palladium complexes, nanoporous palladium and palladium nanoparticles impeded in polymer matrix and magnetic palladium catalysts). Ethanol and methanol direct fuel cell and ORR.

### ***Teaching Experiences***

2001 to 2008 Associated Lecture of Chemistry Assiut University, Egypt.

2008-2016 (till now) Teaching Assistant, Chemistry Department, Virginia Commonwealth University, Richmond, VA, USA.

Some of the courses/labs I taught at VCU and Assiut University are:

- Chemz309 Quantitative Chemical Analysis Lab
- Chemz101 General Chemistry Lab and Recitation
- Chemz102 General Chemistry Lab and Recitation
- Instrumental Analysis Lab (e.g. potentiometry, spectrophotometry ... etc) for graduate students.
- Advanced Inorganic Chemistry Lab (complexes preparation and characterization).
- Advanced Physical Chemistry Lab (surface, kinetics, phase rule, ....etc)

- Gravimetric Chemical Analysis Lab
- Advanced Volumetric Chemical Analysis Lab
- General Physical Chemistry Lab

## **Publications**

*Patents, some recent published materials, and conferences:*

*Note: In recent patents and publications the first and last names were used while in the older publications the first and middle names were used.*

### **Patents:**

1. NON-RARE EARTH MAGNETIC NANOPARTICLES  
United States Patent PCT/US2013/020214, Nov. 07, 2013.  
E. E. Carpenter, Z. J. Huba, K. J. Carroll, **A. Farghaly**, S. N. Khanna, M. Qian and M. Bertino, Non-rare earth magnetic nanoparticles. Google Patents.
2. Invention Disclosure, VCU: THREE-DIMENSIONAL BI-CONTINUOUS NANOPOROUS PLATINUM: A POWERFUL CATALYST AND SENSOR.  
**Ahmed A. Farghaly** and Maryanne M. Collinson

### **Publications:**

1. Microdroplet-Based Potentiometric Redox Measurements on Gold Nanoporous Electrodes. Christopher J. Freeman, **Ahmed A. Farghaly**, Hajira Choudhary, Amy E. Chavis, Kyle T. Brady, Joseph E. Reiner, and Maryanne M. Collinson. *Analytical Chemistry* **2016**, 88 (7), 3768-3774.
2. Conducting polymer-silk biocomposites for flexible and biodegradable electrochemical sensors. Ramendra K. Pal, **Ahmed A. Farghaly**, Congzhou Wang, Maryanne M. Collinson, Subhas C. Kundu, Vamsi K. Yadavalli. *Biosensors and Bioelectronics* **2016**, 81, 294-302.
3. Monoclinic Hydroxyapatite Nanoplates Hybrid Composite with Improved Compressive Strength, and Porosity for Bone Defect Repair: Biomimetic Synthesis and Characterization. Bo Xue,\* **Ahmed A. Farghaly**,\* Zhenzhao Guo, Peng Zhao and Hong Li, Changren Zhou, Lihua Li. *Journal of Nanoscience and Nanotechnology* **2016**, 16 (3), 2254-226.  
**\*Equally Contributed**
4. Potentiometric Measurements in Biofouling Solutions: Comparison of Nanoporous Gold to Planar Gold. **Ahmed A. Farghaly**, Mai Lam, Christopher J. Freeman, Badharinadh Uppalapati and Maryanne M. Collinson. *Journal of The Electrochemical Society* **2016**, 163 (4), H3083-H3087.
5. Photolithographic Micropatterning of Conducting Polymers on Flexible Silk Matrices. Ramendra K. Pal, **Ahmed A. Farghaly**, Maryanne M. Collinson, Subhas C. Kundu, Vamsi K. Yadavalli *Advanced Materials* **2016**, 28 (7), 1406–1412.

6. Electroassisted Codeposition of Sol–Gel Derived Silica Nanocomposite Directs the Fabrication of Coral-like Nanostructured Porous Gold. **Ahmed A. Farghaly** and Maryanne M. Collinson. *Langmuir* **2014**, *30*, (18), 5276-5286.
7. Magnetic field assisted polyol synthesis of cobalt carbide and cobalt microwires. **Ahmed A. Farghaly\***, Zachary J. Huba, and Everett E. Carpenter. *Journal of Nanoparticle Research* **14**, **2012**.
8. Synthesis and characterization of novel polymeric biologically active mixed ligand triazole-3-thiones Complexes. M.A. El-Gahami, S.A. El-Gyar, **A. Abd El-Sameh\*** and S.A. Ibrahim. *Inorganic Chemistry: An Indian Journal* **4** (4), **2009**.
9. Thermal stability, thermokinetic, and decomposition mechanism of copper(II) triazole-3-thiones complexes. S.A. El-Gyar, M.A. El-Gahami, **A. Abd El-Sameh\*** and S.A. Ibrahim. *Inorganic Chemistry: An Indian Journal* **4** (3), **2009**.
10. Synthesis, thermal decomposition, magnetic properties and biological activities of Co(II), Ni(II), Cu(II) and Cd(II) complexes of some triazole-3-thione Schiff bases. S.A. El-Gyar, M.A. El-Gahami, **A. Abd El-Sameh\*** and S.A. Ibrahim. *Polish Journal of Chemistry*, **81**, 1387 (**2007**).

**In preparation:** (Titles are tentative)

11. Mesoporous Hybrid Polypyrrole-Silica Nanocomposite Films with a Strata-Like Structure. **Ahmed A. Farghaly** and Maryanne M. Collinson. (*Submitted to Langmuir* )
12. Three-Dimensional Bi-Continuous Nanoporous Platinum. **Ahmed A. Farghaly** and Maryanne M. Collinson. (*Target Journal: Advanced Materials*)
13. Synthesis of Pd Aerogels and Their Application in Direct Ethanol Fuel Cells. Lamia Nahar, **Ahmed A. Farghaly**, Maryanne M. Collinson, Indika U Arachchige (*Target Journal: JACS*)
14. Synthesis of Pt Aerogels and Their Application in Direct Methanol Fuel Cells. Xiaonan Gao, **Ahmed A. Farghaly**, Maryanne M. Collinson, Indika U Arachchige (*Target Journal: Not determined yet*)

**Fellowships and Awards:**

- 2016 Electrochemical Society Student Membership Award
- 2015 Elsevier Outstanding Reviewer Award- European Journal of Medicinal Chemistry
- 2015 Graduate School Scholarship Award, Virginia Commonwealth University
- 2015 Graduate School Travel Grant Award, Virginia Commonwealth University
- 2015 Electrochemical Society Student Membership Award
- 2014 Electrochemical Society Student Membership Award
- In 2014 Ahmed's participated in the *Through the Looking Glass, VCU microscopy image contest*, Ahmed's HR-SEM image for the nanostructured porous gold corals has been

chosen to join the VCU image gallery and featured on the VCU homepage in August 2014.

- 2010 Teaching and Research Assistant Scholarship at Virginia Commonwealth University
- 2010, Ahmed received Prof. Dr. Raafat Mahmoud award in Chemistry for his research on the biologically active triazole thiol complexes. More than a hundred graduate students competed for it. This work is published in *Polish Journal of Chemistry*, 2007 81, 1387 (Ahmed et. al).
- Ideal/ Role Model Student Award (during undergraduate study)

### ***Professional Membership***

Electrochemical Society

### ***Reference Professors:***

1. Dr. Maryanne M. Collinson. (Ph.D. Dissertation Advisor)  
Professor of Chemistry & Director of Graduate Recruitment  
1001 West Main Street, Department of Chemistry, Virginia Commonwealth University,  
Richmond VA, 23284.  
Email: [mmcollinson@vcu.edu](mailto:mmcollinson@vcu.edu)
2. Dr. Ram B. Gupta  
Associate Dean for Research, School of Engineering  
Professor, Department of Chemical and Life Science Engineering  
Virginia Commonwealth University  
601 West Main Street, Suite 331, Richmond, VA 23284-3068  
Email: [rbgupta@vcu.edu](mailto:rbgupta@vcu.edu)
3. Dr. Hani M.El-Kaderi  
Associate Professor of Inorganic and Materials Chemistry  
1001 West Main Street, Department of Chemistry, Virginia Commonwealth University,  
Richmond VA, 23284.  
Email: [helkaderi@vcu.edu](mailto:helkaderi@vcu.edu)
4. Dr. Joseph Topich  
Assistant Professor of Inorganic Chemistry  
1001 West Main Street, Department of Chemistry, Virginia Commonwealth University,  
Richmond VA, 23284.  
Email: [jtopich@vcu.edu](mailto:jtopich@vcu.edu)

5. Dr. Said A. Ibrahim (M.Sc. Thesis Advisor)  
Professor of Inorganic Chemistry, Chemistry Department, Assiut University, Egypt.  
Former Vice-President for Education & Students' Affairs, Assiut University, Egypt.  
Email: [saidibrahim7@yahoo.com](mailto:saidibrahim7@yahoo.com)
  
6. Prof. Dr. Mohamed A. El-Gahami (M.Sc. Thesis Advisor)  
Professor of Inorganic Chemistry, Chemistry Department, Assiut University, Egypt.  
Former Vice-Dean, Faculty of Education, New Valley, Assiut University, Egypt.  
Email: [maelgahami@yahoo.com](mailto:maelgahami@yahoo.com)
  
7. Dr. Indika U. Arachchige  
Assistant Professor of Inorganic and Materials Chemistry  
1001 West Main Street, Department of Chemistry, Virginia Commonwealth University,  
Richmond VA, 23284.  
Email: [iuarachchige@vcu.edu](mailto:iuarachchige@vcu.edu)